

**URBAN LAND SURFACE TEMPERATURE
MITIGATION BY USING URBAN
GREEN SPACE SIMULATION**



**A Thesis Submitted in Partial Fulfillment of the Requirements for the
Degree of Doctor of Philosophy in Geoinformatics
Suraneree University of Technology
Academic Year 2019**

การลดอุณหภูมิพื้นผิวที่ดินเขตเมืองโดยการจำลองพื้นที่สีเขียวของเมือง



นายเอกลักษณะ สลักคำ

วิทยานิพนธ์นี้เป็นส่วนหนึ่งของการศึกษาตามหลักสูตรปริญญาวิทยาศาสตรดุษฎีบัณฑิต

สาขาวิชาภูมิสารสนเทศ

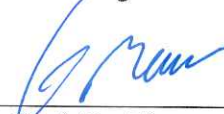
มหาวิทยาลัยเทคโนโลยีสุรนารี

ปีการศึกษา 2562

**URBAN LAND SURFACE TEMPERATURE MITIGATION
BY USING URBAN GREEN SPACE SIMULATION**

Suranaree University of Technology has approved this thesis submitted in partial fulfillment of the requirements for the Degree of Doctor of Philosophy.

Thesis Examining Committee



(Assoc. Prof. Dr. Worawat Meevasana)

Chairperson


(Asst. Prof. Dr. Pantip Piyatadsananon)

Member (Thesis Advisor)


(Assoc. Prof. Dr. Songkot Dasananda)

Member

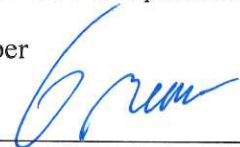

(Assoc. Prof. Dr. Suwit Ongsomwang)

Member

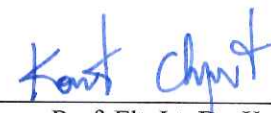

(Assoc. Prof. Dr. Nittaya Kerdprasop)

Member


(Asst. Prof. Dr. Pipat Reungsang)

Member


(Assoc. Prof. Dr. Worawat Meevasana)



(Assoc. Prof. Flt. Lt. Dr. Kontorn Chamnirasart)

Vice Rector for Academic Affairs
and Internationalization

Dean of Institute of Science

เอกลักษณ์ สลักคำ : การลดอุณหภูมิพื้นผิวที่ดินเขตเมือง โดยการจำลองพื้นที่สีเขียวของเมือง (URBAN LAND SURFACE TEMPERATURE MITIGATION BY USING URBAN GREEN SPACE SIMULATION) อาจารย์ที่ปรึกษา : ผู้ช่วยศาสตราจารย์ ดร.พนทิพย์ ปิยะทัศนานนท์, 203 หน้า.

อุณหภูมิภายในเมืองที่เพิ่มสูงขึ้นกลายเป็นประเด็นทางด้านสิ่งแวดล้อมที่สำคัญ เนื่องจากอุณหภูมิพื้นผิวที่ดินและอุณหภูมิอากาศที่เพิ่มสูงขึ้นส่งผลกระทบต่อสุขภาพและความสะดวกสบายของผู้อยู่อาศัยภายในเมือง การปรับปรุงจุลภูมิอากาศ (Microclimate) ควรได้รับการพิจารณาเพื่อสร้างสภาพแวดล้อมที่เหมาะสมต่อการอยู่อาศัย ซึ่งการเพิ่มสัดส่วนพื้นที่สีเขียวของเมืองถือเป็นวิธีบรรเทาปัญหาที่มีประสิทธิภาพวิธีหนึ่ง การวิจัยครั้งนี้มีวัตถุประสงค์หลัก ได้แก่ (1) เพื่อหาวิธีการประมาณค่าอุณหภูมิพื้นผิวที่ดินเขตเมืองที่เหมาะสม (2) เพื่อประมาณค่าอุณหภูมิพื้นผิวที่ดินที่มีความแยกชัดเชิงพื้นที่ที่ดียิ่งขึ้นด้วยวิธีการทางสถิติ (3) เพื่อจำแนกพื้นที่ที่จู้จี้ร้อน โดยอาศัยข้อมูลอุณหภูมิพื้นผิวที่ดินที่ได้รับการปรับปรุงความแยกชัดเชิงพื้นที่ และ (4) เพื่อจำลองการลดอุณหภูมิของพื้นที่จู้จี้ร้อน โดยอาศัยสัดส่วนพื้นที่สีเขียวของเมือง

ผลการวิจัย พบว่า อุณหภูมิพื้นผิวที่ดินที่ประมาณค่าโดยวิธีสพลิทวินโดว (Split-window) มีค่าความคลาดเคลื่อนของอุณหภูมิต่ำที่สุด โดยเฉพาะกรณีที่มีปริมาณไอน้ำในบรรยากาศมากกว่า 2.70 กรัมต่อตารางเซนติเมตร ซึ่งการศึกษาครั้งนี้วิธีสพลิทวินโดวเป็นวิธีที่มีความเหมาะสมต่อการนำไปใช้ประมาณค่าอุณหภูมิพื้นผิวที่ดินภายในเมือง อย่างไรก็ตาม ค่าปริมาณไอน้ำในบรรยากาศเป็นปัจจัยหนึ่งที่มีผลต่อความคลาดเคลื่อนของอุณหภูมิพื้นผิวที่ดินที่ได้จากการประมาณค่า ขณะที่การปรับปรุงความแยกชัดเชิงพื้นที่ของข้อมูลอุณหภูมิพื้นผิวที่ดินด้วยวิธีการทางสถิติ พบว่าอุณหภูมิพื้นผิวที่ดินที่ได้รับการปรับปรุงความแยกชัดเชิงพื้นที่ด้วยวิธีการทางสถิติมีค่าความคลาดเคลื่อนของอุณหภูมิลดลง โดยความคลาดเคลื่อนของอุณหภูมิพื้นผิวที่ดินลดลงมากกว่า 0.30 องศาเซลเซียส สำหรับพื้นที่จู้จี้ร้อนที่ถูกจำแนกด้วยข้อมูลอุณหภูมิพื้นผิวที่ดินที่ได้รับการปรับปรุงความแยกชัดเชิงพื้นที่นั้น ได้แก่ พื้นที่เปิดโล่ง สนามกีฬา และพื้นที่สิ่งปลูกสร้าง โดยพื้นที่จู้จี้ร้อนส่วนใหญ่จะพบบริเวณเดิม แต่ขอบเขตของพื้นที่จะเปลี่ยนแปลงไปตามสภาพอากาศ สำหรับการวิเคราะห์ที่ดินและสิ่งปกคลุมดินของพื้นที่สิ่งปลูกสร้างประเภทอาคารค้าปลีกประกอบด้วยพื้นที่อาคาร ถนน และพื้นที่สีเขียว อย่างไรก็ตาม พื้นที่สีเขียวมีสัดส่วนพื้นที่น้อยกว่าพื้นที่ประเภทอื่น ๆ ขณะที่การลดอุณหภูมิพื้นผิวที่ดินของพื้นที่จู้จี้ร้อน พบว่า พื้นที่สีเขียวต้องมีขนาดพื้นที่คิดเป็นสัดส่วนมากกว่า 0.30 ของพื้นที่ (ร้อยละ 30 ของพื้นที่) จึงจะสามารถลดอุณหภูมิพื้นผิวที่ดินของพื้นที่จู้จี้ร้อนให้มีอุณหภูมิใกล้เคียง หรือเท่ากับพื้นที่รอบข้าง อย่างไรก็ตาม เนื่องจากข้อจำกัดเรื่อง

พื้นที่ภายในเขตเมือง การลดอุณหภูมิเขตเมืองด้วยวิธีอื่น ๆ ควรได้รับการพิจารณาเพื่อใช้ร่วมกับวิธีการเพิ่มสัดส่วนพื้นที่สีเขียวของเมือง นอกจากนี้ พื้นที่สีเขียวจะมีอิทธิพลต่อการลดอุณหภูมิได้มากยิ่งขึ้นเมื่ออุณหภูมิของสภาพอากาศมีค่าสูง



สาขาวิชาภูมิสารสนเทศ
ปีการศึกษา 2562

ลายมือชื่อนักศึกษา _____

ลายมือชื่ออาจารย์ที่ปรึกษา _____

EKKALUK SALAKKHAM : URBAN LAND SURFACE TEMPERATURE
MITIGATION BY USING URBAN GREEN SPACE SIMULATION.

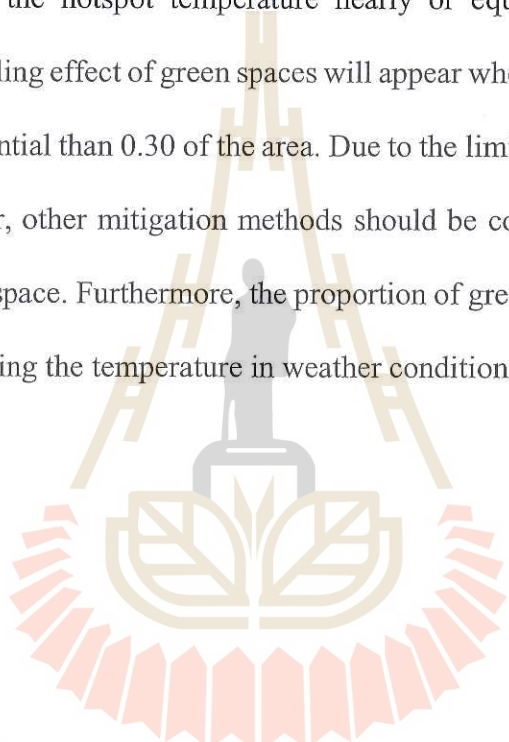
THESIS ADVISOR : ASST. PROF. PANTIP PIYATADSANANON,
Ph.D., 203, PP.

RADIATIVE TRANSFER EQUATION / IMPROVED MONO-WINDOW /
GENERALIZE SINGLE-CHANNEL / SPLIT-WINDOW / SUBPIXEL LST /
URBAN LAND SURFACE TEMPERATURE / URBAN GREEN SPACE /

The problem from the rising temperature in urban areas becomes a critical environmental issue. Because high surface and air temperature environments negatively impact human health and comfort. Therefore, urban microclimate improvement is a crucial consideration regarding archive sustainability in a city. Based on the literature reviews, urban green spaces play the most effective heat mitigation. The principal objective of this research include (1) to explore the optimum method for ULST estimation, (2) to estimate subpixel LST data using statistical-based method, (3) to identify the hotspots areas based on subpixel LST data, and (4) to simulate hotspot mitigation associated with proportions of green space in urban area.

Regarding the finding, the split-window algorithm is the optimum method in ULST estimation for this study. This algorithm provides the lowest NRMSE values in most cases, which had the amount of atmospheric water vapor content larger than 2.70 g cm^{-2} . Furthermore, the amount of atmospheric water vapor content plays an essential role in terms of accuracy. It shows that the subpixel LST data provides lower error than estimated LST data, with the differentiated temperature larger than $0.3 \text{ }^{\circ}\text{C}$. Based on

subpixel LST data, the hotspot areas are found in bare-lands, race tracks, and built-up areas. Most of the hotspot areas occur at the same locations. However, the boundaries of the hotspot areas are different, depending on the weather conditions. The main LULC types in hotspot areas are commercial areas, constructions, roads, and green space. However, the proportion of green space is deficient when compared with other LULC types. To decrease the hotspot temperature nearly or equal to surrounding areas temperature, the cooling effect of green spaces will appear when the proportion of green space is more substantial than 0.30 of the area. Due to the limited available land area in most cities, however, other mitigation methods should be considered to use with the proportion of green space. Furthermore, the proportion of green space has a significant influence on decreasing the temperature in weather conditions with high temperature.



มหาวิทยาลัยเทคโนโลยีสุรนารี

School of Geoinformatics

Academic Year 2019

Student's Signature

Advisor's Signature




ACKNOWLEDGMENTS

Foremost, I would like to express my sincere gratitude to my advisor, Asst. Prof. Dr. Pantip Piyatadsananon, for her continuous support, her patience, enthusiasm, helpful suggestions, and also support my study with One Research One Graduate (OROG) scholarship. Furthermore, I would like to thank the chairperson and committee members, Assoc. Prof. Dr. Worawat Meevasana, Assoc. Prof. Dr. Suwit Ongsomwang, Assoc. Prof. Dr. Songkot Dasananda, Assoc. Prof. Dr. Nittaya Kerdprasop and Asst. Prof. Dr. Pipat Reungsang for their several useful comments on my work. I wish to extend my special thanks to Dr. Tanakorn Sritarapipat for his helpful comments, Dr. Siripon Kamontum and Asst. Prof. Rinhathai Kitthanarut for their suggestions and recommendations on statistical analysis.

Thanks are also due to the School of Geoinformatics, Institute of Science, Suranaree University of Technology, for allowing me to pursue a Ph.D. program in geoinformatics and to learn more about geoinformatics techniques, which are useful for my work in the future. Also, I would like to thank the Buriram Rajabhat University for the scholarship granted for my study.

Special thanks to great help in ground-based temperature surveying and UAV imaging by students of Geography and Geoinformation Department, Buriram Rajabhat University. Also, I would like to thank my colleagues at the School of Geoinformatics, and my colleagues at the Department of Geography and Geoinformation, Buriram Rajabhat University, for their help and warm encouragement during my study.

Finally, I would like to express my deepest gratitude to my family for giving me eternal love, care and support. Also, I would like to thank Miss Suwimol Yothin for her patience and understanding devoted to me during the period of the study.

Ekkaluk Salakkham



CONTENTS

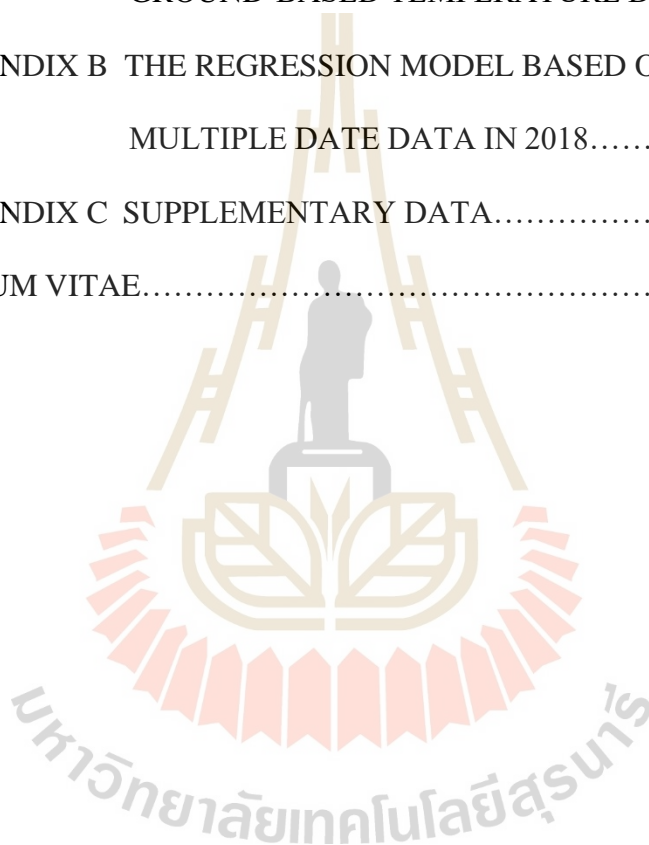
	Page
ABSTRACT IN THAI.....	I
ABSTRACT IN ENGLISH	III
ACKNOWLEDGEMENT.....	V
CONTENTS.....	VII
LIST OF TABLES.....	X
LIST OF FIGURES.....	XII
LIST OF ABBREVIATION.....	XV
CHAPTER	
I INTRODUCTION.....	1
1.1 Background and significances of the study.....	1
1.2 Research objectives.....	7
1.3 Scope and limitations.....	7
1.4 Benefits of the study.....	8
1.5 Study area.....	9
II LITERATURE REVIEWS.....	11
2.1 UHIs phenomena.....	11
2.2 LST estimation using LANDSAT-8 imagery data.....	26
2.3 Subpixel LST estimation.....	37
2.4 Hotspot analysis.....	42
2.5 Urban green spaces.....	47

CONTENTS (Continued)

	Page
III RESEARCH METHODOLOGY	55
3.1 Conceptual framework.....	55
3.2 Data preparation.....	56
3.3 Research procedures.....	58
IV RESULTS AND DISCUSSION	71
4.1 To Explore the optimum method for ULST estimation.....	71
4.2 To Estimate subpixel LST data using the statistical-based method.....	82
4.3 To Identify the hotspots areas based on subpixel LST data.....	94
4.4 To Simulate hotspot mitigation from proportions of green space in the urban area.....	106
V CONCLUSION AND SUGGESTIONS	134
5.1 Optimum Method in ULST Estimation.....	134
5.2 Subpixel LST Estimation by Using Statistical-based Method.....	135
5.3 Hotspot Analysis for Subpixel LST Data.....	136
5.4 Hotspot Mitigation.....	136
5.5 Suggestions.....	137
REFERENCES.....	140
APPENDICES.....	177

CONTENTS (Continued)

	Page
APPENDIX A RELATIONSHIP BETWEEN ESTIMATED LST DATA USING THE OPTIMUM METHOD AND GROUND-BASED TEMPERATURE DATA.....	178
APPENDIX B THE REGRESSION MODEL BASED ON MULTIPLE DATE DATA IN 2018.....	180
APPENDIX C SUPPLEMENTARY DATA.....	182
CURRICULUM VITAE.....	203

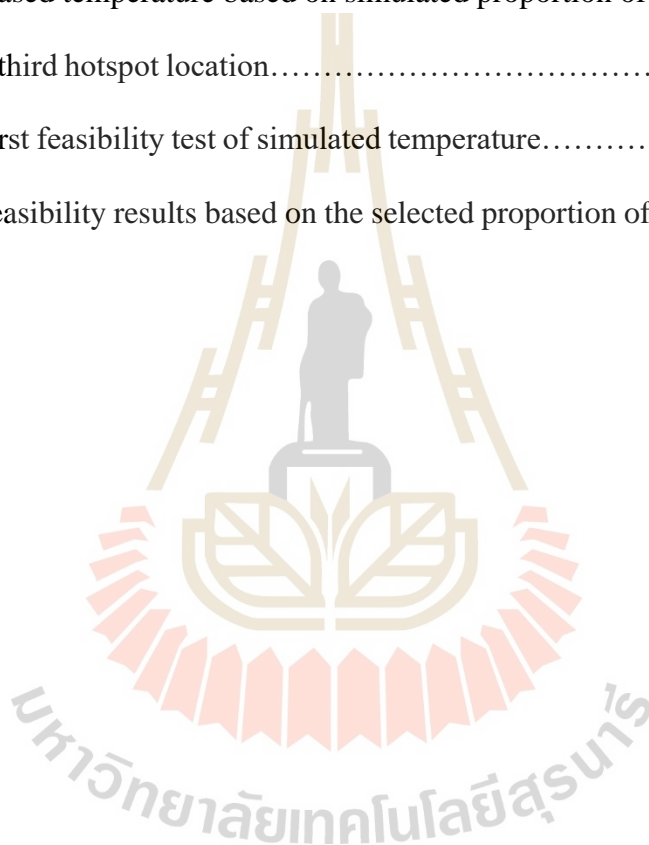


LIST OF TABLES

Table	Page
1.1 The population statistic in 2017.....	4
2.1 The advantages and disadvantages of each method.....	36
3.1 Data used in the research.....	57
3.2 Atmospheric parameters in 2014, 2016, and 2018.....	61
3.3 Spectral indices used in this study.....	65
4.1 The average, maximum and minimum LST data (°C).....	75
4.2 RMSE and NRMSE Values	76
4.3 Regression statistics used in subpixel LST estimation.....	82
4.4 The average, maximum and minimum temperature (°C).....	89
4.5 RMSE and NRMSE values.....	90
4.6 The independent sample t-test results.....	93
4.7 Moran's I result based on data in 2014, 2016, and 2018.....	94
4.8 The average, maximum, and minimum temperature in the hotspot and surrounding areas (°C).....	103
4.9 The differentiated temperature (°C).....	104
4.10 The Pearson correlation statistics.....	106
4.11 The regression statistics.....	110
4.12 The regression models.....	111
4.13 Decreased temperature based on simulated proportion of green space at the first hotspot location.....	112

LIST OF TABLES (Continued)

Table		Page
4.14	Decreased temperature based on simulated proportion of green space at the second hotspot location.....	118
4.15	Decreased temperature based on simulated proportion of green space at the third hotspot location.....	123
4.16	The first feasibility test of simulated temperature.....	131
4.17	The feasibility results based on the selected proportion of green space (°C)..	132



LIST OF FIGURES

Figure	Page
1.1 Buriram municipality.....	9
2.1 Two-layer classification of thermal modification.....	16
2.2 The radiative transfer process over Earth surface in TIR region.....	30
3.1 Conceptual framework	56
3.2 Conceptual process of the first objective.....	58
3.3 Ground-based temperature surveying concept.....	59
3.4 Distribution of sample points and sample sites.....	60
3.5 Conceptual processes of the second objective.....	64
3.6 Conceptual processes of the third objective.....	68
3.7 Conceptual processes of the fourth objective.....	69
4.1 Estimated LST data on January 21, 2018.....	72
4.2 Estimated LST data on February 6, 2018.....	72
4.3 Estimated LST data on March 26, 2018.....	73
4.4 Estimated LST data on April 11, 2018.....	73
4.5 High spatial resolution image map.....	74
4.6 RMSE values based on monthly results.....	76
4.7 NRMSE values based on monthly results.....	76
4.8 LST data and subpixel LST data in 2014 and 2016.....	85
4.9 LST data and Subpixel LST data in 2018.....	87

LIST OF FIGURES (Continued)

Figure	Page
4.10 Compared sample between ground-based temperature, LST, and subpixel LST on April 11, 2018.....	88
4.11 RMSE values based on LST and subpixel LST data.....	90
4.12 NRMSE values based on LST and subpixel LST data.....	91
4.13 Hotspot areas in 2018.....	96
4.14 Hotspot areas on January 21, 2018.....	97
4.15 Hotspot areas on February 6, 2018.....	97
4.16 Hotspot areas on March 26, 2018.....	98
4.17 Hotspot areas on April 11, 2018.....	98
4.18 The daily cumulative rainfall.....	99
4.19 The selected hotspot area: the first location.....	101
4.20 The selected hotspot area: the second location.....	101
4.21 The selected hotspot area: the third location.....	102
4.22 The scatter plots based on the proportion of green space and subpixel LST data in 2018.....	107
4.23 The scatter plots based on the proportion of green space and subpixel LST data in March and April 2014 and 2016.....	108
4.24 The test of normality based on subpixel LST data in April 2018.....	109
4.25 The first hotspot location mitigation based on January 21, 2018.....	113
4.26 The first hotspot location mitigation based on February 6, 2018.....	115
4.27 The first hotspot location mitigation based on March 26, 2018.....	116

LIST OF FIGURES (Continued)

Figure		Page
4.28	The first hotspot location mitigation based on April 11, 2018.....	117
4.29	The second hotspot location mitigation based on January 21, 2018.....	119
4.30	The second hotspot location mitigation based on February 6, 2018.....	120
4.31	The second hotspot location mitigation based on March 26, 2018.....	121
4.32	The second hotspot location mitigation based on April 11, 2018.....	122
4.33	The third hotspot location mitigation based on January 21, 2018.....	124
4.34	The third hotspot location mitigation based on February 6, 2018.....	125
4.35	The third hotspot location mitigation based on March 26, 2018.....	126
4.36	The third hotspot location mitigation based on April 11, 2018.....	127
4.37	Decreased temperature and proportion of green space.....	128

LIST OF ABBREVIATIONS

ATSR	= Along Track Scanning Radiometer
BI	= Bare Soil Index
CLHI	= Canopy Layer Heat Island
DisTrad	= Disaggregation procedure for radiometric surface temperature
EM	= Emissivity Modulation
ERS-1	= European Remote Sensing Satellite
ET	= Effective Temperature Index
FVC	= Fractional Vegetation Cover
GHGs	= Greenhouse Gases
GSC	= Generalized Single-channel method
HUTs	= High-resolution Urban Thermal Sharpener
IBI	= Index-based Built-up Index
IMW	= Improved Mono-window algorithm
ISA	= Impervious Surface Area
ITOS	= Improved TIROS Operational Satellite
LSE	= Land Surface Emissivity
LST	= Land Surface Temperature
LULC	= Land-use and Land-cover
LWIR	= Long Wavelength Infrared
MAE	= Mean Absolute Error
MNDWI	= Modified Normalized Difference Water Index

LIST OF ABBREVIATIONS (Continued)

MW	= Mono-window algorithm
NDBaI	= Normalized Difference Bareness Index
NDBI	= Normalized Difference Built-up Index
NDISI	= Normalized Difference Impervious Surface Index
NDMI	= Normalized Difference Moisture Index
NDVI	= Normalized Difference Vegetation Index
NDWI	= Normalized Difference Water Index
NRMSE	= Normalized Root Mean Square Error
OLI	= Operational Land Imager
PCI	= Park Cool Island
PBIM	= Pixel Block Intensity Modulation
RMSE	= Root Mean Square Error
RTE	= Radiative Transfer Equation
RTM	= Radiative Transfer Model
SAVI	= Soil-adjusted Vegetation Index
SR	= Scanning Radiation
SST	= Sea Surface Temperature
SUHI	= Surface Urban Heat Island, Surface UHI
SW	= Split-window method
TB	= Brightness Temperature
TGCI	= Brightness-Temperature-Grade-Change-Index
TIR	= Thermal Infrared

LIST OF ABBREVIATIONS (Continued)

TIRS	= Thermal Infrared Sensor
TIROS	= Television and Infrared Observation Satellite
TOA	= Top-of-Atmosphere
TsHARP	= Thermal Sharpening
UBHI	= Urban Boundary Heat Island
UBL	= Urban Boundary Layer
UCL	= Urban Canopy Layer
UHI	= Urban Heat Island
UI	= Urban Index
ULST	= Urban Land Surface Temperature
URI	= Urban-Heat-Island-Ratio
USGS	= United States Geological Survey
UTFVI	= Urban Thermal Field Variance Index
VOCs	= Volatile Organic Compounds
WAI	= Weighted-Average-Intensity

CHAPTER I

INTRODUCTION

1.1 Background and significances of the study

1.1.1 Background of the problem

Under a scenario of urbanization, natural landscapes are transformed into anthropogenic urban lands (Voogt and Oke, 2003), and urbanization also has resulted in intensive concentrations of the population and built-up environment (Chen, Yao, Sun and Chen, 2014). Regarding these effects, cities are now facing the problem of rising temperatures (Dimoudi et al., 2014; Giannopoulou et al., 2011; Taha, 2015; Zinzi and Agnoli, 2012). Most of the world's cities show higher temperatures in urban areas than in rural areas (Schwarz, Schlink, Franck and GroBmann, 2012), where air and surface temperatures of urban areas are higher than those of its surrounding rural areas (He, Liu, Zhuang, Zhang and Liu, 2007). This phenomenon is called the urban heat island (Voogt and Oke, 2003).

Numerous previous studies have examined the UHIs in large cities, which are defined as a metropolitan area, but less often considered are the non-mega cities, especially in Asia (Wu, Lung and Jan, 2013). Karl, Diaz and Kukla (1988) strongly indicated that the influence of urbanization on long-term temperature records had been detected even for cities with a population less than 10,000.

UHI phenomena have been studied by ground-based observations taken from fixed thermometer networks or by transverse with thermometers mounted on vehicles (Voogt and Oke, 2003). The traditional method is only valid where there is enough number of weather stations located over urban and rural areas (Ayanlade, 2016; Stewart and Oke, 2006), and a well-designed network of stations is required (Hu and Brunsell, 2015). Furthermore, in situ data offers high temporal resolution and long-term coverage but lacks spatial details (Weng, 2009). Satellites are an invaluable tool for UHI studies because of their ability to detect thermal features of the earth's surface with broad spatial resolution. They can provide dense time-synchronized and continuous grids of temperature data over an entire city to perform a larger and more regular-sampling than surface observations (Arnfield, 2003; Hung, Uchihama, Ochi and Yasuoka, 2006; Streutker, 2002). High-temperature environments negatively impact human health and comfort (Stewart and Oke, 2012), and also increase the mortality and morbidity of cardiovascular and respiratory diseases (Tian, Li, Zhang and Guo, 2013; Vaneckova, Beggs, Dear and McCracken, 2008). Furthermore, high temperature leads to an increase in fossil-fuel consumption to cooling down especially in summertime (Armson, Stringer and Ennos, 2012; Gaitani et al., 2011; Mahmuda and Webb, 2016). As a result, this process increases the emission of air pollutants (Abdul-Wahab, Bakheit and Al-Alawi, 2005; Elsayed, 2012; Van and Bao, 2008) as well as greenhouse gases (Leong, Chng, Ong, Choo and Laili, 2015).

Therefore, mitigating the impact of the UHI is a crucial mission in achieving sustainability in a city (Gaitani et al., 2011). Human has attempted to modify the environment to reduce the heat for good lives. Despite the use of a wind tunnel concept, the use of high albedo materials, and also increasing the wetlands and green

spaces are considered consequently. Regarding the previous works, it can be concluded that the use of vegetation in UHI mitigation is the most effective landscape strategy (Vidrih and Medved, 2013). Because this method addresses the real cause of the problem (Dimoudi and Nikolopoulou, 2003; Stabler, Martin and Brazel, 2005), and also reduces the heat stress produced by UHIs (Lin, Wu, Zhang and Yu, 2011). Furthermore, urban green space also provides other ecosystem services, such as pollution reduction and biodiversity habitat (Norton et al., 2015).

In conclusion, UHIs phenomena can occur even in a small city where the population is less than 10,000. The problem from the rising temperature in the urban areas becomes a critical environmental issue because the high surface and air temperature environments negatively impact human health and comfort. Therefore, urban microclimate improvement is a crucial consideration regarded to archive sustainability in a city. Green surfaces and parks play the most effective heat mitigation, especially in hot and humid countries. Not only the ability in heat reduction but urban green space also provides other ecosystem services, such as pollution reduction and biodiversity habitat. In the UHIs studies, at present, remotely sensed data are a unique source of information to define surface urban heat islands and provide a new avenue in UHIs observations.

1.1.2 Significances of the study

Firstly, the apparent change of LULC has occurred both in Buriram Town municipal area and surrounding areas since 2012. Most of the changes have occurred in bare lands, which changed into built-up areas, such as housing estates and hotels and townhouses. As a result, the increase of built-up areas causes a rise in temperature in Buriram Town Municipality and tends to occur in many places. Based on the population

statistic in 2017, as shown in Table 1.1, Buriram Town Municipality represents a small town with a high density of population as an example of several towns in the North-east of Thailand.

Table 1.1 The population statistic in 2017.

	Municipality	Type	Area (Sq.Km)	Population (2017)	Density
1	Buriram	Town Municipality	6.00	27,150	4,525.00
2	Phon	Town Municipality	3.00	11,189	3,729.67
3	Nakhon Ratchasima	City Municipality	37.50	129,680	3,458.13
4	Surin	Town Municipality	11.39	39,168	3,438.81
5	Roi Et	Town Municipality	11.63	35,671	3,067.15
6	Kranuan	Town Municipality	3.77	10,310	2,734.75
7	Udonthani	City Municipality	47.70	130,274	2,731.11
8	Ubon Ratchathani	City Municipality	29.04	76,271	2,626.41
9	Khon Kaen	City Municipality	46.00	120,143	2,611.80
10	Pak Chong	Town Municipality	15.25	34,947	2,291.61
11	Maha Sarakham	Town Municipality	24.14	52,507	2,175.10
12	Kantharalak	Town Municipality	8.68	18,795	2,165.32
13	Warin Chamrap	Town Municipality	12.90	27,249	2,112.33
14	Yasothon	Town Municipality	9.71	20,345	2,095.26
15	Kalasin	Town Municipality	16.96	33,745	1,989.68
16	Wang Sa-pung	Town Municipality	6.07	11,737	1,933.61
17	Phibun Mangsahan	Town Municipality	6.00	10,669	1,778.17
18	Ban Phai	Town Municipality	16.20	28,153	1,737.84

Table 1.1 The population statistic in 2017 (Continued).

	Municipality	Type	Area (Sq.Km)	Population (2017)	Density
19	Det Udom	Town Municipality	8.10	13,854	1,710.37
20	Loei	Town Municipality	12.41	21,013	1,693.23
21	Nonsong- Namkham	Town Municipality	6.10	10,116	1,658.36
22	Si Khiu	Town Municipality	11.63	17,875	1,536.97
23	Taa bor	Town Municipality	12.62	17,761	1,407.37
24	Nong Khai	Town Municipality	35.15	47,949	1,364.13
25	Bua Yai	Town Municipality	10.63	13,978	1,314.96
26	Chum Phae	Town Municipality	24.55	31,347	1,276.86
27	Chaiyaphum	Town Municipality	30.78	36,588	1,188.69
28	Buakhao	Town Municipality	9.95	11,713	1,177.19
29	Muang Pak	Town Municipality	12.11	14,121	1,166.06
30	Nong Samrong	Town Municipality	24.85	28,247	1,136.70
31	Sisaket	Town Municipality	36.66	41,246	1,125.10
32	Nakhon Phanom	Town Municipality	24.13	26,337	1,091.46
33	Nang Rong	Town Municipality	20.77	21,336	1,027.25
34	Sakon Nakhon	City Municipality	54.54	53,237	976.11
35	Mukdahan	Town Municipality	35.55	33,696	947.85
36	Ban dung	Town Municipality	20.95	15,836	755.89
37	Amnat Charoen	Town Municipality	38.00	25,964	683.26
38	Nong Bua Lamphu	Town Municipality	39.50	21,613	547.16
39	Ban Thum	Town Municipality	61.97	17,945	289.58

Source: (The Bureau of Registration Administration, 2018).

Secondly, in this study, the ULST mitigation focuses on the third-level classification of LULC in a small density town at a micro-climate scale. The LULC types are classified as trees, shrubs, grasslands, bare lands, constructions, roads, and wetlands. At this level, the LULC types are shown as the typical mixed LULC. The urban growth relies on this concept can reduce the ULST, and the present urban area would consider this result to alternatively adjust some areas for ULST reduction.

Thirdly, to use LST values given by a sensor onboard a satellite, these must have gone through processes of validation and calibration that provide an estimation of the uncertainty of the value (Simo et al., 2016). This information is obtained primarily with ground-based data used for comparison (Simo et al., 2016). Until now, the validation of thermal infrared satellite products at moderate resolution was mostly performed over homogeneous surfaces such as lakes, deserts, and dense or very homogeneous vegetation covers (Guillevic et al., 2012). As the land surface is heterogeneous at the satellite pixel level, promising temperature-based validation based upon in-situ measurements is limited to homogeneous land surface types (Coll, Galve, Sanchez and Caselles, 2010). However, the accuracy of LSTs retrieved from heterogeneous or mixed pixels remains questionable (Liu, Hiyama and Yamaguchi, 2006).

Finally, satellite remote sensing is an excellent tool for examining the UHI effect (Zhou, Chen, Wang and Zhan, 2011). Satellite thermal infrared resolution resolves the scales of urban-rural LST differences; however, it is not sufficient to resolve most urban features (roads and buildings) to study microclimates and human comfort in urban areas (Dominguez, Kleissl, Luvall and Rickman, 2011). Therefore,

downscaling LST is a significant method to improve the spatial resolution of mixed pixels retrieved from low-resolution sensors (Sattari, Hashim and Pour, 2018).

1.2 Research objectives

The principal objective of this research is to simulate hotspot mitigation associated with proportions of green space in an urban area. Based on this intention, there are four specific objectives proposed for this research:

1.2.1 To explore the optimum method for ULST estimation.

1.2.2 To estimate subpixel LST data using the statistical-based method.

1.2.3 To identify the hotspots areas based on subpixel LST data.

1.2.4 To simulate hotspot mitigation associated with proportions of green space in an urban area.

1.3 Scope and limitations

1.3.1 This study focused on the ULST at Buriram municipality in summer. LANDSAT-8 imagery data obtained on January 21, February 6, March 26, and April 11, 2018, were implemented in this study.

1.3.2 The ground-based temperature surveying was done during 10.00 - 12.00 a.m., which closed to the time that the satellite obtains the data at 10.30 a.m. on the same date of LANDSAT-8.

1.3.3 The simulation of the potential scenarios of ULST hotspot mitigation focused only on the amount of urban green space in the variation of LULC and LST data.

1.3.4 The purpose of the mitigation is to reduce the hotspot temperature nearly or equal to the temperature of the surrounding area. Furthermore, the minimum proportions of green space, which can decrease the hotspot temperature higher than at least the decreased temperature in hotspot areas, were selected for hotspot temperature mitigation. It should be noted that at least the decreased temperature in hotspot areas was calculated based on the differentiated maximum temperature between hotspot areas and surrounding areas.

1.3.5 The optimum method in ULST estimation was explored based on LST algorithms used in this study, namely radiative transfer equation, improved-mono window, generalized-single channel, and split-window algorithm, by considering the lowest NRMSE value.

1.3.6 Although the thermal infrared bands in delivered data products were resampling to 30 meters, the estimated LST data based on resampling thermal bands are not actual high spatial-like data at 30 meters. Therefore, the statistical-based method was applied to estimate the relative LST data, which are high spatial-like data at 30 meters, based on scaling factors. In this study, the results based on the statistical-based method are called subpixel LST data.

1.4 Benefits of the study

1.4.1 Contributions to the knowledge

- 1.4.1.1 The subpixel LST estimation using the statistical-based method.
- 1.4.1.2 The location of hotspot areas within urban areas.
- 1.4.1.3 The efficiency of using vegetation to mitigate the ULST.

1.4.2 Contributions to relevant stakeholders

1.4.2.1 Urban planner and landscape planner would use the result of this study to mitigate the ULST of hotspots in the urban area.

1.4.2.2 Urban planners or relevant organizations may use the protocol of this study in terms of studying processes to apply to other areas for ULST mitigation.

1.4.2.3 Provincial organizations may consider the result of this study to set up some urban landscape to reduce the ULST in urban areas.

1.5 Study area

In this study, Buriram Town Municipality, as shown in Figure 1.1, is selected as the study area, to represent a small town with a high density of population.

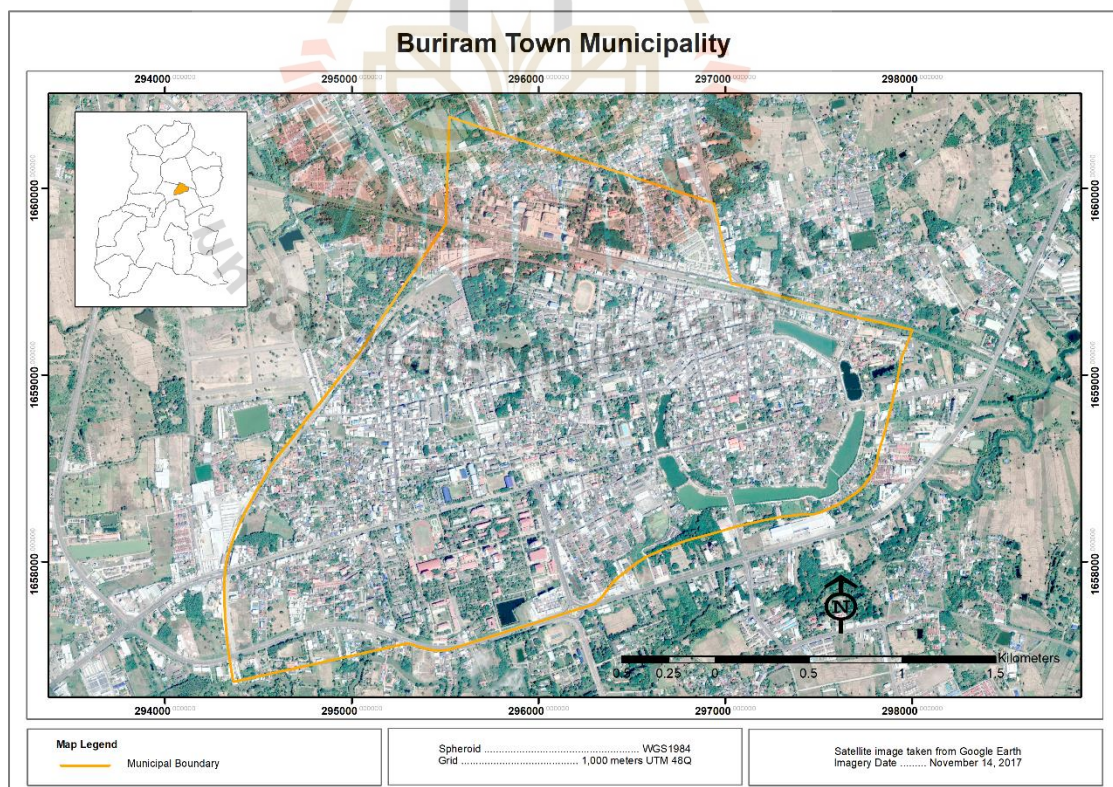
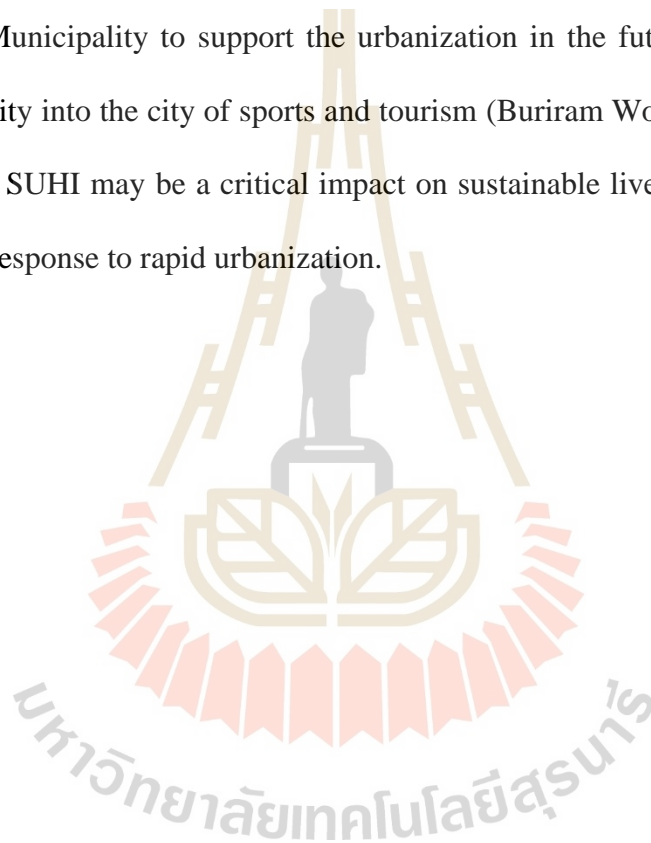


Figure 1.1 Buriram municipality.

Recently, nearly 30,000 populations live in the municipal area with a total area of approximately six square-kilometers (Buriram Municipality, 2016). There are many determinants in rapid urbanization, despite the success in the football club and motorsport, the famous tourist attractions, e.g., ancient sandstone sanctuaries, extinct volcanoes, and also the variety of cultures (Tourism Authority of Thailand, 2017). Furthermore, the local government plans to improve the city from Town Municipality to the City Municipality to support the urbanization in the future and also plans to develop the city into the city of sports and tourism (Buriram World, 2016). Regarding these effects, SUHI may be a critical impact on sustainable livelihood if there are no active plans response to rapid urbanization.



CHAPTER II

LITERATURE REVIEWS

This chapter provides fundamental knowledge on several topics, (1) UHIs phenomena, (2) LST estimation using LANDSAT-8 imagery data, (3) subpixel LST data estimation, (4) hotspot analysis and (5) urban green spaces. Each topic contains the summary at the end, which leads to the significance of this research. The context is as follows.

2.1 UHIs phenomena

Apparently, Luke Howard discovered UHIs phenomena in 1818; later, Gordon Manley was the first one who named urban heat island in 1958 (Chang, 2016; Zhang, Wu and Chen, 2010). The UHIs phenomena occur where air and surface temperatures of urban areas are higher than those of its surrounding rural areas (He, Liu, Zhuang, Zhang and Liu, 2007). However, the urban thermal environment varies not only from its rural surroundings but also within the urban area due to intra-urban differences in land use and surface characteristics (Hart and Sailor, 2009). With recent developments in cities, there is no distinct borderline between urban and rural areas as a result of urban growth. Therefore, the UHI can be considered in terms of the difference between the central parts of the city and its surrounding areas (Ngie, Abutaleb, Ahmed, Darwish and Ahmed, 2014). UHIs phenomena are well recognized in large cities, also in small ones (Blazejczyk, Bakowska and Wieclaw, 2006). The influence of urbanization on long-

term temperature records has been detected even for cities with a population of less than 10,000 (Karl, Diaz and Kukla, 1988).

2.1.1 Causations of UHI

The UHI phenomena are generally seen as being caused by a reduction in latent heat flux and an increase in sensible heat in urban areas as vegetated and evaporating soil surfaces are replaced by relatively impervious low albedo (solar reflectivity) paving and building materials (Imhoff, Zhang, Wolfe and Bounoua, 2010). The modification of the land surface in the urban area to build surfaces enhance the energy storage and the heat release (Carnielo and Zinzi, 2013). The effect of the building is considered one of the main reasons for the UHI effect. The building also alters the reception of solar radiation casting shadows and change surface roughness and local wind field. Most of the materials used in the construction provide a low albedo surface, resulting in increased absorption of solar radiation in the daytime. After sunset, the pavements and buildings will slowly begin to release the stored heat energy it accumulated throughout the day. However, as the buildings and pavement start to cool off, the air around them begins to heat up, consequently maintaining elevated temperature into the night (Thomas and Zachariah, 2011).

Clustered and interconnected transport areas also tend to mainly increase LST (Dugord, Lauf, Schuster and Kleinschmit, 2014). Furthermore, the sky view factor is also understood to be another factor leading to urban and rural temperature differences (Thomas and Zachariah, 2011). The sky view factor is a good proxy for population density. Strictly sky view factor will be low where density is high (Giridharan, Ganesan and Lau, 2004).

The increase in the urban population produces more heat emission (Xu, Dan, Dan and Lu, 2009). Metabolic heat, which is produced by human bodies, also contributes to UHI. The large population density in the urban region makes the total amount of heat throw out by the human bodies be significant in terms of the heat budget (Thomas and Zachariah, 2011). However, anthropogenic heat is also produced from heating and cooling processes in buildings and vehicles (Mackey, Lee and Smith, 2012).

Finally, local meteorological conditions and geography also affect the magnitude of a UHI (Fabrizi, Bonafoni and Biondi, 2010). The UHI intensity is negatively correlated with precipitation while positively correlated with wind speed, and the relation between the UHI intensity and evaporation varies with the seasons; namely, the intensity is positively correlated with summer evaporation but negatively correlated with winter evaporation (Ga, NiMa, Jun and CiRen, 2011).

Regarding the previous literature, it can be concluded that the energy storage of the buildings, clustering traffic, large population density, and hot and dry season are the major causes of UHI occurrences.

2.1.2 Impacts of UHI

As UHI effects lead to increased temperatures within cities, they deteriorate our living environment. High environmental temperatures are deleterious to health and comfort; prolonged exposure can be an instrument to the incidence of stroke, heart diseases, and pulmonary disorders (Elsayed, 2012). Many studies have reported that high temperatures increase the mortality and morbidity of cardiovascular (Tian, Li, Zhang and Guo, 2013), circulatory, respiratory diseases (Vaneckova, Beggs, Dear and McCracken, 2008), and the transmission of infectious diseases (Tomlinson, Chapman,

Thornes and Baker, 2011). Furthermore, the impact of heatwaves is often felt most active in towns and cities where populations are concentrated, and where the climate is often unintentionally modified to produce a UHI (Tan et al., 2010; Tomlinson et al., 2011).

High temperatures also lead to increased energy demand for cooling buildings and air conditioning costs, especially in summertime (Mahmuda and Webb, 2016). Air quality deterioration occurs due to increased electricity demand, whereby most of the power utility companies generate electricity by burning fossil fuel. As a result, this process increases the emissions of air pollutants such as sulfur dioxide, nitrogen oxide, particulate matter as well as GHGs like carbon dioxide and methane (Leong, Chng, Ong, Choo and Laili, 2015). High temperature and high solar energy also tended to increase the daytime ground-level ozone concentration, since, higher temperatures accelerate the chemical reaction that produces ground-level ozone, or smog (Abdul-Wahab, Bakheit and Al-Alawi, 2005; Van and Bao, 2008), and also cause an increase in the emissions of biogenic hydrocarbons as well as higher evaporation rates of synthetic VOCs (Elsayed, 2012). Furthermore, the UHI makes the polluted materials cannot be diffused quickly so that the urban area was polluted heavily (Cai, Du, Xue and Li, 2008).

Not only air pollution, but the UHIs can also affect water quality. The United States Environmental Protection Agency (2017a) reported that high pavement and rooftop surface temperatures could heat storm-water runoff, which drains into storm sewers and raises water temperatures as it is released into streams, rivers, ponds, and lakes. Water temperature affects all aspects of aquatic life, especially the metabolism and reproduction of many aquatic species. Rapid temperature changes in

aquatic ecosystems resulting from warm storm-water runoff can be particularly stressful, even fatal to aquatic life.

Finally, UHIs can also impact local weather, alter local wind patterns, spur the development of clouds and fog, and influence the rates of precipitation (Liu and Zhang, 2011). The UHIs can enhance and possibly initiate thunderstorms and rainfall (Dixon and Mote, 2003). Shepherd, Pierce and Negri (2002) suggested that within 30-60 km downwind of the metropolis, the average increase in monthly rainfall could be as high 28 percent. However, it depends on the size of the city and its surrounding geographic features (Lin, Chen, Chang and Sheng, 2011).

Regarding the previous literature, it can be concluded that UHIs lead to an increase in electricity demand for cooling. In the electricity generating process, the burning of fossil fuel increases the emissions of air pollutants which directly impact human health. Furthermore, UHIs can also impact local weather, local wind patterns, and influence the rates of precipitation downwind of the areas.

2.1.3 UHI types

UHI can be categorized into two broad types; the first one is the Atmospheric UHIs, and the second one is the Surface UHIs (Zhou, Zhao, Liu, Zhang and Zhu, 2014). Their specific details are as follows.

2.1.3.1 Atmospheric UHIs

Atmospheric UHIs are best expressed under calm and clear conditions at night (Stathopoulou and Cartalis, 2007). Atmospheric UHIs are commonly analyzed at two scales; the first one is the urban canopy layer, and the second one is the urban boundary layer (Oke, 1976; Voogt, 2004), as shown in Figure 2.1.

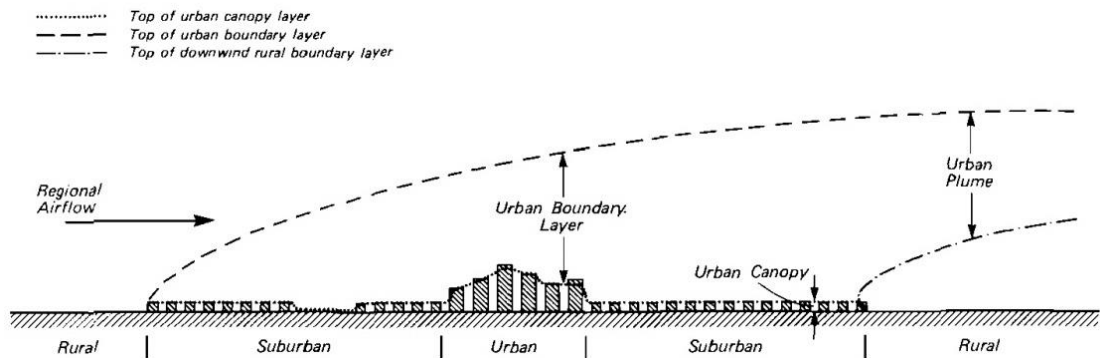


Figure 2.1 Two-layer classification of thermal modification (Oke, 1976).

Based on Figure 2.1, the UCL is the layer of the urban atmosphere extending upwards from the surface to approximately mean building height. In-situ sensors typically detect the canopy layer heat island at standard (screen-level) meteorological height or from the traverse of vehicle-mounted sensors (Voogt and Oke, 2003). The UCL is a micro-scale concept, its climate being dominated by the nature of the immediate surroundings (especially site materials and geometry). The depth of this layer may also be a function of wind speed, shrinking as stronger airflow allows influences from above to penetrate (Oke, 1976).

On the other hand, the UBL is situated directly above the UCL, which may be 1 km or more in thickness at daytime, shrinking to hundreds of meters or less at night (Voogt, 2004). This is a local or mesoscale concept referring to that portion of the planetary boundary layer whose characteristics are affected by the presence of an urban area at its lower boundary. The top of the urban boundary heat island is commonly capped by a temperature inversion, giving some correspondence with the upper limit of urban pollution (Oke, 1976). The UBHI observation is made from more specialized sensor platforms such as tall towers, radiosonde or tethered balloon flights, or aircraft-mounted instruments (Voogt and Oke, 2003).

In general, air temperature UHI has high temporal resolution with extensive time coverage, and can adequately describe the temporal variation of the UHI effect (Li, Zhou and Ouyang, 2013). However, the limited footprint of a ground-based measurement and the sparse distribution of observations make it difficult to capture a broad distribution of temperature over highly heterogeneous urban areas. To solve these problems, usually, a well-designed network of stations is required (Hu and Brunzell, 2015). On the other hand, many studies of the UHI effect have been based on LST (Shen, Huang, Zhang, Wu and Zeng, 2016).

LST is a crucial variable required for a wide variety of applications, e.g., climatological, hydrological, biogeochemical, agricultural, and change detection studies. It is maintained by the incoming solar and long-wave irradiation, the outgoing terrestrial infrared radiation, the sensible and latent heat flux, and the ground heat flux. Therefore, LST is a good indicator of the energy balance at the earth's surface (Dash, 2005). In studies of urban climate change, the LST has been recognized as one of the most critical parameters affecting the UHI phenomenon (Liu and Zhang, 2011).

LST has proved to be close to atmospheric temperatures due to the transference of energy emitted from the land surface to the atmosphere (Nichol, 1996; Nichol and Wong, 2008; Sun, Chen, Chen and Lu, 2012; Weng, 2009; Weng and Quattrochi, 2006). However, surface temperatures can be both higher and more variable than concurrent air temperatures due to the complexity of the surface types in urban environments and variations in urban topography (Imhoff et al., 2010).

2.1.3.2 Surface UHIs

Surface UHIs are mostly found in summer midday (Imhoff et al., 2010). The remotely sensed UHI has been termed the SUHI (Voogt and Oke, 2003). The first SUHI observation, from satellite-based sensors, was reported by Rao in 1972. He used 7.4 km resolution thermal measurements from the Scanning Radiation onboard the ITOS-1 to demonstrate that the New York City-Philadelphia-Baltimore-Washington, DC, the urban corridor can be roughly delineated with such data (Matson, McClain, McGinnis and Pritchard, 1978).

Remotely sensed data have been widely used in the study of SUHIs phenomena based on LST data. In the studies of the SUHI characteristics, Zhou, Zhao, et al. (2014), Zhou, Qian, Li, Li and Han (2014) and Du et al. (2016) indicated that the SUHI differed significantly by season and characterized by a higher intensity in summer than in winter. Furthermore, Zhou, Zhao, et al. (2014) and Du et al. (2016) found that UHI intensity in the daytime was stronger than that at night. Xu et al. (2009) also indicated that SUHI demonstrates a single-center or double-centers at night, while the UHI demonstrates multi-centers at daytime. Considering the investigation of the UHI intensity, Xu, Chen, Dan and Qiu (2011) used Weighted-Average-Intensity and Urban-Heat-Island-Ratio, which were used in evaluating single-temporal UHI adaptation, in describing heat island intensity and in depicting development degree of heat island, respectively. Brightness Temperature and Brightness-Temperature-Grade-Change-Index also be used in the analysis of dynamic characteristics of UHI at different times adopting.

Another important key point is the most apparent dependence of the LST on different land cover types (Bokaie, Zarkesh, Arasteh and Hosseini, 2016; Walawender, Szymanowski, Hajto and Bokwa, 2014). Temperature decreased where the plant density or the amount of water increased, and vice versa (Uysal and Polat, 2015). Therefore, increasing the water area is an effective way to alleviate UHI (Dan, Wu, Dan, Qiu and Xu, 2010). In contrast, increasing the build-up area causes a rise in temperature (Uysal and Polat, 2015) since there is a strong positive relationship exists between mean LST and percent impervious surface area (Li et al., 2011).

Areas with high temperatures are primarily located in the center of the city or nearby counties, while low-temperature areas are in the suburbs of counties (Ga et al., 2011). High average temperatures occurred in industrial and commercial area (Cai, Du and Xue, 2011; Dobrovolny, 2013; Li et al., 2011; Rinner and Hussain, 2011; Van and Bao, 2008, 2010; Xu et al., 2009), and also in the areas with having a high density of buildings, residents (Cai et al., 2011), roads, and transportations (Cai et al., 2011; Xu et al., 2009). In contrast, low average temperature occurred in parks and recreational land, water bodies (Rinner and Hussain, 2011), and also around the regions with large areas of grassland, trees, and water bodies (Cai et al., 2011). Moreover, in suburban and rural areas, where agricultural land remains with full vegetation cover, the LST is usually low (Van and Bao, 2008, 2010).

Temperature statistics of main land cover types showed that built-up and bare land had higher surface temperatures than natural land covers, implying the warming effect caused by the urbanization with the natural landscape being replaced by urban areas (Xu, Qin and Wan, 2010). Changes in LULC and population shifts resulted in significant variation in the spatiotemporal patterns of the

UHIs due to the loss of water bodies and vegetated surfaces (Zhang, Qi, et al., 2013). UHI intensity might be enhanced by intensified urbanization, wherein the built-up area expands, there is increased heat from human activity, and there is more artificial heat input to the atmosphere (Ga et al., 2011). The heat island effect is getting stronger, along with the cities' development. The features of the heat island effect have a close relation to changes in the process of urbanization. The expansion of urban space and the distribution of industrial zones have evident impacts on the intensity of the heat island (Dan et al., 2010). Therefore, Gobakis et al. (2011) developed a model for UHI phenomenon prediction using neural network techniques.

Furthermore, Ahmed, Kamruzzaman, Zhu, Rahman and Choi (2013) simulated land cover changes and their impacts on LST in Dhaka, Bangladesh. This study first identified patterns of land cover changes between the periods and investigated their impacts on LST; second, they applied an artificial neural network to simulate land cover change; and finally, estimated their impacts on LST in respective periods. However, Zhou, Qian, et al. (2014) suggested that percent of imperviousness was the best predictor on LST with relatively consistent explanatory power across seasons, which alone explained approximately 50 percent of the total variation in LST in winter, and up to 77.9 percentage for summer. Vegetation-related variables, particularly tree canopy, were a good predictor of LST during summer and fall.

Since the LST data are based on the LULC types, several pieces of research are also focused on the relationship between LST and vegetation index. Correlation studies between NDVI and LST showed a negative correlation between these two parameters (Bokaie et al., 2016; Leong et al., 2015; Zhang et al., 2010). The highest the NDVI, the lower is the temperature, and vice versa (Leong et al., 2015).

However, Weng, Lu and Schubring (2004) indicated that LST possessed a slightly stronger negative correlation with the unmixed vegetation fraction than with NDVI for all land cover types across the spatial resolution (30 to 960 m). Correlations reached their most influential at the 120 m resolution, which is believed to be the operational scale of LST, NDVI, and vegetation fraction images. Furthermore, Chen, Zhao, Li and Yin (2006) found that correlations between NDVI, NDWI, and temperature are negative when NDVI is limited in range, but the positive correlation is shown between NDBI and temperature.

Not only the relationship between LST and LULC but also the relationship between LST and social factors. Huang, Zhou and Cadenasso (2011) found that variation in LST co-occurred with social variables. Neighborhoods with lower income, more poverty, less education, more ethnic minorities, more older people, and high crime risk tended to have higher LST. Also, energy consumption, Du et al. (2016) indicated that energy consumption, average temperature, and the urban area had a significant positive correlation with UHI intensity.

Another critical point is the relationship between LST and air pollutants. El-Gammal, Youssef, Ali and Madkour (2011) and Feizizadeh and Blaschke (2013) found that LST and PM₁₀ show the negative correlation. Moreover, El-Gammal et al. (2011) also indicated that the correlation between nitrogen dioxide and LST is positive, whereas the results of sulfur dioxide show that the correlation is negative. Furthermore, Al-Seroury (2012) also indicated the high correlation between LST and hydrocarbons, carbon monoxide, nitrogen oxide, and sulfur dioxide.

Finally, some research focused on the impacts of the UHI phenomena. Liu and Zhang (2011) used the UTFVI to describe the UHI effect quantitatively, and further assessed the ecological valuation of Hong Kong UHI. Also, the impact on Health, Tomlinson et al. (2011) found that concentrations of very high-risk people live within the UHI. Wu, Lung and Jan (2013) also indicated that the empirical result demonstrated intensified SUHI in large and medium-sized cities in subtropical areas during heat waves, which could result in heat stress risks of residents. Dong et al. (2014) also found that the heat-health risk demonstrates a spatial-temporal pattern with a higher risk in the urban area, lower risk in the borderland between urban and rural areas, and lowest risk in the rural area. Furthermore, Wibowo, Kuswantoro, Ardiansyah, Rustanto and Shidiq (2016) found that the active temperature index explains that conditions as warm, uncomfortable, increase stress due to sweating and blood flow and may cause a cardiovascular disorder.

Regarding the previous studies, it can be concluded that UHI can be categorized as the Atmospheric UHIs and the Surface UHIs. The atmospheric UHI is commonly analyzed at two scales, namely, UCL and UBL. Atmospheric UHI has high temporal resolution with extensive time coverage but lacks spatial details. Therefore, many studies of the UHI effect have been based on LST as SUHI.

Numerous studies are focused on the study of characteristics of SUHI and the relationship between LST and LULC. In detail, coarse and moderate spatial resolution image data are used in SUHI characteristic studies. The results indicated that a higher intensity characterizes SUHIs in summer than in winter, and the SUHI intensity in the daytime is stronger than that at night. Furthermore, the SUHIs demonstrate a single-center or double-centers at night, but SUHI demonstrates multi-centers in the

daytime. In the local scale, LANDSAT and ASTER imagery data are used in the studies of the relationship between land-use and land-cover and LST. The results indicate that the most apparent dependence of the LST on different land cover types. Built-up and bare land have higher surface temperatures than natural land covers, despite wetlands and vegetated areas. The areas with high SUHI effects are the industrial regions and the areas having a high density of buildings, transportation, and residents. However, the temperature can be decreased when the plant density or the amount of water increased and vice versa. Apart from the study of the relationship between LST and LULC, LST and SUHI also correlate with the air pollutants, social factors, and also the impact of SUHIs on human health.

2.1.4 UHI mitigation

The UHI phenomenon is generally seen as being caused by a reduction in latent heat flux and an increase in sensible heat in urban areas as vegetated and evaporating soil surfaces are replaced by relatively impervious low albedo (solar reflectivity) paving and building materials (Imhoff et al., 2010). Therefore, urban planners and natural resource managers should gain insights into the importance of balancing the relative amount of various types of urban morphology features and optimizing their spatial distributions (Srivanit and Kazunori, 2011). Besides, urban planners and designers should strengthen the construction of ecological corridors to facilitate mass and energy exchange between urban areas and their surroundings (Du et al., 2016).

The use of urban surfaces with a high reflection coefficient, and planting trees and vegetation, is low-cost strategies that reduce the city's temperature and cooling energy demands. It could also prevent the formation of smog within the city (Akbari and Leanna, 2008; Khodakarami and Ghobadi, 2016).

Carnielo and Zinzi (2013) suggested that the increase of solar reflectance or urban materials is a strategy aimed at reducing surface and air temperatures, and also mitigating the UHI. Increasing the solar reflectance of the urban materials is an emerging strategy that gained interest among the stakeholder to mitigate the urban temperatures, as well as to improve the energy performance of buildings. Furthermore, Mackey et al. (2012) suggested that the albedo increases produced more significant cooling than the vegetation increases. Especially, reflective roofs have proven themselves competent, and this is likely because they provided the highest amount of cooling for the smallest amount of money invested. Vegetation that is dense enough to provide the desired cooling seems to have high installation and maintenance costs that prevent it from having the same widespread cooling effects of reflective roofs.

The more albedo values produce more significant cooling conditions than the more vegetation covering space. Another critical point to remember is urban green space not only achieves temperature reductions in an urban area, but urban green space also provides other ecosystem services, such as pollution reduction and biodiversity habitat (Norton et al., 2015). These ecosystem services play a role in creating salutogenic urban environments that can help mitigate human health problems, such as asthma, allergies, obesity, and increased stress. It has been shown that lack of green spaces in cities contributes to health disparities among people in lower and higher-

income neighborhoods (Declet-Barreto, Brazel, Martin, Chow and Harian, 2013; Jennings, Gaither and Gragg, 2012; Wilson, 2009).

Not only urban green space, but wetlands also mitigate the intensity and spread of UHI (Bokaie et al., 2016; Thomas and Zachariah, 2011). Wetlands are, on average, colder than their surrounding landscapes. It indicates that the cooling effects of wetlands are significant in urban environments. Area and shape can impact the cooling effect of wetlands in urban regions. However, the cooling effect of wetlands does not linearly correlate with the wetland area. It indicates that the cooling effect has a threshold as the wetland area increases, and it is reasonable to benefit more stakeholders by substituting a large water body with several small water bodies of the same total area (Sun et al., 2012). The rationale behind the use of water bodies originates in the enhanced evaporation of the water bodies during the daytime, but the high heat capacity of water suppresses the diurnal and annual cycle water, and water temperatures remain relatively high after evening and season transitions (Steenefeld, Koopmans, Heusinkveld and Theeuwes, 2014).

Finally, wind speed has widely been reported to have decreased the intensity of heat island effect in urban areas (Rajagopalan, Lim and Jamei, 2014). Thus, wind tunnel or air path is a choice to mitigate the UHI in high-density cities. Ng, Yuan, Chen, Ren and Fung (2011) suggested that one of the most significant factors is urban morphology, especially the podium layer, and its implication to the urban air ventilation environment. These areas require the most significant design and planning intervention and improvement. For building block disposition, city planners need to factor in the prevailing wind understanding to street layout and building disposition design. City planners also initially estimate the possible urban air ventilation environment of the

urban areas with average velocity ratios. Adjust the pedestrian-level wind speeds and predicting the bio-climate conditions of the city have become possible.

Regarding the previous literature, it can be concluded that human has attempted to modify the environment to reduce the heat for good lives. Despite the use of a wind tunnel concept, it is increasing the solar reflectance, increasing the urban green spaces, or wetlands. However, the increase in urban green spaces is the most effective strategy in UHIs mitigation. Regarding the cooling effect not only occurs in the vegetated areas but also in the surrounding areas. Furthermore, vegetation provides other ecosystem services, such as pollution reduction and biodiversity habitat.

2.2 LST estimation using LANDSAT-8 imagery data

The LST retrieval technology from remote sensing data made significant progress, and various methods have been proposed (Gao et al., 2015). The concept of remote temperature measurements using satellite thermometers can be dated back at the least to the late 1950s, and remote LST measurements to the early 1960s with the launch of TIROS (Dash, 2005). The LST estimation algorithms, with the LSEs, are known a priori, can be roughly grouped into three categories: single-channel methods, multi-channel methods, and multi-angle methods (Li et al., 2010; Li, Tang, et al., 2013). Many efforts have been devoted to the last two algorithms, and they can provide better results than single-channel on a global scale (Bhavanibhai, 2013; Li et al., 2010).

The single-channel method uses the radiance measured by the satellite sensor in a single channel (Li, Tang, et al., 2013) which is based on the use of a radiative transfer model along with atmospheric water vapor and temperature profiles to correct the at-sensor radiance to surface radiance, followed by an emissivity model to separate the

surface radiance into temperature and emissivity (Price, 1983; Schmugge, Hook and Coll, 1998; Scott and Chedin, 1981). Therefore, the accuracy of the single-channel method depends on the accuracy of the RTM used, and mainly on how well the atmospheric profiles represent the real state of the atmosphere over the studies area at the time of the satellite measurements (Coll, Caselles, Valor and Niclos, 2012).

Furthermore, Sobrino, Jimenez-Munoz and Paolini (2004) indicated that the primary constraint of this method is that it needs the atmospheric parameters, which can be calculated from in-situ radiosoundings launched simultaneously with the satellite passes or using a radiative transfer code like MODTRAN. In order to avoid the dependence on radiosounding in the RTE method, Qin, Karnieli and Berliner (2001) developed the MW algorithm for obtaining LST, which estimated from LANDSAT-5 imagery, and Jimenez-Munoz and Sobrino (2003) developed the GSC (Sobrino et al., 2004). However, Bhavanibhai (2013) indicated that the most useful method to correct remotely sensed radiance is using two radiometric measurements for which atmospheric absorption properties are different, as can be measured at two different channels known as the split-window method or at two different observation angles known as the multi-angle method.

The multi-channel method or the split-window was firstly proposed by McMillin in 1975 to determine the sea surface temperature (Rozenstein, Qin, Derimian and Karnieli, 2014). Encouraged by the success of the split-window method for estimating the SST from space measurements, many efforts have been made since the late 1980s to extend the split-window method to retrieve the LST (Li, Tang, et al., 2013). The first effort to retrieve LST from satellites was made by Price (1984), by adopting the AVHRR sea surface temperature split-window algorithm over agricultural land.

The split-window algorithm uses two spectral bands at approximately 11 and 12 μm , which are affected by different atmospheric absorption (McMillin, 1975), assuming that the emissivity in the channels used for the split-window is similar (Dash, Gottsche, Olesen and Fischer, 2002). Land surface brightness temperatures are then calculated as a linear combination of the two channels (Weng, 2009). This algorithm does not require accurate information about the atmospheric profiles during satellite acquisition, such algorithms have been widely used in LST retrieval from several sensors (Du, Ren, Qin, Meng and Zhao, 2015), but only an estimated of the column integrated water vapor content (French, Norman and Anderson, 2003). Furthermore, this algorithm can be used for atmospheric correction from the difference in top-of-atmosphere radiance in two spectral channels (Yang, Wong, Menenti and Nichol, 2015).

Finally, the multi-angles method is based on a similar principle of the split-window algorithm, but different absorption is due to different atmospheric path-lengths for different observation angles. The measurements can be made from one satellite or simultaneously from two satellites (Dash, 2005). This method was primarily grown after the first sensor launch in July 1991 to operate in dual-angle mode, the Along Track Scanning Radiometer onboard the first ERS-1 (Bhavanibhai, 2013).

As one of the most critical aspects of the land surface, LST has been the central topic of developing methodologies to be measured from space (Avdan and Jovanovska, 2016). Several platforms currently include in its sensor configuration one or more thermal bands. However, the LANDSAT series data is one of the most widely used satellite images for LST retrieving because of its free download available from the website of USGS (Liu and Zhang, 2011), and also have long term records data.

Furthermore, the high spatial resolution and regular revisit times of the LANDSAT mission are coarse enough for global coverage, yet details enough to characterize human-scale processes such as the dynamics of urban growth (Masek, Lindsay and Goward, 2000). The LANDSAT image also has been utilized for local-scale studies of UHI (Kumar, Bhaskar and Padmakumari, 2012; Weng, 2001; Yuan and Bauer, 2007). Lauwaet et al. (2016) also indicated that its series is the foremost data source for fine-scale SUHI analysis.

LANDSAT-8 was successfully launched in 2013 and deployed into orbit with two instruments on-board, the Operational Land Imager and the Thermal Infrared Sensor with two spectral bands in the LWIR (Rozenstein et al., 2014). However, band 11 is significantly more contaminated by stray light than Band 10. It is recommended that users refrain from using Band 11 data in the quantitative analysis, including the use of Band 11 in split-wind surface temperature retrieval algorithms (United States Geological Survey, 2018).

Regarding the previous literature, it can be concluded that the presence of two TIR bands of LANDSAT-8 shows the possibility of applying split-window algorithms (Jimenez-Munoz, Sobrino, Skokovic, Matter and Cristobal, 2014a) and single-channel method in LST estimation. Based on the single-channel concept, there are three LST estimation methods, namely the radiative transfer equation-based method, the mono-window method, and the generalized single-channel method (Li, Tang, et al., 2013).

2.2.1 Radiative transfer equation

The transmission of the surface emitted radiance through the atmosphere to the satellite and its interaction with the active elements of the atmosphere is expressed as radiative transfer and it is described by the RTE as Figures 2.2 and equation 2.1 (Bhavanibhai, 2013).

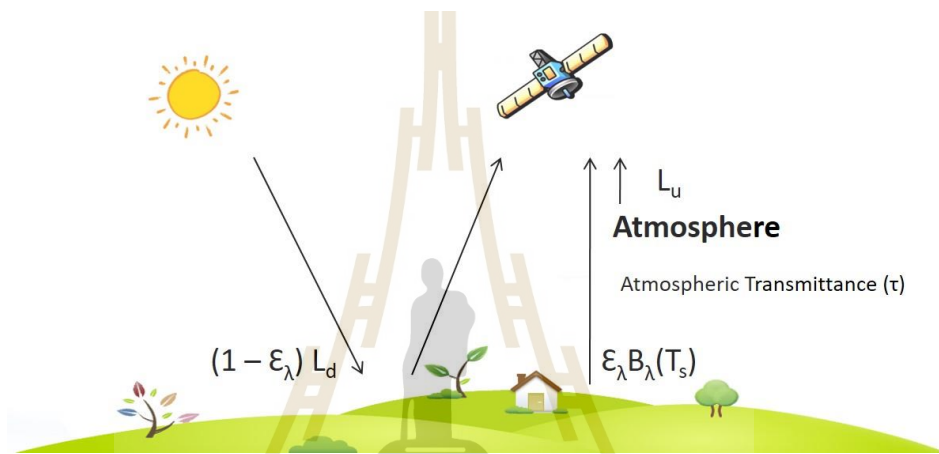


Figure 2.2 The radiative transfer process over the Earth surface in the TIR region.

Source: Modified from (Bhavanibhai, 2013).

$$L_{\text{sensor}, \lambda} = \varepsilon_{\lambda} B_{\lambda}(T_s) \tau_{\lambda} + L_u + (1 - \varepsilon_{\lambda}) L_d \tau_{\lambda} \quad (2.1)$$

Where L_{sensor} is the at-sensor radiance or TOA radiance, i.e., the radiance measured by the sensor, ε is the land surface emissivity, $B_{\lambda}(T_s)$ is Planck radiance at surface temperature T_s , τ_{λ} is the atmospheric transmittance, L_u is the up-welling path radiance, and L_d is the downwelling sky radiance at Earth's surface.

Considering the equation 2.1, the first term stands for the surface-emitted radiance after being attenuated by the atmosphere, the second term corresponds to the up-welling sky radiance emitted by the atmosphere towards the sensor, and the third

term represents the down-welling radiation reaches the sensor after being reflected from the Earth's surface (Bhavanibhai, 2013). Based on RTE, it is possible to estimate LST by inversion of Plank's law (Skokovic et al., 2014). The LST is obtained from equation 2.2.

$$\text{LST} = \frac{C_2}{\lambda \ln \left\{ \frac{C_1}{\lambda^5 \left[\frac{L_{\text{sensor}} - L_u - \tau(1-\varepsilon)L_d}{\tau\varepsilon} \right] + 1} \right\}} \quad (2.2)$$

Where L_{sensor} is thermal radiance at the sensor level, ε is land-surface emissivity, τ is atmospheric transmissivity, L_u and L_d are up-welling, and down-welling atmospheric radiance, respectively, and C_1 and C_2 are constant coefficient.

However, the primary constraint of this method is that it needs the atmospheric parameters; atmospheric transmissivity (τ), down-welling atmospheric radiance (L_d) and up-welling atmospheric radiance (L_u), which can be calculated from in-situ radiosoundings launched simultaneously with the satellite passes, or using a radiative transfer codes like MODTRAN (Sobrino et al., 2004). Furthermore, the use of radiosounding is hampered by the insufficient density of the network, and timing (time of satellite pass) gives the poor representativity in some cases (in the arid region or near coastal areas). The reanalysis data is bound to introduce significant errors due to the spatial and temporal variability of the atmosphere. Only satellite sounder can provide acute information, but there are very fewer instruments which are having thermal imager channels with the sounder instrument. The method based on the

radiative transfer approach does not seem to be applied even though it can be used quite effectively for validating other methods (Bhavanibhai, 2013).

2.2.2 Mono-window algorithm

The mono-window algorithm was developed to obtain LST individually from LANDSAT-5 (Thematic Mapper channel 6, TM6) data by Qin et al. (2001) (Li, Tang, et al., 2013). However, Wang, Qin, et al. (2015) improved the mono-window algorithm for LST estimation from LANDSAT-8. The LST can be obtained from equation 2.3.

$$\text{LST} = \frac{1}{C} [a(1 - C - D) + (b(1 - C - D) + C + D)T_B - DT_a] \quad (2.3)$$

$$\text{With } C = \varepsilon\tau \quad (2.4)$$

$$D = \frac{1}{(1 - \tau)[1 + (1 - \varepsilon)\tau]} \quad (2.5)$$

Where a and b are constant coefficients, ε is the land surface emissivity, τ is the total atmospheric transmissivity, T_B is the at-sensor brightness temperature, and T_a is the mean atmospheric temperature.

This algorithm uses only the near-surface air temperature and water vapor content instead of atmospheric profiles using empirical linear relationships between the atmospheric transmittance and the water vapor content and between the mean atmospheric temperature and the near-surface air temperature (Li, Tang, et al., 2013). This method is used when the ground truth data is not available (Zhang, Wang and Li, 2006). The necessitates three main parameters are emissivity, transmittance, and mean

atmospheric temperature (Bhavanibhai, 2013; Kikon, Singh, Singh and Vyas, 2016). However, the major drawback of this method is, it requires near-surface air temperature at the time of satellite overpass for deriving mean atmospheric temperature (Bhavanibhai, 2013). Furthermore, one of the limitations of this model is the range of water vapor for which it was designed, 0.4 to 3 g cm⁻², which limits LST retrieval beyond these values. Moreover, there is no reference source in near-surface air temperature acquisition, an important practical issue when one wishes to retrieve LST over large areas (Cristobal, Jimenez-Munoz, Sobrino, Ninyerola and Pons, 2009).

2.2.3 Generalized single-channel algorithm

The generalized single-channel algorithm was developed by Jimenez-Munoz and Sobrino (2003) to obtain LST from LANDSAT-5, based on RTE (Cristobal et al., 2009). However, in 2014, Jimenez-Munoz, Sobrino, Skokovic, Matter and Cristobal (2014b) improved the method for LANDSAT-8. The LST is obtained from equation 2.6 (Skokovic et al., 2014).

$$\text{LST} = \gamma[\varepsilon^{-1}(\psi_1 L_{\text{sensor}} + \psi_2) + \psi_3] + \delta \quad (2.6)$$

$$\text{With } \gamma = \frac{T_B^2}{b_\gamma L_{\text{sensor}}} \quad (2.7)$$

$$\delta = T_B - \frac{T_B^2}{b_\gamma} \quad (2.8)$$

Where L_{sensor} is thermal radiance at sensor level, b_y equal 1,256 K, 1,324 K, and 1,199 K for TM6, TIRS-1 (Band 10), and TIRS-2 (Band 11), respectively, T_B is at-sensor brightness temperature, ϵ is the land surface emissivity, and ψ_1, ψ_2, ψ_3 can be obtained as a function of the total atmospheric water vapor content (w).

This method is also used when the ground truth data is not available (Zhang et al., 2006) and requires only atmospheric columnar water vapor content-dependent on atmospheric correction (Bhavanibhai, 2013; Cristobal et al., 2009). Furthermore, this algorithm can be applied to different thermal sensors using the same equation and coefficient (Li, Tang, et al., 2013). However, the optimal performance of this method is observed for the atmospheric with water vapor content in the range of 0.5 to 2.0 g cm^{-2} (Jimenez-Munoz et al., 2009; Vlassova et al., 2014).

2.2.4 Split-window algorithm

The split-window algorithm mainly eliminates atmospheric effects based on differential absorption in two thermal bands (Bhavanibhai, 2013). Furthermore, many efforts have made to extend the split-window algorithm because this algorithm assumes that the land surface emissivity values in both TIR channels are known (Mao, Qin, Shi and Gong, 2005; Price, 1984). Using the split-window algorithm, the TIRS band 10 and 11 provide the atmospheric rectification for the thermal infrared data (Cuenca, Ciotti and Hagimoto, 2013; Irons, Dwyer and Barsi, 2012). The developed split-window algorithm by Jimenez-Munoz et al. (2014b) presents in equation 2.9 (Skokovic et al., 2014):

$$\begin{aligned}
T_s = & T_i + C_1(T_i - T_j) + C_2(T_i - T_j)^2 + C_0 \\
& + (C_3 + C_4w)(1 - \varepsilon) + (C_5 + C_6w)\Delta\varepsilon
\end{aligned} \tag{2.9}$$

Where C_0 to C_6 is the Split Window coefficients, T_i and T_j are at-sensor brightness temperature at Bands i and j , respectively, ε is the land surface emissivity which obtained from $\varepsilon = 0.5(\varepsilon_i + \varepsilon_j)$ and $\Delta\varepsilon = (\varepsilon_i - \varepsilon_j)$.

The split-window algorithm requires the retrieval of several coefficients. These coefficients are retrieval from statistical fits performed over a simulated database. Simulated data are obtained from atmospheric profile data sets used as inputs to the MODTRAN radiative transfer code (Jimenez-Munoz et al., 2014b). However, the split-window coefficients specific for each sensor (Keramitsoglou, Kiranoudis, Ceriola, Weng and Rajasekar, 2011). Furthermore, the coefficients depend on the atmospheric state and the surface emissivity, and they are chosen in order to minimize the error in the LST determination. Numerous studies have done to estimate these coefficients over the sea and land surface, but sometimes fixed values are utilized, imposing significant errors to the results (Vazquez, Reyes and Arboledas, 1997).

Regarding the previous literature, LANDSAT-8 imagery data can be used in LST estimation by using RTE, MW, GSC, and SW algorithm. However, each method contains its limitations and errors. The conclusion of the advantages and disadvantages of each algorithm are shown in Table 2.1.

Table 2.1 The advantages and disadvantages of each method.

Methods	Advantages	Disadvantages
Radiative Transfer Equation	<ul style="list-style-type: none"> • Uses only one thermal band. • Can be used quite effectively for validating other methods (Bhavanibhai, 2013). 	<ul style="list-style-type: none"> • Requires certain atmospheric parameters, namely atmospheric transmissivity, down-welling, and up-welling atmospheric radiance, which can be calculated from in-situ radiosoundings launched simultaneously with the satellite passes or using a radiative transfer code like MODTRAN. • The use of radiosounding is hampered by the insufficient density of the network and timing (time of satellite pass) (Bhavanibhai, 2013).
Improve Mono-window	<ul style="list-style-type: none"> • Uses only one thermal band. • Requires the near-surface air temperature and water vapor content instead of atmospheric profiles. • Appropriate to use when the ground truth data is not available (Zhang et al., 2006). 	<ul style="list-style-type: none"> • Requires certain atmospheric parameters. • One of the limitations of this model is the range of water vapor for which it is designed, 0.4 to 3 g cm⁻² (Cristobal et al., 2009). • The near-surface air temperature is an important parameter used in the practical, atmospheric temperature calculation. However, there is no reference source in near-surface air temperature acquisition (Cristobal et al., 2009). • The relationships between transmittance and water vapor content depend on not well-defined “high” and “low” air temperature values, whereas the relationship between the sufficient atmospheric temperature (T_a) and the near-ground temperature (T_0) are given for absolute standard atmospheres (Jimenez-Munoz et al., 2009).
Generalized Single-channel	<ul style="list-style-type: none"> • Uses only one thermal band. • Uses only water vapor content as an atmospheric parameter in atmospheric function estimation. • Can be applied to different thermal sensors using the same equation and coefficient (Li, Tang, et al., 2013). • If T_a is not available, LST retrieval using only water vapor content is the right choice when the atmospheric water vapor content is low or intermediate (Cristobal et al., 2009). 	<ul style="list-style-type: none"> • Requires certain atmospheric parameters. • The atmospheric functions may be obtained more precisely from water vapor content and air temperature but through more complex models. • The optimal performance of this method is observed for the atmospheric with water vapor content in the range of 0.5 to 2 g cm⁻² (Vlassova et al., 2014).

Table 2.1 The advantages and disadvantages of each method (Continued).

Methods	Advantages	Disadvantages
Split-window	<ul style="list-style-type: none"> • Does not require accurate information about the atmospheric profiles during satellite acquisition. • Uses only water vapor content • Can be used for atmospheric correction from the difference in TOA radiance in two spectral channels (Yang et al., 2015). 	<ul style="list-style-type: none"> • Uses two or more thermal bands. • Requires several coefficients which depend on the atmospheric state. Fixed coefficient values are utilized, imposing significant errors in the results (Vazquez et al., 1997).

2.3 Subpixel LST estimation

Thermal infrared satellite images and derived LST are variables of interest in many remote sensing implementations (Rodriguez-Galiano, Pardo-Iguzquiza, Sanchez-Castillo, Chica-Olmo and Chica-Rivas, 2012). The analysis of UHI at finer scale studies requires the LST at a higher spatial resolution than that provided by the currently available satellite thermal sensors (Liu and Pu, 2008; Lu and Weng, 2006). Furthermore, Dominguez, Kleissl, Luvall and Rickman (2011) indicated that satellite TIR resolution resolves the scales of urban-rural LST differences; however, it is not sufficient to resolve most urban features to study microclimates and human comfort in urban areas. Sobrino, Oltra-Carrio, Soria, Bianchi and Paganini (2012) suggested that spatial resolution finer than 50 m are required to estimate the SUHI effect at the district level correctly. In contrast, spatial resolution coarser than 50 m underestimates the effect and does not distinguish between the different zones inside the city.

Based on the previous studies, there are many terms referred to subpixel LST estimation, such as thermal sharpening, downscaling LST, disaggregation of LST (Zhan et al., 2013). Although many terms have been used, they can be categorized as statistical-based methods and physical-based methods (Liu, Hiyama and Yamaguchi, 2006).

2.3.1 The physical-based method

The physical scaling is based on the laws of physics (Liu et al., 2006) and uses modulation method (Weng, Fu and Gao, 2014). This method generally uses with the isothermal assumption under coarse resolution to retrieve the fraction and the emissivity of components (Yang, Pu, Zhao, Huang and Wang, 2011). However, Weng et al. (2014) indicated that the isothermal assumption that underpins various modulation methods for retrieving component temperature or emissivity might not be valid, especially within the urban landscape with a mixture of different temperature components.

The most common modulation-based algorithms include the PBIM developed by Guo and Moore (1998) and the Emissivity Modulation method developed by Nichol (2009). The PBIM was developed to add spatial detail to LANDSAT-TM thermal band images based on the use of visible and near-infrared bands to identify topographic variations (Guo and Moore, 1998). This method is also used by Stathopoulou and Cartalis (2009) in AVHRR LST downscaling, but they used LANDSAT-TM as higher spatial resolution data. Dominguez et al. (2011) indicated that this method is not applicable to flat urban areas with very heterogeneous land covers. Zhu, Guan, Millington and Zhang (2013) also indicated that in the PBIM method based on Stathopoulou and Cartalis (2009), TIR data with a higher resolution is required as the input.

Moreover, Jung and Park (2014) indicated that PBIM had been proposed to fuse the panchromatic and TIR images of LANDSAT-5 TIR images for terrestrial Earth observation applications. This method has added the right amount of spatial details to the TIR images; however, it has not preserved thermal information of the TIR

images. On the other hand, the EM method makes a simplifying assumption that the thermal emittance is uniform within the low-resolution pixels and utilizes the emissivity data at a higher resolution to perform disaggregation. However, these data sets are usually unavailable (Zhu et al., 2013), and Dominguez et al. (2011) also indicated that emissivity is not the primary determinant of LST during the daytime, and the accuracy of the land class-based emissivities is questionable when emissivities libraries are used.

Regarding the statements mentioned above, the physical-based methods contain a lot of technical limitations due to the requirement of many independent measurements (Zaksek and Ostir, 2012), and the limited by the complexity of these methods which is much more complicated than statistical-based methods (Sattari, Hashim and Pour, 2018). Therefore, the statistical models have become the most prevalent owing to their ease of use, simplicity, robustness and acceptable downscaling accuracy (Pan et al., 2018; Yang, Li, Pan, Zhang and Cao, 2017; Zhou et al., 2016).

2.3.2 The statistical-based method

The statistical method is based on the correlation between LST and other ancillary data, likewise, LULC indices and other factors. This technic is based on fitting an ordinary least-squares regression function between each index (the predictors) and the LST derived from the satellite image at coarse resolution. The residual is introduced in the model to take into account the dependence of LST spatial variability on various environmental factors other than the employed predictors (Bonafoni, 2016).

The most common statistical-based downscaling algorithms include the DisTrad and the TsHARP, which were developed by Kustas, Norman, Anderson and French (2003) and Agam, Kustas, Anderson, Li and Neale (2007), respectively. DisTrad algorithm uses a quadratic regression relationship between LST and NDVI; on

the other hand, TsHARP exploits the linear relationship between LST and FVC (Mukherjee, Joshi and Garg, 2014; Zhou et al., 2016). These two models present the linear or non-linear relationship between LST and vegetation index (Pan et al., 2018). The models mentioned above are mainly applied to areas covered by a high vegetation fraction (Zhu et al., 2013). However, these indices are unsuitable for LST downscaling in urban areas (Dominguez et al., 2011; Nichol, 2009; Stathopoulou and Cartalis, 2009).

Zhu et al. (2013) indicated that LST disaggregation in the heterogeneous areas, especially urban areas, is very difficult to achieve. Furthermore, Yang, Cao, Pan, Li and Zhu (2017) also indicated that for complex urban areas with varying land cover types, multiple scale factors must be integrated to achieve high downscaling precision. Testing of the statistical-based method is still in a preliminary stage for applications in urban areas (Essa, Kwast, Verbeiren and Batelaan, 2013; Sattari et al., 2018); also, there are few studies focus on improving LST downscaling in urban areas with several mixed surface types (Yang, Li, et al., 2017; Zhu et al., 2013).

Based on the previous studies, Dominguez et al. (2011) developed the HUTs to increase the resolution of thermal infrared data to that of visible and near-infrared data by fitting the relationship between radiometric surface temperature, NDVI and surface albedo. As a result, HUTS showed an improvement of over 0.5 °C and over 17 percentage in MAE and RMSE from non-sharpening. Essa et al. (2013) adapted the DisTrad method for downscaling the LST over urban areas using the relationship between LST and impervious percentage. This new approach shows improved downscaling results over urban areas for all evaluated resolutions, especially in an environment with mixed land covers. Sattari et al. (2018) developed an adaptive TsHARP algorithm to downscale the LST by utilizing an impervious surface index in

urban areas. It was found that all evaluated resolutions attained superior results compared with the traditional methods over urban imagery, mainly, the environments with heterogeneous land covers. Bonafoni (2016) carried out a downscaling from the coarser spatial resolution of the LST images to finer spatial resolution using the relationship between LST and spectral indices; however, the results indicated that the best regression models include both vegetation and built-up /soil spectral indices.

Furthermore, Bonafoni, Anniballe, Gioli and Toscano (2016) developed a new downscaling algorithm for LST images with the considering three generalized land cover classes, i.e., built-up, vegetation and open water. NDVI, NDBI, and NDWI were computed from LANDSAT data to represent those three classes. The overall RMSE with respect to 1 meter airborne ground spatial improves from 3.3 °C (USGS) to 3.0 °C with the new method, that also showed better results concerning other regressive downscaling technics and they also pointed out the impact of the predictor of resolving specific thermal details, showing that the image sharpening topic is still an open issue.

In conclusion, finer-scale studies, such as the analysis of UHI, require LST data at a higher spatial resolution than those provided by the available current satellite thermal sensors. The LST data can be improved the spatial resolution using the downscaling methods, which can be categorized as a physical-based method and a statistical-based method. The physical-based methods contain a lot of technical limitations, such as the limitation in thermal information preservation and the use of emissivity to perform disaggregation. In contrast, the statistical-based methods are the most prevalent owing to their simplicity, robustness, and acceptable downscaling accuracy. Furthermore, recent models have been developed based on this method to perform the subpixel LST data estimation in urban areas. However, previous studies

pointed out the impact of the predictor of resolving specific thermal details. A suggestion for improvement in areas with complex land-cover is the use of independent specific regression indices either derived for different LULC types or deriving those indices based on multiple linear regression analysis within the urban class. In this study, spectral indices, which are derived for different LULC types, are used to avoid the use of emissivities, which is not the primary determinant of LST during the daytime. Therefore, the statistical-based method is selected to estimate subpixel LST data. Moreover, LANDSAT-8 imagery data, which are used in this study, can be appropriately used with this method because spectral reflectance in visible, near-infrared and short-wave wavelength can be processed as several spectral indices and used as the scaling factors in multiple regression modeling.

2.4 Hotspot analysis

The significance of hotspot analysis is capable of allowing statistical-based estimates of spatial variation in thermal aggregation (Feyisa, Meiby, Jenerette and Pauliet, 2016). The identification of the hotspots helps to identify areas of priority for the implementation of mitigation and adaptation strategies (Adeyeri, Akinsanola and Ishola, 2017).

There are different methods in spatial patterns analysis and detecting hotspots, such as cluster analysis, spatial autocorrelation, and mapping technic. The nearest neighbor index is a simple method for testing clustering in the data, but this method does not account for spatial autocorrelation of events. The kernel density estimation is another method in hotspot detection. This method creates a smooth, continuous surface of the density of observations. However, the user must specify the grid cell, bandwidth,

and thematic threshold, which can lead to different results depending on the values chosen. This mapping technic does not provide statistically significant hotspots. In contrast, the spatial autocorrelation analysis provides a statistically significant hotspot and accounts for spatial autocorrelation of events (Mailman school of public health, n.d.).

The spatial autocorrelation analysis can be categorized as global and local measures of spatial association. Karlstrom and Ceccato (2002) indicated that global measures of spatial association provide a tool for testing for spatial patterning over a whole study area while local measures test for local patterns of spatial association. On the other hand, local measures can be understood as a complementary source of information on a specific spatial pattern.

2.4.1 Moran's I

Moran's I (Moran's Index) is a global measure of the correlation among neighboring observations in a pattern (Boots and Getis, 1998). It evaluates whether the pattern expressed is clustered, dispersed, or random. The Moran's I statistic for spatial autocorrelation is given as; (ESRI, 2016).

$$I = \frac{n \sum_{i=1}^n \sum_{j=1}^n w_{i,j} z_i z_j}{S_0 \sum_{i=1}^n z_i^2} \quad (2.10)$$

Where z_i is the deviation of an attribution for feature i from its mean ($x_i - \bar{x}$), $w_{i,j}$ is the spatial weight between feature i and j , n is equal to the total number of features, and S_0 is the aggregate of all the spatial weights:

$$S_0 = \sum_{i=1}^n \sum_{j=1}^n w_{i,j} \quad (2.11)$$

The Z_I score for the statistic is computed as:

$$Z_I = \frac{I - E[I]}{\sqrt{V[I]}} \quad (2.12)$$

$$\text{Where: } E[I] = -1 / (n - 1) \quad (2.13)$$

$$V[I] = E[I^2] - E[I]^2 \quad (2.14)$$

The spatial autocorrelation (Global Moran's I) is an inferential statistic, in which the results of the analysis are always interpreted within the context of its null hypothesis. For the Global Moran's I statistic, the null hypothesis states that the data is randomly distributed. When the Z score is significant (or small) enough and falls outside the desired significance, the null hypothesis can be rejected. A Moran's Index value near +1.0 indicates clustering, while an index value near -1.0 indicates dispersion (ESRI, 2016; Prasannakumar, Vijith, Charutha and Geetha, 2011).

2.4.2 Getis-Ord G_i^*

The local Getis-Ord statistic provides a criterion for identifying clusters of high or low values, indicating the presence of significant local spatial clusters (Karlstrom and Ceccato, 2002). The Getis-Ord G_i^* statistic has been used in hotspot analysis in many previous studies. Ren et al. (2016) used the Getis-Ord G_i^* statistic to detect the spatial position of hot-and cool-spot clustering regions of urban forest LST based on an optimal threshold-distance scale. Furthermore, they studied how human

activities and ecological factors jointly influence LST in clustering regions (hot or cold spots) of urban forests. Feyisa et al. (2016) also used Getis-Ord G_i^* to explore thermal aggregation in different parts of the city and to examine thermal variation among urban and rural landscapes.

Moreover, the hotspot analysis was intended to evaluate how thermal aggregation is related to distance from the city center and the dynamics of land cover types. Adeyeri et al. (2017) identified the hotspot areas using Getis-Ord G_i^* and investigated SUHI characteristics over Abuja, Nigeria. The results found that significant hotspots of high LST were recorded in built-up areas and bare surfaces, while significant cold spots were found over vegetation surfaces. Furthermore, Tran et al. (2017) assessed the impacts of LULC change and urbanization on UHI using hotspot analysis (Getis-Ord G_i^* statistics) and urban landscape analysis.

This technic characterizes the presence of hot spots (high clustered values) and cold spots (low clustered values) over an entire area by looking at each feature (LST value) within the context of the proximity features (Ord and Getis, 1995). A feature with a high value is highlighted but may not be a statistically significant hot spot. As a significant hot spot, a feature will have a high value and be surrounded by other features with high values as well (ArcGIS Pro, 2018). The Getis-ord local statistic is given as:

$$G_i^* = \frac{\sum_{j=1}^n w_{i,j} x_j - \bar{X} \sum_{j=1}^n w_{i,j}}{S \sqrt{\frac{n \sum_{j=1}^n w_{i,j}^2 - (\sum_{j=1}^n w_{i,j})^2}{n-1}}} \quad (2.15)$$

Where x_j is the attribute value for feature j , w_{ij} is the spatial weight between feature i and j , n is equal to the total number of feature and:

$$\bar{X} = \frac{\sum_{j=1}^n x_j}{n} \quad (2.16)$$

$$S = \sqrt{\frac{\sum_{j=1}^n x_j^2}{n} - (\bar{X})^2} \quad (2.17)$$

The G_i^* statistic is a Z-score, so there are not any further calculations required. Wang, Tian, Huang, Wang and Wei (2015) indicated that statistically significant positive Z score, the higher the value is, which belongs to a high-value spatial agglomeration (hotspot area). In contrast, for statistically significant negative Z scores, the value is, the closer the low value (cold spot) clustering is, which indicates that the location of values around i is relatively low (below average), i belongs to a low-value spatial agglomeration (cold spot area).

In conclusion, the identification of the hotspots helps to identify areas of priority for the implementation of mitigation and adaptation strategies. However, there are different methods in spatial patterns analysis and hotspots investigation, such as cluster analysis, spatial autocorrelation, and mapping technic. The spatial autocorrelation analysis, which is selected in this study, can provide the statistically significant hotspot and account for spatial autocorrelation of events. This method can be categorized as global or local indicators of spatial association. The Moran' I, which is the global

indicator, is selected to analyze the pattern of the data. On the other hand, Getis-Ord G_i^* , which is a local indicator, is used in hotspots investigation.

2.5 Urban green spaces

It is widely understood that urban green spaces have a natural ability to reduce local air and ground temperature (Zupancic, Westmacott and Bulthuis, 2015). Vegetation controls temperature by evapotranspiration and shading (Nichol and Wong, 2005; Oke, 1988), whereas paved areas without vegetation have no cooling by evapotranspiration, and they transfer most incoming radiation to the urban atmosphere as heat (Nichol and Wong, 2005). On the other hand, shading affects human comfort since it will alter our perceived temperature, which is dependent more on the radiation flow between ourselves and the local environment than on convection (Matzarakis, Rutz and Mayer, 2007). If the loss of vegetation causes the UHI, adding vegetation to urban areas could potentially reduce its magnitude (Armson, Stringer and Ennos, 2012).

Urban green spaces are broadly defined as all types of vegetation found in the urban environment (Maimaitiyming, 2013). Therefore, green spaces refer to those land uses that are covered with natural or human-made vegetation in the built-up areas and planning areas (Wu, 1999). However, Jim and Chen (2003) indicated that green spaces in cities exist mainly as semi-natural areas, managed parks and gardens, supplemented by scattered vegetated pockets associated with roads and incidental locations.

Perini and Magliocco (2014) indicated that the difference cooling effect of vegetation could be noticed depending on the number of green areas and vegetation type, which vary with plant-specific thermal and optical characteristics (Taha, 1997). Li, Zhou, Ouyang, Xu and Zheng (2012) reported that a ten percent increase in green

space cover produces a 0.86 °C decrease in LST. Moreover, Feyisa, Dons and Meiby (2014) found that the temperature dropped by 0.02 °C for every percentage increase in tree canopy cover. Therefore, it can be concluded that the increase in vegetation cover or increase the amount of green areas can reduce the air and surface temperature (Dimoudi and Nikolopoulou, 2003; Feyisa et al., 2014; Giridharan, Lau, Ganesan and Givoni, 2008; Kong, Yin, James, Hutyra and He, 2014; Kuo, 2000; Li et al., 2012).

However, Vannier, Vasseur, Hubert-Moy and Baudry (2011) found that the calculated percent cover of green space varied greatly across spatial resolution, decreasing significantly with the decrease of spatial resolution. Urban green space is generally highly fragmented in the urban landscape, resulting in a large number of small patches. These small patches can only be effectively mapped using high spatial resolution imagery data. Li, Zhou, et al. (2013) also found that the relationship between LST and percentage cover of green space was negative across the spatial resolution. The magnitudes of the decrease of LST by percent cover of green space were generally higher at finer spatial resolution. Furthermore, imagery with higher spatial resolution could more accurately quantify the spatial of green space.

On the other hand, vegetation type also plays an essential role in a cooling effect. Both grass and trees can effectively cool surface and so can provide regional cooling, helping reduce the UHI in hot weather (Armson et al., 2012). However, Ng, Chen, Wang and Yuan (2012) indicated that trees were more effective than grass surfaces in the cooling pedestrian area. Grass helps lower temperature in parks since grass has a higher albedo than asphalt or most building roofs (Thundiyil, 2003), but grass has little effect upon local air or globe temperatures, so should have little effect on human comfort, whereas tree shade can provide active local cooling (Armson et al., 2012).

However, Shashua-Bar, Pearlmutter and Erell (2009) found that the combination of shade trees over grass in a hot-arid region was the most effective landscape strategy. Onishi, Cao, Ito, Shi and Imura (2010) also found that the maximum reduction of the surface temperature of individual parking lots could be up to 9.26 °C in summer by planting 30 percent trees and 70 percent grass.

In terms of trees types, deciduous trees have been identified as most important for providing thermal comfort in parks since they provide shade in hot months but do not block needed warmth from the sun in cold month (Hwang, Lin and Matzarakis, 2011; Lin and Lin, 2010). During summer, both deciduous and evergreen trees provide similar cooling effects, but in winter, the evergreen tree park was much cooler and below the neutral comfort conditions (Cohen, Potchter and Matzarakis, 2012; Zhang, Lv and Pan, 2013). However, green spaces with a predominance of mixed trees appear to have the most significant cooling ability in terms of UHI mitigation and providing thermal comfort and relief from heat stress (Chen, Yao, Sun and Chen, 2014; Perini and Magliocco, 2014; Zhang, Lv, et al., 2013).

The density and size of trees are also significantly playing an essential role in the green area cooling effect (Shashua-Bar, Tsiros and Hoffman, 2010). Lin and Lin (2010) found that the cooling efficiency of urban parks is mostly influenced by leaf color and foliage density. Shashua-Bar, Tsiros and Hoffman (2012) indicated that trees with dense canopy coverage were the best for decreasing air temperature, particularly on the hottest days. Not only canopy density, but Zhang, Lv, et al. (2013) also found that canopy area and tree height also had a significant influence on temperature reduction and relative humidity increase.

The urban parks are one of the essential areas in urban thermal environmental improvement and UHI effects mitigation. Ren et al. (2013) found that urban park size (area and perimeter) had a significant positive relationship with PCI. Therefore, larger parks have stronger cooling effects than smaller ones. Cao, Onishi, Chen and Imura (2010) indicated that mean and maximum PCI intensity values increased in all seasons, but especially in spring and summer. However, Chang, Li and Chang (2007), Cao et al. (2010), and Ren et al. (2013) found that park size is non-linearly correlated to PCI intensity. Furthermore, Ren et al. (2013) also indicated that the possibility that PCI intensity increases gradually with increases in urban park size when the size is more significant than a certain threshold.

Cao et al. (2010) found that the possibility that significant PCI only exists when parks larger than a certain threshold (2 ha in the study). However, Oliveira, Andrade and Vaz (2011) found that small space (0.24 ha) was cooler than the surrounding areas, either in the sun or in the shade. These differences were higher in hotter days and mainly related to the mean radiant temperature. These results confirm the potential contribution of green areas, even small ones, as a mitigation measure of the adverse effects of the UHI and the potential additional effects of global warming in cities.

However, as is known to us, it is hard to increase the number of urban parks due to limited land resources for urban greening and many political reasons (Declét-Barreto et al., 2013; Jenerette, Harlan, Stefanov and Martin, 2011). Therefore, urban planners must understand how to design urban parks to maximize their PCI intensity and mitigate the UHI effect (Ren et al., 2013). Because the park characteristics also play different roles in the PCI phenomenon (Cao et al., 2010; Chang et al., 2007; Feyisa et al., 2014; Ren et al., 2013).

Ren et al. (2013) found that urban park shape (perimeter /area) had a significant negative relationship with PCI intensity, both in summer and autumn, but the effects were stronger in cold seasons (Chen et al., 2014). Increasing complexity in shape, the cooling effect of urban parks decreased. Thus, the rounder of the urban park shape, the better cooling island effect is (Ren et al., 2013). Furthermore, Feyisa et al. (2014) found that small parks with a shape closer to that of a circle have higher thermal contrast with their immediate surroundings than elongated parks. Cao et al. (2010) also found that the irregular and belt-shape parks tend to have low PCI intensity, while the compactness of PCI may benefit PCI development. However, parks that have more irregular shapes tended to have higher park cooling distance, indicating that the larger area of the zone where irregular parks are in contact with the surrounding non-park landscape may increase the distance within which parks influence the thermal environment (Feyisa et al., 2014). Moreover, Cao et al. (2010) also indicated that complex shapes contributing to greater cooling distance.

However, the composition of land cover features is another important factor. Cao et al. (2010) found that PCI intensity is mainly determined by the area of tree and shrub inside the park as well as the park shape. Zhou, Huang and Cadenasso (2011) also indicated that the composition of land cover features is more important in determining LST than their configuration. Mainly, woody vegetation results in the highest temperature difference. These results suggest that the impact of urbanization on UHI can be mitigated not only by balancing the relative amount of various land cover features but also by optimizing their spatial configuration.

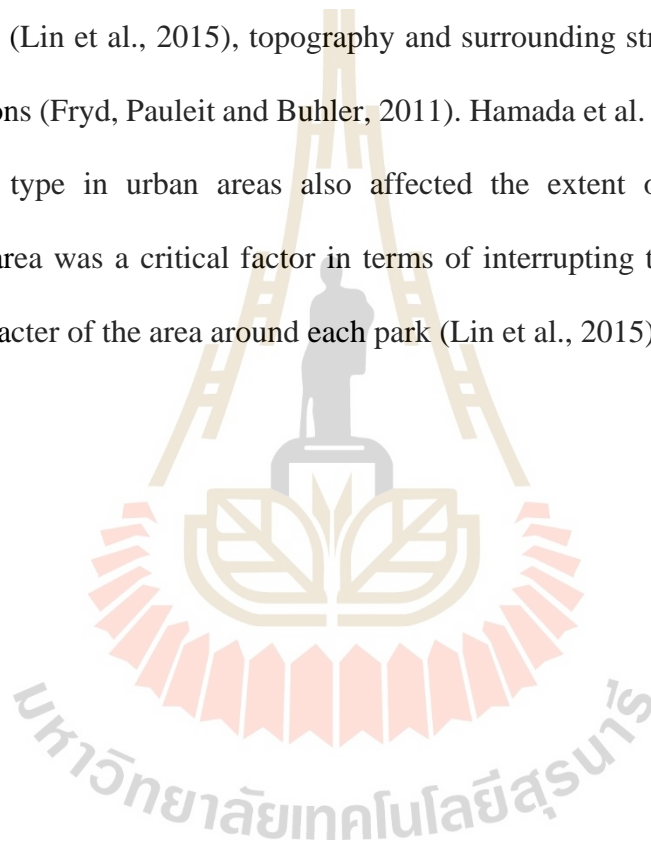
Furthermore, Yu and Hien (2006) indicated that the cooling effects of city green areas are reflected not only in vegetated areas but also in the surrounding area, particularly at the leeward side of the green area. Hamada and Ohta (2010) found that the difference is more significant during the day than during the night in summer, whereas in winter, the opposite relationship is correct. During the night, the cooling effect of the green area reached 200-300 m in the urban area. During the day, the cooling effect exceeded 300 m and varied widely, although there is no correlation beyond 500 m. Hamada, Tanaka and Ohta (2013) also found that the cooling effect is found to extend in any directions into the urban areas. Furthermore, Doick, Peace and Hutchings (2014) also found that the extension of the cooling effect beyond the green space boundary is the greatest during low wind speeds, as observed during the atmospherically stable conditions typical of a heatwave.

Moreover, the connectivity of urban green spaces also affected the cool urban islands negatively (Chen et al., 2014). At the neighborhood level, increased green space cover and high connectivity between neighborhood-level green spaces are associated with cooler air temperatures and reduced UHI effects, particularly on hot days (Steeneveld, Koopmans, Heusinkveld, Hove and Holtslag, 2011). More closely linked and continuous green spaces have stronger cool island effects than smaller patches of green space (Li, Zhou, et al., 2013; Li et al., 2012). Therefore, maximizing the connectivity of many scattered parks throughout the urban environment (rather than in one concentrated spot) will maximize cooling effects beyond park boundaries by breaking up the micro effects of the urban form that can cause hotter and cooler pocket (Doick et al., 2014; Hamada and Ohta, 2010).

Green façade and green roofs may be a useful alternative in areas where there is limited capacity for tree planting (Zupancic et al., 2015). Green façade is one of the vertical greenery systems in which climbing plants or vine plants that are rooted in the limited ground area around the buildings are trained to cover unique support structures such as fences or columns. The green façade can mitigate UHI effects and provide considerable relief from heat stress (Koyama, Yoshinaga, Hayashi and Maeda, 2013). On the other hand, a green roof is a vegetated layer that is grown on a building roof to replace that part of the natural landscape that was destroyed when the building was constructed (United States Environmental Protection Agency, 2017b).

However, Ng et al. (2012) indicated that roof greening was ineffective for human thermal comfort near the ground. Perini and Magliocco (2014) also indicated that green areas on the ground (grass, shrubs, trees) are more effective compared to green roofs in reducing summer potential temperatures. However, green roofs are more effective in decreasing the cooling load of buildings; this is an essential aspect since in very dense urban areas due to a lack of space it may be not possible to add more vegetation on the ground, even if green areas have a higher positive effect on outdoor summer temperatures and comfort. Furthermore, Murphy (2015) suggested that adding green space at ground level in an urban setting may be impossible, so taking advantage of the real estate afforded on commercial roofs to increase green space is a crucial strategy for UHI mitigation. Zupancic et al. (2015) also indicated that the combined benefits of green roofs and walls for cooling and pollution mitigation make them an essential alternative in high-density urban areas where ground space for greening is limited.

In conclusion, it is clearly shown that there are many factors play an essential role in the cooling effect of parks on surrounding landscape, i.e., park size (Feyisa et al., 2014; Lin, Yu, Chang, Wu and Zhang, 2015; Yu and Hien, 2006), park shape (Cao et al., 2010; Feyisa et al., 2014), vegetation density (Cao et al., 2010; Feyisa et al., 2014), tree species (Feyisa et al., 2014), weather patterns (Yu and Hien, 2006), season temperature (Cao et al., 2010), distance from park (Feyisa et al., 2014), location, spatial configuration (Lin et al., 2015), topography and surrounding structures in addition to wind conditions (Fryd, Pauleit and Buhler, 2011). Hamada et al. (2013) also found that the land-use type in urban areas also affected the extent of park cooling. The commercial area was a critical factor in terms of interrupting the cooling extension; also, the character of the area around each park (Lin et al., 2015).



CHAPTER III

RESEARCH METHODOLOGY

This chapter provides details of the research methodology, which explains the nature of this study. This research inclines to the quantitative research, which conducts statistical tools to evaluate the results obtained from the remote sensing data. Numerical data of the LST from the remote sensing were extracted and validated statistically with the in-situ data on the same date and almost the same time. As a result, the simulation of green open space presents the proportion of area adjustment to reduce the LST. Therefore, this research consists of three main topics, (1) conceptual framework, (2) data preparation, and (3) research procedures to conduct the research systematically. Their specific details are as follows.

3.1 Conceptual framework

Initially, the conceptual framework presents the flow of research concepts with some major procedures to provide the holistic of the study. In order to achieve the aim of this study, four main-parts were studied response to four objectives stated in Section 1.2, as detailed in the flowchart illustrated in Figure 3.1.

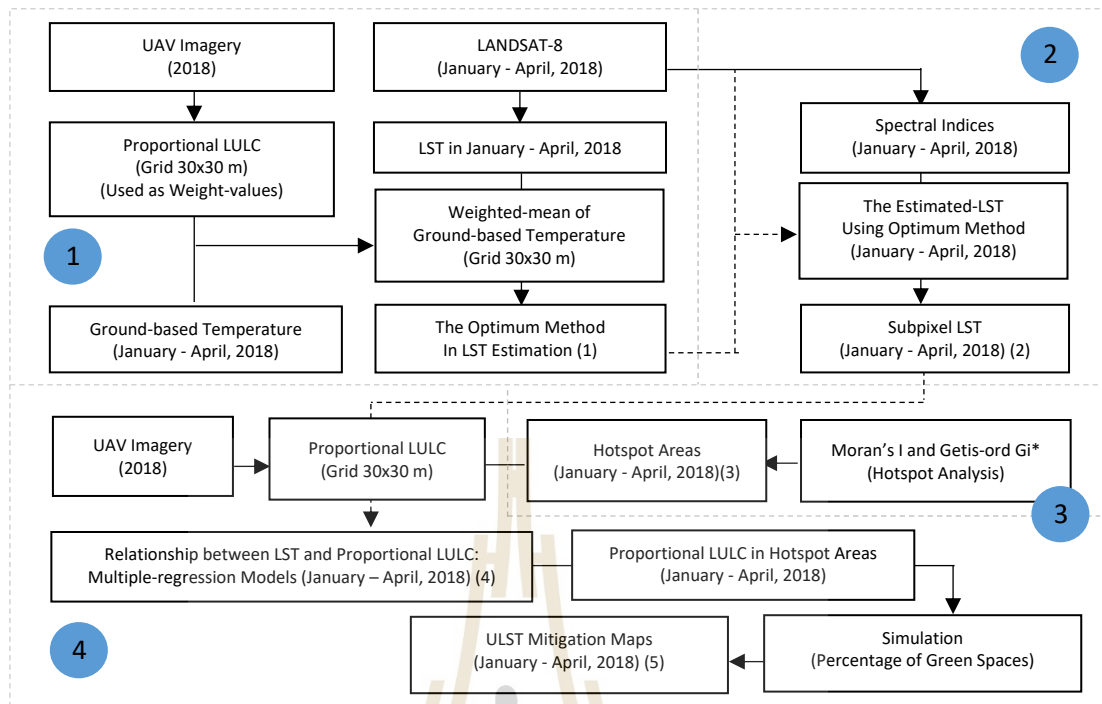


Figure 3.1 Conceptual framework.

According to Figure 3.1, the first part devotes to exploring the optimum method for ULST estimation following with the subpixel LST data estimation using a statistical-based method corresponds to the second objective. Then the subpixel LST data used in hotspot analysis identifies the hotspot areas corresponded to the third objective. Lastly, the final part related to the fourth objective, which simulates hotspot mitigation associated with proportions of green space in an urban area.

3.2 Data preparation

The following table (Table 3.1) is the list of data with their sources acquired in this research.

Table 3.1 Data used in the research.

Data	Date	Sources
LANDSAT-8 data Path /Row: 128 /50	January 21, February 6, March 26, April 11, 2018 March 20, April 5, 2016 March 31, April 16, 2014	U.S. Geological Survey (USGS)
UAV imagery data	March - April 2018	Surveying
High spatial resolution images	January 5, 2014 December 18, 2016	Google earth
Ground-based temperature data	Same date of the LANDSAT-8	Surveying
Atmospheric parameters • Air temperature • Relative humidity	Same date of the LANDSAT-8	Hydro and Agro Informatics Institute (HAII) website
Atmospheric parameters • Transmittance • Up-welling and down-welling atmospheric radiance	Same date of the LANDSAT-8	NASA atmospheric correction parameter calculator website

Note: Data in 2014 and 2016 were used in the feasibility test of the simulated temperature.

LANDSAT-8 imagery data, used in the ULST estimation, obtained from the USGS website, as shown in Table 3.1. The high spatial resolution image obtained from the UAV between March and April 2018. Additionally, the high spatial resolution imagery in 2014 and 2016, obtained from the Google Earth, were rectified using an image-to-image method based on the high spatial resolution imagery from UAV in 2018. The ground-based temperature surveying had done between 10.00 – 12.00 a.m. on the same date of the Landsat-8 satellite captured the data over the study area around 10.30 a.m. The atmospheric parameters (air temperature and relative humidity data), gathered between 10.00 - 11.00 a.m., obtained on the same date of LANDSAT-8 imagery data from Hydro and Agro Informatics Institute (HAII) website. The transmittance, up-welling, and down-welling atmospheric radiance were also gathered at the same date of LANDSAT-8 imagery data from the NASA atmospheric correction parameter calculator website.

3.3 Research procedures

The research procedures consist of four parts response to the four objectives stated in Section 1.2. The details of the processes are described in section 3.3.1 - 3.3.4.

3.3.1 To explore the optimum method for ULST estimation

In order to explore the optimum method in the ULST extraction, RTE, IMW, GSC, and SW algorithm, as equation 2.2, 2.3, 2.6, and 2.9, respectively, were used in the calculations. As a result, then, the ULST of each method was assessed with the ground-based temperature data using NRMSE. The conceptual process is shown in Figure 3.2.

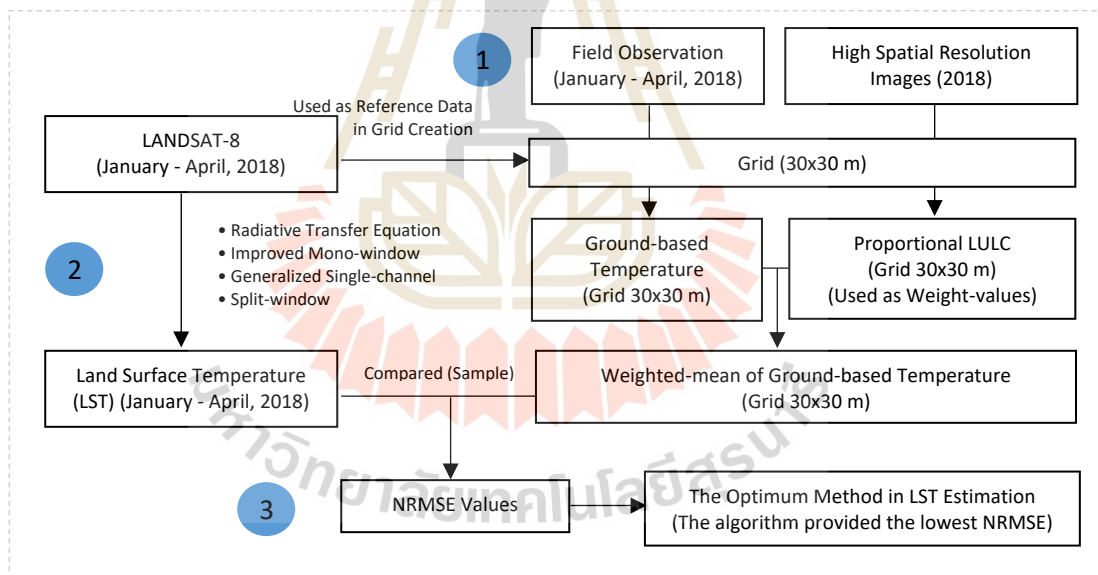


Figure 3.2 Conceptual process of the first objective.

In order to achieve the first objective, the LANDSAT-8 image was initially used as the reference data in 30x30 meters grid creation. Then, the numbers of sample points were calculated by dividing the total area of the study area with the coverage area of pixel size. Actually, the coverage area of a pixel size should be closed to the

spatial resolution of the thermal band (100 meters), so the coverage area of pixel size could be considered into 2 cases, either 3x3 pixels (90x90 meters) or 4x4 (120x120 meters) pixels. In this study, the pixel size of 3x3 pixels per sample was used, because this pixel size is within the coverage area of thermal band data. Based on the 3x3 pixels, the coverage area of pixel size is 8,100 square meters, and the total area of the study area is around six million square meters. At least several sample points are about 740.74; however, the total number of sample points is 900 points.

On the other hand, ground-based temperature data were collected from 9 neighboring sample points per one site with responding to the spatial resolution of the thermal band. At least several sites are 83 sites; however, the total number of sites is 100, which fulfills the total number of sample points. The stratified random sampling method was used in data collection. The concept of the ground-based temperature surveying is shown in Figure 3.3.

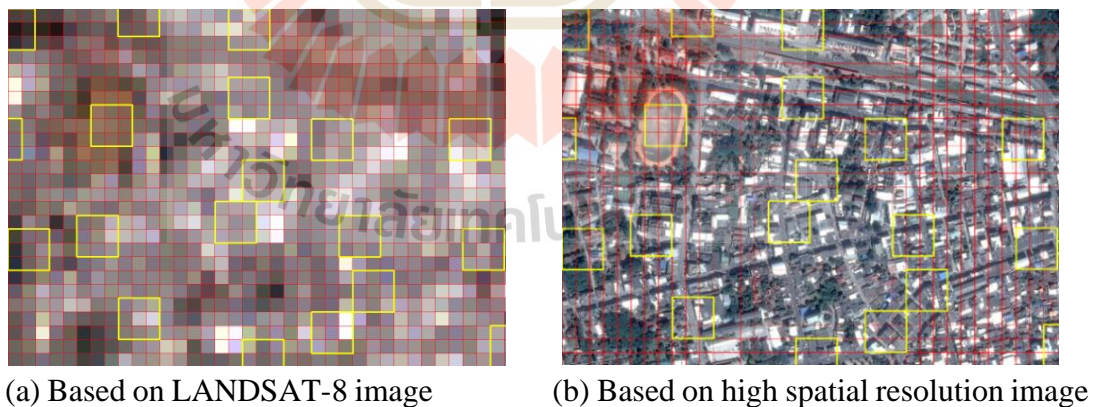


Figure 3.3 Ground-based temperature surveying concept.

Figure 3.3(a) shows the grids on LANDSAT-8 imagery data, whereas Figure 3.3(b) shows the grids on high-resolution imagery data at the same location. The red grids are the sample points generated based on the LANDSAT-8 imagery data; on the other hand, the yellow grids are the surveying sites. The ground-based data were collected from 9 neighboring sample points per site. The total number of sites is 100, as shown in Figure 3.4.

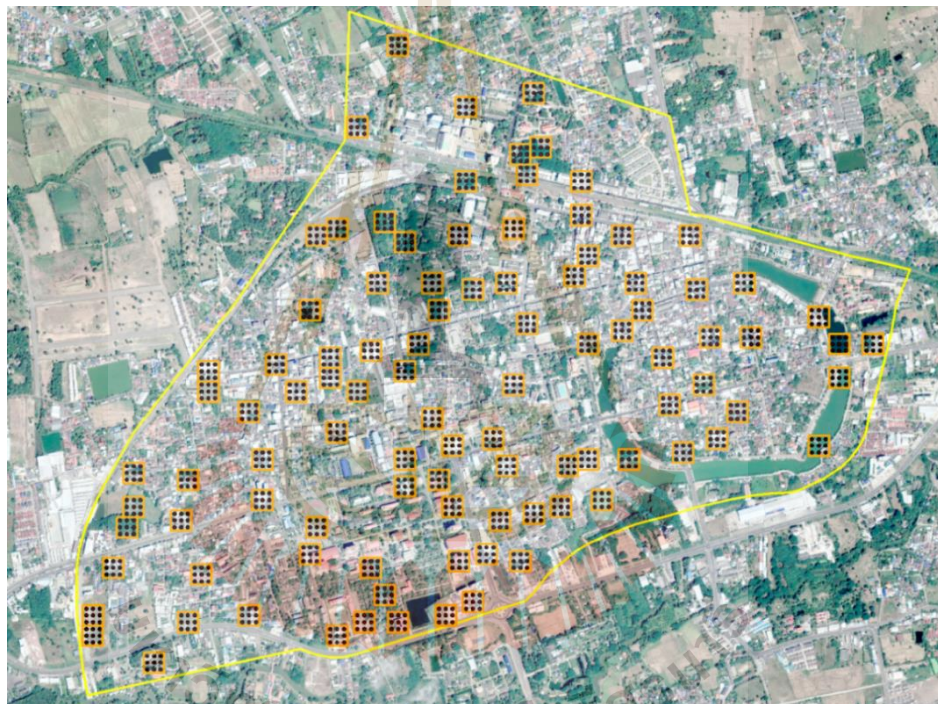


Figure 3.4 Distribution of sample points and sample sites.

Based on Figure 3.4, the sample sites are shown in the orange squares; on the other hand, the sample points are shown as the points in the sample sites. The numbers of sample sites are 100. One sample site contains nine sample points; therefore, the total sample points are 900. All samples were collected within the Buriram municipal area, the yellow line representing the boundary of the municipality.

Generally, the arithmetic means temperature data were calculated from each grid. The proportion of LULC within each grid was used as the weight values. In ground-based temperature surveying, all LULC temperatures within each grid were measured and averaged using the arithmetic means method. The obtained arithmetic means temperature data were used as the reference data and compared with the estimated ULST data from each method.

The ULST data were extracted using RTE, IMW method developed by Wang et al. (2015), GSC method developed by Jimenez-Munoz, Sobrino, Skokovic, Matter and Cristobal (2014), and SW method developed by Jimenez-Munoz et al. (2014). The atmospheric parameters in 2014, 2016, and 2018, which used in the LST estimation based on each method, are shown in Table 3.2.

Table 3.2 Atmospheric parameters in 2014, 2016, and 2018.

Atmospheric Parameters		2014		2016	
		Mar 31	Apr 16	Mar 20	Apr 5
Air Temperature (T ₀) (K)		313.2	311.2	309.8	311.2
Air Temperature (T ₀) (°C)		40.05	38.05	36.65	38.05
Relative Humidity		0.42	0.53	0.50	0.39
Water Vapor Content		3.17	3.57	3.14	2.67
Method	Atmospheric Parameters	Mar 31	Apr 16	Mar 20	Apr 5
RTE	Transmittance (τ)	0.56	0.47	0.57	0.64
	Up-welling	3.97	4.42	3.88	3.37
	Down-welling	6.08	6.68	6.03	5.38
IMW	Atmospheric Temperature (T _a)(K)	305.23	303.39	302.11	303.39
	Transmittance (τ)	0.61	0.55	0.61	0.67
GSC	Atmospheric Function (ψ_1)	1.51	1.63	1.50	1.38
	Atmospheric Function (ψ_2)	-8.41	-10.05	-8.31	-6.55
	Atmospheric Function (ψ_3)	4.13	4.70	4.09	3.43
SW	Water Vapor Content	3.17	3.57	3.14	2.67

Note: 1. Transmittance, up-welling, and down-welling used in the RTE method were obtained from NCEP.

2. The transmittance used in IMW was calculated based on the mono-window method.

Table 3.2 Atmospheric parameters in 2014, 2016, and 2018 (Continued).

		2018			
Atmospheric Parameters		Jan 21	Feb 6	Mar 26	Apr 11
Air Temperature (T ₀) (K)		303.9	293.1	302.9	309.3
Air Temperature (T ₀) (°C)		30.75	19.95	29.75	36.15
Relative Humidity		0.63	0.60	0.65	0.44
Water Vapor Content		2.86	1.52	2.79	2.72
Method	Atmospheric Parameters	Jan 21	Feb 6	Mar 26	Apr 11
RTE	Transmittance (τ)	0.53	0.80	0.54	0.60
	Up-welling	3.92	1.63	3.78	3.56
	Down-welling	6.00	2.67	5.86	5.65
IMW	Atmospheric Temperature (T _a)(K)	296.69	286.79	295.78	301.65
	Transmittance (τ)	0.65	0.80	0.65	0.65
GSC	Atmospheric Function (ψ ₁)	1.42	1.15	1.41	1.39
	Atmospheric Function (ψ ₂)	-7.25	-2.97	-6.99	-6.70
	Atmospheric Function (ψ ₃)	3.69	1.81	3.60	3.49
SW	Water Vapor Content	2.86	1.52	2.79	2.72

Note: 1. Transmittance, up-welling, and down-welling used in the RTE method were obtained from NCEP.

2. The transmittance used in IMW was calculated based on the mono-window method.

According to Table 3.2, the near-surface air temperature (T₀) and relative humidity obtained from the Hydro and Agro Informatics Institute (HAI) website were taken from the Huai Rat Station located near Buriram Town Municipality. These parameters were used in the water vapor content calculation in equation 3.1 (Liu and Zhang, 2011).

$$w_i = \left\{ 0.59 \times RH \times \exp \left[\frac{17.27 \times (T_0 - 273.15)}{237.3 + (T_0 - 273.15)} \right] \right\} + 0.1697 \quad (3.1)$$

Where w_i is the water vapor content (g cm^{-2}), T_0 is the near-surface air temperature (K), and RH is the relative humidity (Decimal). The water vapor content, near-surface air temperature and relative humidity are the average values.

The water vapor content data are used in the transmittance calculation in the IMW algorithm, the atmospheric function in the GSC algorithm, and also used in the SW algorithm. Not only the water vapor content calculation, but this parameter is also used in the atmospheric temperature (T_a) calculation, which is an essential parameter in the IMW algorithm.

The transmittance, up-welling, and down-welling atmospheric radiance obtained from the NASA atmospheric correction parameter calculator (Barsi, Schott, Palluconi and Hook, 2005). The calculator uses the National Centers for Environmental Prediction (NCEP) modeled global atmospheric profiles interpolated to a particular date, time, and location as the input for the MODTRAN radiative transfer code and a suite of the integrative algorithm to infer the up-welling, down-welling radiances and site-specific transmission (Weng and Fu, 2014). It is noted that the mid-latitude summer model was used in this study because there is no tropical model.

Lastly, the RMSE values of each LST estimation algorithm were calculated based on equation 3.2, by comparing the estimated LST data with the weighted arithmetic mean temperature of each grid. Then, the RMSE values were normalized to NRMSE values by using equation 3.3. The NRMSE value, which has no unit and the range of the value, between 0-1, facilitates the comparison between datasets. The smaller the value is, the better the performance of the model. Eventually, the method in which provides the lowest NRMSE values considers as an optimum method in ULST estimation.

$$\text{RMSE} = \sqrt{\frac{1}{n} \sum (\text{estimate value} - \text{observe value})^2} \quad (3.2)$$

Where estimate value is the estimated LST data; on the other hand, observe value is the weighted arithmetic mean temperature of each grid or ground-based temperature data, respectively.

$$\text{NRMSE} = \frac{\text{RMSE}}{\text{maximum observation} - \text{minimum observation}} \quad (3.3)$$

Where maximum and minimum observations are the maximum and minimum temperature of in-situ data.

3.3.2 To estimate subpixel LST data using a statistical-based method

According to the second objective, the subpixel LST data were calculated based on the statistical-based method. Regarding the accuracy assessment, the subpixel LST data were compared with ground-based temperature data using NRMSE values. The conceptual processes are shown in Figure 3.5.

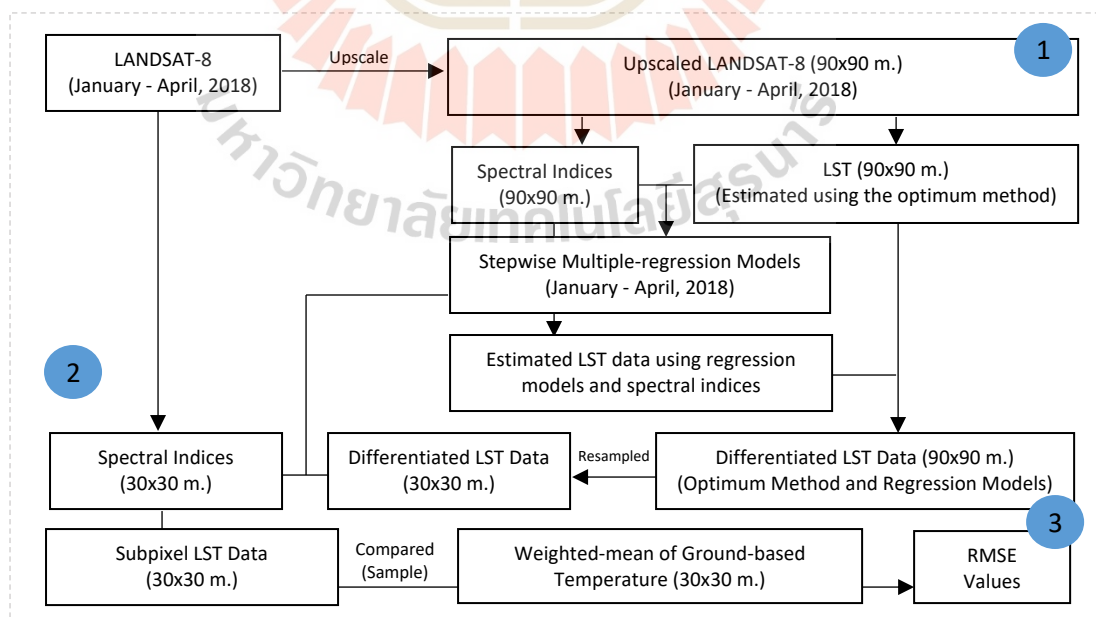


Figure 3.5 Conceptual processes of the second objective.

Firstly, LANDSAT-8 images were upscaled to 90x90 meters using the aggregation method based on the average statistic, as shown in Figure 3.5. The estimated ULST (T_{90}) and spectral indices (SI_{90}) were processed using the upscaled LANDSAT-8 images.

The spectral indices were used as the scaling factors. Different scaling factors were applied at varying application areas (Zhan et al., 2012), and selected based on the characteristics of the study area (Yang, Li, Pan, Zhang and Cao, 2017). In this research, spectral indices used as the scale factors are shown in Table 3.3.

Table 3.3 Spectral indices used in this study.

Spectral Indices	Equation	References
UI	$(SWIR2 - NIR) / (SWIR2 + NIR)$	Kawamura, Jayamana and Tsujiko (1996)
NDBI	$(SWIR1 - NIR) / (SWIR1 + NIR)$	Zha, Gao and Ni (2003)
IBI	$[(NDBI - (SAVI + MNDWI)/2) / [(NDBI + (SAVI + MNDWI)/2)]$	Xu (2008)
NDISI	$TIR - [(MNDWI + NIR + SWIR1)/3] / TIR + [(MNDWI + NIR + SWIR1)/3]$	Xu (2010)
BI	$(SWIR1 + RED) - (NIR + BLUE) / (SWIR1 + RED) + (NIR + BLUE)$	Rikimaru and Miyatake (1997)
NDBaI	$(SWIR1 - TIR1) / (SWIR1 + TIR1)$	Zhao and Chen (2005)
NDVI	$(NIR - RED) / (NIR + RED)$	Rouse, Haas, Schell, Deering and Harlan (1974)
SAVI	$[(NIR - RED) / (NIR + RED + 0.5)] \times (1 + 0.5)$	Huete (1988)
FVC	$[(NDVI - NDVI_{min}) / (NDVI_{max} - NDVI_{min})]^2$	Gillies and Carlson (1995)
NDWI	$(GREEN - NIR) / (GREEN + NIR)$	McFeeters (1996)
NDMI	$(NIR - SWIR1) / (NIR + SWIR1)$	Wilson and Sader (2002)
MNDWI	$(GREEN - SWIR1) / (GREEN + SWIR1)$	Xu (2006)
Surface Albedo	$(0.356BLUE + 0.130RED + 0.373NIR + 0.085SWIR1 + 0.072SWIR2 - 0.018) / 1.016$	Liang (2000) and Gercek, Guven and Oktay (2016)

Based on Table 3.3, the UI, NDBI, IBI, NDISI, BI, and NDBaI represent the impervious surfaces. NDVI, SAVI, and FVC represent the vegetation areas. The SAVI and FVC were chosen regarding the study of Xu (2008), which indicated that the SAVI is more sensitive than NDVI in detecting vegetation in the low-plant covered

areas such as urban areas. Besides, Weng, Lu and Schubring (2004) investigated the relationship between LST and vegetation abundance through various scales. The results showed a stronger relationship between LST and vegetation fraction than NDVI in different spatial resolutions and different land-use types. Commonly, the spectral indices represent the wetlands, and soil moisture is NDWI, NDMI, and MNDWI. Also, the surface albedo was chosen since Small (2006) found a close relationship between surface temperature and surface albedo in urban areas.

Then the coarse resolution data, T_{90} and SI_{90} were regressed into the model using a stepwise method to avoid multicollinearity. These regression models were used in LST estimation at 90 m (\widehat{T}_{90}), resulting in:

$$\widehat{T}_{90} = a_0 \pm a_1 SI_{90.x1} \pm a_2 SI_{90.x2} \pm a_3 SI_{90.x3} \pm \dots \pm a_i SI_{90.xi} \quad (3.4)$$

Where \widehat{T}_{90} is the estimated LST data at 90 m resolution, while $SI_{90.xi}$ are the upscale spectral indices data at 90 m resolution. The numbers of spectral indices depend on the result using the stepwise method.

Afterward, the temperature residuals (ΔT_{90}) were calculated, as the differentiated between the upscale LST (T_{90}) and the estimated LST data at 90 m resolution (\widehat{T}_{90}), resulting in:

$$(\Delta T_{90}) = T_{90} - \widehat{T}_{90} \quad (3.5)$$

The temperature residuals (ΔT_{90}) were disaggregated to 30 m resolution (ΔT_{30}) using the bi-linear resampling and added to the regression models in order to obtain the 30 m sharpener temperature (\widehat{T}_{30}).

In the second part, the sharpener LST data at 30 m (\widehat{T}_{30}) were calculated using the same regression model and regression coefficients, resulting in:

$$\widehat{T}_{30} = a_0 \pm a_1 SI_{30.x1} \pm a_2 SI_{30.x2} \pm a_3 SI_{30.x3} \pm \dots \pm a_i SI_{30.xi} + \Delta T_{30} \quad (3.6)$$

Where \widehat{T}_{30} is the sharpener LST data, $SI_{30.xi}$ are the spectral indices data at 30 m resolution, and ΔT_{30} is the disaggregated temperature residual.

For the accuracy assessment process, the subpixel LST data were compared with ground-based temperature data, which are the same as used in the first objective.

3.3.3 To identify the hotspots areas based on subpixel LST data

According to the third objective, the pattern of the data was identified using Moran's I method. If the data pattern is a cluster, the Getis-ord G_i^* was applied to identify the hotspot areas. The conceptual process is shown in Figure 3.6.

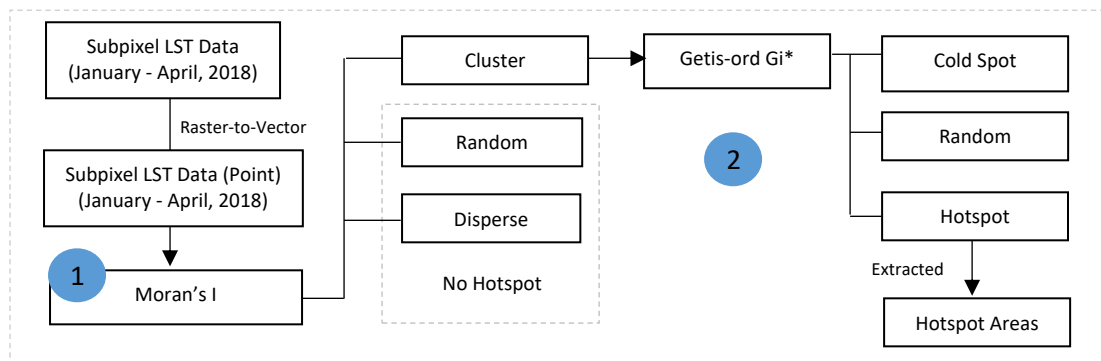


Figure 3.6 Conceptual processes of the third objective.

Initially, the subpixel LST data were converted from raster to vector format into the point pattern. Then, the converted LST points were analyzed using Moran's I method to identify the pattern of the data. Generally, in case that the pattern of the data is a cluster, it is a hotspot area. In contrast, if the patterns of the data are random or disperse, there are no hotspot areas.

The threshold distance, identified as the hotspot area, was set to 30 meters, corresponding to the spatial resolution of subpixel LST data. The Getis-ord G_i^* results present hotspot, random, and cold spot. In this study, all statistically significant hotspot occurred in January to April 2018 were selected and combined to represent the hotspot areas.

3.3.4 To simulate hotspot mitigation from proportions of green space in an urban area

Regarding the final objective, it is essential to simulate hotspot mitigation associated with proportions of green space in an urban area. The relationships between monthly subpixel LST data and the proportional LULC in sample points were

determined using regression analysis. Then, the monthly regression models were applied to the hotspot areas. The conceptual process was shown in Figure 3.7.

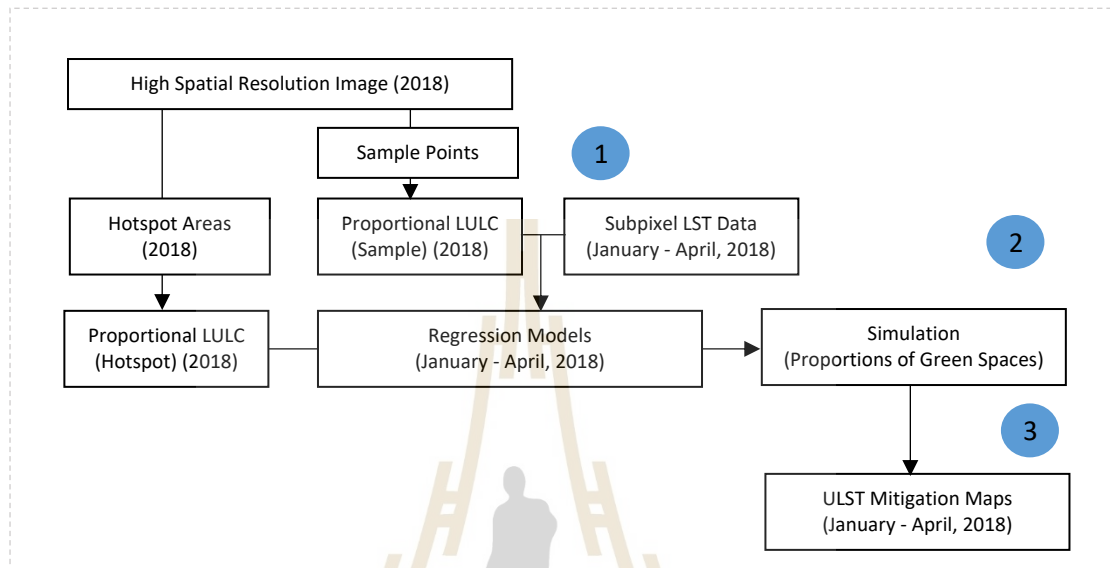
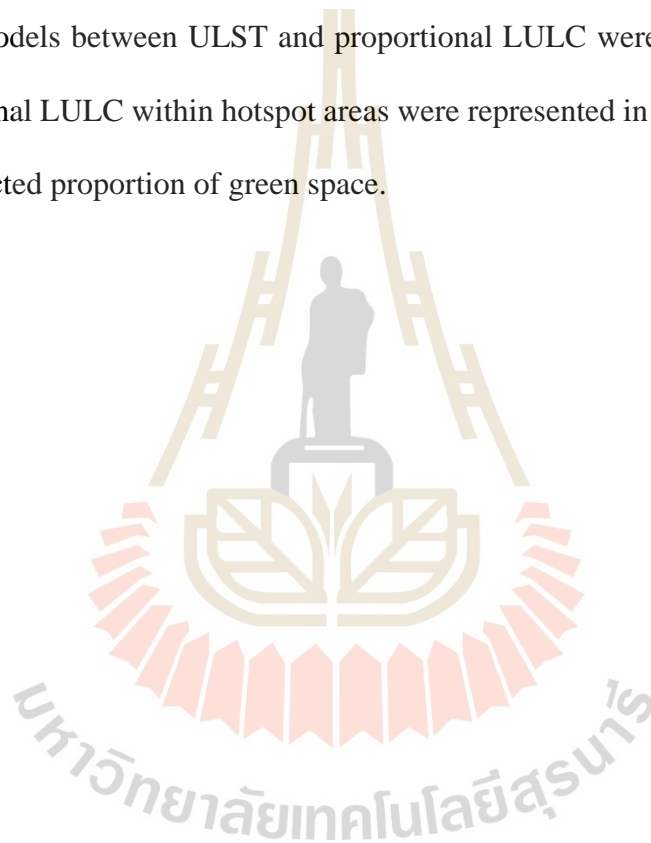


Figure 3.7 Conceptual processes of the fourth objective.

The subpixel LST data and the proportional LULC in sample points were used in regression modeling, as shown in Figure 3.7. The proportional LULC in hotspot areas were extracted using visual interpretation. Then, the percentages of LULC data in hotspot areas were represented in the regression model by using the different proportions of green space in order to generate the different scenarios of the hotspot mitigation. The purpose of the mitigation is to reduce the hotspot temperature nearly or equal to the temperature of the surrounding area. Afterward, the LST mitigation maps were generated based on the results of the mitigating simulation method.

Lastly, the feasibility of the simulated temperature was examined to explore the correctness of the results. The feasibility test processes were separated into two parts. Firstly, the same proportions of LULC were selected and used as the

reference data to compare with the simulation results. Secondly, the selected proportions of green space in hotspot mitigation were used with the data in 2014 and 2016, to explore the effects of these proportion of green space in hotspot mitigation. It should be noted that LANDSAT-8 images obtained between March and April in 2014 and 2016 were extracted the ULST data using the optimum method, and also estimated the subpixel LST data. The proportional LULC within the hotspot areas and the regression models between ULST and proportional LULC were also explored. Then, the proportional LULC within hotspot areas were represented in the regression models with the selected proportion of green space.



CHAPTER IV

RESULTS AND DISCUSSION

This chapter reports significant results obtained from the research, as described in the research procedures stated in Chapter III. Its content composes of four principal works; (1) optimum method for ULST estimation, (2) subpixel LST data estimation using the statistical-based method, (3) hotspots area identification based on the subpixel LST data, and (4) simulation of hotspot mitigation associated with proportions of green space in an urban area. Their details are as follows.

4.1 Optimum method for ULST estimation

The first objective results are separated into two parts, (1) the LST estimation results, and (2) the accuracy assessment. Their specific detail is as followed.

4.1.1 LST estimation results

The estimated LST data on January 21, February 6, March 26, and April 11 in 2018, is illustrated in Figure 4.1 - 4.4, respectively. Following with a high spatial resolution image map in Figure 4.5. Furthermore, the average, maximum, and minimum LST data are shown in Table 4.1.

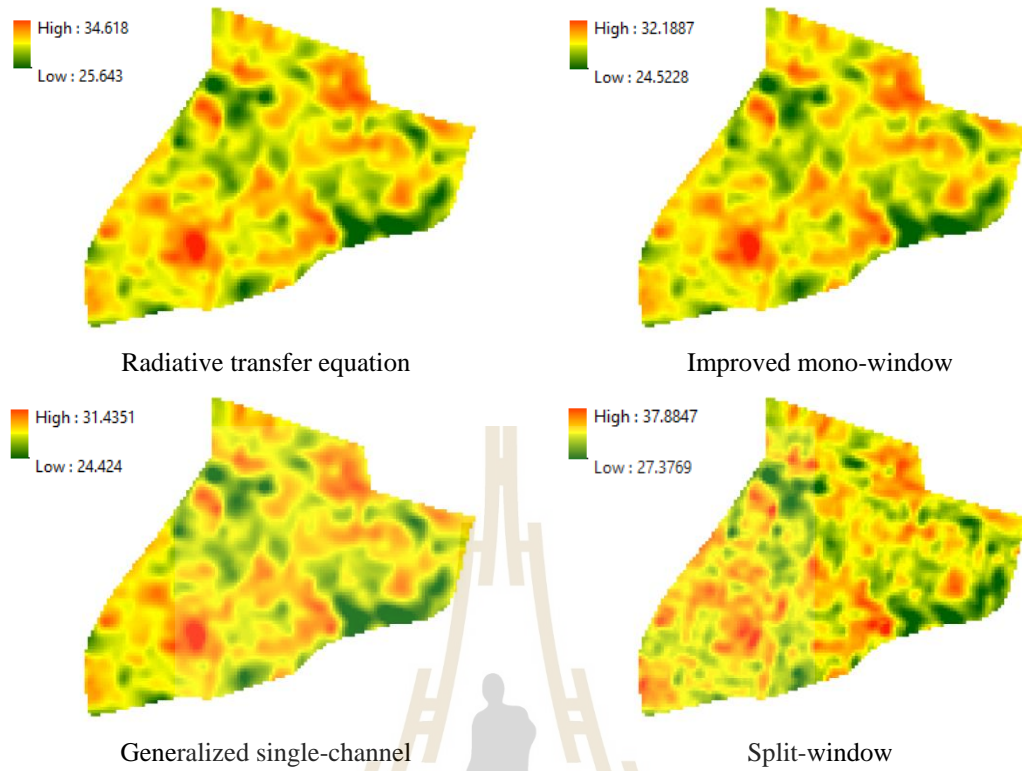


Figure 4.1 Estimated LST data on January 21, 2018.

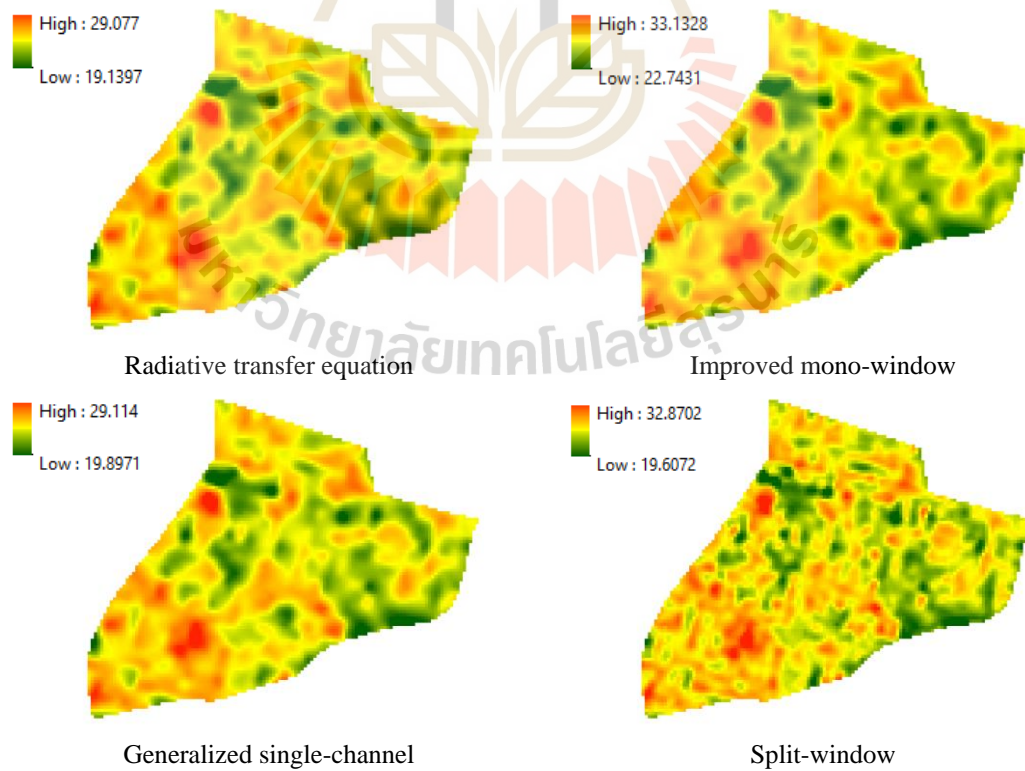


Figure 4.2 Estimated LST data on February 6, 2018.

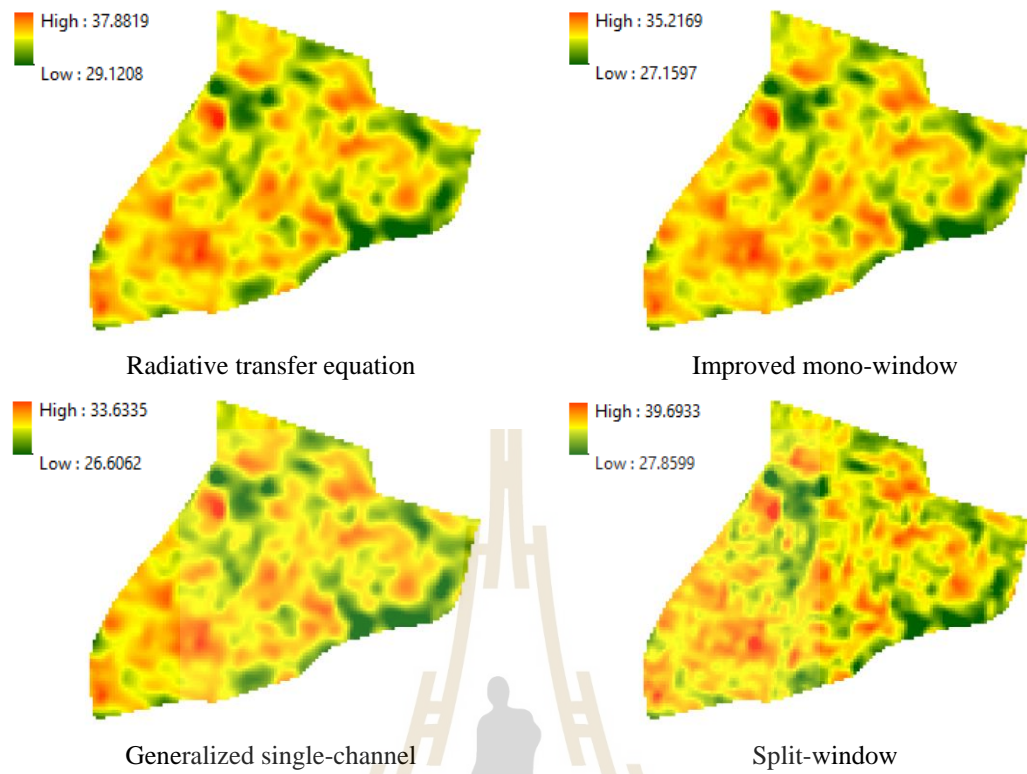


Figure 4.3 Estimated LST data on March 26, 2018.

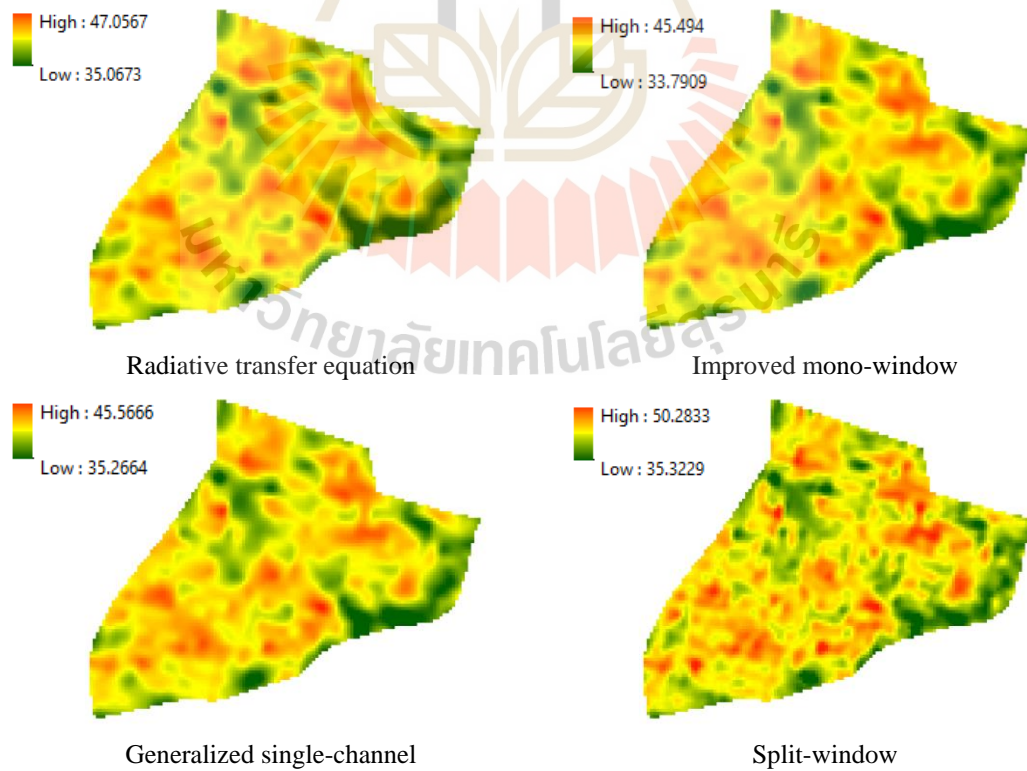


Figure 4.4 Estimated LST data on April 11, 2018.

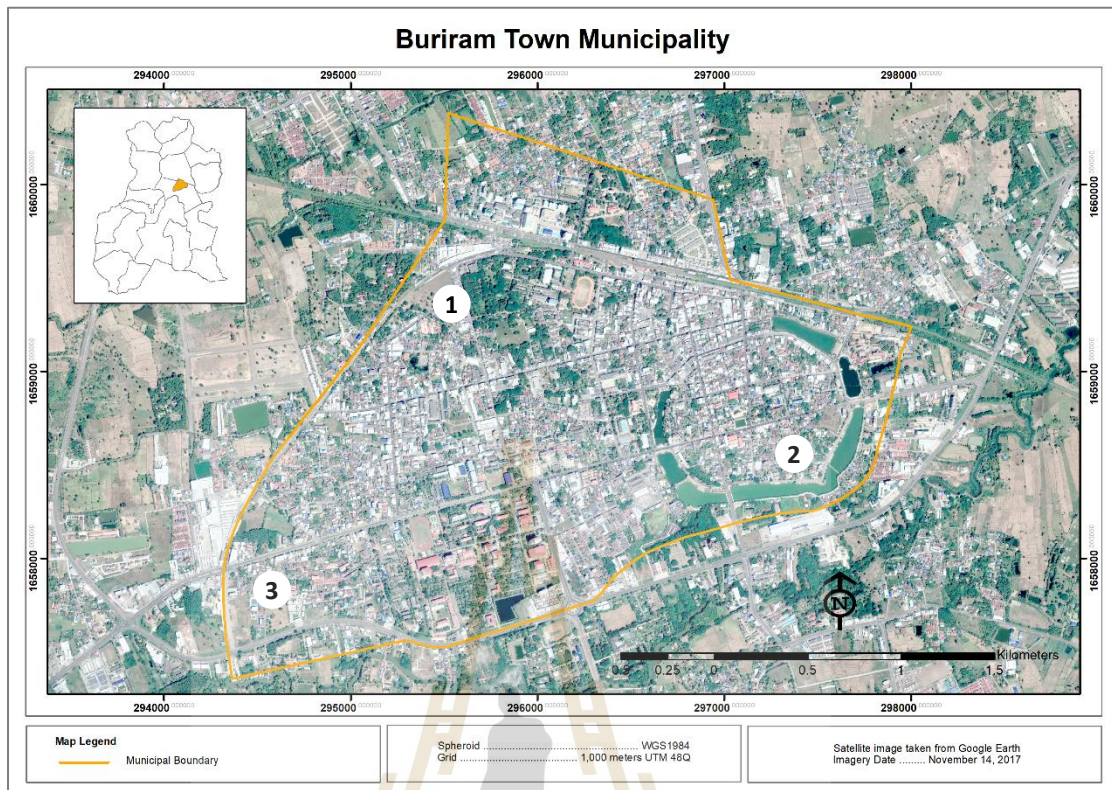


Figure 4.5 High spatial resolution image map.

All maps based on the SW method show a more complex surface than others, as shown in Figure 4.1-4.4. In contrast, all maps based on single-channel methods, namely, RTE, IMW, and GSC, are quite similar. The cold spots occur in the North-West and South-East area of the city, where are urban forest (as sample number 1) and wetlands (as sample number 2). In contrast, the areas with high temperature are occurred in the bare-land (as sample number 3) and built-up area, where is the most of the city, as shown in Figure 4.5.

Table 4.1 The average, maximum, and minimum LST data (°C).

		January 21	February 6	March 26	April 11
RTE	Average	30.821	25.258	34.087	42.330
	Minimum	25.643	19.140	29.121	35.067
	Maximum	34.618	29.077	37.882	47.057
IMW	Average	28.863	29.241	31.785	40.883
	Minimum	24.523	22.743	27.160	33.791
	Maximum	32.189	33.133	35.217	45.494
GSC	Average	28.444	25.573	30.590	41.494
	Minimum	24.424	19.897	26.606	35.266
	Maximum	31.435	29.114	33.633	45.567
SW	Average	33.863	27.637	34.602	43.465
	Minimum	27.377	19.607	27.860	35.323
	Maximum	37.885	32.870	39.693	50.283

Note: The data were obtained in 2018.

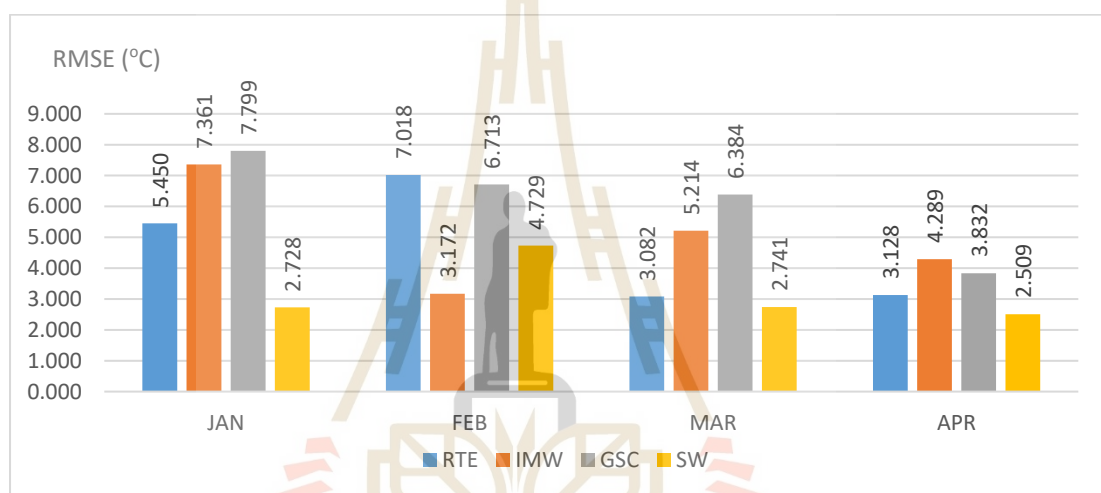
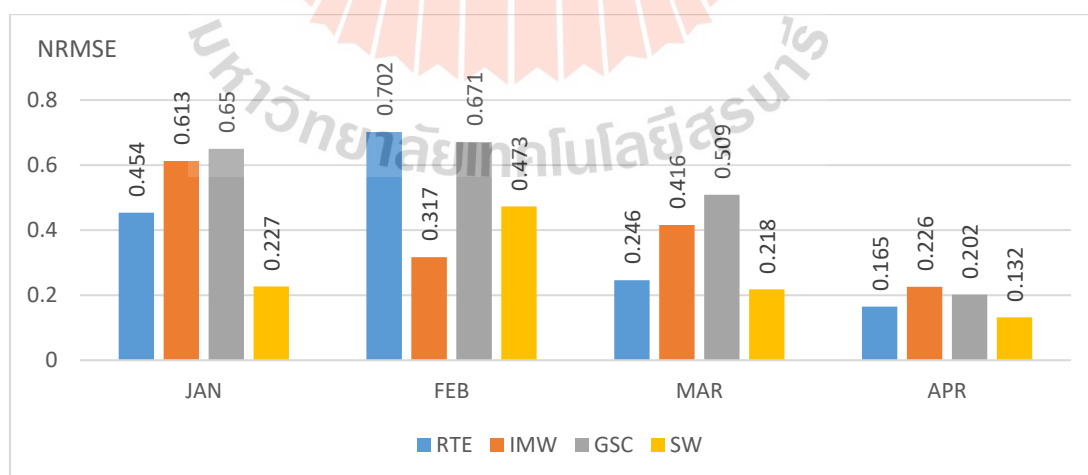
According to Table 4.1, all of LST estimation algorithms provide the highest average LST on April 11, 2018, as 42.330 °C, 40.883 °C, 41.494 °C, and 43.465 °C, based on RTE, IMW, GSC, and SW algorithm, respectively. In contrast, almost LST estimation algorithms, namely RTE, GSC, and SW algorithm, provide the lowest average LST on February 6, 2018. Focusing on the LST estimation algorithms, the SW algorithm provides the highest average LST on January 21, March 26, and April 11 in 2018 as 33.863 °C, 34.602 °C, and 43.465 °C, respectively. However, on February 6, 2018, the IMW algorithm provides the highest average temperature as 27.637 °C.

4.1.2 Accuracy assessment

The accuracy assessment is processed to explore the optimum method in ULST estimation by considering the LST estimation method provides the lowest NRMSE values. The RMSE and NRMSE values, as shown in Table 4.2 and Figure 4.6 - 4.7.

Table 4.2 RMSE and NRMSE Values.

Methods	RMSE /NRMSE	January 21, 2018	February 6, 2018	March 26, 2018	April 11, 2018
RTE	RMSE (°C)	5.450	7.018	3.082	3.128
	NRMSE	0.454	0.702	0.246	0.165
IMW	RMSE (°C)	7.361	3.172	5.214	4.289
	NRMSE	0.613	0.317	0.416	0.226
GSC	RMSE (°C)	7.799	6.713	6.384	3.832
	NRMSE	0.650	0.671	0.509	0.202
SW	RMSE (°C)	2.728	4.729	2.741	2.509
	NRMSE	0.227	0.473	0.218	0.132

**Figure 4.6** RMSE values based on monthly results.**Figure 4.7** NRMSE values based on monthly results.

Considering the RMSE values, the SW algorithm provided the lowest RMSE values on January 21, March 26, and April 11 in 2018, as shown in Table 4.2 and Figure 4.6, while, the IMW algorithm provided the lowest RMSE value on February 6, 2018. Basically, NRMSE values relate to RMSE values. The SW algorithm also provided the lowest NRMSE values on January 21, March 26, and April 11 in 2018, as shown in Table 4.2 and Figure 4.7. The IMW algorithm provided the lowest NRMSE value on February 6, 2018. Noticeably, all algorithms provided low error values on April 11, 2018. It can be concluded that the SW algorithm provides the lowest error in most cases, in which the amount of atmospheric water vapor content is more massive than 2.70 g cm^{-2} . On the other hand, the IMW algorithm provides a better result than the SW algorithm on February 6, 2018, with the lowest amount of atmospheric water vapor content (1.52 g cm^{-2}). The differentiated RMSE and NRMSE values between these two algorithms in these cases are quite low as around $1.557 \text{ }^\circ\text{C}$ and 0.156 , respectively.

Therefore, it can be concluded that the SW algorithm is an optimum method in ULST estimation for this study. The SW algorithm provides the lower error than others methods, due to this method does not require much information about the atmospheric profiles during satellite acquisition (Du, Ren, Qin, Meng and Zhao, 2015). The SW algorithm mainly eliminates atmospheric effects based on differential absorption in two thermal bands (Bhavanibhai, 2013). Furthermore, the two thermal infrared channels, used in the SW algorithm, have narrower bandwidths in the thermal infrared (Du et al., 2015; Li, Tang, et al., 2013). Additionally, Caselles, Rubio, Coll and Valor (1998) and Rozenstein, Qin, Derimian and Karnieli (2014) also indicated that

two separating narrow thermal bands had shown the smallest error in the retrieval of LST.

Although the SW algorithm does not require much information about the atmospheric profiles during satellite acquisition, this algorithm requires the retrieval of several coefficients (Du et al., 2015). For this reason, the LST retrieval method based on the SW algorithm is sensitive to water vapor content and coefficients. The coefficients used in this study are based on the study of Jimenez-Munoz, Sobrino, Skokovic, Matter and Cristobal (2014). According to a study by Vazquez, Reyes and Arboledas (1997), the coefficients depend on the atmospheric state; however, the fixed values are sometimes utilized, causing significant errors to the results. Therefore, the fixed values of the coefficient may provide error to the result.

As the single-channel methods, RTE, IMW, and GSC algorithm depend on the accuracy of the radiative transfer model and the atmospheric profiles such as transmissivity, atmospheric up-welling, and down-welling radiance, atmospheric water vapor content, and air temperature (Jimenez-Munoz et al., 2009). Therefore, it is noted that it is essential to obtain accurate atmospheric parameters for single-channel LST retrieval (Li et al., 2010). The accuracy of the single-channel method relies on the accuracy of the RTM and the atmospheric profiles representing the real state of the atmosphere over the studies area at the orbital time (Coll, Caselles, Valor and Niclos, 2012).

In this study, the errors based on the RTE algorithm may come from the atmospheric model used in the calculation of the atmospheric parameters. Since the study area located in the tropical zone, whereas the model provided by using the NCEP

model presents the mid-latitude summer and mid-latitude winter models. Furthermore, Jimenez-Munoz et al. (2009) indicated that these data are useful for a global scale.

The errors based on the IMW algorithm may come from the essential atmospheric parameters used in this algorithm. Firstly, there is no reference source in near-ground air temperature (T_0) acquisition, which is used in the sufficient atmospheric temperature (T_a), an important practical issue when one wishes to retrieve LST over a large area (Cristobal, Jimenez-Munoz, Sobrino, Ninyerola and Pons, 2009). Secondly, the relationships between transmittance and water vapor content depend on not well-defined “high” and “low” air temperature values, whereas the relationship between T_a and T_0 are given for absolute standard atmospheres (Jimenez-Munoz et al., 2009). As a study of Qin, Karnieli and Berliner (2001) indicated that high transmittance due to low water vapor in the atmospheric profile is the best condition for accurate LST retrieval. Commonly, the atmospheric water vapor is the most significant in governing the change of atmospheric transmittance in the thermal range of the spectrum. Therefore, the parameter of atmospheric transmittance required for LST retrieval is usually estimated through atmospheric water vapor content (Qin et al., 2001; Wang et al., 2015). As same as a result studied by Wang et al. (2015), it can be concluded that the LST retrieval method is sensitive to water vapor content estimated error.

The GSC algorithm provides a higher error than other methods. The basis of this algorithm relies on the estimation of the so-called atmospheric function, which is assumed to be dependent only on water vapor content values (Jimenez-Munoz et al., 2009). As noted by Cristobal and other in 2009 and Chen, Zhao, Ye and Hu in 2011 (Chen, Zhao, Ye and Hu, 2011); Cristobal et al. (2009), the atmospheric functions may be obtained more precisely from water vapor content and air temperature through more

complicated models. As the dependence on the water vapor content, the atmospheric component is the main absorber in the thermal infrared region. Basically, the up-welling and down-welling radiances depend on other parameters as mean atmospheric temperature, and surface pressure (Jimenez-Munoz and Sobrino, 2003). However, it was confirmed that in the case of T_a is not available, the LST retrieval using only water vapor content is the right choice when the atmospheric water vapor content is the low or intermediate temperature (Cristobal et al., 2009). Since input data were minimized to only one atmospheric parameter, an error in water vapor content estimation could increase the error in the LST retrievability of the single-channel algorithm. This exploration is confirmed with a study by Jimenez-Munoz and others (2015) (Jimenez-Munoz and Sobrino, 2003; Wang et al., 2015) that the possible errors in LST retrieval of the single-channel algorithm are also expected to be increased with the amount of atmospheric water vapor content.

It should be pointed out that the IMW, GSC, and SW algorithm is directly based on the water vapor content values (Jimenez-Munoz and Sobrino, 2003). Based on the results, it is showed that the accuracy of the estimated LST data depends on the amount of atmospheric water vapor content data, which is the main absorber in the thermal infrared region. This parameter was estimated by considering the near-surface air temperature and relative humidity values, which were taken from the local meteorological station; therefore, the error may occur when applied to any large area.

Apart from the atmospheric correction parameters, the surface emissivity is also required, as stated by Vlassova and others in 2014 (Vlassova et al., 2014). However, these methods assume that the surface is homogeneous, and radiances are directly correlated with emissivity values of materials and derived to LST. In fact, these

emissivity values are based on land cover classification data, which have not considered the multiple scattering and reflection caused by urban geometry (Yang, Wong, Menenti and Nichol, 2015). The study area, Buriram Town Municipality, appears as heterogeneous land use/land covers, causing different reflectance of the spectrum. It can be explained regarding the study by Feng and others in 2015 (Feng, (Feng, Foody, Aplin and Gosling, 2015) that relatively coarse spatial resolution may be strongly affected by mixed pixels, whereby each pixel comprises a mixture of two or more land cover types.

Lastly, the limitations of ground-based temperature data also provide the error to the results. The ground-based temperature surveying was done during 10.00 - 12.00 a.m., which closed to the time that the satellite obtains the data at 10.30 a.m. on the same date of LANDSAT-8. The additional test of the correlation between ground-based temperature data and the estimated LST data using the optimum method is mentioned in Appendix A.

Regarding the finding, the SW algorithm is an optimum method in USLT estimation for this study. The errors may occur due to the atmospheric parameter estimation, emissivity estimation, and also the limitations in ground-based temperature surveying. Another critical point is that the amount of atmospheric water vapor content data plays a vital role in terms of accuracy. It is noted that the atmospheric water vapor content data must be carefully considered regarding the use of the SW algorithm.

4.2 Subpixel LST data estimation using the statistical-based method

The second objective results are separated into three parts, including (1) the regression modeling, (2) the subpixel LST data, and (3) the accuracy assessment. The specific details are as followed.

4.2.1 Regression modeling

The obtained regression statistics used in subpixel LST estimation are shown in Table 4.3.

Table 4.3 Regression statistics used in subpixel LST estimation.

Years	Months	R	R ²	Adjusted R ²	Equations
2014	March 31	0.922	0.849	0.845	40.222 + 8.131 NDISI + 20.879 AB + 2.595 MNDWI
	April 16	0.937	0.879	0.876	33.883 + 8.968 NDISI + 18.787 AB
2016	March 20	0.945	0.893	0.888	55.542 + 8.128 NDISI - 10.041 AB + 12.165 MNDWI - 5.443 UI + 28.514 NDBaI
	April 5	0.941	0.886	0.881	46.256 + 7.551 NDISI + 4.600 BI + 5.097 MNDWI + 6.868 NDMI
2018	January 21	0.893	0.798	0.792	31.361 + 5.158 NDISI + 23.610 AB + 2.940 MNDWI
	February 6	0.978	0.956	0.954	26.811 + 5.421 NDISI + 19.986 AB - 2.067 MNDWI - 4.354 UI - 6.257 NDVI
	March 26	0.943	0.890	0.885	26.574 + 7.540 NDISI + 50.785 AB + 5.619 MNDWI - 1.324 UI
	April 11	0.927	0.859	0.854	38.446 + 10.657 NDISI + 30.655 AB + 5.068 MNDWI

Note: Data in 2014 and 2016 were used in the feasibility test of the simulated temperature.

The results of R-values, R² values, and adjusted R² values are in the same direction, as shown in Table 4.3. The highest R-value, R² value, and adjusted R² value are found on February 6, 2018, like 0.978, 0.956, and 0.954, respectively. In contrast, the lowest R-value, R² value, and adjusted R² value are found on January 21, 2018, like 0.893, 0.798, and 0.792, respectively.

Regarding the equations used in this study, NDISI is included in all models, while MNDWI and surface albedo are also found in all models, except April 16, 2014, and April 5, 2016, respectively. Although there are many spectral indices represented the impervious surface, NDISI is different from others because this index uses the thermal band in the calculation. The UI and NDBI are similar, but these indices use different short-wave infrared bands. Essa, Verbeiren, Kwast, Voorde and Batelaan (2012) reported that the extract full land information using NDBI is often mixed with noise caused by vegetation within the urban fabric. Furthermore, Xu (2008) indicated that IBI can significantly enhance the built-up land features versus non-built-up features within a mixed landscape and effectively suppress the background noise. However, Essa et al. (2012) reported that IBI was not able to differentiate LST within the urban pixels as in vegetated areas.

The MNDWI, which represents the wetlands, is also included in almost models. Focusing on the study area, it surrounds with circular canals in the South-Eastern part. As a supporting reason explored by Xu (2006), it was indicated that MNDWI is more suitable to enhance and extract water information for a water region with a background dominated by built-up areas. Regarding its advantage, it reduces and removes the noise of built-up land over the NDWI, as stated in a study of Essa and others in 2012 (Essa et al., 2012), due to the obtained information about moisture and vegetation.

Similar to MNDWI, surface albedo is also included in almost models. The relationships between the surface albedo and the LST have shown in a few studies. For instance, Small (2006) found a close relationship between surface temperature and surface albedo in urban areas. Furthermore, Zaksek and Ostir (2012) also indicated that

land surface albedo quantifiers the part of the energy that is absorbed and transformed into heat and latent fluxes; thus, it correlates with the LST.

Other spectral indices, represented the impervious surface areas (UI, BI, and NDBaI), are also selected in some models. The studies of Yuan and Bauer (2007), Essa et al. (2012), and Essa, Kwast, Verbeiren and Batelaan (2013) reported that the impervious surface constitutes the most significant portion accounted for the majority of the LST variations within the urban space. Their studies show a strong linear relationship among LST and impervious surfaces, regardless of the acquisition day. Most of the models have not considered vegetation indices; however, the NDVI included in the model only on February 6, 2018. Essa et al. (2012) reported that NDVI has a higher correlation with LST since the image was taken in a season with high vegetation cover. This study has surveyed during the summer period with low vegetation cover; therefore, other spectral indices may provide more influence. Furthermore, vegetation indices may have a high correlation with others.

It should be pointed out that other spectral indices are selected to provide the higher R^2 values than the models with only NDISI, MNDWI, and albedo. Corresponding with Yang, Cao, Pan, Li and Zhu (2017) reported that multiple relevant remote sensing indices could characterize LULC precisely, especially in non-vegetated areas. Yang et al. (2017) also indicated that for complex urban areas with varying land cover types, multiple scale factors must be integrated to achieve high downscaling precision.

It can be concluded that the implementation of a statistical-based method in subpixel LST data estimation must consider several issues. Firstly, the spectral indices, which are used as scaling factors, represent the impervious surface area, is

recommended in modeling. Secondly, the characteristics of the area and the study period also play an essential role in scaling factors selection. Thirdly, to avoid multicollinearity, stepwise multiple regression modeling should be applied. Also, the residual is added to the model. Due to other associated variables, which are not considered, also affect the accuracy of the model. Lastly, besides considering R^2 value, the error of the model, which is assessed as section 4.2.3, is considered. The supplement test of subpixel LST estimation using a regression model based on multiple date data in 2018 is mentioned in Appendix B.

4.2.2 The subpixel LST data

The LST data and subpixel LST data in 2014 and 2016 are illustrated in Figure 4.8. Followed with Figure 4.9 illustrates the LST data and the subpixel LST data in 2018. Furthermore, the average, maximum, and minimum temperatures in 2014, 2016, and 2018 are shown in Table 4.4.

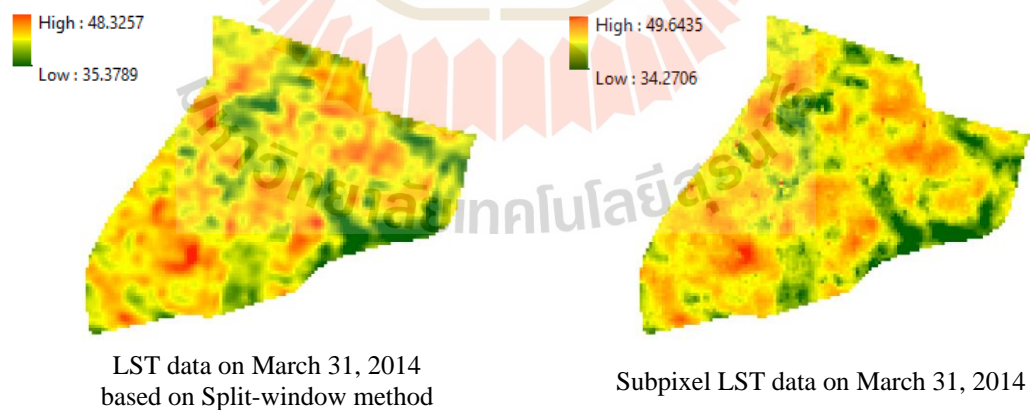


Figure 4.8 LST data and subpixel LST data in 2014 and 2016.

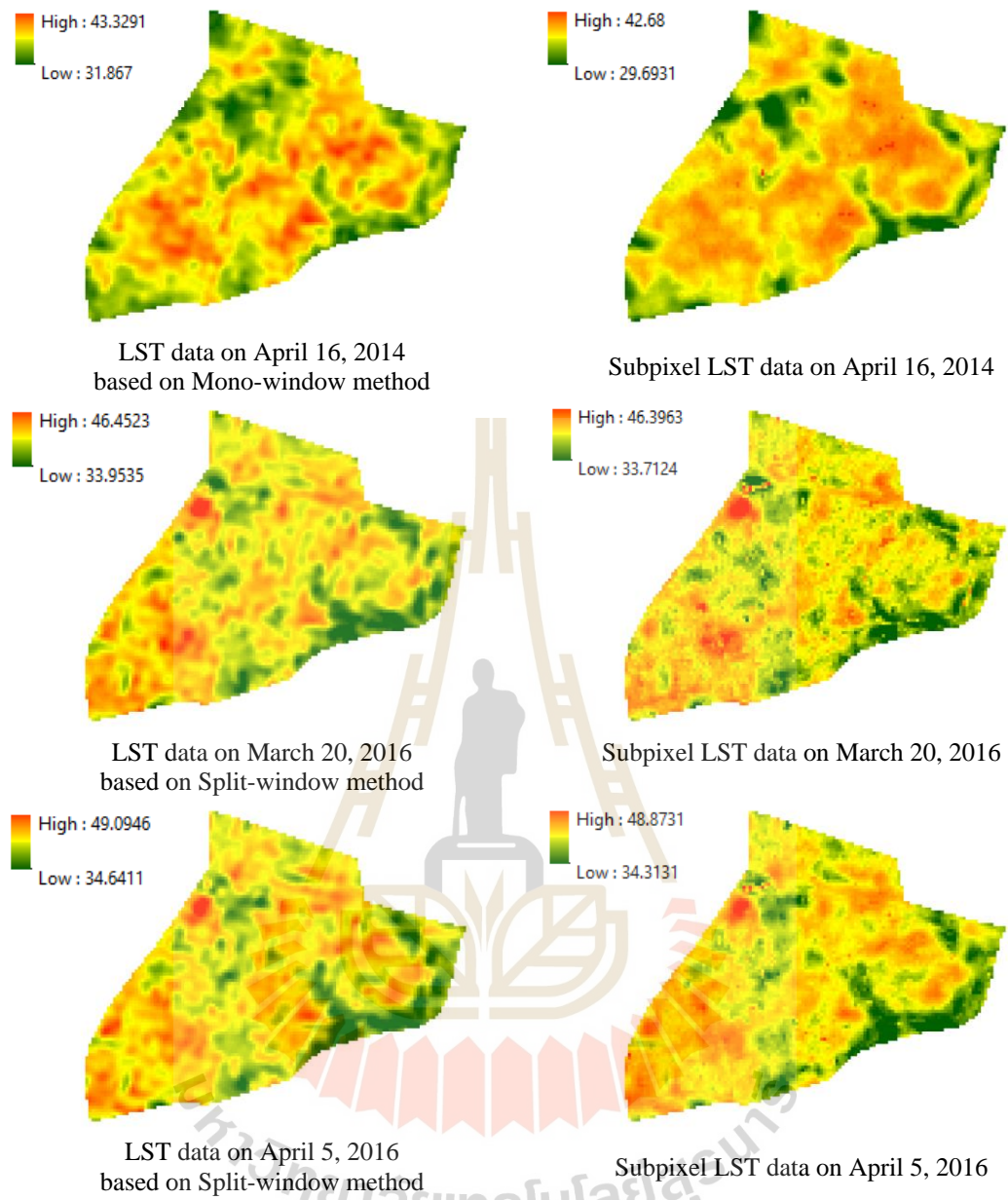


Figure 4.8 LST data and subpixel LST data in 2014 and 2016 (Continued).

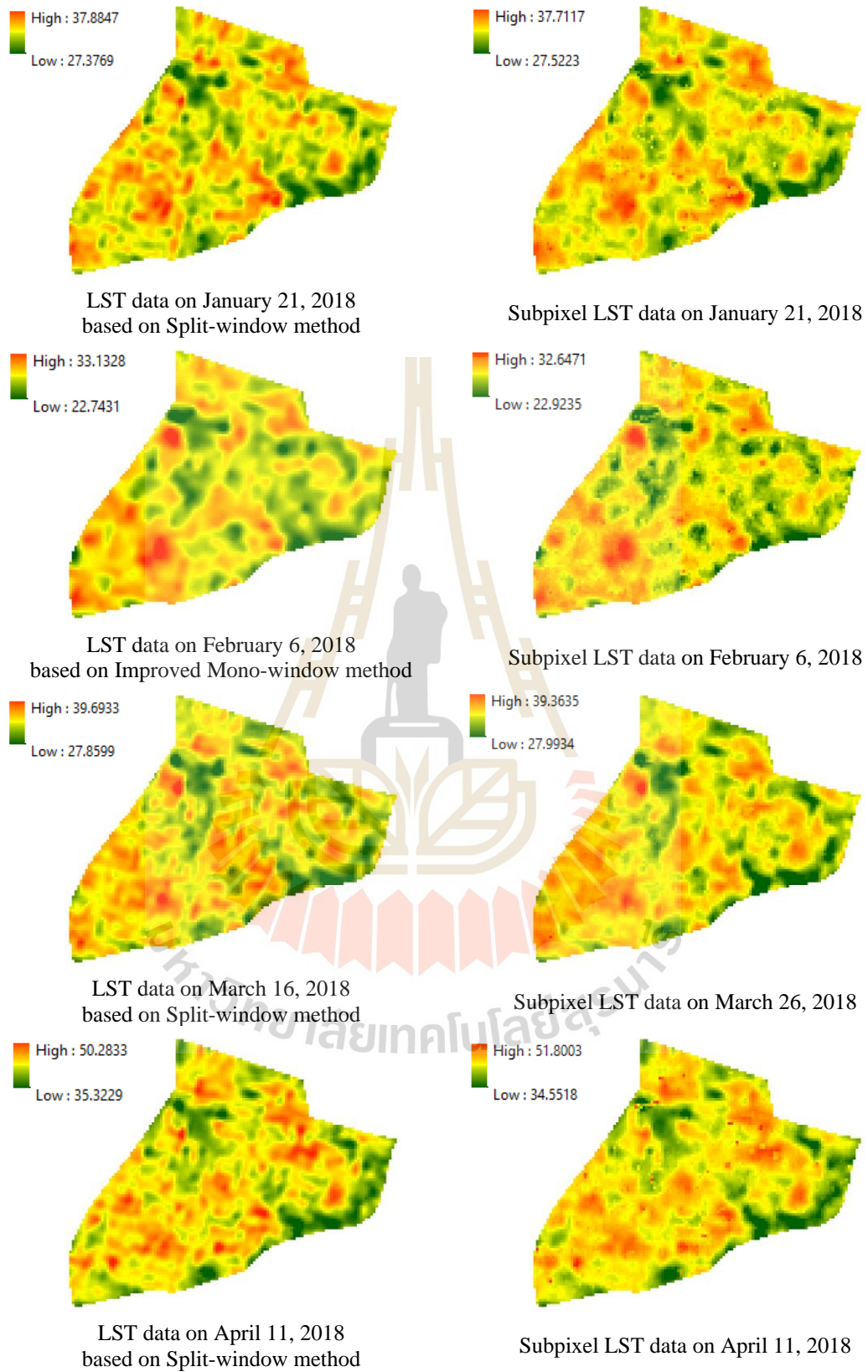


Figure 4.9 LST data and Subpixel LST data in 2018.

LST maps and subpixel LST maps show the same location of cold spots and hotspots as Figure 4.8 and Figure 4.9. However, the subpixel LST maps show a more complex surface than LST maps. Many high-temperature locations occur as spots. The sample ground-based temperature data, LST data based on the SW method, and subpixel LST data are shown in Figure 4.10.

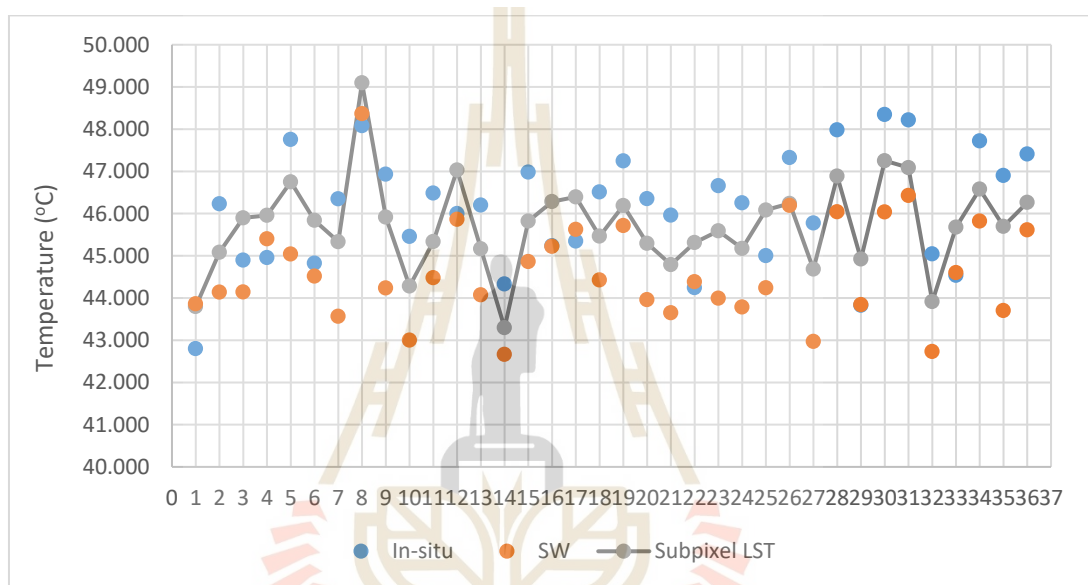


Figure 4.10 Compared samples between ground-based temperature, LST, and subpixel LST on April 11, 2018.

Most of the samples, which are randomly selected, show that subpixel LST data are closer to ground-based temperature data than LST data as Figure 4.10. Almost LST data based on the SW algorithm are quite low when compare with subpixel LST data and the ground-based temperature data. However, almost all of the subpixel LST data are still lower than ground-based temperature data.

Table 4.4 The average, maximum, and minimum temperature (°C).

Years	Months	Data	Average	Minimum	Maximum
2014	March 31	LST	42.534	35.378	48.326
		Subpixel LST	43.060	34.271	49.644
	April 16	LST	38.096	31.867	43.329
		Subpixel LST	38.680	29.693	42.680
2016	March 20	LST	40.282	33.953	46.452
		Subpixel LST	41.187	33.712	46.396
	April 5	LST	42.587	34.641	49.095
		Subpixel LST	43.071	34.313	48.873
2018	January 21	LST	33.863	27.377	37.885
		Subpixel LST	34.105	27.522	37.712
	February 6	LST	29.241	22.743	33.133
		Subpixel LST	29.273	22.924	32.647
	March 26	LST	34.602	27.860	39.693
		Subpixel LST	35.015	27.993	39.363
	April 11	LST	43.465	35.323	50.283
		Subpixel LST	44.465	34.552	51.800

Note: Data in 2014 and 2016 were used in the feasibility test of the simulated temperature.

All average temperatures based on subpixel LST data are higher than LST data, as shown in Table 4.4. The highest average LST data and subpixel LST data are found on April 11, 2018, as 43.465 °C and 44.465 °C, respectively. In contrast, the lowest average LST data and subpixel LST data are found on February 6, 2018, as 29.241 °C and 29.273 °C, respectively. Furthermore, based on minimum temperature, most of subpixel LST data are lower than LST data, except January 21, February 6, and March 26 in 2018. On the other hand, based on maximum temperature, most of subpixel LST data are lower than LST data, except March 31, 2014, and April 11, 2018.

4.2.3 The accuracy assessment

The RMSE and NRMSE values were calculated based on the subpixel LST data and ground-based temperature data on January 21, February 6, March 26, and April 11 in 2018. The results are shown in Table 4.5, and Figures 4.11 - 4.12. Furthermore, the independent sample t-test was applied, as shown in Table 4.6, in order to determine

whether there is a statistically significant difference between LST data and subpixel LST data.

Table 4.5 RMSE and NRMSE values.

Data	RMSE /NRMSE	LST	Subpixel LST	Differentiated RMSE /NRMSE
January 21, 2018	RMSE (°C)	2.728	2.413	0.315
	NRMSE	0.227	0.201	0.026
February 6, 2018	RMSE (°C)	3.172	2.658	0.514
	NRMSE	0.317	0.266	0.051
March 26, 2018	RMSE (°C)	2.741	2.354	0.387
	NRMSE	0.218	0.188	0.030
April 11, 2018	RMSE (°C)	2.509	2.091	0.418
	NRMSE	0.132	0.110	0.022

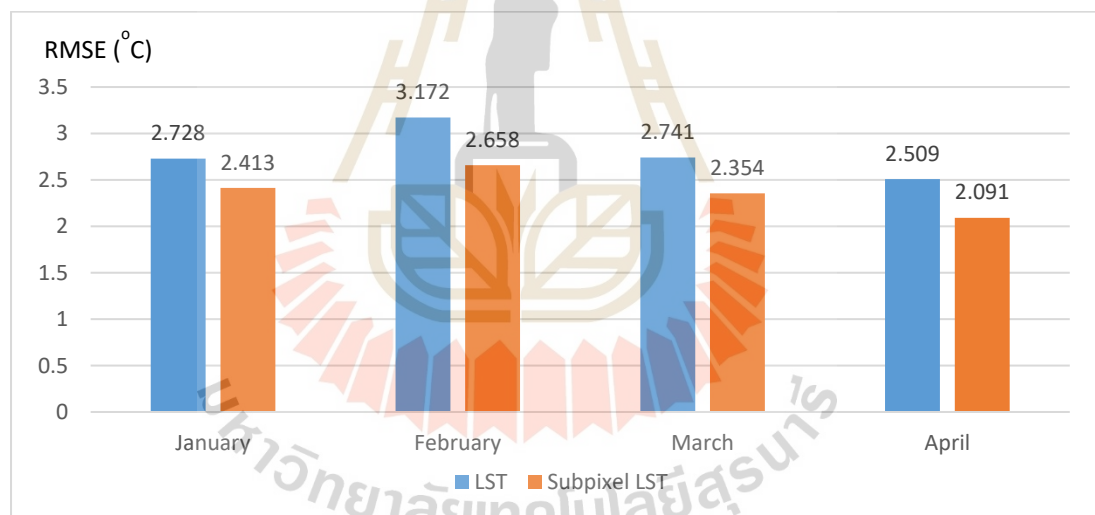


Figure 4.11 RMSE values based on LST and subpixel LST data.

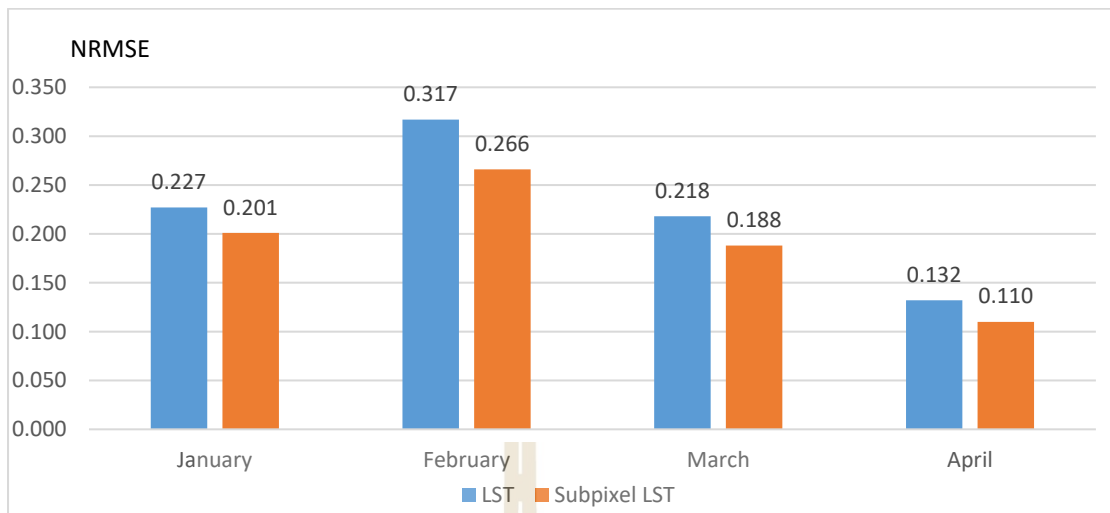


Figure 4.12 NRMSE values based on LST and subpixel LST data.

The RMSE and NRMSE values of LST data are higher than subpixel LST data in all months, as shown in Table 4.5 and Figures 4.11-4.12. The differentiated RMSE values are higher than 0.300 °C, while the differentiated NRMSE values are higher than 0.022. The lowest RMSE and NRMSE values are found on April 11, 2018. In contrast, the highest RMSE and NRMSE values are found on February 6, 2018. Similar to LST data estimation, the amount of atmospheric water vapor content plays an important role in terms of accuracy.

The error sources based on subpixel LST data may come from the LST estimation algorithm, the atmospheric parameters calculation, and land surface emissivity estimation. Corresponding to Zhou et al. (2016) indicated that the error of the original LST is subject to sources such as the parameterization of atmospheric influences and the estimation of land surface emissivity. These parameters play an essential role in LST calculation and also resulted in a subpixel LST calculation process. These error sources present the errors to the results, although the relationship

between LST data and spectral indices was high, and the regression models can provide accurate results.

The basic idea of most LST disaggregation methods is to find an assumed scale-independent relationship between LST and some predictor variables from the low-resolution image (Zhu, Guan, Millington and Zhang, 2013). If the relationships between LST and predictors have not changed associated with spatial resolution, then a detailed high-resolution LST can be estimated by predictors using such relationships (Yang et al., 2017). The scale effect depends on the ratio of the native resolution to the target resolution. Note that the scale effect is defined as the error in the downscaled LST at the target resolution, whereby the error is induced by the LST-descriptors relationship at the native resolution (Zhou et al., 2016). Ghosh and Joshi (2014) reported that a ratio that exceeds four could cause a significant scale effect. The scale effect is intrinsically caused by the different probability distribution of the LST and its descriptors at the native and target resolutions. It depends on the values of the descriptors, the phenology, and the ratio of the native resolution to the target resolution. However, removing the scale effect can only slightly improve the accuracy of the downscaled LST (Zhou et al., 2016).

Another critical point is the coarser resolution of the TIR band is not calculated based on the original data. TIR bands are acquired at the 100-meters resolution but are resampled to 30 meters in delivered data products (United States Geological Survey, 2018). In the subpixel LST data estimation process, TIR bands were upscaled to 90 meters closed to the original resolution; however, the data had already changed. On the other hand, the visible, near-infrared, and short-wave bands used in spectral indices also upscaled to 90 meters. The upscale spectral indices based on these

bands are not the real values at this resolution, but the values were also calculated based on the conventional method in the upscaled process. Zhu et al. (2013) suggested that the quoted precisions of the LST disaggregation may be over over-estimated due to the low spatial resolution data being rebuilt and simulated from fine spatial resolution data.

Table 4.6 The independent sample t-test results.

Data	Levene's Test for Equality of Variances		t-test for Equality of Means		
	F	Sig	t	df	Sig (2-tailed)
January 21, 2018	1.299	0.254	-8.403	1798	0.000
February 6, 2018	3.628	0.057	-12.209	1798	0.000
March 26, 2018	3.538	0.060	-7.731	1798	0.000
April 11, 2018	3.688	0.055	-10.842	1798	0.000

Note: 1. Significance level at 0.05

2. t-statistic, df, and sig (2-tailed) are based on equal variance assumed.

Firstly, the variance of LST data and subpixel LST data are tested based on Levene's test. The null hypothesis of variance test states that the variances of LST data and subpixel LST data are equal. Based on Table 4.6, all p-value of Levene's test is more significant than 0.05; therefore, the variance in LST data and subpixel LST data are not significantly different. Then, based on equal variances assumed, the null hypothesis of the t-test states that the LST data and subpixel LST data are not significantly different. Based on Table 4.6, all p-value of the t-test for equality of means is less than 0.05; therefore, the LST data and subpixel LST data are significantly different at a significant level of 0.05.

Regarding the finding, the LST data and subpixel LST data are significantly different at a significant level of 0.05. The errors of subpixel LST data are lower than the LST data. The differentiated RMSE values are higher than 0.300 °C in all months. However, the errors of subpixel LST data may come from the scale effect and spatial resolution of data, which are used in spectral indices and the LST estimation process. Also, errors based on the LST estimation process, despite algorithm, the atmospheric parameters calculation, and also LSE estimation, can provide the error to the results.

4.3 Hotspot areas identification based on subpixel LST data

The third objective results were separated into three parts, (1) Moran's I results, (2) hotspot areas identification based on Getis-Ord G_i^* results, and (3) characteristics of the selected hotspot areas. Their specific details are described as followed.

4.3.1 Moran's I results

Firstly, the data pattern was identified using Moran's I method, and the results are shown in Table 4.7.

Table 4.7 Moran's I result on data in 2014, 2016, and 2018.

Years	Months	Z-score	Moran's index	Pattern
2014	March 31	55.956	0.928	Cluster
	April 16	57.509	0.954	Cluster
2016	March 20	50.007	0.829	Cluster
	April 5	55.280	0.917	Cluster
2018	January 21	55.184	0.915	Cluster
	February 6	55.185	0.915	Cluster
	March 26	55.903	0.927	Cluster
	April 5	55.197	0.915	Cluster

Note: Data in 2014 and 2016 were used in the feasibility of simulated temperature tests.

The null hypothesis of Moran's I statistic states that the data is randomly distributed. Based on Table 4.7, all Z-scores values are more significant than 50.000; therefore, all data are not randomly distributed. To identify the pattern of the data, if Moran's index value near +1.0 indicates clustering, while an index value near -1.0 indicates dispersion (ESRI, 2016; Prasannakumar, Vijith, Charutha and Geetha, 2011). According to the results, all months show Moran's index values more significant than 0.900, which close to +1.0. Therefore, it can be concluded that all data patterns are clustered. As a result, these data identify the hotspot areas that occur during this period using Getis-Ord G_i^* .

4.3.2 Hotspot area identification based on Getis-Ord G_i^* results

The hotspot areas that occurred from January to April in 2018 are illustrated in Figure 4.13. Followed with Figures 4.14 - 4.17, the hotspots on January 21, February 6, March 26, and April 11 in 2018 are illustrated respectively. The data in 2014 and 2016 were used in feasibility test of simulated temperature; therefore, the hotspot areas that occurred in 2018 were used in hotspot mitigation.

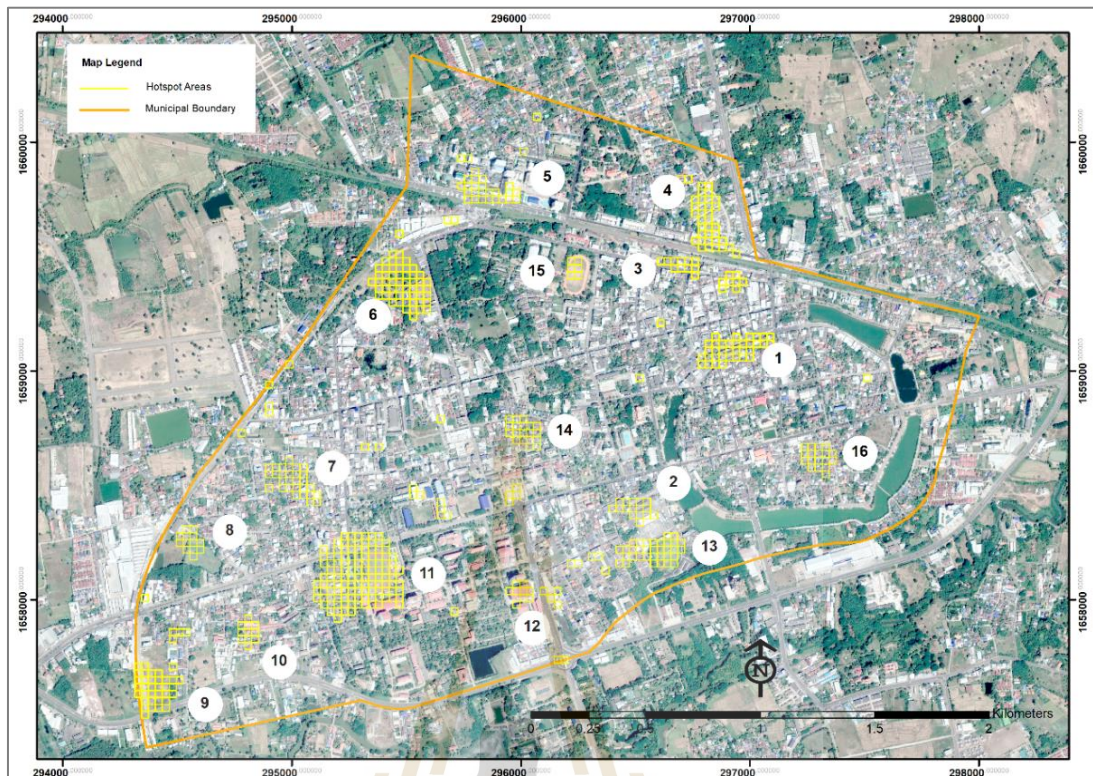


Figure 4.13 Hotspot areas in 2018.

Based on Figure 4.13, hotspot areas occur in bare-lands (Number 6, 8, 9, and 13) and race tracks (numbers 11 and 15). These areas are quite similar because some parts of these areas are covered with dry grass. Only some part of the location number 13 is actually bare-land used as the parking lot. Furthermore, most of the hotspot areas occur in built-up areas. In this case, the hotspot areas occurred in residential areas (number 4, 7, 10, 14, 16, and some parts of 13), commercial areas (number 1, 2, and 3), some part of the educational institution as parking lots in Buriram Rajabhat University (number 12), and government institutions as hospital (number 5).

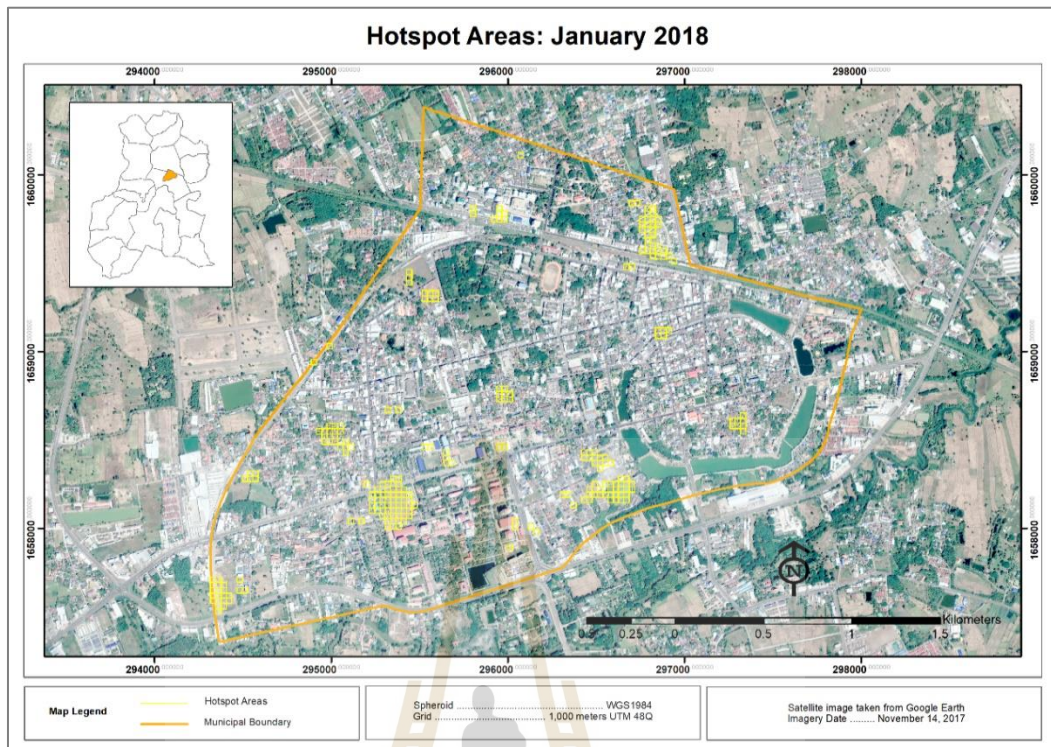


Figure 4.14 Hotspot areas on January 21, 2018.

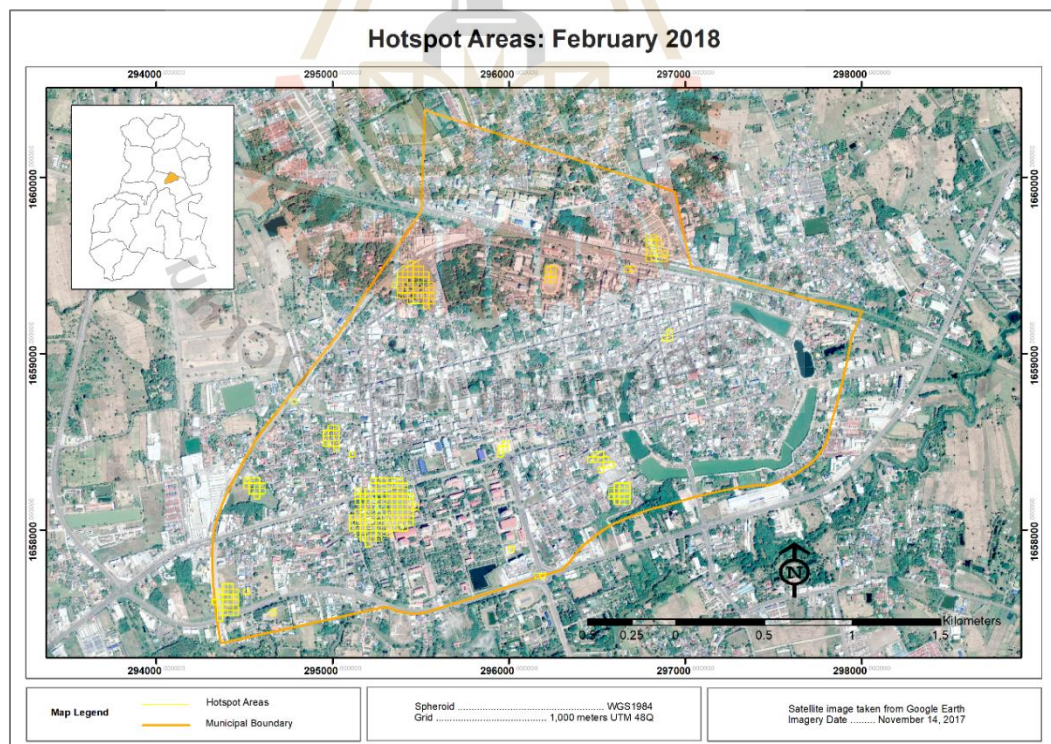


Figure 4.15 Hotspot areas on February 6, 2018.

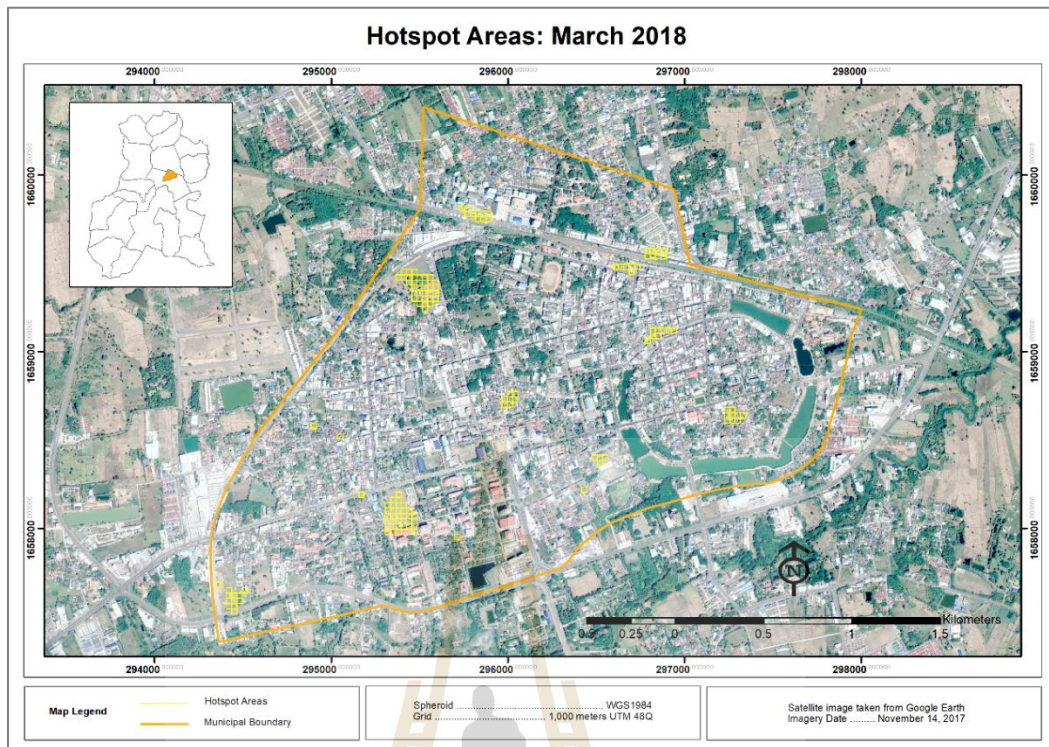


Figure 4.16 Hotspot areas on March 26, 2018.

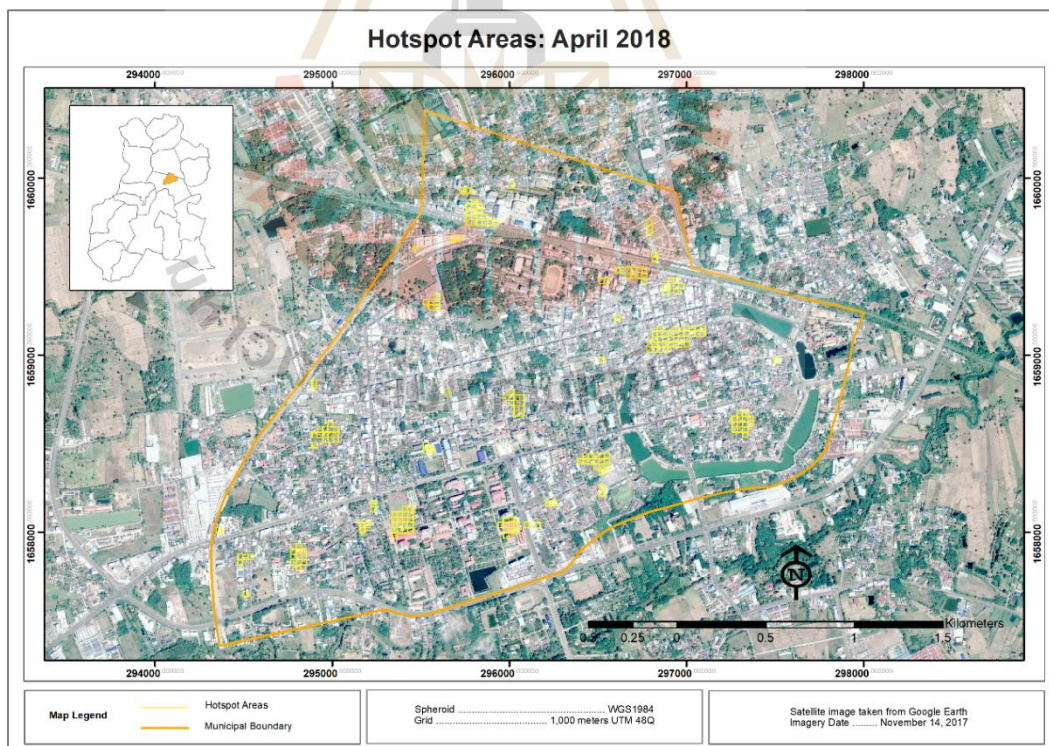


Figure 4.17 Hotspot areas on April 11, 2018.

Most of the hotspot areas occur at the same location, as shown in Figures 4.14-4.17. Nevertheless, the boundaries of the hotspot areas are different, depending on the weather conditions. For example, on February 6, 2018, with the lowest temperature, almost hotspot areas occur at the bare-lands. Due to the bare-lands temperature are higher than other LULC, and the differentiated LST between bare-lands and other LULC is large. Another sample is the hotspot occurs in April. Focusing on the hotspot number 13 (as mentioned in Figure 4.13), this hotspots location appears on January 21 and February 6 in 2018, but this hotspot disappeared in April 11, 2018, due to rainfall before the satellite obtained the data, as shown in Figure 4.18.

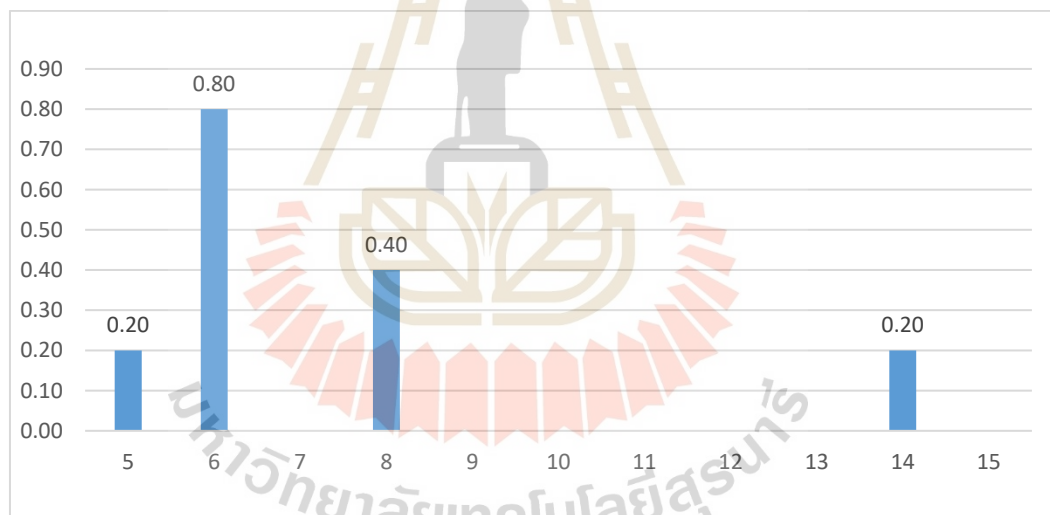


Figure 4.18 The daily cumulative rainfall.

According to Figure 4.18, the cumulative rainfall data were obtained from the Hydro and Agro Informatics Institute (HAI) website. There was rainfall on April 5, 6, and 8, while the satellite obtained the data on April 11, 2018.

Regarding the finding, the hotspot areas occurred in bare-lands, race tracks, and built-up areas. Corresponding with Adeyeri, Akinsanola and Ishola (2017) who indicated that significant hotspots of high LST were recorded in built-up areas and bare surfaces. Also, Xu, Qin and Wan (2010) indicated that temperature statistics of main land cover types showed that built-up and bare land had higher surface temperatures than natural land covers. Generally, areas with high temperatures are primarily located in the center of the city (Ga, NiMa, Jun and CiRen, 2011). Also, high average temperatures always occur in commercial area (Cai, Du and Xue, 2011; Dobrovolny, 2013; Li et al., 2011; Rinner and Hussain, 2011; Van and Bao, 2008, 2010; Xu, Dan, Dan and Lu, 2009), and also in the areas with having a high density of buildings, residents (Cai et al., 2011), roads, and transportations (Cai et al., 2011; Xu et al., 2009). In contrast, low average temperature occurs in parks and recreational land, water bodies (Rinner and Hussain, 2011), and also around the regions with large areas of grassland, trees, and water bodies (Cai et al., 2011).

4.3.3 Characteristics of the selected hotspot areas

The selected hotspot locations are illustrated in Figure 4.19 - 4.21. Furthermore, the average, minimum, and maximum temperatures in hotspot areas and surrounding areas are shown in Table 4.8, followed by Table 4.9. It shows the differentiated temperature between maximum temperature in hotspot areas and surrounding areas. The supplementary data of the selected hotspot locations are mentioned in Appendix C.



Figure 4.19 The selected hotspot area: the first location.



Figure 4.20 The selected hotspot area: the second location.



Figure 4.21 The selected hotspot area: the third location.

The first hotspot location (Figure 4.19) covers some parts of the market and some commercial zone in the municipality. The proportion of main LULC types in this area are construction and road as 0.76 and 0.24, respectively.

The second hotspot location (Figure 4.20) covers some part of the market, where are Buriram Night Bazaar, and some residential areas. The proportion of main LULC types in this hotspot location is construction, road, and green space as 0.71, 0.26, and 0.03, respectively.

The third hotspot location (Figure 4.21) covers some part of the commercial areas, where is located near the train station. In the past, some area of this hotspot location was the market. The proportion of main LULC types in this area are construction, road, and green space as 0.70, 0.29, and 0.01, respectively.

Typically, the hotspot pixels are surrounded with adjacent pixels, which has a radius around 30 meters of one pixel. The LULC in 2014, 2016, and 2018 are not absolutely changed; therefore, the LULC types and the proportional LULC in 2014 - 2018 in these hotspot locations are the same. Lastly, the hotspot boundaries in 2018 are used as the hotspot boundaries in 2014 and 2016 to explore the feasibility of the simulated temperature.

Table 4.8 The average, maximum, and minimum temperature in the hotspot and surrounding areas (°C).

		2014		2016		2018			
		March 31	April 16	March 20	April 5	January 21	February 6	March 26	April 11
Hotspot 1	Min.	44.27	41.02	41.10	44.21	34.35	28.70	35.35	47.80
	Max.	46.12	42.68	43.57	46.19	36.29	31.26	37.36	49.12
	Mean	45.46	41.44	42.14	45.22	35.34	29.77	36.57	48.33
Surround	Min.	43.91	40.56	40.47	43.34	33.49	27.95	34.93	46.06
Hotspot 1	Max.	45.69	41.55	42.81	45.94	35.79	30.17	37.00	47.59
	Mean	45.06	41.19	41.87	44.83	34.79	29.34	36.00	47.09
	Min.	44.15	40.98	42.25	44.84	35.44	30.15	36.65	47.41
Hotspot 2	Max.	46.09	42.51	43.94	46.31	37.24	32.16	37.31	49.06
	Mean	45.47	41.46	43.14	45.67	36.22	31.04	36.95	48.35
	Min.	42.81	40.43	42.25	43.44	34.61	29.85	35.90	45.86
Surround	Max.	45.39	41.33	43.05	45.73	35.87	30.77	37.08	47.43
Hotspot 2	Mean	44.66	40.99	42.68	44.79	35.34	30.38	36.49	46.75
	Min.	44.90	40.81	41.72	44.92	35.25	29.68	35.91	47.64
	Max.	45.90	42.34	43.78	46.13	36.29	32.00	37.46	48.42
Hotspot 3	Mean	45.56	41.29	42.57	45.40	35.58	30.61	37.03	47.91
	Min.	44.45	40.49	41.12	44.70	34.44	28.63	35.04	46.35
	Max.	45.58	41.13	43.15	45.80	35.77	30.89	37.10	47.52
Surround	Mean	45.17	40.85	42.43	45.29	35.23	30.18	36.52	47.03

Note: Data in 2014 and 2016 were used in feasibility test of the simulated temperature.

Table 4.9 The differentiated temperature (°C).

	2014		2016		2018			
	March 31	April 16	March 20	April 5	January 21	February 6	March 26	April 11
Hotspot 1	46.12	42.68	43.57	46.19	36.29	31.26	37.36	49.12
Surrounding areas	45.69	41.55	42.81	45.94	35.79	30.17	37.00	47.59
Differentiate	0.43	1.13	0.76	0.25	0.50	1.09	0.36	1.53
Hotspot 2	46.09	42.51	43.94	46.31	37.24	32.16	37.31	49.06
Surrounding areas	45.39	41.33	43.05	45.73	35.87	30.77	37.08	47.43
Differentiate	0.70	1.18	0.89	0.58	1.37	1.39	0.23	1.63
Hotspot 3	45.90	42.34	43.78	46.13	36.29	32.00	37.46	48.42
Surrounding areas	45.58	41.13	43.15	45.80	35.77	30.89	37.10	47.52
Differentiate	0.32	1.21	0.63	0.33	0.52	1.11	0.36	0.90

Note: Data in 2014 and 2016 were used in feasibility test of the simulated temperature.

According to the scope and limitations of the study (stated in Chapter 1, Section 3.4), the purpose of the mitigation is to reduce the hotspot temperature nearly or equal to the temperature of the surrounding area. To explore at least the decreased temperature, the differentiated temperature between the maximum temperature in hotspot areas surrounding areas, as shown in Table 4.8, was calculated. The differentiated temperature, as at least the decreased temperature, is shown in Table 4.9.

In the first hotspot location, at least the decreased temperature on January 21, February 6, March 26, and April 11 in 2018 are around 0.50 °C, 1.09 °C, 0.36 °C, and 1.53 °C, respectively. While at least the decreased temperature in the second hotspot location is around 1.37 °C, 1.39 °C, 0.23 °C, and 1.63 °C, respectively. Lastly, at least the decreased temperature in the third hotspot location is around 0.52 °C, 1.11 °C, 0.36 °C, and 0.90 °C, respectively.

The proportions of green space, which can reduce the hotspot temperature around 0.50 - 2.00 °C, is considered and reported. Due to at least the decreased temperature is around 0.23 - 1.63 °C. Furthermore, the minimum proportion of green

space should mitigate almost data from January 21, February 6, March 26, and April 11 in 2018.

Regarding the finding, the largest portions of LULC in hotspot locations is impervious surface, including constructions and roads. While the green space is very low when compared with other LULC types. This causation leads to SUHI occurrence in this location. Due to the reduction in latent heat flux and an increase in sensible heat in urban areas as vegetated and evaporating soil surfaces are replaced by relatively impervious low albedo (solar reflectivity) paving and building materials (Imhoff, Zhang, Wolfe and Bounoua, 2010). Also, the modification of the land surface in the urban area to build surfaces enhance the energy storage and the heat release (Carnielo and Zinzi, 2013).

This result corresponding to the UHI phenomenon occurs in a small town, as same as the exploration of Blazejczyk and others (Blazejczyk, Bakowska and Wieclaw, 2006), also, the concept of UHI in terms of the difference between the central part of the city and its surrounding areas (Ngie, Abutaleb, Ahmed, Darwish and Ahmed, 2014). As a result, shown in Figure 4.13, the hotspot locations occur on January 21, February 6, March 26, and April in 2018. These hotspot areas occurred in bare-lands, race tracks, and built-up areas. In the case of built-up areas, the hotspot areas occurred in residential areas, commercial areas, education institutions, and government institutions. As confirmed with a study by Adeyeri et al. (2017), they indicated that the hotspot in the city could also occurred in bare-lands. Furthermore, the results were corresponding with Dobrovolny (2013), Li et al. (2011), Rinner and Hussain (2011), (Cai et al., 2011) and Xu et al. (2009) who indicated that the hotspot in the city occurred

in the commercial area because there is a high density of buildings, residents, and transportations.

4.4 Simulation of hotspot mitigation from proportions of green space in the urban area

The results of this section are separated into three parts, (1) the regression modeling, (2) the proportion of green space used in hotspot mitigation, and (3) the feasibility test of the simulated temperature. Their specific details are as followed.

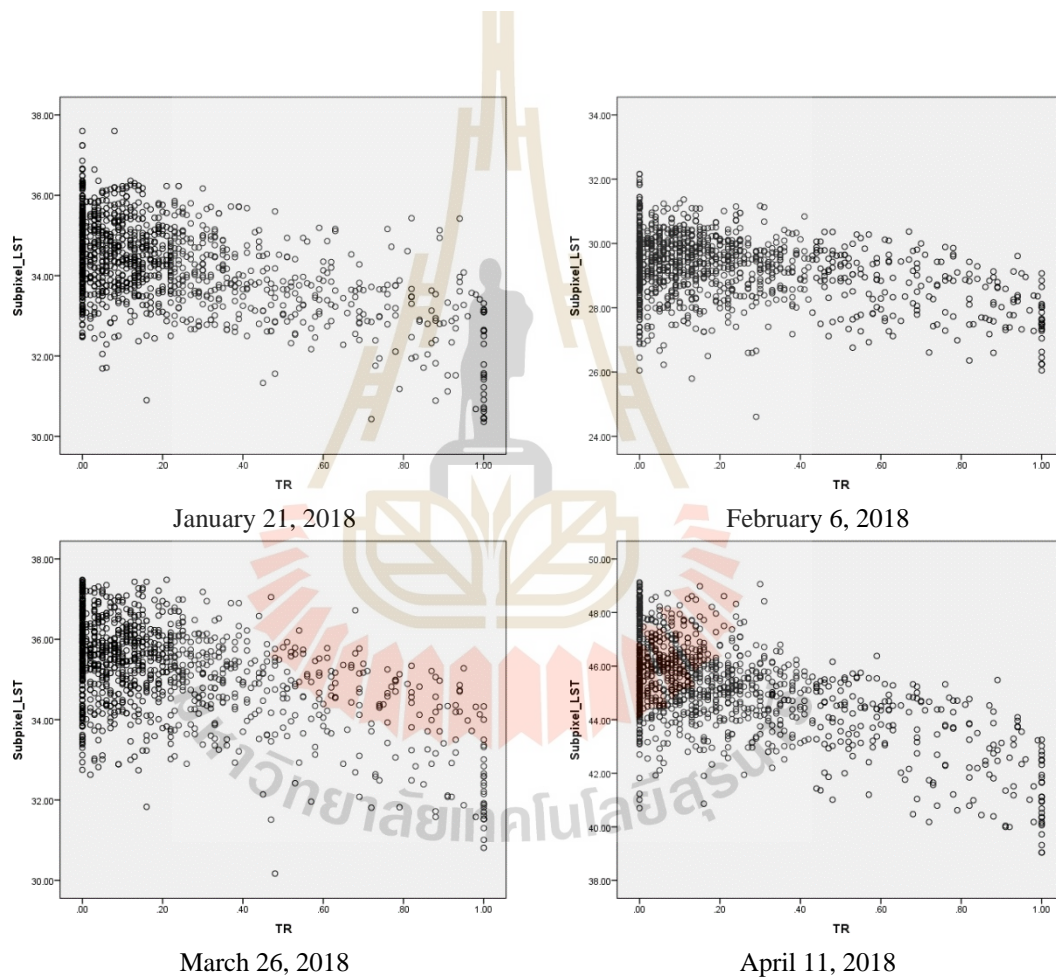
4.4.1 Regression modeling

The proportional LULC, which comprises of green space, construction, and road, were selected regarding the significant types of LULC found in hotspot areas. Firstly, Pearson correlation, which is suitable for interval and ratio variables (SPSS Tutorials, 2019), was applied to explore the relationship between these proportions of LULC and subpixel LST data. Table 4.10 shows Pearson correlation statistics between these LULC types and subpixel LST data.

Table 4.10 The Pearson correlation statistics.

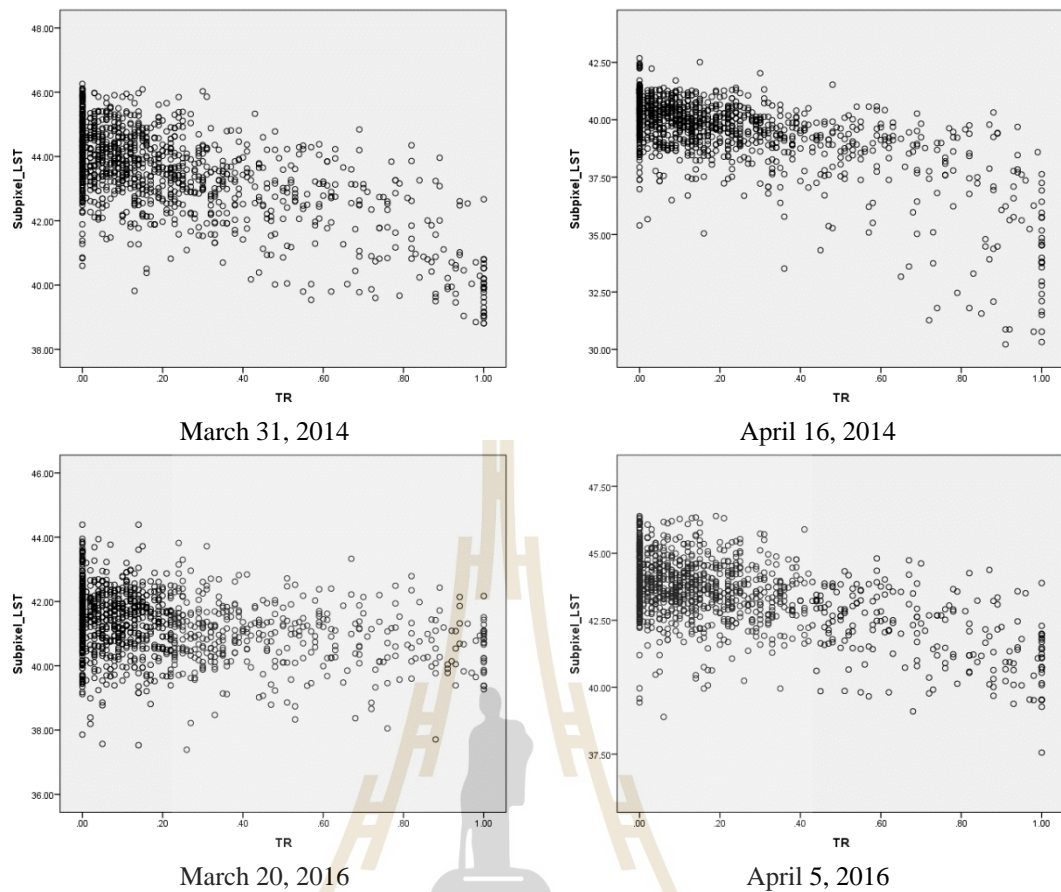
Subpixel LST	Green Space	Construction	Road
March 31, 2014	- 0.662	0.484	0.207
April 16, 2014	- 0.682	0.528	0.176
March 20, 2016	- 0.281	0.138	0.171
April 5, 2016	- 0.567	0.388	0.210
January 21, 2018	- 0.542	0.396	0.169
February 6, 2018	- 0.370	0.227	0.169
March 26, 2018	- 0.545	0.359	0.219
April 11, 2018	- 0.620	0.477	0.163

The proportion of green space provides a higher correlation with subpixel LST data than the proportion of construction and road, as shown in Table 4.10. Therefore, regression modeling was focused on the proportion of green space and subpixel LST data. Then, the scatter plots were used to explore the relationship between the proportion of green space and subpixel LST data, as shown in Figure 4.22 and Figure 4.23.



Note: [TR] was represented the proportion of green space.

Figure 4.22 The scatter plots based on the proportion of green space and subpixel LST data in 2018.



Note: [TR] was represented the proportion of green space.

Figure 4.23 The scatter plots based on the proportion of green space and subpixel LST data in March and April 2014 and 2016.

Based on Figures 4.22 - 4.23, the relationship between the proportion of green space and subpixel LST data is assumed to be linear. Accordingly, the test of normality was applied. The example result of the normality test was shown in Figure 4.24.

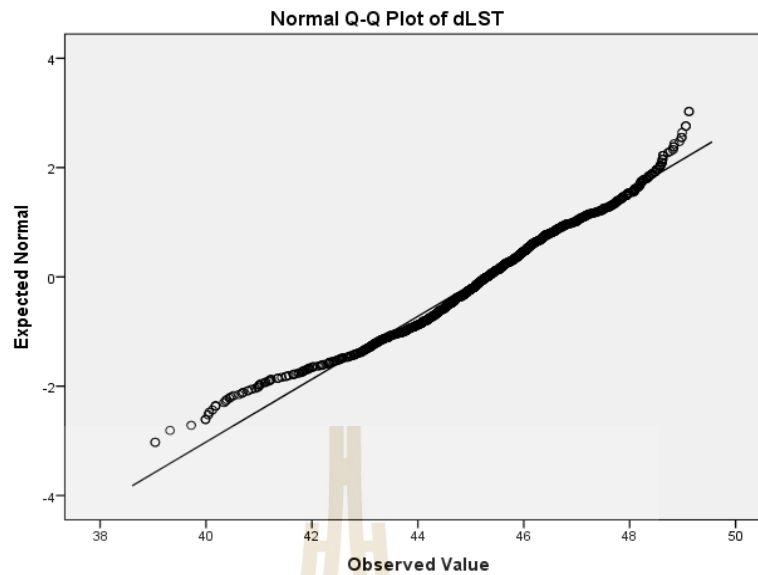


Figure 4.24 The test of normality based on subpixel LST data in April 2018.

The normal QQ plot provides a visual comparison of the dataset to a standard normal distribution. Points on the normal QQ plot indicate the univariate normality of the dataset. If the data is normally distributed, the points fall on the linear referencing line. If the data is not normally distributed, the points deviate from the linear referencing line (ESRI, 2019). It is found that most of the data are normally distributed, as shown in Figure 4.24; therefore, all data are used. Seventy percent of the data were randomly selected and used in regression modeling. On the other hand, the rest 30 percent of the data was used in the accuracy assessment by considering RMSE values. The results of the regression statistics are in Table 4.11.

Table 4.11 The regression statistics.

Data	R	R ²	Adjust R ²	Equation	RMSE (°C)
March 31, 2014	0.691	0.478	0.477	44.347 - 3.683 [TR]	1.085
April 16, 2014	0.706	0.498	0.497	40.501 - 4.631 [TR]	1.274
March 20, 2016	0.319	0.102	0.101	41.538 - 1.212 [TR]	0.998
April 5, 2016	0.594	0.353	0.353	44.152 - 3.007 [TR]	1.113
January 21, 2018	0.582	0.338	0.338	34.833 - 2.428 [TR]	0.965
February 6, 2018	0.408	0.167	0.166	29.594 - 1.551 [TR]	0.906
March 26, 2018	0.577	0.333	0.332	35.851 - 2.623 [TR]	0.998
April 11, 2018	0.648	0.420	0.419	46.195 - 4.310 [TR]	1.404

Note: [TR] represents the proportion of green space.

The highest R, R², and adjusted R² values are on April 16, 2014. In contrast, the lowest R, R², and adjusted R² values are on March 20, 2016, as shown in Table 4.11. The RMSE values are around 1.00 °C; therefore, the obtained regression models provided high errors. Since other variables also play an important role in temperature estimation, such as location, the albedo of the used materials in construction, weather conditions (wind speed, moisture), mixed pixels, urban design (Sattari, Hashim and Pour, 2018). This study focuses on the relationship between the proportion of LULC and subpixel LST data; therefore, other variables, as mentioned above, are not considered. To improve the accuracy of the equations, therefore, the residuals are included in the equations. The regression models used in subpixel LST data estimation are shown in Table 4.12.

Table 4.12 The regression models.

Data	Equation
March 31, 2014	44.347 - 3.683 [TR] + e
April 16, 2014	40.501 - 4.631 [TR] + e
March 20, 2016	41.538 - 1.212 [TR] + e
April 5, 2016	44.152 - 3.007 [TR] + e
January 21, 2018	34.833 - 2.428 [TR] + e
February 6, 2018	29.594 - 1.551 [TR] + e
March 26, 2018	35.851 - 2.623 [TR] + e
April 11, 2018	46.195 - 4.310 [TR] + e

Note: [TR] and e represent the proportion of green space, and residuals, respectively.

Based on Table 4.12, [TR] represents the proportion of green space, and e is the residuals. In the simulation process, the residuals are calculated from the differentiated temperature between the estimated LST data, which are based on the regression model and subpixel LST data. Furthermore, it should be noted that the residuals are calculated pixel by pixel.

Regarding the finding, although the LULC and the proportional LULC in the area is the same, the temperature is different. The difference in temperature comes from other parameters, which play an essential role to temperature, despite the vegetation density (Cao, Onishi, Chen and Imura, 2010; Feyisa, Dons and Meiby, 2014), tree species (Feyisa et al., 2014), location (Lin, Yu, Chang, Wu and Zhang, 2015). In this study, the variable used in regression modeling depends on the proportion of green space only; therefore, the residual should be added to the models to improve accuracy.

4.4.2 The proportion of green space used in hotspot mitigation

In order to explore the minimum proportion of green space applied in hotspot temperature decreasing, the maximum decreased temperature is considered. The results of the proportion of green space as 0.15, 0.30, 0.45, and 0.60 of the area used in accordance with three hotspot locations are in Tables 4.13 - 4.15. Furthermore, Figure 4.25 to Figure 4.28 illustrate the simulated maps based on the first hotspot location. Followed with Figure 4.29 to Figure 4.32 illustrate the simulated maps based on the second hotspot location. Lastly, Figure 4.33 to Figure 4.36 illustrate the simulated maps based on the third hotspot location. The supplementary data in this section are mentioned in Appendix C.

Table 4.13 Decreased temperature based on the simulated proportion of green space at the first hotspot location.

Proportion of green space		January 21, 2018		February 6, 2018		March 26, 2018		April 11, 2018	
		Decrease Temperature	ΔT						
0.15	Min	33.98	0.36	28.47	0.23	34.96	0.39	47.16	0.65
	Max	35.93	0.36	31.02	0.23	36.97	0.39	48.48	0.65
	Mean	34.98	0.36	29.54	0.23	36.18	0.39	47.68	0.65
0.30	Min	33.62	0.73	28.23	0.47	34.56	0.79	46.51	1.29
	Max	35.57	0.73	30.79	0.47	36.57	0.79	47.83	1.29
	Mean	34.62	0.73	29.30	0.47	35.78	0.79	47.04	1.29
0.45	Min	33.25	1.09	28.00	0.70	34.17	1.18	45.86	1.94
	Max	35.20	1.09	30.56	0.70	36.18	1.18	47.18	1.94
	Mean	34.25	1.09	29.07	0.70	35.39	1.18	46.39	1.94
0.60	Min	32.89	1.46	27.77	0.93	33.78	1.57	45.22	2.59
	Max	34.84	1.46	30.33	0.93	35.79	1.57	46.54	2.59
	Mean	33.89	1.46	28.84	0.93	35.00	1.57	45.74	2.59

Note: ΔT is the differentiated temperature between the actual temperature and decreased temperature.

To decrease the hotspot temperature nearly or equal to surrounding areas, at least the decreased temperature on January 21, February 6, March 26, and April 11, 2018, are around 0.50 °C, 1.09 °C, 0.36 °C, and 1.53 °C, respectively. Based on Table 4.13, the proportion of green space around 0.15 of the area can only decrease the hotspot temperature on March 26, 2018. To decrease the hotspot temperature on January 21 and March 26 in 2018, the proportion of green space around 0.30 of the area is needed. Furthermore, with this proportion of green space, the decreased temperature on April 11, 2018, is closed to at least the decreased temperature. However, to decrease the hotspot temperature more than at least the decreased temperature on January 21, March 26, and April 11, 2018, the proportion of green space around 0.45 of the area is needed. Although the proportion of green space is increased to 0.60 of the area, the decreased temperature on February 6, 2018, is still lower than at least the decreased temperature with the differentiated temperature around 0.16 °C. Therefore, the proportion of green space around 0.45 of the area is the minimum proportion of green space to mitigate the first hotspot location.

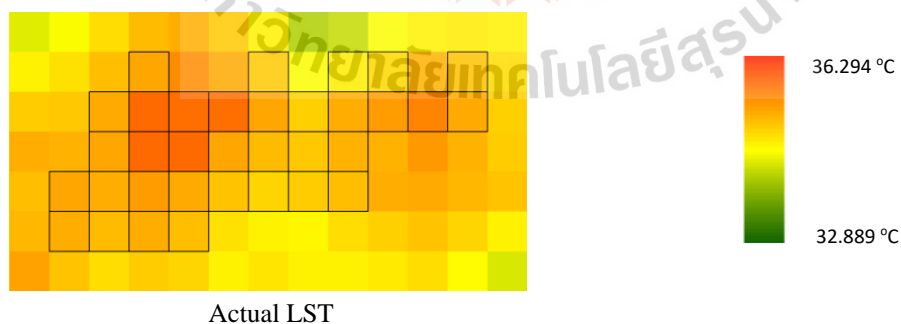


Figure 4.25 The first hotspot location mitigation based on January 21, 2018.

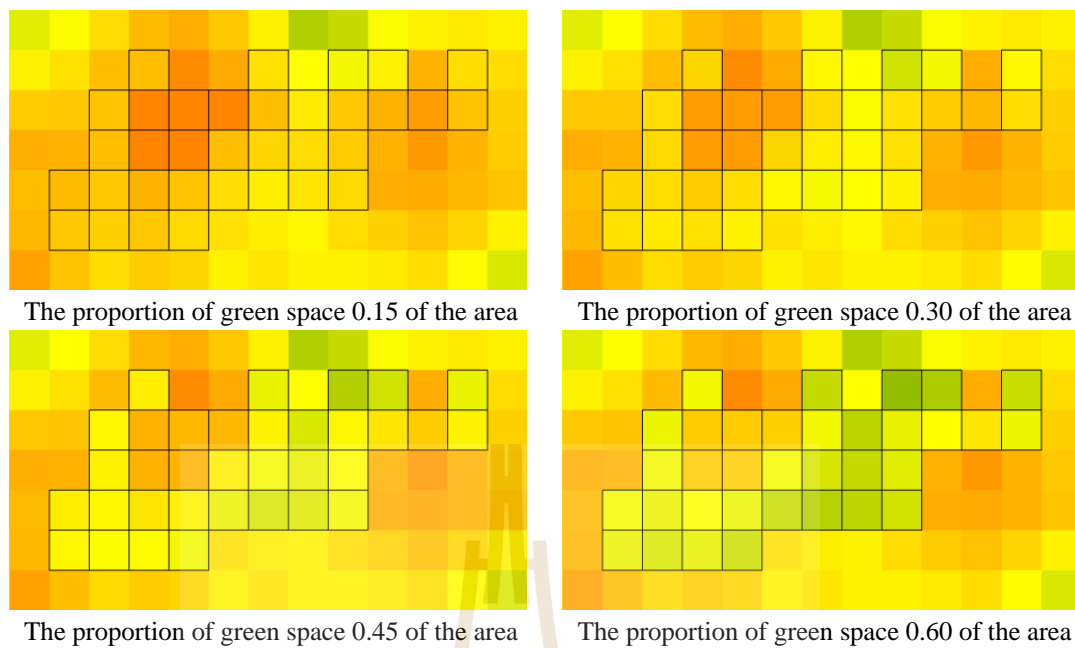


Figure 4.25 The first hotspot location mitigation based on January 21, 2018 (Continued).

According to the explored result, it must be confirmed by simulating the proportions of green space into each image corresponding with the generated LST. On January 21, 2018, the hotspot temperature was closed to the temperature of the surrounding area when the proportion of green space is increased to 0.15 of the area, as shown in Figure 4.25. The differentiated temperature between decreased temperature and the minimum decreased temperature is around 0.14 °C. The hotspot temperature is decreased by more than the minimum decreased temperature when the proportion of green space is increased to 0.30 in the area. Furthermore, the hotspot temperature is decreased over 1.00 °C when the proportion of green space is increased by more than 0.45 of the area.

It should be noted that the hotspot boundaries were generated based on the hotspot areas in all months. Therefore, the decreased temperature in some areas, which are the actual hotspot in this month, is lower than the surrounding areas and illustrated as green color in this map.

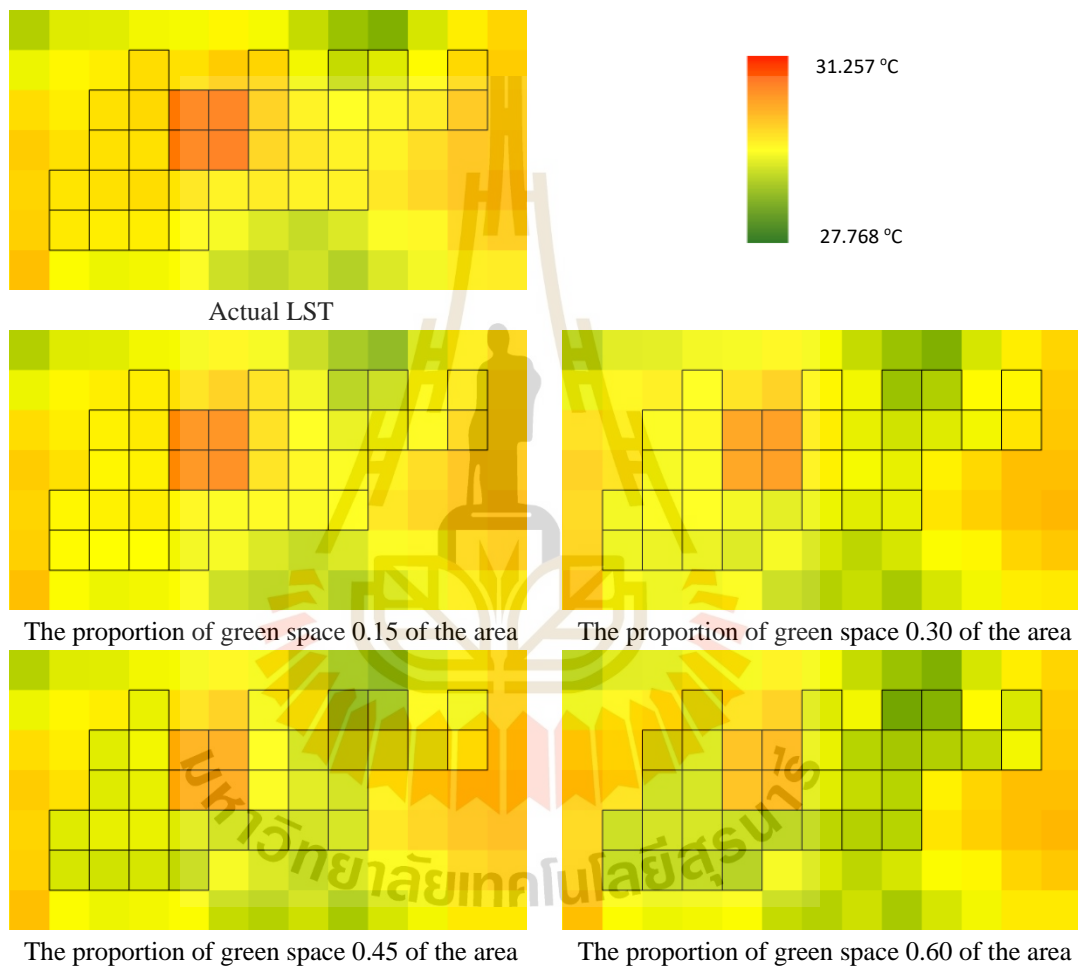


Figure 4.26 The first hotspot location mitigation based on February 6, 2018.

On February 6, 2018, the differentiated temperature between the decreased temperature and surrounding area temperature was more than 0.50 °C when the proportion of green space was increased to 0.45 of the area, as shown in Figure 4.26. Although the proportion of green space was increased to 0.60 in the area, the decreased

temperature was still less than the minimum decreased temperature. The differentiated temperature between the decreased temperature and surrounding area temperature was around 0.39 °C and 0.16 °C when the proportion of green space was increased to 0.45 and 0.60 of the area, respectively.

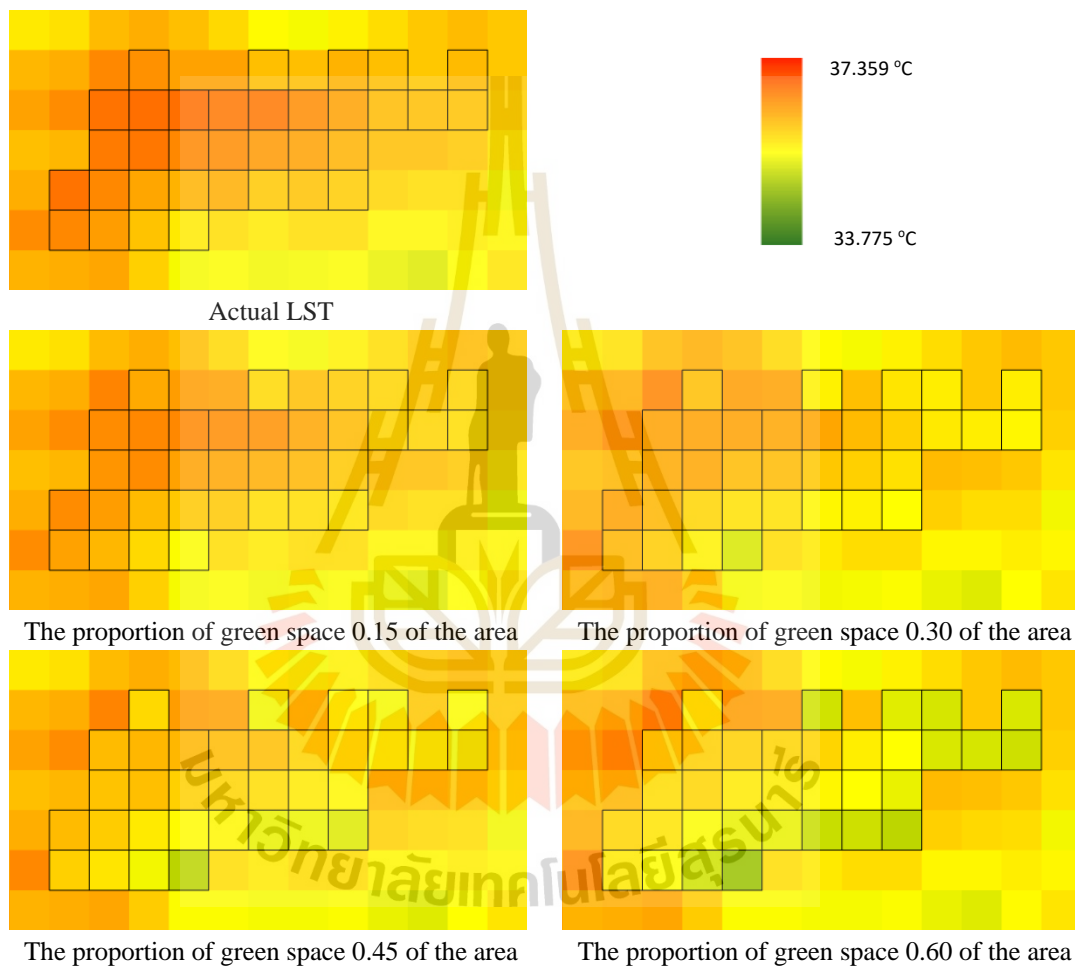


Figure 4.27 The first hotspot location mitigation based on March 26, 2018.

The hotspot temperature, on March 26, 2018, was decreased more than the minimum decreased temperature when the proportion of green space was increased to 0.15 of the area, as shown in Figure 4.27. Furthermore, the hotspot temperature could

be decreased over 0.50 °C and 1.00 °C when the proportion of green space was increased to 0.30 and 0.45 of the area, respectively.

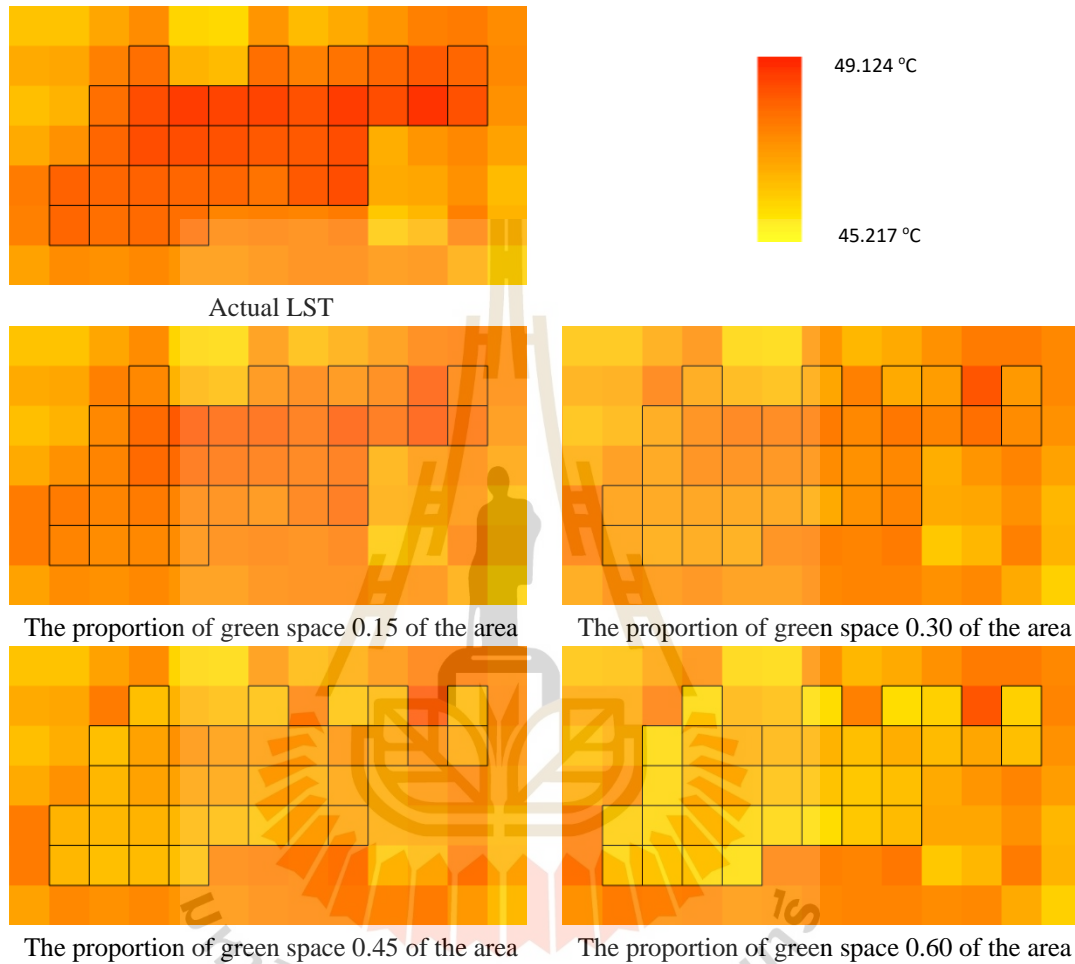


Figure 4.28 The first hot spot location mitigation based on April 11, 2018.

The hotspot temperature, on April 11, 2018, was closed to the surrounding areas temperature when the proportion of green space was increased to 0.30 of the area, as shown in Figure 4.28. To decrease the hotspot temperature more than the minimum decreased temperature, the minimum proportion of green space around 0.45 of the area was needed. Furthermore, the hotspot temperature could be decreased by more than 2.00 °C, when the proportion of green space was increased to 0.60 of the area.

Table 4.14 Decreased temperature based on simulated proportion of green space at the second hotspot location.

Proportion of green space		January 21, 2018		February 6, 2018		March 26, 2018		April 11, 2018	
		Decrease Temperature	ΔT						
0.15	Min	35.07	0.27	29.91	0.17	36.26	0.29	46.76	0.47
	Max	36.88	0.36	31.93	0.23	36.92	0.39	48.51	0.65
	Mean	35.89	0.36	30.82	0.23	36.60	0.39	47.74	0.63
0.30	Min	34.71	0.15	29.68	0.09	35.87	0.16	46.12	0.26
	Max	36.51	0.73	31.70	0.47	36.72	0.79	48.36	1.29
	Mean	35.56	0.66	30.61	0.42	36.23	0.72	47.17	1.18
0.45	Min	34.35	0.51	29.45	0.33	35.47	0.55	45.47	0.91
	Max	36.15	1.09	31.47	0.70	36.33	1.18	47.71	1.94
	Mean	35.19	1.03	30.38	0.66	35.84	1.11	46.53	1.82
0.60	Min	33.98	0.87	29.22	0.56	35.08	0.94	44.82	1.55
	Max	35.78	1.46	31.23	0.93	35.93	1.57	47.06	2.59
	Mean	34.83	1.39	30.15	0.89	35.45	1.50	45.88	2.47

Note: ΔT is the differentiated temperature between actual temperature and decreased temperature.

To decrease the hotspot temperature nearly or equal to surrounding areas, the minimum decreased temperature on January 21, February 6, March 26, and April 11, 2018, was around 1.37 °C, 1.39 °C, 0.23 °C, and 1.63 °C, respectively. Based on Table 4.14, the proportion of green space around 0.15 and 0.30 of the area could only decrease the hotspot temperature more than the minimum decreased temperature on March 26, 2018. On April 11, 2018, to decrease the hotspot temperature more than the minimum decreased temperature, the proportion of green space around 0.45 of the area was needed. However, with this proportion of green space, the decreased hotspot temperature still less than the minimum decreased temperature on January 21 and February 6 in 2018. When the proportion of green space was increased to 0.60 in the area, the almost hotspot temperature was decreased more than the minimum decreased temperature, except on February 6, 2018, with the differentiated temperature around 0.46 °C. Therefore, the proportion of green space around 0.60 of the area is the minimum proportion of green space in the second hotspot location mitigation.

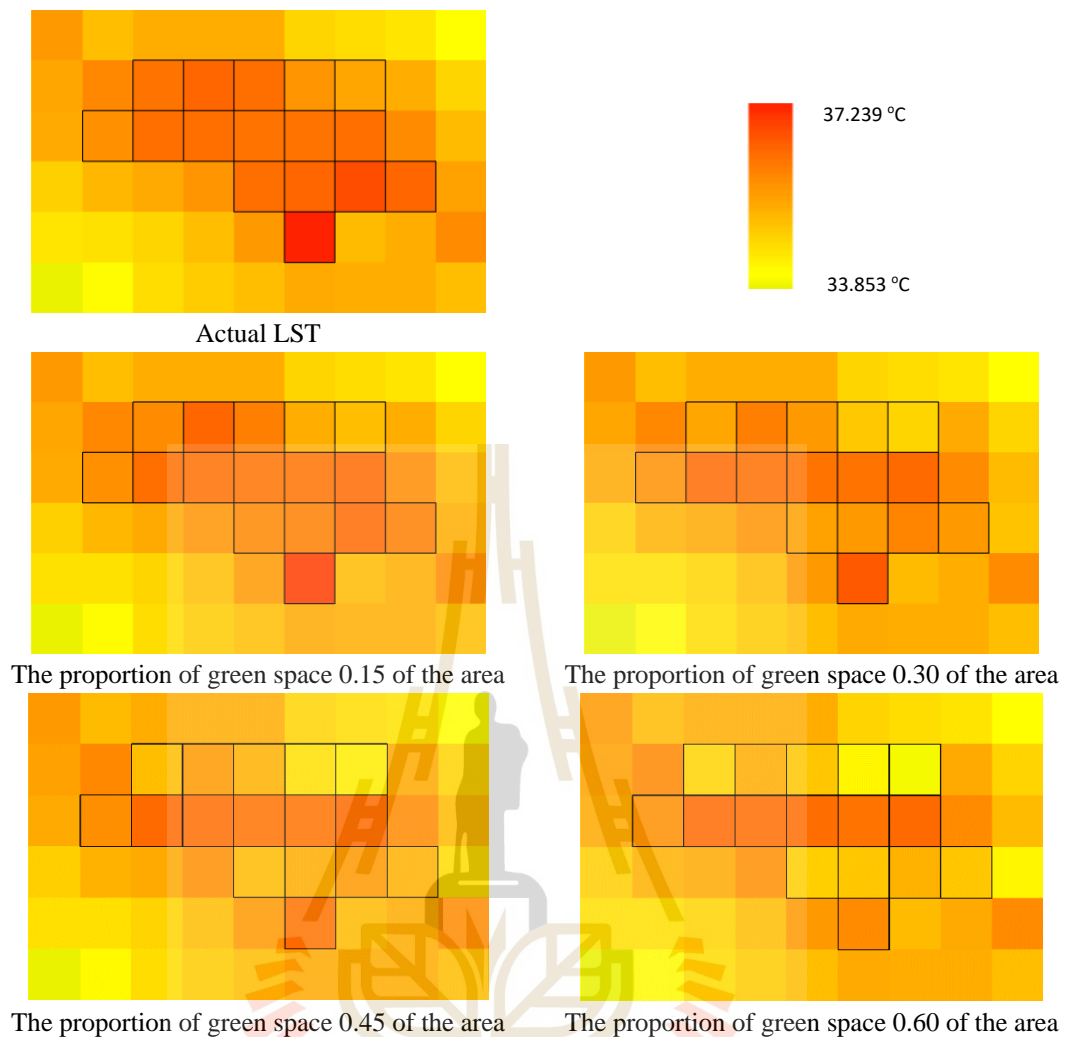


Figure 4.29 The second hotspot location mitigation based on January 21, 2018.

Based on Figure 4.29, the hotspot temperature, on January 21, 2018, was closed to the surrounding areas temperature when the proportion of green space was increased to 0.45 of the area. The differentiated temperature between decreased temperature and the minimum decreased temperature was around 0.28 °C. To decrease the hotspot temperature more than at the minimum decreased temperature, at least proportion of green space around 0.60 of the area was needed.

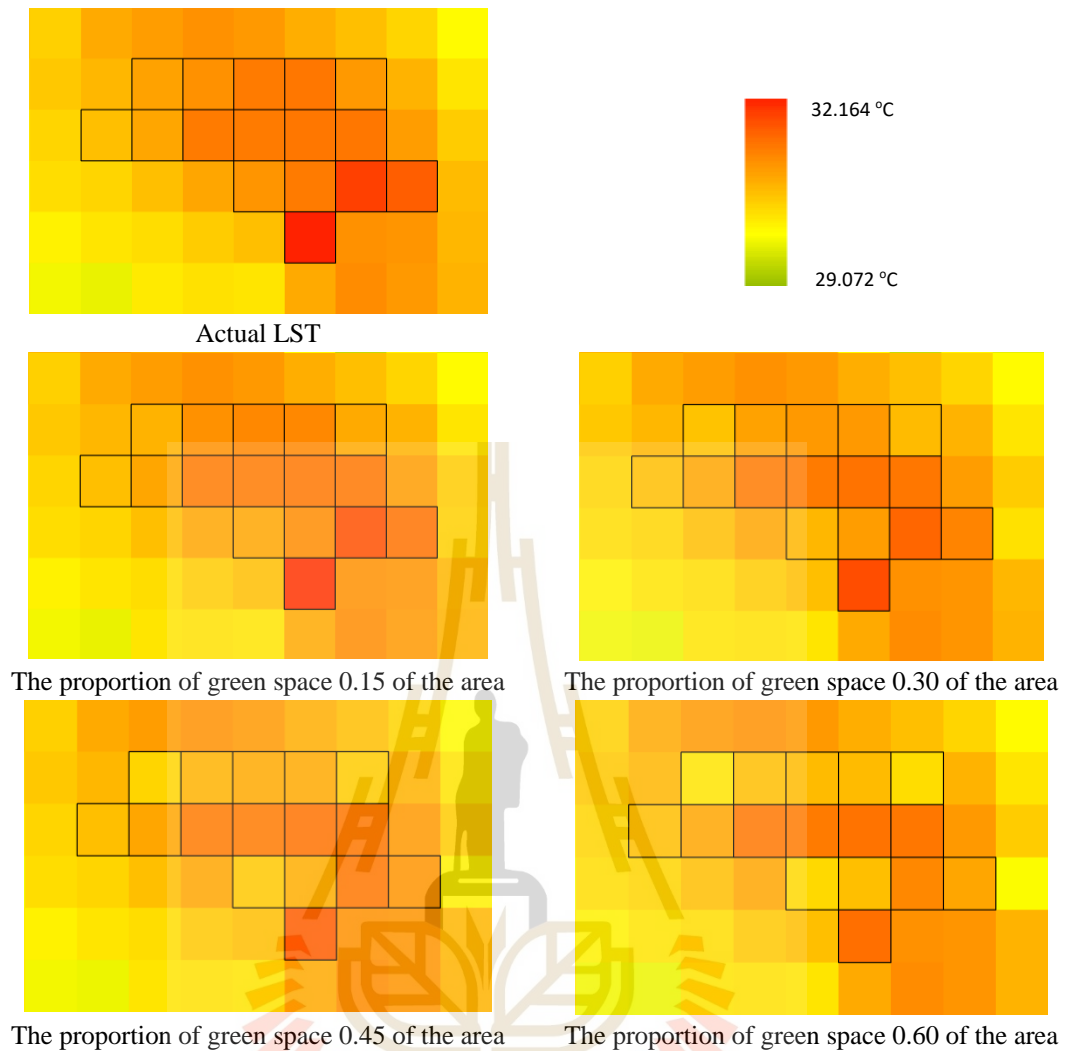


Figure 4.30 The second hotspot location mitigation based on February 6, 2018.

Based on Figure 4.30, the differentiated temperature between the decreased temperature and surrounding areas temperature was more than $0.50\text{ }^{\circ}\text{C}$ when the proportion of green space was increased to 0.45 of the area. Although the proportion of green space was increased to 0.60 of the area, the decreased temperature was still less than the minimum decreased temperature.

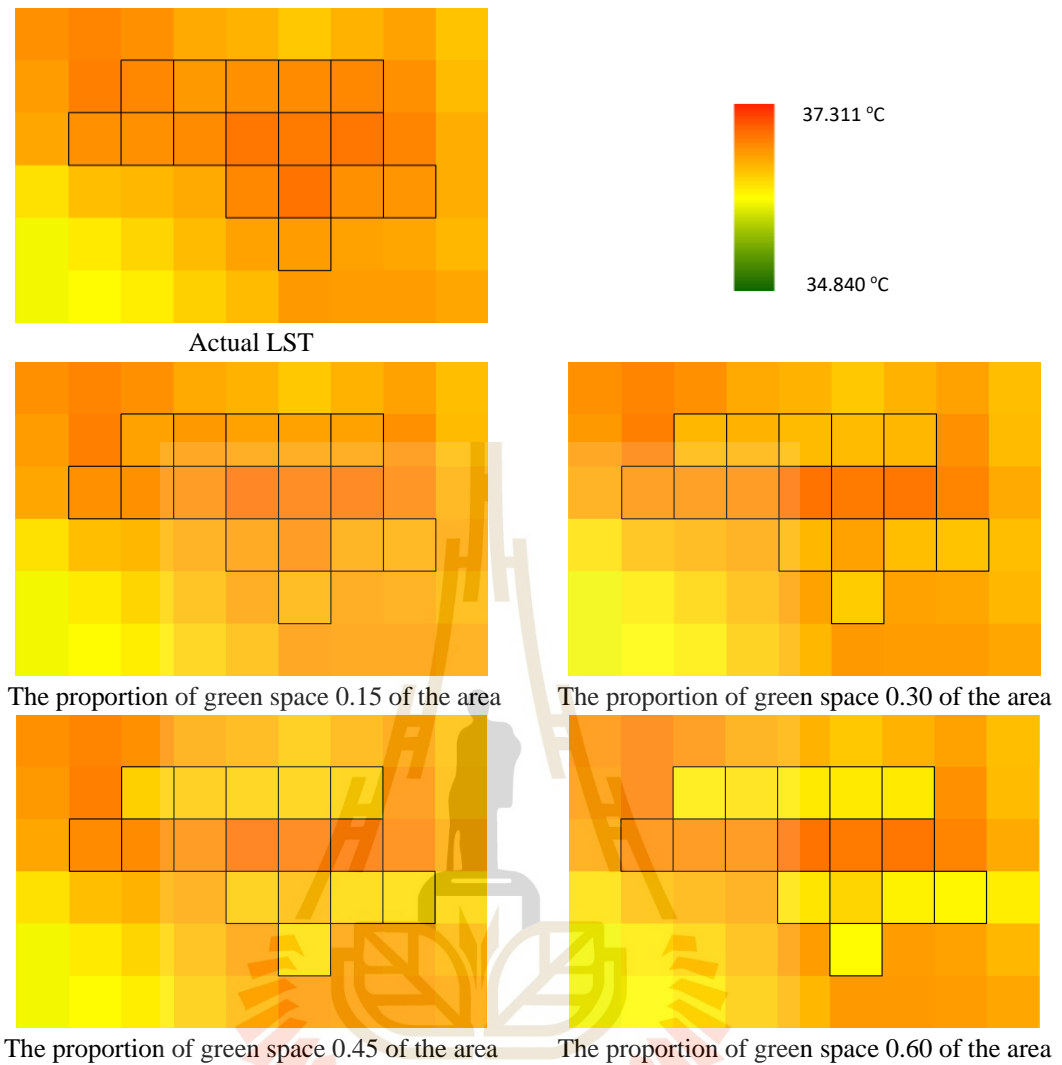


Figure 4.31 The second hotspot location mitigation based on March 26, 2018.

Based on Figure 4.31, the hotspot temperature, on March 26, 2018, was decreased more than the minimum decreased temperature when the proportion of green space was increased to 0.15 of the area. Furthermore, the hotspot temperature could be decreased over 0.50 °C and 1.00 °C when the proportion of green space was increased to 0.30 and 0.45 of the area.

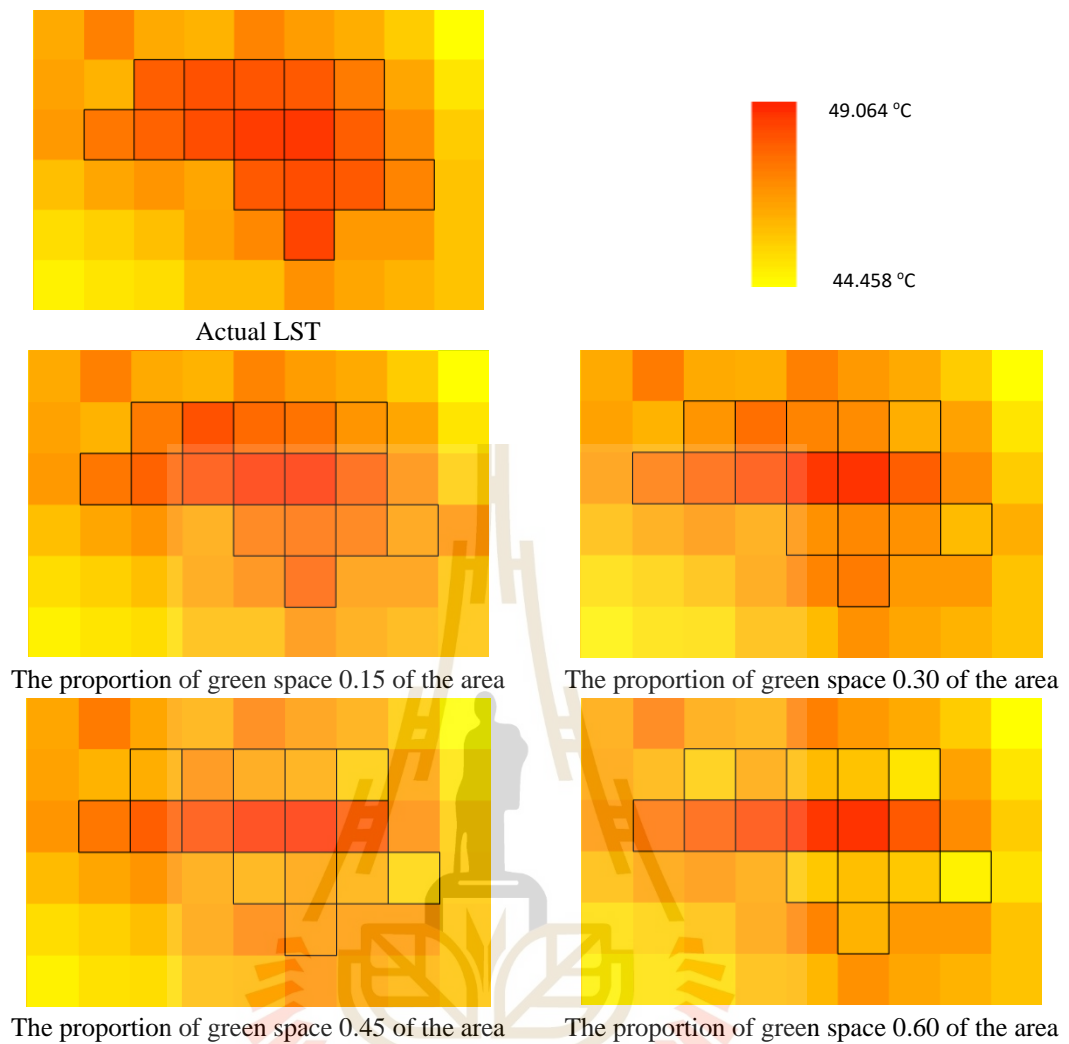


Figure 4.32 The second hotspot location mitigation based on April 11, 2018.

On April 11, 2018, the hotspot temperature was closed to the surrounding areas temperature when the proportion of green space was increased to 0.30 of the area, as shown in Figure 4.32. To decrease the hotspot temperature more than the minimum decreased temperature, the minimum proportion of green space around 0.45 of the area was needed. Furthermore, the hotspot temperature could be decreased by more than 2.00 °C, when the proportion of green space was increased to 0.60 of the area.

Table 4.15 Decreased temperature based on simulated proportion of green space at the third hotspot location.

Proportion of green space		January 21, 2018		February 6, 2018		March 26, 2018		April 11, 2018	
		Decrease Temperature	ΔT						
0.15	Min	34.89	0.19	29.44	0.12	35.52	0.21	47.04	0.34
	Max	35.92	0.36	31.76	0.23	37.07	0.39	47.81	0.65
	Mean	35.28	0.33	30.42	0.21	36.65	0.36	47.34	0.58
0.30	Min	34.52	0.56	29.21	0.36	35.13	0.60	46.40	0.99
	Max	35.56	0.73	31.53	0.47	36.67	0.79	47.16	1.29
	Mean	34.91	0.69	30.19	0.44	36.26	0.75	46.69	1.23
0.45	Min	34.16	0.92	28.98	0.59	34.73	1.00	45.75	1.64
	Max	35.20	1.09	31.30	0.70	36.28	1.18	46.52	1.94
	Mean	34.55	1.06	29.96	0.68	35.86	1.14	46.04	1.88
0.60	Min	33.79	1.29	28.74	0.82	34.34	1.39	45.10	2.28
	Max	34.83	1.46	31.07	0.93	35.89	1.57	45.87	2.59
	Mean	34.19	1.42	29.72	0.91	35.47	1.54	45.40	2.52

Note: ΔT is the differentiated temperature between actual temperature and decreased temperature.

To decrease the hotspot temperature nearly or equal to surrounding areas, the minimum decreased temperatures on January 21, February 6, March 26, and April 11, 2018, were around 0.52 °C, 1.11 °C, 0.36 °C, and 0.90 °C, respectively. Based on Table 4.15, when the proportion of green space was increased to 0.15 of the area, only the hotspot temperature on March 26, 2018, could be decreased more than the minimum decreased temperature. To decrease the hotspot temperature more than the minimum decreased temperature on January 21 and April 11 in 2018, the proportion of green space around 0.30 of the area was needed. However, although the proportion of green space was increased to 0.45 and 0.60 of the area, the decreased hotspot temperature on February 6, 2018, is still less than the minimum decreased temperature. Therefore, the proportion of green space around 0.30 of the area was the minimum proportion of green space in the third hotspot location mitigation.

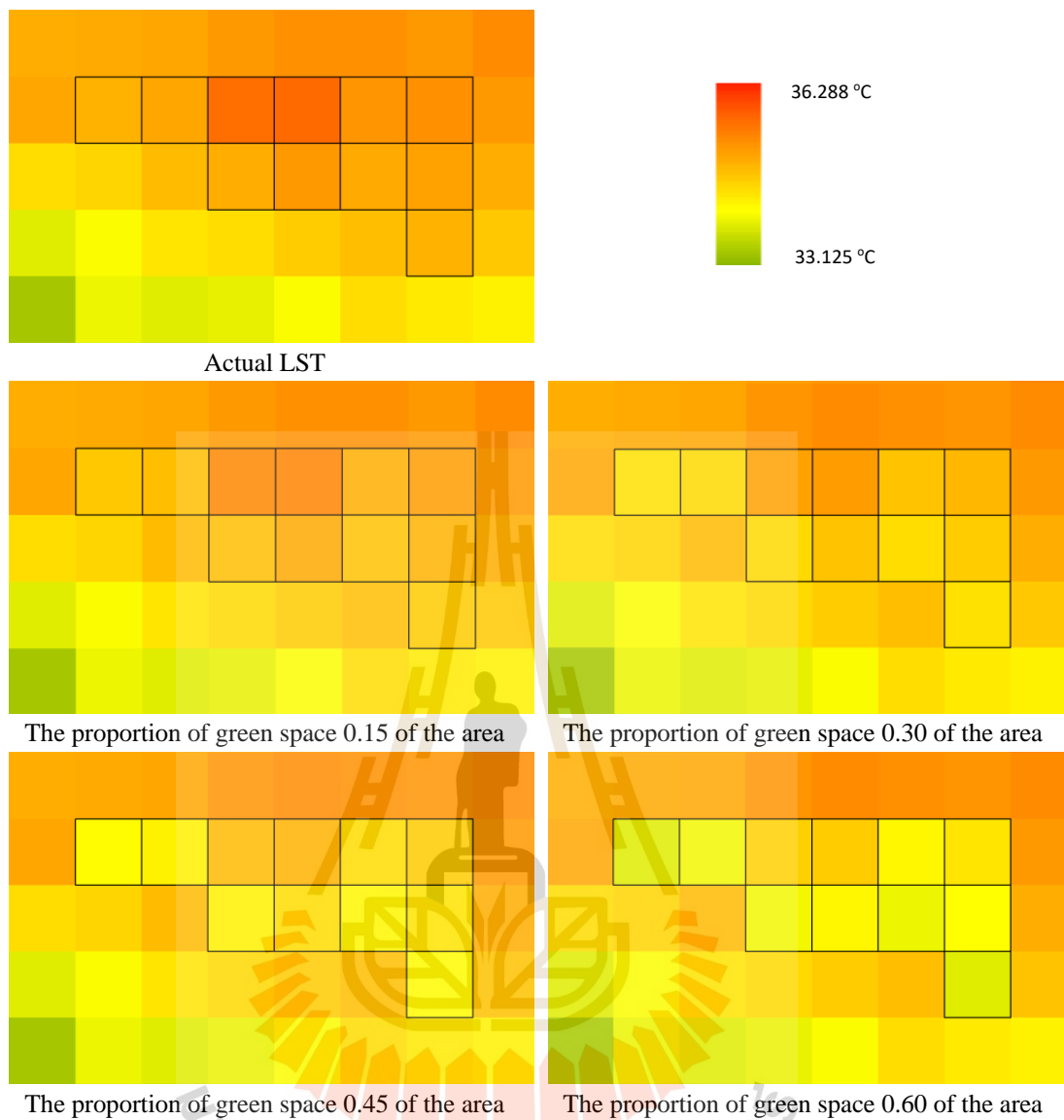


Figure 4.33 The third hotspot location mitigation based on January 21, 2018.

Based on Figure 4.33, the hotspot temperature, on January 21, 2018, was closed to the surrounding areas temperature when the proportion of green space was increased to 0.15 of the area. The differentiated temperature between decreased temperature and the minimum decreased temperature was around 0.16 °C. To decrease the hotspot temperature more than the minimum decreased temperature, the proportion of green space around 0.30 of the area was needed. Furthermore, the hotspot

temperature was decreased over 1.00 °C when the proportion of green space was increased by more than 0.45 in the area.

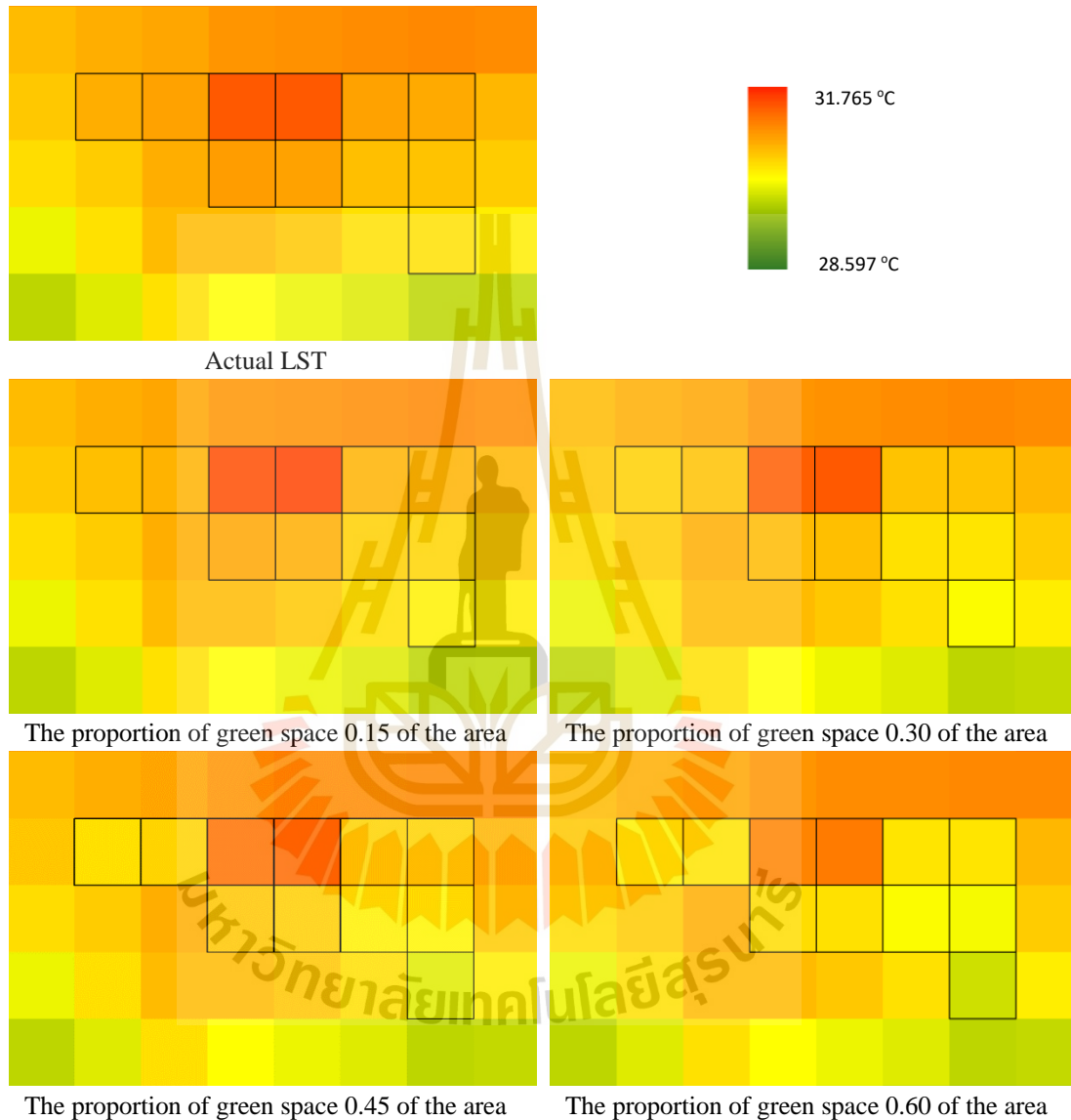


Figure 4.34 The third hotspot location mitigation based on February 6, 2018.

Based on Figure 4.34, the differentiated temperature between the decreased temperature and surrounding areas temperature was more than 0.50 °C when the proportion of green space was increased to 0.45 of the area. Although the proportion of

green space was increased to 0.60 of the area, the decreased temperature was still less than the minimum decreased temperature. The differentiated temperature between the decreased temperature and surrounding areas temperature was around 0.41 °C and 0.18 °C when the proportion of green space was increased to 0.45 and 0.60 of the area, respectively.

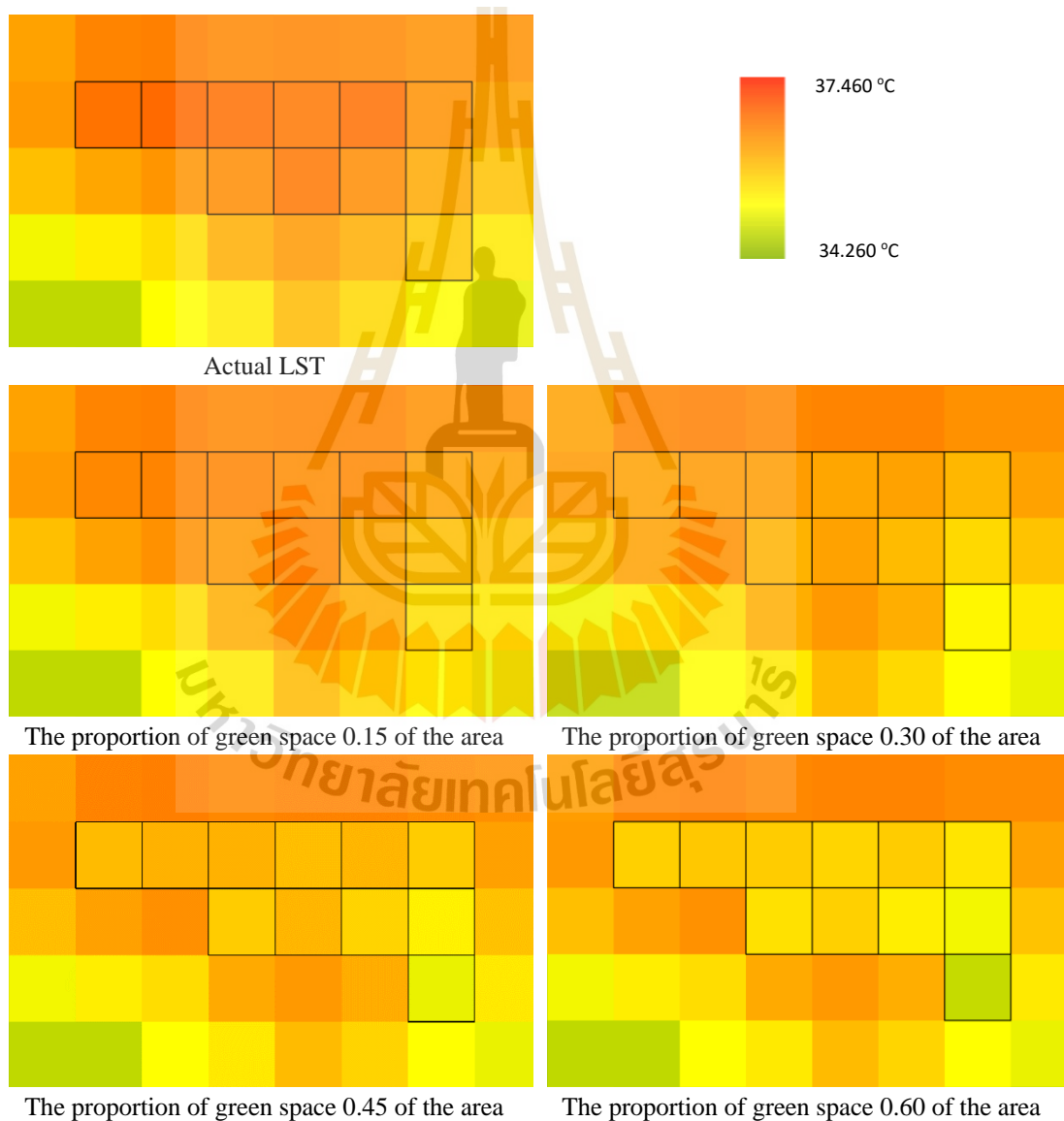


Figure 4.35 The third hotspot location mitigation based on March 26, 2018.

On March 26, 2018, as shown in Figure 4.35, the hotspot temperature was decreased more than the minimum decreased temperature when the proportion of green space was increased to 0.15 of the area. Furthermore, the hotspot temperature could be decreased over 0.50 °C and 1.00 °C when the proportion of green space was increased to 0.30 and 0.45 of the area, respectively.

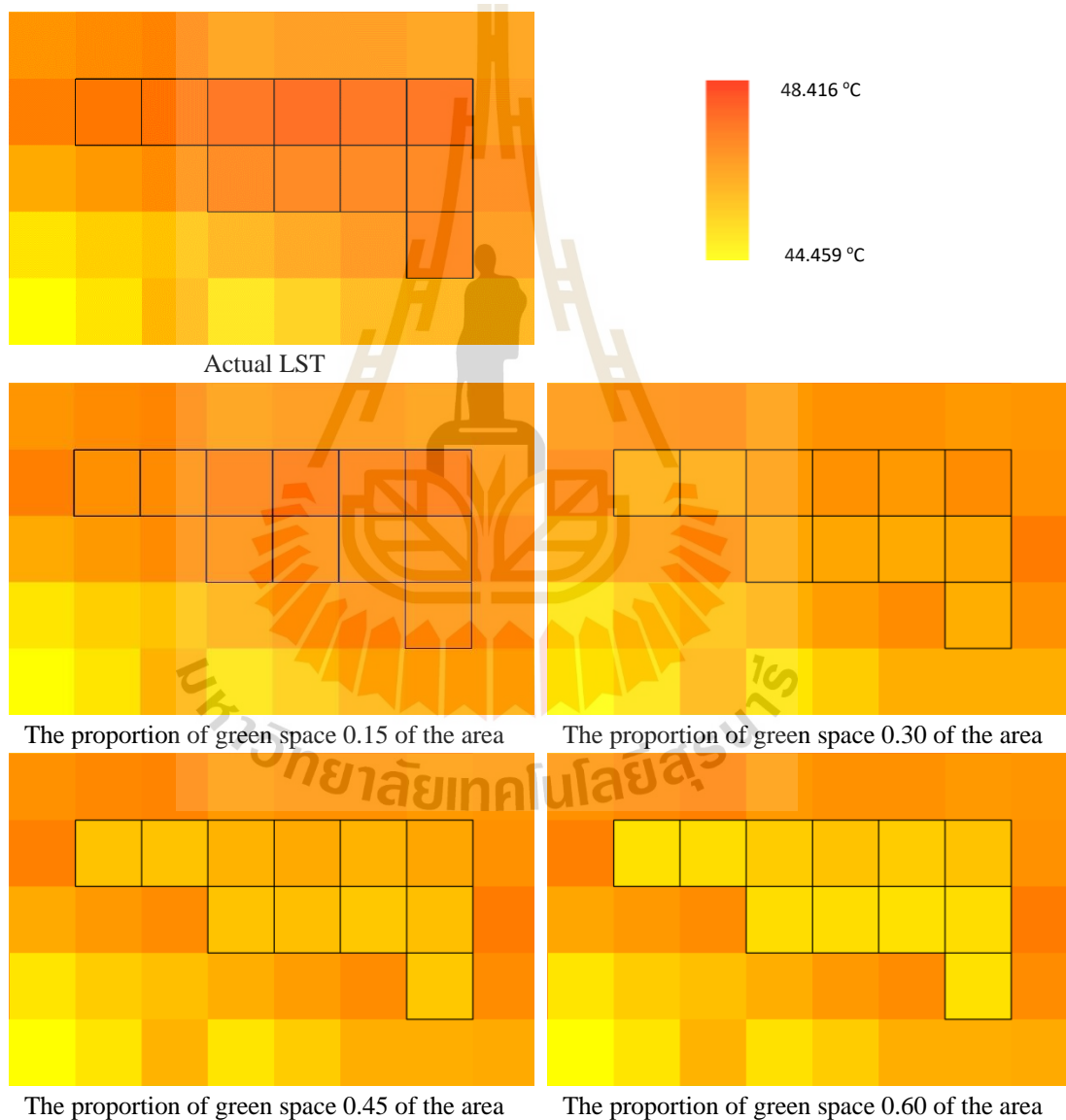


Figure 4.36 The third hotspot location mitigation based on April 11, 2018.

Based on Figure 4.36, the hotspot temperature, on April 11, 2018, was closed to the temperature of the surrounding area when the proportion of green space was increased to 0.15 in the area. To decrease the hotspot temperature more than the minimum decreased temperature, the minimum proportion of green space around 0.30 of the area was needed. Furthermore, the hotspot temperature could be decreased by more than 2.00 °C, when the proportion of green space was increased to 0.60 of the area.

Regarding the finding, it can be concluded that to decrease the hotspot temperature nearly or equal to surrounding areas temperature, the proportion of green space as 0.45, 0.60, and 0.30 of the area are the minimum proportions of green space required to mitigate associated with the first, second, and the third hotspot location, respectively.

The proportion of green space directly impacts on the decreased temperature. Besides, the cooling effect of green space also depends on the weather condition, as shown in Figure 4.37.

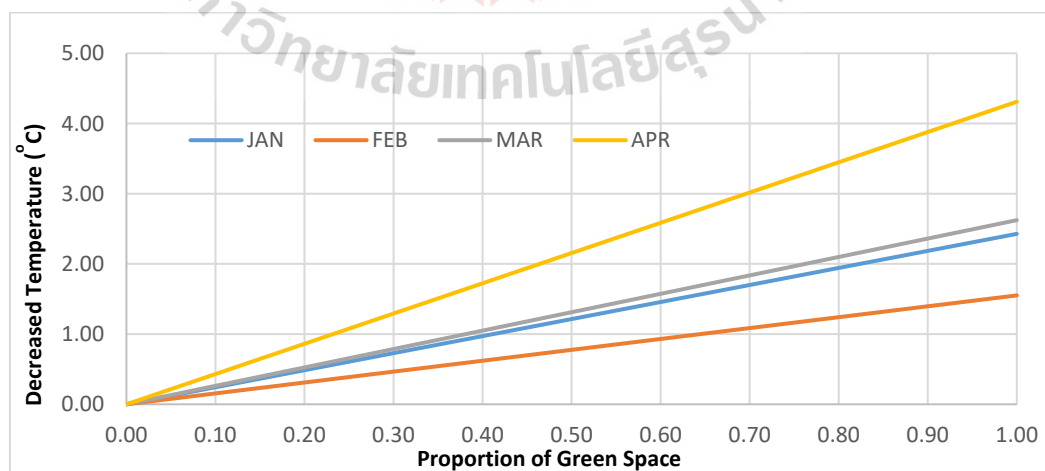


Figure 4.37 Decreased temperature and proportion of green space.

Considering the hottest month of this study, on April 11, 2018, the temperature could be decreased more rapidly than the temperature on February 6, 2018. To decrease the temperature around 1.00 °C, the proportion of green space, around 0.20 of the area, was needed on April 11, 2018. In contrast, to decrease the temperature, around 1.00 °C, the proportion of green space around 0.65 of the area was needed on February 6, 2018. Furthermore, on April 11, 2018, the differentiated temperature of the proportion of green space from 0.00 to 1.00 in the area was significant at around 4.00 °C. Whereas on February 6, 2018, the differentiated temperature of the proportion of green space from 0.00 to 1.00 of the area as small as around 1.50 °C

Therefore, it can be concluded that the proportion of green space has a significant influence on decreasing the high temperature. Corresponding with Armson, Stringer and Ennos (2012) who indicated that both grass and trees could effectively cool surface and provide regional cooling, helping reduce the UHI in hot weather.

Regarding Figure 4.20 and Figure 4.21, there were existing green space found in some areas in the second and the third hotspot locations as 0.03 and 0.01 of the area, respectively. However, the proportion of green space was rarely compared with other LULC types in hotspot areas, since these hotspot areas were explored as commercial areas. According to a few green-space areas, this condition rarely reduces the extremely high temperature of these hotspot areas. Considering to reduce the very high temperature of these extreme hotspots, a large green-space area is recommended response to the study by Perini and Magliocco (2014), who found that a different cooling effect of green space can be noticed depending on the number of green spaces and vegetation type.

However, due to the limitation of land resources for urban greening, the optimizing urban park shapes (Ren et al., 2013), also the connectivity of urban green spaces (Chen, Yao, Sun and Chen, 2014) should be considered as the ULST mitigation strategies, especially in the new urban expansion.

Increasing complexity in shape, the cooling effect of urban parks decreased; thus, the rounder of the urban park shape, the better is the cooling island effect (Ren et al., 2013). Furthermore, Feyisa et al. (2014) found that small parks with a shape closer to that of a circle have higher thermal contrast with their immediate surroundings than elongated parks. Cao et al. (2010) also found that the irregular and belt-shape parks tend to have low PCI intensity, while the compactness of PCI may benefit PCI development.

On the other hand, the connectivity of urban green spaces also affected the cool urban island negatively (Chen et al., 2014). At the neighborhood level, increased green space cover and high connectivity between neighborhood-level green spaces are associated with cooler air temperatures and reduced UHI effects, particularly on hot days (Steenefeld, Koopmans, Heusinkveld, Hove and Holtslag, 2011). More closely linked and continuous green spaces have stronger cool island effects than smaller patches of green space (Li, Zhou and Ouyang, 2013; Li, Zhou, Ouyang, Xu and Zheng, 2012). As confirmed with studies of Hamada and Ohta in 2010, and Doick and others in 2014 (Doick, Peace and Hutchings, 2014; Hamada and Ohta, 2010), maximizing the connectivity of many scattered parks throughout the urban environment (rather than in one concentrated spot) can maximize cooling effects beyond park boundaries by breaking up the micro effects of the urban form that can cause hotter and colder pocket.

4.4.3 Feasibility of the simulated temperature

In the first feasibility test of simulated temperature, the same proportions of LULC were selected and used as the reference data to compare with the simulation results. It is noted that the increasing proportion of green space focuses on the proportion of roads initially, according to the space along the roads are public areas in the city. Secondly, the proportion of constructions is considered regarding insufficient green space along the roads. The supplementary data of this section are mentioned in Appendix C. The results of the first feasibility test are in Table 4.16.

Table 4.16 The first feasibility test of simulated temperature.

Hotspot Location	Proportion of green space	RMSE (°C)			
		March 31, 2014	April 16, 2014	March 20, 2016	April 5, 2016
1	0.45	0.31	0.46	0.37	0.44
2	0.60	0.30	0.39	0.23	0.39
3	0.30	0.21	0.31	0.38	0.31

All RMSE values are lower than 0.50 °C, regarding Table 4.16. It seems that the simulated values are slightly higher than the sample values. According to the influent variables, it is noted that there are several variables influent the temperature in the area, such as the location, albedo of the materials in the area. Basically, the simulated results are calculated by considering the pixel within the hotspot locations, regardless of location and albedo of the materials in the area. While the sample areas are selected from a whole study area. Furthermore, this comparison is processed to explore the feasibility of the simulated temperature with the same proportional LULC.

In the second part, the selected proportions of green space in hotspot mitigation were used with the data in 2014 and 2016, to explore the effects of these proportion of green space in hotspot mitigation. The results of the simulation are in Table 4.17.

Table 4.17 The feasibility results based on the selected proportion of green space (°C).

Hotspot Location		March 31, 2014		April 16, 2014		March 20, 2016		April 5, 2016	
		Decrease Temperature	ΔT						
1	Min	42.62	1.66	38.94	2.08	40.55	0.55	42.86	1.35
	Max	44.46	1.66	40.60	2.08	43.02	0.55	44.84	1.35
	Mean	43.80	1.66	39.35	2.08	41.59	0.55	43.87	1.35
2	Min	41.94	1.33	38.20	1.67	41.52	0.44	43.04	1.08
	Max	44.33	2.21	39.73	2.78	43.21	0.73	45.22	1.80
	Mean	43.36	2.11	38.81	2.65	42.44	0.69	43.95	1.72
3	Min	43.80	0.85	39.59	1.07	41.35	0.28	44.02	0.69
	Max	44.79	1.10	40.95	1.39	43.49	0.36	45.43	0.90
	Mean	44.47	1.05	39.98	1.32	42.29	0.35	44.57	0.86

Note: 1. The selected proportion of green space is 0.45, 0.30, and 0.60 of the area, following Hotspot location.

2. ΔT is the differentiated temperature between the actual temperature and decreased temperature.

The selected proportion of green space around 0.45 of the area was used in the first hotspot temperature to decrease the hotspot temperature nearly or equal to the temperature of the surrounding area. At least the decreased temperature on March 31, 2014, April 16, 2014, March 20, 2016, and April 5, 2016, were around 0.43 °C, 1.13 °C, 0.76 °C, and 0.25 °C, respectively. Based on the details in Table 4.17, the selected proportion of green space could reduce almost temperature data, except on March 20, 2016. However, on March 20, 2016, there was a little differentiated temperature of the decreased temperature and at least a decreased temperature (around 0.21 °C).

Considering the second hotspot location, the green space around 0.60 was used in hotspot temperature decreasing. To decrease the hotspot temperature nearly or equal to surrounding areas temperature, the minimum decreased temperatures on March 31, 2014, April 16, 2014, March 20, 2016, and April 5, 2016, were around 0.70 °C, 1.18 °C, 0.89 °C, and 0.58 °C, respectively. Based on Table 4.17, the selected proportion of green space can decrease almost data, except on March 20, 2016. However, on March 20, 2016, there was a little differentiated temperature of the decreased temperature and the minimum decreased temperature was around 0.16 °C.

Lastly, the selected proportion of green space around 0.30 of the area was used in the third hotspot temperature in order to decrease the hotspot temperature nearly or equal to the temperature of the surrounding area. The minimum decreased temperatures on March 31, 2014, April 16, 2014, March 20, 2016, and April 5, 2016, were around 0.32 °C, 1.21 °C, 0.63 °C, and 0.33 °C, respectively. Based on Table 4.17, the selected proportion of green space could decrease almost data, except on March 20, 2016. However, there was a little differentiated temperature of the decreased temperature, and the minimum decreased temperature (around 0.27 °C).

Regarding the finding, all hotspot temperature could be decreased more than the minimum decreased temperature in all months, except on March 20, 2016. Nevertheless, the decrease temperature on this date was closed to the surrounding temperature.

CHAPTER V

CONCLUSION AND SUGGESTIONS

This chapter contains the summary of the achievements of all works carried out in this thesis response to four objectives, (1) to explore the optimum method for ULST estimation, (2) to estimate subpixel LST data using statistical-based method, (3) to identify the hotspots areas based on subpixel LST data, and (4) to simulate hotspot mitigation associated with proportions of green space in urban area. The conclusion and suggestions are addressed as follows.

5.1 Optimum method in ULST estimation

Regarding the finding, the SW algorithm is an optimum method in ULST estimation for this study. This algorithm provides the lowest NRMSE values in most cases, which had the amount of atmospheric water vapor content more than 2.70 gm^{-2} . The errors occur according to the atmospheric parameter estimation, emissivities estimation, and also the limitations in ground-based temperature surveying. All maps based on the SW method show a more complex surface than single-channel methods. All maps based on the single-channel methods, namely, RTE, IMW, and GSC, are quite similar.

Another critical point is that the amount of atmospheric water vapor content data plays an essential role in terms of accuracy. This atmospheric parameter is the main absorber in the thermal infrared region. Therefore, to select the optimum method in

LST estimation, the amount of atmospheric water vapor content data should be considered.

5.2 Subpixel LST estimation by using the statistical-based method

In this part, the conclusion of the study is separated into two parts, including (1) the regression modeling, and (2) subpixel LST data. Their specific details are as follows.

5.2.1 The regression modeling

Regarding the results in this study, the important scaling factors in subpixel LST data estimation are NDISI, MNDWI, and surface albedo. The selected scaling factors depend on the characteristics of the areas, and also the study period. However, to obtain the regression model with the highest R^2 value, the model cannot be fixed with individual spectral indices, due to other spectral indices, which are almost represented the impervious surface areas, are also selected to increase the R^2 value.

5.2.2 The subpixel LST data

The LST data and subpixel LST data are significantly different at a significant level of 0.05. The errors of subpixel LST data are less than the LST data. The differentiated RMSE values are more than 0.300 °C in all months. The errors of subpixel LST data come from the scale effect and spatial resolution of data, which are used in spectral indices and the LST estimation process. The atmospheric parameters calculation and also LST estimation can provide the error to the results.

5.3 Hotspot analysis for subpixel LST data

The hotspot areas occurred in bare-lands, race tracks, and built-up areas. Focusing on the selected hotspot locations, where are commercial areas, the main LULC types are construction, road, and green spaces. However, the proportion of green space in these hotspot locations is very low compared with others.

Another critical point is, with the low-temperature condition as 19.95 °C on February 6, 2018, the hotspot mostly occurred in bare-lands. In contrast, with the high-temperature condition as around 29.75 °C or higher temperatures on January 21, March 26, and April 11, 2018, the hotspot can occur both in bare-lands and built-up areas. Besides, the weather parameter such as moisture also plays an essential role in the appearance of the hotspots. For example, the rainfall before the satellite obtained the data in April, which influences the appearance of hotspot areas in bare-lands (parking lot).

5.4 Hotspot mitigation

In this part, the results are separated into two parts, including (1) the regression models, and (2) the proportion of green space in ULST mitigation. Their specific details are as follows.

5.4.1 The regression models

The proportion of green space correlates with subpixel LST data than the proportion of construction and road, according to Pearson correlation results. However, the obtained regression models, which are based on the only proportion of green space, provide the RMSE values are around 1.00 °C. Since other variables also play an important role in temperature estimation. This study focuses on the relationship

between the proportion of LULC and subpixel LST data; therefore, other variables are not considered. To improve the accuracy of the equations, therefore, the residuals are included in the equations.

5.4.2 The proportion of green space in ULST mitigation

Regarding the finding, the proportion of green space directly impacts on the decreased temperature. Noticeably, the proportion of green space has a significant influence on the decrease in the temperature in weather conditions with high temperatures. Furthermore, the cooling effect of green spaces will appear when the amount of green space is large enough. To mitigate the selected hotspot location, the proportion of green space around 0.30-0.60 of the area is needed. Due to the limitation of the available land area in most cities, other mitigation methods should be considered to use with the proportion of green space.

5.5 Suggestions

The suggestions are separated into two parts, (1) suggestions in implementation and (2) suggestions in further research. Their specific details are as follows.

5.5.1 The suggestion in implementation

5.5.1.1 To estimate more accurate LST data, the LST estimation algorithm should be considered based on the weather condition, especially the amount of atmospheric water vapor content data. Based on the results, the SW algorithm is an optimum method used in LST estimation with atmospheric water vapor content larger than 2.70 g cm^{-2} . In contrast, with the low amount of atmospheric water vapor content as 1.52 g cm^{-2} on February 6, 2018, the IMW algorithm should be considered. Because this method provides a lower error than the SW algorithm with this condition.

5.5.1.2 To improve the spatial resolution by using statistical-based methods, the spectral indices as scaling factors should be considered and selected based on the characteristics of the area. However, the spectral indices represent the impervious surface areas that are recommended in statistical-based method development. Regarding the LULC type, it is the most significant portion of the urban area. Furthermore, to avoid multicollinearity, stepwise multiple regression modeling should be applied. Also, the residual should be added to the model. Due to other associated variables, which are not considered, they also affect the accuracy of the model.

5.5.1.3 This cooling effect based on the results depends on the proportion of green spaces only. However, other mitigation methods, including the use of urban surfaces with a high reflection coefficient or high albedo, the wind tunnel concept, and also the increase of the wetlands, can be used together to reduce the temperature in hotspot areas.

5.5.1.4 The results of this study should be considered in urban planning, especially in the new urban expansion. Furthermore, the amount of green space should be large enough, as around 0.30 of the area of higher, to control the temperature in the cities.

5.5.2 Suggestions in future research

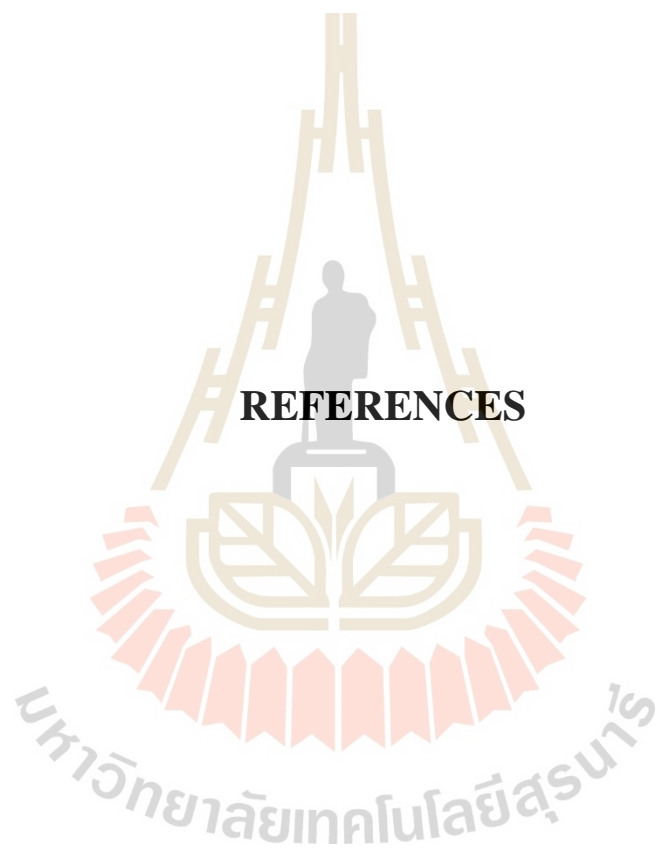
5.5.2.1 The high spatial and also high temporal data play an essential role in urban climate study. Other downscaling techniques, which can downscale both spatial resolution and temporal resolution, should be considered. However, the spatial scale, which is provided by those methods, does not properly estimate the SUHI effect

at the district level. Therefore, this study focuses only on the spatial resolution of LST data using the statistical-based method.

5.5.2.2 The subpixel LST data used in this study are processed based on the relationship between LST data and spectral indices as ancillary data. Therefore, the temperature data is not the actual data. The actual temperature data with high spatial resolution, which can be obtained by using the UAV with a thermal sensor, should be considered. Due to a lack of equipment, LANDSAT-8 imagery data are used in this study.

5.5.2.3 The mitigation maps are created based on the simulated results to show the mitigated temperature in the hotspot areas. When the proportional LULC is changed as the proportion of green space is increased; however, the cooling effect of green space will occur in hotspot and surrounding areas. Due to the relationship between the temperature in hotspot and surrounding areas, also the cooling extent of green space does not explore in this study. Therefore, mitigation maps cannot illustrate this phenomenon. The specific software should be considered to illustrate the possible occurrence.

5.5.2.4 This study focuses on the proportion of green space used in ULST mitigation. Therefore, to implement these results, future research should focus on site selection to increase the green space.



REFERENCES

REFERENCES

- Abdul-Wahab, S. A., Bakheit, C. S., and Al-Alawi, S. M. (2005). Principal Component and Multiple Regression Analysis in Modeling of Ground-Level Ozone and Factors Affecting Its Concentrations. **Environmental Modelling & Software**. 20: 1263-1271.
- Adeyeri, O. E., Akinsanola, A. A., and Ishola, K. A. (2017). Investigating Surface Urban Heat Island Characteristics over Abuja, Nigeria: Relationship between Land Surface Temperature and Multiple Vegetation Indices. **Remote Sensing Applications: Society and Environment**. 7: 57-68.
- Agam, N., Kustas, W. P., Anderson, M. C., Li, F., and Neale, C. M. U. (2007). A Vegetation Index Based Technique for Spatial Sharpening of Thermal Imagery. **Remote Sensing of Environment**. 107: 545-558.
- Ahmed, B., Kamruzzaman, M., Zhu, X., Rahman, M. S., and Choi, K. (2013). Simulating Land Cover Changes and Their Impacts on Land Surface Temperature in Dhaka, Bangladesh. **Remote Sensing**. 5: 5969-5998.
- Akbari, H., and Leanna, S. R. (2008). Urban Surfaces and Heat Island Mitigation Potentials. **Journal of the Human-Environment System**. 11(2): 85-101.
- Al-Seroury, F. A. (2012). Temporal Changes of Air Pollutants and Land Surface Temperature Around Jeddah Desalination Power Plant, KSA. **Journal of American Science**. 8(2): 503-508.
- ArcGIS Pro. (2018, May 31, 2018). **How Hot Spot Analysis (Getis-Ord Gi*) works** [On-line]. Available: <http://pro.arcgis.com/en/pro-app/tool-reference/spatial-statistics/h-how-hot-spot-analysis-getis-ord-gi-spatial-stati.htm>.

- Armson, D., Stringer, P., and Ennos, A. R. (2012). The Effect of Tree Shade and Grass on Surface and Globe Temperatures in an Urban Area. **Urban Forestry and Urban Greening**. 11: 245-255.
- Arnfield, A. J. (2003). Two Decades of Urban Climate Research: A Review of Turbulence, Exchanges of Energy and Water, and the Urban Heat Island. **International Journal of Climatology**. 23: 1-26.
- Avdan, U., and Jovanovska, G. (2016). Algorithm for Automated Mapping of Land Surface Temperature Using LANDSAT-8 Satellite Data. **Journal of Sensors**. 2016: 1-8.
- Ayanlade, A. (2016). Seasonality in the Daytime and Night-Time Intensity of Land Surface Temperature in a Tropical City Area. **Science of the Total Environment**. 557-558: 415-424.
- Barsi, J. A., Schott, J. R., Palluconi, F. D., and Hook, S. J. (2005, September, 7). **Validation of a Web-Based Atmospheric Correction Tools for Single Thermal Band Instruments**. Paper presented at the Proc. SPIE 5882, Earth Observing Systems X, 58820E.
- Bhavanibhai, S. D. (2013). **Thermal Infrared Remote Sensing over Land Surface: Retrieval and Applications of Land Surface Temperature**. (Doctor of Philosophy), Sardar Patel University, Gujarat, India.
- Blazejczyk, K., Bakowska, M., and Wieclaw, M. (2006). *Urban Heat Island in Large and Small Cities*. 6th International Conference on Urban Climate, Goteborg, Sweden.

- Bokaie, M., Zarkesh, M. K., Arasteh, P. D., and Hosseini, A. (2016). Assessment of Urban Heat Island Based on the Relationship between Land Surface Temperature and Land Use /Land Cover in Tehran. **Sustainable Cities and Society**. 23: 94-104.
- Bonafoni, S. (2016). Downscaling of LANDSAT and MODIS Land Surface Temperature over the Heterogeneous Urban Area of Milan. **IEEE Journal of Selected Topics in Applied Earth Observations and Remote Sensing**. 9(5): 2019 - 2027.
- Bonafoni, S., Anniballe, R., Gioli, B., and Toscano, P. (2016). Downscaling LANDSAT Land Surface Temperature over the Urban Area of Florence. **European Journal of Remote Sensing**. 49(1): 553-569.
- Boots, B. N., and Getis, A. (1998). **Point Pattern Analysis: Scientific Geography Series 8**: SAGE Publications.
- Buriram Municipality. (2016). **Buriram City** [On-line]. Available: http://www.buriramcity.go.th/images/datacontent/kong/vichakarn/plan3y2558/section02_2558.pdf.
- Buriram World. (2016). [On-line]. Available: <https://www.buriramworld.com/>.
- Cai, G., Du, M., and Xue, Y. (2011). Monitoring of Urban Heat Island Effect in Beijing Combining ASTER and TM Data. **International Journal of Remote Sensing**. 32(5): 1213-1232.
- Cai, G., Du, M., Xue, Y., and Li, S. (2008). *Analysis of an Urban Heat Sink Using Thermal Inertia Model from ASTER Data in Beijing, China*. 2008 IEEE International Geoscience and Remote Sensing Symposium.

- Cao, X., Onishi, A., Chen, J., and Imura, H. (2010). Quantifying the Cool Island Intensity of Urban Parks Using ASTER and IKONOS Data. **Landscape and Urban Planning**. 96: 224-231.
- Carnielo, E., and Zinzi, M. (2013). Optical and Thermal Characterisation of Cool Asphalts to Mitigate Urban Temperatures and Building Cooling Demand. **Building and Environment**. 60: 56-65.
- Caselles, V., Rubio, E., Coll, C., and Valor, E. (1998). Thermal Band Selection for the PRISM Instrument 3: Optimal Band Configurations. **Journal of Geophysical Research**. 103: 17057-17067.
- Chang, C. R., Li, M. H., and Chang, S. D. (2007). A Preliminary Study on the Local Cool-Island Intensity of Taipei City Parks. **Landscape and Urban Planning**. 80: 386-395.
- Chang, H. T. (2016). *A Temporal and Spatial Analysis of Urban Heat Island in Basin City Utilizing Remote Sensing Techniques*. The International Archives of the Photogrammetry, Remote Sensing and Spatial Information Sciences, Prague, Czech Republic.
- Chen, A., Yao, X. A., Sun, R., and Chen, L. (2014). Effect of Urban Green Patterns on Surface Urban Cool Islands and Its Seasonal Variations. **Urban Forestry and Urban Greening**. 13: 646-654.
- Chen, F., Zhao, X., Ye, H., and Hu, H. (2011). *Retrieving Land Surface Temperature from LANDSAT TM Using Different Atmospheric Products as Ancillary Data*. Spatial Data Mining and Geographic Knowledge Services (ICSDM), Fuzhou, China.

- Chen, X., Zhao, H., Li, P., and Yin, Z. (2006). Remote Sensing Image-Based Analysis of the Relationship between Urban Heat Island and Land Use /Cover Changes. **Remote Sensing of Environment**. 104(2): 133-146.
- Cohen, P., Potchter, O., and Matzarakis, A. (2012). Daily and Seasonal Climatic Conditions of Green Urban Open Spaces in the Mediterranean Climate and Their Impact on Human Comfort. **Building and Environment**. 51: 285-295.
- Coll, C., Caselles, V., Valor, E., and Niclos, R. (2012). Comparison between Different Sources of Atmospheric Profiles for Land Surface Temperature Retrieval from Single Channel Thermal Infrared Data. **Remote Sensing of Environment**. 117: 199-210.
- Coll, C., Galve, J. M., Sanchez, J. M., and Caselles, V. (2010). Validation of LANDSAT-7/ETM+ Thermal-Band Calibration and Atmospheric Correction with Ground-Based Measurements. **IEEE Transactions on Geoscience and Remote Sensing**. 48(1): 547-555.
- Cristobal, J., Jimenez-Munoz, J. C., Sobrino, J. A., Ninyerola, M., and Pons, X. (2009). Improvements in Land Surface Temperature Retrieval from the LANDSAT Series Thermal Band Using Water Vapor and Air Temperature. **Journal of Geophysical Research**. 114. doi:10.1029/2008JD010616.
- Cuenca, R. H., Ciotti, S. P., and Hagimoto, Y. (2013). Application of LANDSAT to Evaluate Effects of Irrigation Forbearance. **Remote Sensing**. 5: 3776-3802.
- Dan, S., Wu, J., Dan, B., Qiu, W., and Xu, H. (2010). *Evolution of Urban Heat Island Effect in Middle and Small Cities in Sichuan Basin*. 2010 Second IITA International Conference on Geoscience and Remote Sensing.

- Dash, P. (2005). **Land Surface Temperature and Emissivity Retrieval from Satellite Measurements**. (Doktors der Naturwissenschaften), Institut für Meteorological und Klimaforschung.
- Dash, P., Gottsche, F. M., Olesen, F. S., and Fischer, H. (2002). Land Surface Temperature and Emissivity Estimation from Passive Sensor Data: Theory and Practice-Current Trends. **International Journal of Remote Sensing**. 23(13): 2563-2594.
- Declet-Barreto, J., Brazel, A. J., Martin, C. A., Chow, W. T. L., and Harian, S. L. (2013). Creating the Park Cool Island in an Inner-City Neighborhood: Heat Mitigation Strategy for Phoenix, AZ. **Urban Ecosystems**. 16: 617-635.
- Dimoudi, A., and Nikolopoulou, M. (2003). Vegetation in the Urban Environment: Microclimate Analysis and Benefits. **Energy and Building**. 35: 69-76.
- Dimoudi, A., Zoras, S., Kantzioura, A., Stogiannou, X., Kosmopoulos, P., and Pallas, C. (2014). Use of Cool Materials and Other Bioclimatic Interventions in Outdoor Places in order to Mitigate the Urban Heat Island in a Medium Size City in Greece. **Sustainable Cities and Society**. 13: 89-96.
- Dixon, P. G., and Mote, T. L. (2003). Patterns and Causes of Atlanta's Urban Heat Island - Initiated Precipitation. **Journal of Applied Meteorology**. 42: 1273-1284.
- Dobrovolny, P. (2013). The Surface Urban Heat Island in the City of Brno (Czech Republic) Derived from Land Surface Temperatures and Selected Reasons for Its Spatial Variability. **Theoretical and Applied Climatology**. 112: 89-98.

- Doick, K. J., Peace, A., and Hutchings, T. R. (2014). The Role of One Large Greenspace in Mitigating London's Nocturnal Urban Heat Island. **Science of the Total Environment**. 493: 662-671.
- Dominguez, A., Kleissl, J., Luvall, J. C., and Rickman, D. L. (2011). High-resolution Urban Thermal Sharpener (HUTS). **Remote Sensing of Environment**. 115: 1772-1780.
- Dong, W., Liu, Z., Zhang, L., Tang, Q., Liao, H., and Li, X. e. (2014). Assessing Heat Health Risk for Sustainability in Beijing's Urban Heat Island. **Sustainability**. 6: 7334-7357.
- Du, C., Ren, H., Qin, Q., Meng, J., and Zhao, S. (2015). A Practical Split-Window Algorithm for Estimating Land Surface Temperature from LANDSAT-8 Data. **Remote Sensing**. 7: 647-665.
- Du, H., Wang, D., Wang, Y., Zhao, X., Qin, F., Jiang, H., and Cai, Y. (2016). Influence of Land Cover Types, Meteorological Conditions, Anthropogenic Heat and Urban Area on Surface Urban Heat Island in the Yangtze River Delta Urban Agglomeration. **Science of the Total Environment**. 571: 461-470.
- Dugord, P. A., Lauf, S., Schuster, C., and Kleinschmit, B. (2014). Land Use Patterns, Temperature Distribution, and Potential Heat Stress Risk: The Case Study Berlin, Germany. **Computers, Environment and Urban Systems**. 48: 86-98.
- El-Gammal, M. I., Youssef, R. A., Ali, R. R., and Madkour, A. G. (2011). Estimation of Seasonal Variation of Air Pollutants, NO₂, SO₂, PM₁₀ and Land Surface Temperature (LST) of Nile Delta Region. **New York Science Journal**. 4(10): 36-45.

- Elsayed, I. S. M. (2012). Mitigation of the Urban Heat Island of the City of Kuala Lumpur, Malaysia. **Middle-East Journal of Scientific Research**. 11(11): 1602-1613.
- ESRI. (2016). **How Spatial Autocorrelation (Global Moran's I) Works** [On-line]. Available: <http://desktop.arcgis.com/en/arcmap/10.3/tools/spatial-statistics-toolbox/h-how-spatial-autocorrelation-moran-s-i-spatial-st.htm>.
- ESRI. (2019). **Normal QQ plot and general QQ plot** [On-line]. Available: <https://desktop.arcgis.com/en/arcmap/latest/extensions/geostatistical-analyst/normal-qq-plot-and-general-qq-plot.htm>.
- Essa, W., Kwast, J. v. d., Verbeiren, B., and Batelaan, O. (2013). Downscaling of Thermal Images over Urban Areas Using the Land Surface Temperature-impervious Percentage Relationship. **International Journal of Applied Earth Observation and Geoinformation**. 23: 95-108.
- Essa, W., Verbeiren, B., Kwast, J. v. d., Voorde, T. V. d., and Batelaan, O. (2012). Evaluation of the DisTrad Thermal Sharpening Methodology for Urban Areas. **International Journal of Applied Earth Observation and Geoinformation**. 19: 163-172.
- Fabrizi, R., Bonafoni, S., and Biondi, R. (2010). Satellite and Ground-Based Sensors for the Urban Heat Island Analysis in the City of Rome. **Remote Sensing**. 2: 1400-1415.
- Feizizadeh, B., and Blaschke, T. (2013). Examining Urban Heat Island Relations to Land Use and Air Pollution: Multiple Endmember Spectral Mixture Analysis for Thermal Remote Sensing. **IEEE Journal of Selected Topics in Applied Earth Observations and Remote Sensing**. 6(3): 1749-1756.

- Feng, X., Foody, G., Aplin, P., and Gosling, S. N. (2015). Enhancing the Spatial Resolution of Satellite-Derived Land Surface Temperature Mapping for Urban Areas. **Sustainable Cities and Society**. 19: 341-348.
- Feyisa, G. L., Dons, K., and Meiby, H. (2014). Efficiency of Parks in Mitigating Urban Heat Island Effect: An Example from Addis Ababa. **Landscape and Urban Planning**. 123: 87-95.
- Feyisa, G. L., Meiby, H., Jenerette, G. D., and Pauliet, S. (2016). Locally optimized separability enhancement indices for urban land cover mapping: Exploring environmental consequences of rapid urbanization in Addis Ababa, Ethiopia. **Remote Sensing of Environment**. 175: 14-31.
- French, A. N., Norman, J. M., and Anderson, M. C. (2003). A Simple and Fast Atmospheric Correction for Spaceborne Remote Sensing of Surface Temperature. **Remote Sensing of Environment**. 87: 326-333.
- Fryd, O., Pauleit, S., and Buhler, O. (2011). The Role of Urban Green Space and Trees in Relation to Climate Change. **CAB Reviews: Perspectives in Agriculture, Veterinary Science, Nutrition and Natural Resources**. 6(53): 1-14.
- Ga, Z., NiMa, Y., Jun, J., and CiRen, P. (2011). Characteristics of Urban Heat Island Effect in Lhasa City. **Science in Cold and Arid Regions**. 3(1): 70-77.
- Gaitani, N., Spanou, A., Saliari, M., Synnefa, A., Vassilakopoulou, K., Papadopoulou, K., Pavlou, K., Santamouris, M., Papaioannou, M., and Lagoudaki, A. (2011). Improving the Microclimate in Urban Areas: a Case Study in the Centre of Athens. **Building Services Engineering Research & Technology**. 32(1): 53-71.

- Gao, C., Zhao, E., Li, C., Qian, Y., Ma, L., Tang, L., Jiang, X., and Huo, H. (2015). Study of Aerosol Influence on Nighttime Land Surface Temperature Retrieval Based on Two Methods. **Advances in Meteorology**. 2015. doi:10.1155/2015/496458
- Gercek, D., Guven, I. T., and Oktay, I. C. (2016). *Analysis of the Intra-City Variation of Urban Heat Island and Its Relationship to Land Surface /Cover Parameters*. XXIII ISPRS Congress, Commission VIII Prague, Czech Republic.
- Ghosh, A., and Joshi, P. K. (2014). Hyperspectral Imagery for Disaggregation of Land Surface Temperature with Selected Regression Algorithms over Different Land Use Land Cover Scenes. **ISPRS Journal of Photogrammetry and Remote Sensing**. 96: 76-93.
- Giannopoulou, K., Livada, I., Santamouris, M., Saliari, M., Assimakopoulos, M., and Caouris, Y. G. (2011). On the Characteristics of the Summer Urban Heat Island in Athens, Greece. **Sustainable Cities and Society**. 1: 16-28.
- Gillies, R. R., and Carlson, T. N. (1995). Thermal Remote Sensing of Surface Soil-water Content with Partial Vegetation Cover for Incorporation into Climate Models. **Journal of Applied Meteorology**. 34: 745-756.
- Giridharan, R., Ganesan, S., and Lau, S. S. Y. (2004). Daytime Urban Heat Island Effect in High-Rise and High-Density Residential Developments in Hong Kong. **Energy and Building**. 36: 525-534.
- Giridharan, R., Lau, S. S. Y., Ganesan, S., and Givoni, B. (2008). Lowering the Outdoor Temperature in High-Rise High-Density Residential Developments of Coastal Hong Kong: The Vegetation Influence. **Building and Environment**. 24: 1583-1593.

- Gobakis, K., Kolokotsa, D., Synnefa, A., Saliari, M., Giannopoulou, K., and Santamouris, M. (2011). Development of a Model for Urban Heat Island Prediction Using Neural Network Techniques. **Sustainable Cities and Society**. 1: 104-115.
- Guillevic, P. C., Privette, J. L., Coudert, B., Palecki, M. A., Demarty, J., Otle, C., and Augustine, J. A. (2012). Land Surface Temperature Product Validation Using NOAA's Surface Climate Observation Networks - Scaling Methodology for the Visible Infrared Imager Radiometer Suite (VIIRS). **Remote Sensing of Environment**. 124: 282-298.
- Guo, L. J., and Moore, J. M. (1998). Pixel Block Intensity Modulation: Adding Spatial Detail to TM Band 6 Thermal Imagery. **International Journal of Remote Sensing**. 19(13): 2477-2491.
- Hamada, S., and Ohta, T. (2010). Seasonal Variations in the Cooling Effect of Urban Green Areas on Surrounding Urban Areas. **Urban Forestry and Urban Greening**. 9: 15-24.
- Hamada, S., Tanaka, T., and Ohta, T. (2013). Impacts of Land Use and Topography on the Cooling Effect of Green Areas on Surrounding Urban Areas. **Urban Forestry and Urban Greening**. 12: 426-434.
- Hart, M. A., and Sailor, D. J. (2009). Quantifying the Influence of Land-Use and Surface Characteristics on Spatial Variability in the Urban Heat Island. **Theoretical and Applied Climatology**. 95: 397-406.
- He, J. F., Liu, J. Y., Zhuang, D. F., Zhang, W., and Liu, M. L. (2007). Assessing the Effect of Land Use /Land Cover Change on the Change of Urban Heat Island Intensity. **Theoretical and Applied Climatology**. 90: 217-226.

- Hu, L., and Brunzell, N. A. (2015). A New Perspective to Assess the Urban Heat Island through Remotely Sensed Atmospheric Profiles. **Remote Sensing of Environment**. 158: 393-406.
- Huang, G., Zhou, W., and Cadenasso, M. L. (2011). Is Everyone Hot in the City? Spatial Pattern of Land Surface Temperatures, Land Cover and Neighborhood Socioeconomic Characteristics in Baltimore, MD. **Journal of Environmental Management**. 92: 1753-1759.
- Huete, A. (1988). A Soil-adjusted Vegetation Index (SAVI). **Remote Sensing of Environment**. 25: 295-309.
- Hung, T., Uchihama, D., Ochi, S., and Yasuoka, Y. (2006). Assessment with Satellite Data of the Urban Heat Island Effects in Asian Mega Cities. **International Journal of Applied Earth Observation and Geoinformation**. 8: 34-48.
- Hwang, R. L., Lin, T. P., and Matzarakis, A. (2011). Seasonal Effects of Urban Street Shading on Long-Term Outdoor Thermal Comfort. **Building and Environment**. 46(4): 863-870.
- Imhoff, M. L., Zhang, P., Wolfe, R. E., and Bounoua, L. (2010). Remote Sensing of the Urban Heat Island Effect across Biomes in the Continental USA. **Remote Sensing of Environment**. 114: 504-513.
- Irons, J. R., Dwyer, J. L., and Barsi, J. A. (2012). The Next LANDSAT Satellite: The LANDSAT Data Continuity Mission. **Remote Sensing of Environment**. 122: 11-21.

- Jenerette, G. D., Harlan, S. L., Stefanov, W. L., and Martin, C. A. (2011). Ecosystem Services and Urban Heat Riskscape Moderation: Water, Green Spaces, and Social Inequality in Phoenix, USA. **Journal of Applied Ecology**. 21: 2637-2651.
- Jennings, V., Gaither, C. J., and Gragg, R. S. (2012). Promoting Environmental Justice Through Urban Green Space Access: A Synopsis. **Environmental Justice**. 5(1): 1-7.
- Jim, C. Y., and Chen, S. (2003). Comprehensive Greenspace Planning Based on Landscape Ecology Principles in Compact Nanjing City, China. **Landscape and Urban Planning**. 998: 1-22.
- Jimenez-Munoz, J. C., Cristobal, J., Sobrino, J. A., Soria, G., Ninyerola, M., and Pons, X. (2009). Revision of the Single-Channel Algorithm for Land Surface Temperature Retrieval from LANDSAT Thermal-Infrared Data. **IEEE Transactions on Geoscience and Remote Sensing**. 47(1): 339-349.
- Jimenez-Munoz, J. C., and Sobrino, J. A. (2003). A Generalized Single-Channel Method for Retrieving Land Surface Temperature from Remote Sensing Data. **Journal of Geophysical Research**. 108: 1-9.
- Jimenez-Munoz, J. C., Sobrino, J. A., Skokovic, D., Matter, C., and Cristobal, J. (2014a). Land Surface Temperature Retrieval Methods from LANDSAT-8 Thermal Infrared Sensor Data. **IEEE Geoscience and Remote Sensing Letters**. 11(10): 1840-1843.

- Jimenez-Munoz, J. C., Sobrino, J. A., Skokovic, D., Matter, C., and Cristobal, J. (2014b). Land Surface Temperatures Retrieval Methods from LANDSAT-8 Thermal Infrared Sensor Data. **IEEE Geoscience and Remote Sensing Letters**. 11(10): 1840-1843.
- Jung, H. S., and Park, S. W. (2014). Multi-sensor Fusion of LANDSAT-8 Thermal Infrared (TIR) and Panchromatic (PAN) Images. **Sensors**. 14: 24425-24440.
- Karl, T. R., Diaz, H. F., and Kukla, G. (1988). Urbanization: Its Detection and Effect in the United States Climate Record. **Journal of Climate**. 1: 1099-1123.
- Karlstrom, A., and Ceccato, V. (2002). A New Information Theoretical Measure of Global and Local Spatial Association. **The Review of Regional Research**. 22: 13-40.
- Kawamura, M., Jayamana, S., and Tsujiko, Y. (1996). Relation between Socail and Environmental Conditions in Colombo Sri Lanka and the Urban Index Estimated by Satellite Remote Sensing Data. **International Archives of Photogrammetry and Remote Sensing**. 31: 321-326.
- Keramitsoglou, I., Kiranoudis, G. T., Ceriola, G., Weng, Q., and Rajasekar, U. (2011). Identification and Analysis of Urban Surface Temperature Patterns in Greater Athens, Greece, Using MODIS Imagery. **Remote Sensing of Environment**. 115: 3080-3090.
- Khodakarami, J., and Ghobadi, P. (2016). Urban Pollution and Solar Radiation Impacts. **Renewable and Sustainable Energy Reviews**. 57: 965-976.
- Kikon, N., Singh, P., Singh, S. K., and Vyas, A. (2016). Assessment of Urban Heat Island (UHI) on Noida City, India Using Multi-Temporal Satellite Data. **Sustainable Cities and Society**. 22: 19-28.

- Kong, F., Yin, H., James, P., Hutyra, L. R., and He, H. S. (2014). Effects of Spatial Pattern of Greenspace on Urban Cooling in a Large Metropolitan Area of Eastern China. **Landscape and Urban Planning**. 128: 35-47.
- Koyama, T., Yoshinaga, M., Hayashi, H., and Maeda, K. I. (2013). Identification of Key Plant Traits Contributing to the Cooling Effects of Green Facades Using Freestanding Walls. **Building and Environment**. 66: 96-103.
- Kumar, K. S., Bhaskar, P. U., and Padmakumari, K. (2012). Estimation of Land Surface Temperature to Study Urban Heat Island Effect Using LANDSAT ETM+ Image. **International Journal of Engineering Science and Technology**. 4: 771-778.
- Kuo, B. Y. (2000). **An Analysis of Microclimates in Urban Parks: A Case Study in Taiwan**. (Master), National Cheng Kung University, Taiwan.
- Kustas, W. P., Norman, J. M., Anderson, M. C., and French, A. N. (2003). Estimating Subpixel Surface Temperatures and Energy Fluxes from the Vegetation Index - Radiometric Temperature Relationship. **Remote Sensing of Environment**. 85: 429-440.
- Lauwaet, D., Ridder, K. D., Saeed, S., Brisson, E., Chatterjee, F., Lipzig, N. P. M. v., Maiheu, B., and Hooyberghs, H. (2016). Assessing the Current and Future Urban Heat Island of Brussels. **Urban Climate**. 15: 1-15.
- Leong, Y. P., Chng, L. K., Ong, J., Choo, C. M., and Laili, N. (2015). Preliminary Study of the Impacts of Land Use and Land Cover Change on Land Surface Temperature with Remote Sensing Technique: A Case Study of the Klang Valley and Penang Island, Malaysia. **SEGi Review Journal**. 9: 5-29.

- Li, H., Liu, Q., Zhong, B., Du, Y., Wang, H., and Wang, Q. (2010). *A Single-Channel Algorithm for Land Surface Temperature Retrieval from HJ-1B/IRS Data Based on a Parametric Model*.
- Li, J., Song, C., Cao, L., Zhu, F., Meng, X., and Wu, J. (2011). Impacts of Landscape Structure on Surface Urban Heat Islands: A Case Study of Shanghai, China. **Remote Sensing of Environment**. 115: 3249-3263.
- Li, X., Zhou, W., and Ouyang, Z. (2013). Relationship between Land Surface Temperature and Spatial Pattern of Greenspace: What are the Effects of Spatial Resolution? **Landscape and Urban Planning**. 114: 1-8.
- Li, X., Zhou, W., Ouyang, Z., Xu, W., and Zheng, H. (2012). Spatial Pattern of Greenspace Affects Land Surface Temperature: Evidence from the Heavily Urbanized Beijing Metropolitan Area, China. **Landscape Ecology**. 27: 887-898.
- Li, Z. L., Tang, B. H., Wu, H., Ren, H., Yan, G., Wan, Z., Trigo, I.F., and Sobrino, J. A. (2013). Satellite-Derived Land Surface Temperature: Current Status and Perspective. **Remote Sensing of Environment**. 131: 14-37.
- Liang, S. (2000). Narrowband to Broadband Conversions of Land Surface Albedo Algorithms. **Remote Sensing of Environment**. 76: 213-238.
- Lin, B. S., and Lin, Y. J. (2010). Cooling Effect of Shade Trees with Different Characteristics in a Subtropical Urban Park. **Hortscience**. 45: 83-86.
- Lin, C. Y., Chen, W. C., Chang, P. L., and Sheng, Y. F. (2011). Impact of the Urban Heat Island Effect on Precipitation over a Complex Geographic Environment in Northern Taiwan. **Journal of Applied Meteorology and Climatology**. 50: 339-353.

- Lin, W., Wu, T., Zhang, C., and Yu, T. (2011). Carbon Saving Resulting from the Cooling Effect of Green Areas: A Case Study in Beijing. **Environmental Pollution**. 159: 2148-2154.
- Lin, W., Yu, T., Chang, X., Wu, W., and Zhang, Y. (2015). Calculating Cooling Extents of Green Parks Using Remote Sensing; Method and Test. **Landscape and Urban Planning**. 134: 66-75.
- Liu, D., and Pu, R. (2008). Downscaling Thermal Infrared Radiance for Subpixel Land Surface Temperature Retrieval. **Sensors**. 8: 2695-2706.
- Liu, L., and Zhang, Y. (2011). Urban Heat Island Analysis Using the LANDSAT TM Data and ASTER Data: A Case Study in Hong Kong. **Remote Sensing**. 3: 1535-1552.
- Liu, Y., Hiyama, T., and Yamaguchi, Y. (2006). Scaling of Land Surface Temperature Using Satellite Data: A Case Examination on ASTER and MODIS Products over a Heterogeneous Terrain Area. **Remote Sensing of Environment**. 105: 115-128.
- Lu, D., and Weng, Q. (2006). Spectral Mixture Analysis of ASTER Images for Examining the Relationship between Urban Thermal Features and Biophysical Descriptors in Indianapolis, Indiana, USA. **Remote Sensing of Environment**. 104: 157-167.
- Mackey, C. W., Lee, X., and Smith, R. B. (2012). Remote Sensing the Cooling Effects of City Scale Effort to Reduce Urban Heat Island. **Building and Environment**. 49: 348-358.

- Mahmuda, S., and Webb, R. (2016). Climate Adaptation and Urban Planning for Heat Islands: A Case Study of the Australian Capital Territory. **Australian Planner**. 53(2): 127-142.
- Mailman school of public health. (n.d.). **Hot Spot Detection** [On-line]. Available: <https://www.mailman.columbia.edu/research/population-health-methods/hot-spot-detection>.
- Maimaitiyming, M. (2013). **Effects of Spatial Pattern of Greenspace on Land Surface Temperature: A Case Study of Oasis Aksu, North-West China**. (Master of Science in Geospatial Technologies), Universidade Nova de Lisboa.
- Mallick, J., Singh, C. K., Shashtri, S., Rahman, A., and Mukherjee, S. (2012). Land Surface Emissivity Retrieval Based on Moisture Index from LANDSAT TM Satellite Data over Heterogeneous Surfaces of Delhi City. **International Journal of Applied Earth Observation and Geoinformation**. 19: 348-358.
- Mao, K., Qin, Z., Shi, J., and Gong, P. (2005). A Practical Split-Window Algorithm for Retrieving Land Surface Temperature from MODIS Data. **International Journal of Remote Sensing**. 26(15): 3181-3204.
- Masek, J. G., Lindsay, F. E., and Goward, S. N. (2000). Dynamics of Urban Growth in the Washington DC Metropolitan Area, 1973-1996, from LANDSAT Observations. **International Journal of Remote Sensing**. 21(18): 3473-3486.
- Matson, M., McClain, E. P., McGinnis, D. F., and Pritchard, H. A. (1978). Satellite Detection of Urban Heat Islands. **Monthly Weather Review**. 106: 1725-1734.
- Matzarakis, A., Rutz, F., and Mayer, H. (2007). Modelling Radiation Fluxes in Simple and Complex Environments - Application of the RayMan Model. **International Journal of Biometeorology**. 51(4): 323-334.

- McFeeters, S. K. (1996). The Use of the Normalized Difference Water Index (NDWI) in the Delineation of Open Water Features. **International Journal of Remote Sensing**. 17(7): 1425-1432.
- McMillin, L. M. (1975). Estimation of Sea Surface Temperatures from Two Infrared Window Measurements with Different Absorption. **Journal of Geophysical Research**. 80: 5113-5117.
- Mukherjee, S., Joshi, P. K., and Garg, R. D. (2014). A Comparison of Different Regression Models for Downscaling LANDSAT and MODIS Land Surface Temperature Images over Heterogeneous Landscape. **Advances in Space Research**. 54: 655-669.
- Murphy, S. (2015). **Assessing the Effectiveness of Extensive Green Roofs at Improving Environmental Conditions in Atlanta, Georgia**. (Master of Science), Georgia State University.
- Ng, E., Chen, L., Wang, Y., and Yuan, C. (2012). A Study on the Cooling Effects of Greening in a High-Density City: An Experience from Hong Kong. **Building and Environment**. 47: 256-271.
- Ng, E., Yuan, C., Chen, L., Ren, C., and Fung, J. C. H. (2011). Improving the Wind Environment in High-Density Cities by Understanding Urban Morphology and Surface Roughness: A Study in Hong Kong. **Landscape and Urban Planning**. 101: 59-74.
- Ngie, A., Abutaleb, K., Ahmed, F., Darwish, A., and Ahmed, M. (2014). Assessment of Urban Heat Island Using Satellite Remotely Sensed Imagery: a Review. **South African Geographical Journal**. doi:10.1080/03736245.2014.924864

- Nichol, J. (2009). An Emissivity Modulation Method for Spatial Enhancement of Thermal Satellite Images in Urban Heat Island Analysis. **Photogrammetric Engineering and Remote Sensing**. 75(5): 547-556.
- Nichol, J., and Wong, M. S. (2005). Urban Vegetation Monitoring in Hong Kong Using High Resolution Multispectral Images. **International Journal of Remote Sensing**. 26(5): 903-918.
- Nichol, J. E. (1996). High-Resolution Surface Temperature Patterns Related to Urban Morphology in a Tropical City: A Satellite-Base Study. **Journal of Applied Meteorology**. 35: 135-146.
- Nichol, J. E., and Wong, M. S. (2008). Spatial Variability of Air Temperature and Appropriate Resolution for Satellite-Derived Air Temperature Estimation. **International Journal of Remote Sensing**. 29(24): 7213-7223.
- Norton, B. A., Coutts, A. M., Livesley, S. J., Harris, R. J., Hunter, A. M., and Williams, N. S. G. (2015). Planning for Cooler Cities: A Framework to Prioritise Green Infrastructure to Mitigate High Temperatures in Urban Landscape. **Landscape and Urban Planning**. 134: 127-138.
- Oke, T. R. (1976). The Distinction between Canopy and Boundary-Layer Urban Heat Islands. **Atmosphere**. 14(4): 268-277.
- Oke, T. R. (1988). **Boundary Layer Climates** (2nd ed.). London, New York: Methuen & Co. Ltd. and Methuen, Inc.
- Oliveira, S., Andrade, H., and Vaz, T. (2011). The Cooling Effect of Green Spaces as a Contribution to the Mitigation of Urban Heat: A Case Study in Lisbon. **Building and Environment**. 46: 2186-2194.

- Onishi, A., Cao, X., Ito, T., Shi, F., and Imura, H. (2010). Evaluating the Potential for Urban Heat Island Mitigation by Greening Parking Lots. **Urban Forestry and Urban Greening**. 9: 323-332.
- Ord, J. K., and Getis, A. (1995). Local Spatial Autocorrelation Statistics: Distributional Issues and an Application. **Geographical Analysis**. 27(4): 286-306.
- Pan, X., Zhu, X., Yang, Y., Cao, C., Zhang, X., and Shan, L. (2018). Applicability of Downscaling Land Surface Temperature by Using Normalized Difference Sand Index. **Scientific Reports**. 8(1): 1-14.
- Perini, K., and Magliocco, A. (2014). Effects of Vegetation, Urban Density, Building Height, and Atmospheric Conditions on Local Temperatures and Thermal Comfort. **Urban Forestry and Urban Greening**. 13(3): 1-12.
- Prasannakumar, V., Vijith, H., Charutha, R., and Geetha, N. (2011). Spatio-Temporal Clustering of Road Accidents: GIS based Analysis and Assessment. **Procedia Social and Behavioral Sciences**. 21: 317-325.
- Price, J. C. (1983). Estimating Surface Temperatures from Satellite Thermal Infrared Data - A Simple Formulation for the Atmospheric Effect. **Remote Sensing of Environment**. 13(4): 353-361.
- Price, J. C. (1984). Land Surface Temperature Measurements from the Split-Window Channels of the NOAA-7 Advanced Very High Resolution Radiometer. **Journal of Geophysical Research**. 89: 7231-7237.
- Qin, Z., Karnieli, A., and Berliner, P. (2001). A Mono-Window Algorithm for Retrieving Land Surface Temperature from LANDSAT TM Data and Its Application to the Israel-Egypt Border Region. **International Journal of Remote Sensing**. 22(18): 3719-3746.

- Rajagopalan, P., Lim, K. C., and Jamei, E. (2014). Urban Heat Island and Wind Flow Characteristics of a Tropical City. **Solar Energy**. 107: 159-170.
- Ren, Y., Deng, L. Y., Zuo, S. D., Song, X. D., Liao, Y. L., Xu, C. D., Chen, Q., Hua, L.Z., and Li, Z. W. (2016). Quantifying the Influences of Various Ecological Factors on Land Surface Temperature of Urban Forests. **Environment Pollution**. 216: 519-529.
- Ren, Z., He, X., Zheng, H., Zhang, D., Yu, X., Shen, G., and Guo, R. (2013). Estimation of the Relationship between Urban Park Characteristics and Park Cool Island Intensity by Remote Sensing Data and Field Measurement. **Forests**. 4: 868-886.
- Rikimaru, A., and Miyatake, S. (1997, 20-25 October 1997). **Development of Forest Canopy Density Mapping and Monitoring Model Using Indices of Vegetation, Bare Soil and Shadow**. Paper presented at the 18th Asian Conference on Remote Sensing (ACRS), Kuala Lumpur, Malaysia.
- Rinner, C., and Hussain, M. (2011). Toronto's Urban Heat Island - Exploring the Relationship between Land Use and Surface Temperature. **Remote Sensing**. 3: 1251-1265.
- Rodriguez-Galiano, V., Pardo-Iguzquiza, E., Sanchez-Castillo, M., Chica-Olmo, M., and Chica-Rivas, M. (2012). Downscaling LANDSAT-7 ETM+ Thermal Imagery Using Land Surface Temperature and NDVI Images. **International Journal of Applied Earth Observation and Geoinformation**. 18: 515-527.
- Rouse, J. W., Haas, R. H., Schell, J. A., Deering, D. W., and Harlan, J. C. (1974). Monitoring the Vernal Advancement and Retrogradation (Greenwave effect) of Natural Vegetation. **NASA/GSFC Type III Final Report**: 371p.

- Rozenstein, O., Qin, Z., Derimian, Y., and Karnieli, A. (2014). Derivation of Land Surface Temperature for LANDSAT-8 TIRS Using a Split-Window Algorithm. **Sensors**. 14: 5768-5780.
- Sattari, F., Hashim, M., and Pour, A. B. (2018). Thermal Sharpening of Land Surface Temperature Maps Based on the Impervious Surface Index with the TsHARP Method to ASTER Satellite Data: A Case Study from the Metropolitan Kuala Lumpur, Malaysia. **Measurement**. 125: 262-278.
- Schmugge, T., Hook, S. J., and Coll, C. (1998). Recovering Surface Temperature and Emissivity from Thermal Infrared Multispectral Data. **Remote Sensing of Environment**. 65(2): 121-131.
- Schwarz, N., Schlink, U., Franck, U., and GroBmann, K. (2012). Relationship of Land Surface and Air Temperatures and Its Implications for Quantifying Urban Heat Island Indicators: An Application for the City of Leipzig (Germany). **Ecological Indicators**. 18: 693-704.
- Scott, N. A., and Chedin, A. (1981). A Fast Line-by-Line Method for Atmospheric Absorption Computations: The Automatized Atmospheric Absorption Atlas. **Journal of Applied Meteorology**. 20: 802-812.
- Shashua-Bar, L., Pearlmutter, D., and Erell, E. (2009). The Cooling Efficiency of Urban Landscape Strategies in a Hot Dry Climate. **Landscape and Urban Planning**. 92: 179-186.
- Shashua-Bar, L., Tsiros, I. X., and Hoffman, M. E. (2010). A Modeling Study for Evaluating Passive Cooling Scenarios in Urban Streets with Trees: Case Study Athens, Greece. **Building and Environment**. 45(12): 2798-2807.

- Shashua-Bar, L., Tsiros, L. X., and Hoffman, M. (2012). Passive Cooling Design Options to Ameliorate Thermal Comfort in Urban Streets of a Mediterranean Climate (Athens) under Hot Summer Conditions. **Building and Environment**. 57: 110-119.
- Shen, H., Huang, L., Zhang, L., Wu, P., and Zeng, C. (2016). Long-Term and Fine-Scale Satellite Monitoring of the Urban Heat Island Effect by the Fusion of Multi-Temporal and Multi-Sensor Remote Sensed Data: A 26-Years Case Study of the City of Wuhan in China. **Remote Sensing of Environment**. 172: 109-125.
- Shepherd, J. M., Pierce, H., and Negri, A. J. (2002). Rainfall Modification by Major Urban Areas: Observations from Spaceborne Rain RADAR on the TRMM Satellite. **Journal of Applied Meteorology**. 41: 689-701.
- Simo, G., Garcia-Santos, V., Jimenez, M. A., Marinez-Villagrasa, D., Picos, R., Caselles, V., and Cuxart, J. (2016). LANDSAT and Local Land Surface Temperatures in a Heterogeneous Terrain Compared to MODIS Values. **Remote Sensing**. 8: 1-14.
- Skokovic, D., Sobrino, J. A., Jimenez-Munoz, J. C., Soria, G., Julien, Y., Matter, C., and Cristobal, J. (2014). Calibration and Validation of Land Surface Temperature for LANDSAT-8 TIRS Sensor. Retrieved from https://earth.esa.int/documents/700255/2126408/ESA_Lpve_Sobrino_2014a.pdf
- Small, C. (2006). Comparative Analysis of Urban Reflectance and Surface Temperature. **Remote Sensing of Environment**. 104: 168-189.

- Sobrino, J. A., Jimenez-Munoz, J. C., and Paolini, L. (2004). Land Surface Temperature Retrieval from LANDSAT TM 5. **Remote Sensing of Environment**. 90: 434-440.
- Sobrino, J. A., Oltra-Carrio, R., Soria, G., Bianchi, R., and Paganini, M. (2012). Impact of Spatial Resolution and Satellite Overpass Time on Evaluation of the Surface Urban Heat Island Effects. **Remote Sensing of Environment**. 117: 50-56.
- SPSS Tutorials. (2019). **Pearson Correlations – Quick Introduction** [On-line]. Available: https://www.spss-tutorials.com/pearson-correlation-coefficient/?fbclid=IwAR28XTI84xJcC5Kz80-qyHO6IDNANRMcT0fSuXPXFRRgwNYI_FtGdPX-0BU.
- Srivanit, M., and Kazunori, H. (2011). The Influence of Urban Morphology Indicators on Summer Diurnal Range of Urban Climate in Bangkok Metropolitan Area, Thailand. **International Journal of Civil & Environmental Engineering**. 11(5): 34-46.
- Stabler, L. B., Martin, C. A., and Brazel, A. J. (2005). Microclimates in a Desert City were Related to Land Use and Vegetation Index. **Urban Forestry and Urban Greening**. 3: 137-147.
- Stathopoulou, M., and Cartalis, C. (2007). Daytime Urban Heat Islands from LANDSAT ETM+ and Corine Land Cover Data: An Application to Major Cities in Greece. **Solar Energy**. 81: 358-368.
- Stathopoulou, M., and Cartalis, C. (2009). Downscaling AVHRR Land Surface Temperatures for Improved Surface Urban Heat Island Intensity Estimation. **Remote Sensing of Environment**. 113: 2592-2605.

- Steeneveld, G. J., Koopmans, S., Heusinkveld, B. G., Hove, L. W. A. V., and Holtslag, A. A. M. (2011). Quantifying Urban Heat Island Effects and Human Comfort for Cities of Variable Size and Urban Morphology in the Netherlands. **Journal of Geophysical Research: Atmosphere (1984-2012)**. 116(D20129).
- Steeneveld, G. J., Koopmans, S., Heusinkveld, B. G., and Theeuwes, N. E. (2014). Refreshing the Role of Open Water Surfaces on Mitigating the Maximum Urban Heat Island Effect. **Landscape and Urban Planning**. 121: 92-96.
- Stewart, I., and Oke, T. (2006). *Methodological Concerns Surrounding the Classification of Urban and Rural Climate Stations to Define Urban Heat Island Magnitude*. 6th International Conference on Urban Climate, Goteborg, Sweden.
- Stewart, I. D., and Oke, T. R. (2012). Local Climate Zones for Urban Temperature Studies. **Bull Am Meteorol Soc**. 93(12): 1879-1900.
- Streutker, D. R. (2002). A Remote Sensing Study of the Urban Heat Island of Houston, Texas. **International Journal of Remote Sensing**. 23(13): 2595-2608.
- Sun, R., Chen, A., Chen, L., and Lu, Y. (2012). Cooling Effects of Wetlands in an Urban Region: The Case of Beijing. **Ecological Indicators**. 20: 57-64.
- Taha, H. (1997). Urban Climates and Heat Islands: Albedo, Evapotranspiration, and Anthropogenic Heat. **Energy and Buildings**. 25: 99-103.
- Taha, H. (2015). Meteorological, Emissions and Air-Quality Modeling of Heat-Island Mitigation: REcent Findings for California, USA. **Sustainable Cities and Society**. 19: 207-221.

Tan, J., Zheng, Y., Tang, X., Guo, C., Li, L., Song, G., Zhen, X., Yuan, D., Kalkstein, A.J., Li, F., and Chen, H. (2010). The Urban Heat Island and Its Impact on Heat Waves and Human Health in Shanghai. **International Journal of Biometeorology**. 54: 75-84.

The Bureau of Registration Administration. (2018). **Official Statistics Registration Systems** [On-line]. Available: <http://stat.bora.dopa.go.th/stat/statnew/statTDD/>.

Thomas, G., and Zachariah, E. J. (2011). Urban Heat Island in a Tropical City Interlaced by Wetlands. **Journal of Environmental Science and Engineering**. 5: 234-240.

Thundiyl, K. A. (2003). **Rising Temperatures and Expanding Megacities: Improving Air Quality in Mexico City through Urban Heat Island Mitigation**. (Master in City Planning), Massachusetts Institute of Technology.

Tian, Z., Li, S., Zhang, J., and Guo, Y. (2013). The Characteristic of Heat Wave Effects on Coronary Heart Disease Mortality in Beijing, China: A Time Series Study. **PLoS One**. 8(9).

Tomlinson, C. J., Chapman, L., Thornes, J. E., and Baker, C. J. (2011). Including the Urban Heat Island in Spatial Heat Health Risk Assessment Strategies: A Case Study for Birmingham, UK. **International Journal of Health Geographics**. 10(42): 1-14.

Tourism Authority of Thailand. (2017). **Buriram** [On-line]. Available: <https://www.tourismthailand.org/About-Thailand/Destination/Buri-Ram>.

- Tran, D. X., Pla, F., Latorre-Carmona, P., Myint, S. W., Caetano, M., and Kieu, H. V. (2017). Characterizing the relationship between land use and land cover change and land surface temperature. **ISPRS Journal of Photogrammetry and Remote Sensing**. 124: 119-132.
- United States Environmental Protection Agency. (2017a). **Heat Island Impacts** [On-line]. Available: <https://www.epa.gov/heat-islands/heat-island-impacts>.
- United States Environmental Protection Agency. (2017b). Reducing Urban Heat Islands: Compendium of Strategies - Green Roofs. Retrieved from <https://www.epa.gov/sites/production/files/2014-06/documents/greenroofscompendium.pdf>
- United States Geological Survey. (2018a). **Using the USGS Landsat 8 Product** [On-line]. Available: <https://landsat.usgs.gov/using-usgs-landsat-8-product>.
- United States Geological Survey. (2018b). **What are the band designations for the Landsat satellites?** [On-line]. Available: <https://landsat.usgs.gov/what-are-band-designations-landsat-satellites>.
- Uysal, M., and Polat, N. (2015). An Investigation of the Relationship between Land Surface Temperatures and Biophysical Indices Retrieved from LANDSAT TM in Afyonkarahisar (Turkey). **Technical Gazette**. 22(1): 177-181.
- Van, T. T., and Bao, H. D. X. (2008). A Study on Urban Development through Land Surface Temperature by Using Remote Sensing: in Case of Ho Chi Min City. **VNU Journal of Science, Earth Science**. 24: 160-167.
- Van, T. T., and Bao, H. D. X. (2010). Study of the Impact of Urban Development on Surface Temperature Using Remote Sensing in Ho Chi Minh City, Northern Vietnam. **Geographical Research**. 48(1): 86-96.

- Vaneckova, P., Beggs, P. J., Dear, R. J. d., and McCracken, K. W. J. (2008). Effect of Temperature on Mortality during the Six Warmer Months in Sydney, Australia, between 1993 and 2004. **Environmental Research**. 108: 361-369.
- Vannier, C., Vasseur, C., Hubert-Moy, L., and Baudry, J. (2011). Multiscale Ecological Assessment of Remote Sensing Images. **Landscape Ecology**. 26(8): 1053-1069.
- Vazquez, D. P., Reyes, F. J. O., and Arboledas, L. A. (1997). A Comparative Study of Algorithms for Estimating Land Surface Temperature from AVHRR Data. **Remote Sensing of Environment**. 62: 215-222.
- Vidrih, B., and Medved, S. (2013). Multiparametric Model of Urban Park Cooling Island. **Urban Forestry and Urban Greening**. 12: 220-229.
- Vlassova, L., Perez-Cabello, F., Nieto, H., Martin, P., Riano, D., and Riva, J. d. I. (2014). Assessment of Methods for Land Surface Temperature Retrieval from LANDSAT-5 TM Images Applicable to Multiscale Tree-Grass Ecosystem Modeling. **Remote Sensing**. 6: 4345-4368.
- Voogt, J. A. (2004). **Urban Heat Islands: Hotter Cities** [On-line]. Available: <http://www.actionbioscience.org/environment/voogt.html>.
- Voogt, J. A., and Oke, T. R. (2003). Thermal Remote Sensing of Urban Climates. **Remote Sensing of Environment**. 86: 370-384.
- Walawender, J. P., Szymanowski, M., Hajto, M. J., and Bokwa, A. (2014). Land Surface Temperature Patterns in the Urban Agglomeration of Krakow (Poland) Derived from LANDSAT-7 ETM+ Data. **Pure and Applied Geophysics**. 171: 913-940.

- Wang, F., Qin, Z., Song, C., Tu, L., Karnieli, A., and Zhao, S. (2015). An Improved Mono-Window Algorithm for Land Surface Temperature Retrieval from LANDSAT-8 Thermal Infrared Sensor Data. **Remote Sensing**. 7: 4268-4289.
- Wang, Y. J., Tian, F., Huang, Y., Wang, J., and Wei, C. J. (2015). Monitoring Coal Fires in Datong Coalfield Using Multi-source Remote Sensing Data. **The Transactions of Nonferrous Metals Society of China**. 25: 3421-3428.
- Weng, Q. (2001). A Remote Sensing-GIS Evaluation of Urban Expansion and Its Impact on Surface Temperature in the Zhujiang Delta, China. **International Journal of Remote Sensing**. 22: 1999-2014.
- Weng, Q. (2009). Thermal Infrared Remote Sensing for Urban Climate and Environmental Studies: Methods, Applications, and Trends. **ISPRS Journal of Photogrammetry and Remote Sensing**. 64: 335-344.
- Weng, Q., and Fu, P. (2014). Modeling Annual Parameters of Clear-sky Land Surface Temperature Variations and Evaluating the Impact of Cloud Cover Using Time Series of LANDSAT TIR Data. **Remote Sensing of Environment**. 140: 267-278.
- Weng, Q., Fu, P., and Gao, F. (2014). Generating Daily Land Surface Temperature at LANDSAT Resolution by Fusing LANDSAT and MODIS Data. **Remote Sensing of Environment**. 145: 55-67.
- Weng, Q., Lu, D., and Schubring, J. (2004). Estimation of Land Surface Temperature - Vegetation Abundance Relationship for Urban Heat Island Studies. **Remote Sensing of Environment**. 89: 467-483.

- Weng, Q., and Quattrochi, D. (2006). Thermal Remote Sensing of Urban Areas: An Introduction to the Special Issue. **Remote Sensing of Environment**. 104: 119-122.
- Wibowo, A., Kuswanto, Ardiansyah, Rustanto, A., and Shidiq, I. P. A. (2016). *Spatial Temporal Analysis of Urban Heat Hazard in Tangerang City*. IOP Conference Series: Earth and Environmental Science.
- Wilson, E. H., and Sader, S. A. (2002). Detection of Forest Harvest Type Using Multiple-dates of LANDSAT-TM Imagery. **Remote Sensing of Environment**. 80: 385-396.
- Wilson, S. M. (2009). An Ecological Framework to Study and Address Environmental Justice and Community Health Issues. **Environmental Justice**. 2(1): 15-23.
- Wu, C. D., Lung, S. C. C., and Jan, J. F. (2013). Development of a 3D Urbanization Index Using Digital Terrain Models for Surface Urban Heat Island Effects. **ISPRS Journal of Photogrammetry and Remote Sensing**. 81: 1-11.
- Wu, R. (1999). The Classification of Green Space System. **Chinese Horticulture**. 15(6): 26-32.
- Xu, H. (2006). Modification of Normalized Difference Water Index (NDWI) to Enhance Open Water Features in Remotely Sensed Imagery. **International Journal of Remote Sensing**. 27(14): 3025-3033.
- Xu, H. (2008). A New Index for Delineating Built-up Land Features in Satellite Imagery. **International Journal of Remote Sensing**. 29(14): 4269-4276.

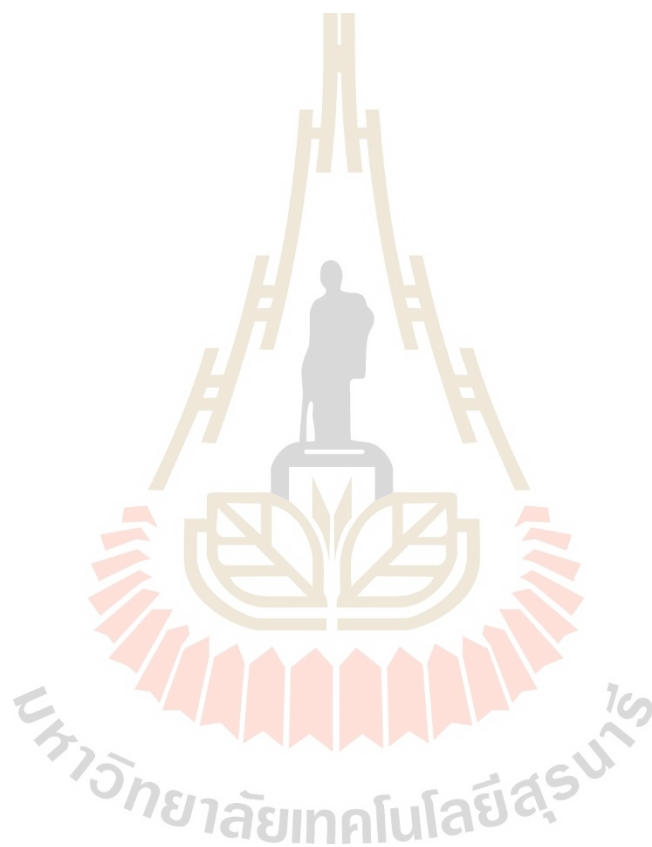
- Xu, H. (2010). Analysis of Impervious Surface and Its Impact on Urban Heat Environment Using the Normalized Difference Impervious Surface Index (NDISI). **Photogrammetric Engineering and Remote Sensing**. 76(5): 557-565.
- Xu, H., Chen, Y., Dan, S., and Qiu, W. (2011). Dynamical Monitoring and Evaluation Methods to Urban Heat Island Effects Based on RS & GIS. **Procedia Environmental Science**. 10: 1228-1237.
- Xu, H., Dan, B., Dan, S., and Lu, Z. (2009). *Analysis of Day-Night Characteristics of Urban Heat Island Effects in Chengdu Based on NOAA AVHRR in Winter*. 2009 Joint Urban Remote Sensing Event.
- Xu, Y., Qin, Z., and Wan, H. (2010). Spatial and Temporal Dynamics of Urban Heat Island and Their Relationship with Land Cover Changes in Urbanization Process: A Case Study in Suzhou, China. **Journal of the Indian Society of Remote Sensing**. 38(4): 654-663.
- Yang, G., Pu, R., Zhao, C., Huang, W., and Wang, J. (2011). Estimation of Subpixel Land Surface Temperature Using an Endmember Index Based Technique: A Case Examination on ASTER and MODIS Temperature Products over a Heterogeneous Area. **Remote Sensing of Environment**. 115: 1202-1219.
- Yang, J., Wong, M. S., Menenti, M., and Nichol, J. (2015). Study of the Geometry Effect on Land Surface Temperature Retrieval in Urban Environment. **ISPRS Journal of Photogrammetry and Remote Sensing**. 109: 77-87.
- Yang, Y., Cao, C., Pan, X., Li, X., and Zhu, X. (2017). Downscaling Land Surface Temperature in an Arid Area by Using Multiple Remote Sensing Indices with Random Forest Regression. **Remote Sensing**. 9(8): 1-18.

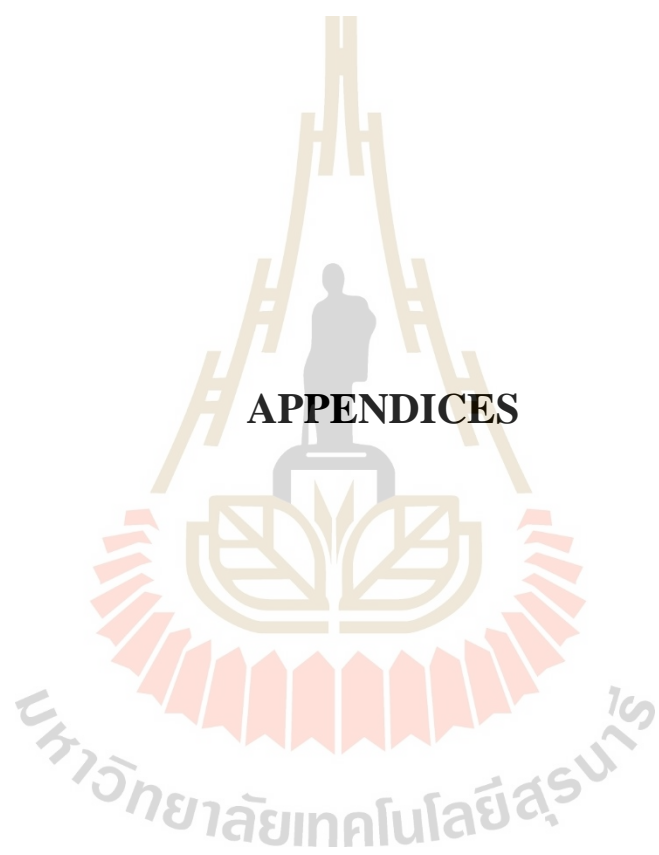
- Yang, Y., Li, X., Pan, X., Zhang, Y., and Cao, C. (2017). Downscaling Land Surface Temperature in Complex Regions by Using Multiple Scale Factors with Adaptive Thresholds. **Sensors**. 17: 1-22.
- Yu, C., and Hien, W. N. (2006). Thermal Benefits of City Parks. **Energy and Building**. 38: 105-120.
- Yuan, F., and Bauer, M. E. (2007a). Comparison of Impervious Surface Area and Normalized Difference Vegetation Index as Indicators of Surface Urban Heat Island Effects in LANDSAT Imagery. **Remote Sensing of Environment**. 106(3): 375-386.
- Yuan, F., and Bauer, M. E. (2007b). Comparison of Impervious Surface Area and Normalized Difference Vegetation Index as Indicators of Surface Urban Heat Island Effects in LANDSAT Imagery. **Remote Sensing of Environment**. 106: 375-386.
- Zaksek, K., and Ostir, K. (2012). Downscaling Land Surface Temperature for Urban Heat Island Diurnal Cycle Analysis. **Remote Sensing of Environment**. 117: 114-124.
- Zha, Y., Gao, J., and Ni, S. (2003). Use of Normalized Difference Built-up Index in Automatically Mapping Urban Areas from TM Imagery. **International Journal of Remote Sensing**. 24(3): 583-594.
- Zhan, W., Chen, Y., Wang, J., Zhou, J., Quan, J., Liu, W., and Li, J. (2012). Downscaling Land Surface Temperatures with Multi-spectral and Multi-resolution Images. **International Journal of Applied Earth Observation and Geoinformation**. 18: 23-36.

- Zhan, W., Chen, Y., Zhou, J., Wang, J., Liu, W., Voogt, J., . . . Li, J. (2013). Disaggregation of Remotely Sensed Land Surface Temperature: Literature Survey, Taxonomy, Issues, and Caveats. **Remote Sensing of Environment**. 131: 119-139.
- Zhang, H., Qi, Z. F., Ye, X. Y., Cai, Y. B., Ma, W. C., and Chen, M. N. (2013). Analysis of Land Use /Land Cover Change, Population Shift, and Their Effects on Spatiotemporal Patterns of Urban Heat Islands in Metropolitan Shanghai, China. **Applied Geography**. 44: 121-133.
- Zhang, J., Wang, Y., and Li, Y. (2006). A C++ Program for Retrieving Land Surface Temperature from the Data of LANDSAT TM /ETM+ Band 6. **Computers & Geosciences**. 32: 1796-1805.
- Zhang, X. X., Wu, P. F., and Chen, B. (2010). Relationship between Vegetation Greenness and Urban Heat Island Effect in Beijing City of China. **Procedia Environmental Science**. 2: 1438-1450.
- Zhang, Z., Lv, Y., and Pan, H. (2013). Cooling and Humidifying Effect of Plant Communities in Subtropical Urban Parks. **Urban Forestry and Urban Greening**. 12: 323-329.
- Zhao, H. M., and Chen, X. (2005, 25-29 July 2005). **Use of Normalized Difference Bareness Index in Quickly Mapping Bare Areas from TM /ETM+**. Paper presented at the IEEE International Geoscience and Remote Sensing Symposium, Seoul, Korea.
- Zhou, D., Zhao, S., Liu, S., Zhang, L., and Zhu, C. (2014). Surface Urban Heat Island in China's 32 Major Cities: Spatial Patterns and Drivers. **Remote Sensing of Environment**. 152: 51-61.

- Zhou, J., Chen, Y., Wang, J., and Zhan, W. (2011). Maximum Nighttime Urban Heat Island (UHI) Intensity Simulation by Integrating Remotely Sensed Data and Meteorological Observation. **IEEE Journal of Selected Topics in Applied Earth Observations and Remote Sensing**. 4(138-146).
- Zhou, J., Liu, S., Li, M., Zhan, W., Xu, Z., and Xu, T. (2016). Quantification of the Scale Effect in Downscaling Remotely Sensed Land Surface Temperature. **Remote Sensing**. 8: 1-24.
- Zhou, W., Huang, G., and Cadenasso, M. L. (2011). Does Spatial Configuration Matter? Understanding the Effects of Land Cover Pattern on Land Surface Temperature in Urban Landscapes. **Landscape and Urban Planning**. 102: 54-63.
- Zhou, W., Qian, Y., Li, X., Li, W., and Han, L. (2014). Relationships between Land Cover and the Surface Urban Heat Island: Seasonal Variability and Effects of Spatial and Thematic Resolution of Land Cover Data on Predicting Land Surface Temperatures. **Landscape Ecology**. 29: 153-167.
- Zhu, S., Guan, H., Millington, A. C., and Zhang, G. (2013). Disaggregation of Land Surface Temperature over a Heterogeneous Urban and Surrounding Suburban Area: A Case Study in Shanghai, China. **International Journal of Remote Sensing**. 34(5): 1707-1723.
- Zinzi, M., and Agnoli, S. (2012). Cool and Green Roofs: An Energy and Comfort Comparison between Passive Cooling and Mitigation Urban Heat Island Techniques for Residential Buildings in the Mediterranean Region. **Energy and Building**. 55: 66-76.

Zupancic, T., Westmacott, C., and Bulthuis, M. (2015). **The Impact of Green Space on Heat and Air Pollution in Urban Communities: A Meta-Narrative System Review** [On-line]. Available: <http://www.davidsuzuki.org/publications/reports/2015/the-impact-of-green-space-on-heat-and-air-pollution-in-urban-communities/>.





APPENDICES

APPENDIX A

RELATIONSHIP BETWEEN ESTIMATED LST DATA

USING THE OPTIMUM METHOD

AND GROUND-BASED TEMPERATURE DATA

To explore the relationship between the estimated LST data using the optimum method and ground-based temperature data, the Pearson correlation was applied. The results of this process were shown in Table A.1.

Table A.1 The Pearson correlation coefficients.

	January 21, 2018	February 6, 2018	March 26, 2018	April 11, 2018
R-values	0.629	0.459	0.420	0.680

Based on Table A.1, it is found that the estimated LST data in January 21, and April 11, 2018, have modulate positive correlation to ground-based temperature data (R-values are higher than 0.500). While the estimated LST data in February 6, and March 26, 2018, have low positive correlation to ground-based temperature data (R-values are less than 0.500). The error based on SW algorithm, despite the water vapour content data, and also the coefficients in algorithm, may affect the correlation of these two variables. Also, the modulate spatial resolution of LANDSAT-8 TIRS bands cannot separate the objects within the coverage areas of spatial resolution as well, especially, the complex area as urban areas, where comprises with various LULC types. Lastly, the limitations in ground-based temperature surveying period, as mentioned in scope

and limitations of the study, also provide the error to the results. Also, the surface temperature relates to the top surface temperature of materials, such as rooftop of buildings and canopy layers of trees. Due to the limitation in temperature measuring, the temperature of these parts of materials cannot be measured.



APPENDIX B

THE REGRESSION MODEL BASED ON MULTIPLE DATE DATA IN 2018

The multiple date data in 2018, which were obtained in January 21, February 6, March 26, and April 11, were used together in regression modeling. Then, the subpixel LST data were estimated using the obtained regression model. The subpixel LST data were compared with ground-based temperature data to calculate the NRMSE values afterwards. The regression statistics based on the multiple date data in 2018 and the NRMSE values were shown in Table B.1 and Table B.2, respectively.

Table B.1 Regression statistics based on multiple date data in 2018.

R	R ²	Adjusted R ²	Equation
0.925	0.855	0.855	25.231 + 7.116 NDISI + 75.824 IBI + 51.586 AB + 22.346 BI - 8.867 UI + 243.918 MNDWI + 88.061 NDVI + 86.272 SAVI - 112.349 NDWI - 32.551 NDBaI

The regression model, which provides the highest R, R², and adjusted R² values, comprises of 10 variables, namely NDISI, IBI, albedo, BI, UI, MNDWI, NDVI, SAVI, NDWI, and NDBaI as shown in Table B.1. It is found that the NDISI, surface albedo, and MNDWI are still included in the model. While NDBI, FVC, and NDMI are excluded in the model. As same as a study by Essa, Verbeiren, Kwast, Voorde and Batelaan (2012), it showed that the extract built-up land information using NDBI is often mixed with noise caused by vegetation within the urban fabric. The FVC has a

high relationship with NDVI, because NDVI is used in FVC calculation. Lastly, Essa et al. (2012) reported that NDMI contains information about moisture and vegetation.

Table B.2 NRMSE values.

Data	NRMSE values		
	LST	Subpixel LST (Monthly models)	Subpixel LST (Multiple date data in 2018)
January 21, 2018	0.227	0.201	0.561
February 6, 2018	0.473	0.266	0.791
March 26, 2018	0.218	0.188	0.540
April 11, 2018	0.132	0.110	0.423

It is found that the monthly regression models provides a better results than the regression model regarding the multiple date data in 2018, as shown in Table B.2. Due to the regression model, which is based on the multiple date data in 2018, is comprised of the most variables. Some variables do not affect the LST data estimation in some cases, however, when compared with the variables in monthly models. Therefore, the insignificant variables may provide the error to the results.

APPENDIX C

SUPPLEMENTARY DATA

This appendix reports more associated details in Chapter 4, namely, the proportional LULC in the selected hotspot locations as shown in Tables C.1 - C.3, and the decreased temperature based on simulated proportions of green space as shown in Tables C.4 - C.15. Furthermore, more associated details in feasibility test of simulated temperature are also reported. The actual and simulated proportional LULC in the feasibility test is shown in Tables C.16 - C.18, and the results based on the first feasibility test, followed with the results based on the second feasibility test as shown in Tables C.19 - C.21, and Tables C.22 - C.24, respectively.

Table C.1 LULC in the first location of hotspot mitigation.

	Areas (square meters)				Proportions			
	TR	BU	RD	Total	TR	BU	RD	Total
1D	-	440.30	459.70	900.00	0.00	0.49	0.51	1.00
1E	-	594.82	305.18	900.00	0.00	0.66	0.34	1.00
2B	-	582.75	317.25	900.00	0.00	0.65	0.35	1.00
2C	-	376.06	523.94	900.00	0.00	0.42	0.58	1.00
2D	-	754.62	145.38	900.00	0.00	0.84	0.16	1.00
2E	-	806.20	93.80	900.00	0.00	0.90	0.10	1.00
3A	-	854.52	45.48	900.00	0.00	0.95	0.05	1.00
3B	-	898.13	1.87	900.00	0.00	1.00	0.00	1.00
3C	-	496.87	403.13	900.00	0.00	0.55	0.45	1.00
3D	-	569.48	330.52	900.00	0.00	0.63	0.37	1.00
3E	-	549.10	350.90	900.00	0.00	0.61	0.39	1.00
4B	-	704.79	195.21	900.00	0.00	0.78	0.22	1.00
4C	-	526.26	373.74	900.00	0.00	0.58	0.42	1.00
4D	-	900.00	-	900.00	0.00	1.00	0.00	1.00

Table C.1 LULC in the first location of hotspot mitigation (Continued).

	Areas (square meters)				Proportions			
	TR	BU	RD	Total	TR	BU	RD	Total
4E	-	900.00	-	900.00	0.00	1.00	0.00	1.00
5B	-	626.65	273.35	900.00	0.00	0.70	0.30	1.00
5C	-	726.87	173.13	900.00	0.00	0.81	0.19	1.00
5D	-	900.00	-	900.00	0.00	1.00	0.00	1.00
6A	-	748.52	151.48	900.00	0.00	0.83	0.17	1.00
6B	-	576.90	323.09	900.00	0.00	0.64	0.36	1.00
6C	-	900.00	-	900.00	0.00	1.00	0.00	1.00
6D	-	900.00	-	900.00	0.00	1.00	0.00	1.00
7B	-	473.52	426.48	900.00	0.00	0.53	0.47	1.00
7C	-	797.27	102.73	900.00	0.00	0.89	0.11	1.00
7D	-	863.93	36.08	900.00	0.00	0.96	0.04	1.00
8A	-	446.02	453.98	900.00	0.00	0.50	0.50	1.00
8B	-	658.76	241.24	900.00	0.00	0.73	0.27	1.00
8C	-	900.00	-	900.00	0.00	1.00	0.00	1.00
8D	-	812.93	87.07	900.00	0.00	0.90	0.10	1.00
9A	-	406.44	493.56	900.00	0.00	0.45	0.55	1.00
9B	-	691.42	208.58	900.00	0.00	0.77	0.23	1.00
10B	-	746.14	153.86	900.00	0.00	0.83	0.17	1.00
11A	-	378.05	521.95	900.00	0.00	0.42	0.58	1.00
11B	-	615.98	284.02	900.00	0.00	0.68	0.32	1.00
Total	-	23,123.30	7,476.70	30,600	0.00	0.76	0.24	1.00

Note: TR, BU, and RD represented tree, construction, and road.

In the first hotspot location, the total areas of green spaces, constructions and road are 0.00, 23,123.30, and 7,476.70 square meters, respectively, as shown in Table C.1. Also, the proportional LULC are 0.00, 0.76, and 0.24, respectively. Furthermore, it is noted that the occurred hotspot area in January 21, 2018 are 3B, 3C, 4B, 4C and 5B area. The occurred hotspot area in February 6, 2018 are 4C, 5B, and 5C area. The occurred hotspot area in March 26, 2018 are 1D, 2B, 2C, 3B, 3C, 4B, 5B, and 6B area. Lastly, all areas are occurred as a hotspot area on April 11, 2018.

Table C.2 LULC in the second location of hotspot mitigation.

	Area (square meters)				Proportions			
	TR	BU	RD	Total	TR	BU	RD	Total
1B	-	849.98	50.02	900.00	0.00	0.94	0.06	1.00
2A	-	657.70	242.30	900.00	0.00	0.73	0.27	1.00
2B	-	714.85	185.15	900.00	0.00	0.79	0.21	1.00
3A	135.73	764.27	-	900.00	0.15	0.85	0.00	1.00
3B	214.45	557.40	128.16	900.00	0.24	0.62	0.14	1.00
4A	32.21	600.85	266.93	900.00	0.04	0.67	0.30	1.00
4B	-	640.04	259.96	900.00	0.00	0.71	0.29	1.00
4C	-	594.89	305.11	900.00	0.00	0.66	0.34	1.00
5A	-	514.99	385.01	900.00	0.00	0.57	0.43	1.00
5B	-	900.00	-	900.00	0.00	1.00	0.00	1.00
5C	-	539.96	360.04	900.00	0.00	0.60	0.40	1.00
5D	-	648.34	251.66	900.00	0.00	0.72	0.28	1.00
6A	-	471.89	428.11	900.00	0.00	0.52	0.48	1.00
6B	-	831.26	68.74	900.00	0.00	0.92	0.08	1.00
6C	-	407.40	492.60	900.00	0.00	0.45	0.55	1.00
7C	-	508.10	391.90	900.00	0.00	0.56	0.44	1.00
Total	382.39	10,201.92	3,815.69	14,400	0.03	0.71	0.26	1.00

Note: TR, BU, and RD represented tree, construction, and road.

The total areas of green spaces, constructions and roads, in the second hotspot locataion, are 382.39, 10,201.92, and 3,815.69 square meters, respectively, as shown in Table C.2. Also, the proportional LULC are 0.03, 0.71, and 0.26, respectively. Furthermore, it is noted that all areas are occurred as a hotspot area on January 21, 2018, except 1B, 5A, and 6A area. The occurred hotspot area in February 6, 2018 are 3B, 4A, 4B, 5A, 5B, 5D, 6B, 6C, and 7C area. The occurred hotspot area in March 26, 2018 are 4B, 5B, 5C, and 6B area. Lastly, all areas are occurred as hotspot area in April 11, 2018, except 7C area.

Table C.3 LULC in the third location of hotspot mitigation.

	Areas (square meters)				Proportions			
	TR	BU	RD	Total	TR	BU	RD	Total
1A	-	709.37	190.63	900.00	0.00	0.79	0.21	1.00
2A	-	900.00	-	900.00	0.00	1.00	0.00	1.00
3A	-	684.95	215.06	900.00	0.00	0.76	0.24	1.00
3B	35.76	379.93	484.30	900.00	0.04	0.42	0.54	1.00
4A	-	598.00	302.00	900.00	0.00	0.66	0.34	1.00
4B	28.22	576.42	295.36	900.00	0.03	0.64	0.33	1.00
5A	-	471.29	428.71	900.00	0.00	0.52	0.48	1.00
5B	-	687.40	212.60	900.00	0.00	0.76	0.24	1.00
6A	58.91	507.20	333.89	900.00	0.07	0.56	0.37	1.00
6B	22.31	877.69	-	900.00	0.02	0.98	0.00	1.00
6C	-	529.18	370.82	900.00	0.00	0.59	0.41	1.00
Total	145.20	6921.43	2833.37	9900.00	0.01	0.70	0.29	0.01

Note: TR, BU, and RD represented tree, construction, and road.

In the third hotspot location, the total areas of green spaces, constructions and roads are 145.20, 6,921.43, and 2,833.37 square meters, respectively. Also, the proportional LULC are 0.01, 0.70, and 0.29, respectively, as shown in Table C.3. Furthermore, it is noted that the occurred hotspot area in January 21, 2018 are 3A and 4A area. Similar to January 21, 2018, the occurred hotspot area in February 6, 2018 are 3A and 4A area. The occurred hotspot area in March 26, 2018 are 1A, 2A, 3A, 4A, 4B, and 5A area. Lastly, all areas are occurred as a hotspot area on April 11, 2018.

Table C.4 The proportion of green space as 0.15 of the area used in the first hotspot location.

	January 21, 2018		February 6, 2018		March 26, 2018		April 11, 2018	
	Decreased temperature	ΔT						
1D	35.09	0.36	29.39	0.23	36.91	0.39	47.54	0.65
1E	34.93	0.36	29.34	0.23	36.58	0.39	47.43	0.65
2B	34.98	0.36	29.44	0.23	36.91	0.39	47.30	0.65
2C	35.05	0.36	29.42	0.23	36.78	0.39	47.44	0.65
2D	34.95	0.36	29.47	0.23	36.60	0.39	47.45	0.65
2E	34.77	0.36	29.29	0.23	36.22	0.39	47.22	0.65
3A	35.07	0.36	29.53	0.23	36.43	0.39	47.30	0.65
3B	35.93	0.36	29.59	0.23	36.97	0.39	47.97	0.65
3C	35.92	0.36	29.48	0.23	36.86	0.39	47.98	0.65
3D	35.21	0.36	29.50	0.23	36.12	0.39	47.56	0.65
3E	34.92	0.36	29.30	0.23	35.62	0.39	47.32	0.65
4B	35.90	0.36	30.89	0.23	36.95	0.39	48.29	0.65
4C	35.93	0.36	30.93	0.23	36.56	0.39	47.96	0.65
4D	35.01	0.36	29.39	0.23	35.90	0.39	47.45	0.65
4E	34.67	0.36	29.12	0.23	34.96	0.39	47.20	0.65
5B	35.89	0.36	30.99	0.23	36.89	0.39	48.17	0.65
5C	35.07	0.36	31.02	0.23	36.49	0.39	47.92	0.65
5D	34.61	0.36	29.22	0.23	35.93	0.39	47.40	0.65
6A	34.57	0.36	29.65	0.23	35.64	0.39	47.22	0.65
6B	35.05	0.36	29.74	0.23	36.85	0.39	48.19	0.65
6C	34.75	0.36	29.67	0.23	36.33	0.39	47.77	0.65
6D	34.38	0.36	29.32	0.23	35.54	0.39	47.16	0.65
7B	34.43	0.36	29.26	0.23	36.49	0.39	47.92	0.65
7C	34.59	0.36	29.41	0.23	36.19	0.39	47.71	0.65
7D	34.48	0.36	29.23	0.23	35.60	0.39	47.72	0.65
8A	33.98	0.36	28.47	0.23	35.84	0.39	47.16	0.65
8B	34.93	0.36	29.02	0.23	36.16	0.39	48.34	0.65
8C	34.88	0.36	29.24	0.23	35.91	0.39	47.93	0.65
8D	34.70	0.36	29.25	0.23	35.42	0.39	47.99	0.65
9A	34.31	0.36	28.70	0.23	35.70	0.39	47.45	0.65
9B	35.21	0.36	29.19	0.23	35.73	0.39	47.97	0.65
10B	35.55	0.36	29.35	0.23	35.68	0.39	48.48	0.65
11A	34.60	0.36	29.59	0.23	35.72	0.39	47.49	0.65
11B	35.00	0.36	29.84	0.23	35.58	0.39	47.86	0.65
Min	33.98	0.36	28.47	0.23	34.96	0.39	47.16	0.65
Max	35.93	0.36	31.02	0.23	36.97	0.39	48.48	0.65
Mean	34.98	0.36	29.54	0.23	36.18	0.39	47.68	0.65

Note: ΔT is the differentiated temperature between actual temperature and decreased temperature.

Table C.5 The proportion of green space 0.30 of the area used in the first hotspot location.

	January 21, 2018		February 6, 2018		March 26, 2018		April 11, 2018	
	Decreased temperature	ΔT						
1D	34.72	0.73	29.16	0.47	36.51	0.79	46.89	1.29
1E	34.57	0.73	29.10	0.47	36.18	0.79	46.78	1.29
2B	34.62	0.73	29.20	0.47	36.51	0.79	46.65	1.29
2C	34.69	0.73	29.19	0.47	36.39	0.79	46.79	1.29
2D	34.59	0.73	29.24	0.47	36.21	0.79	46.80	1.29
2E	34.41	0.73	29.06	0.47	35.83	0.79	46.57	1.29
3A	34.70	0.73	29.30	0.47	36.04	0.79	46.65	1.29
3B	35.57	0.73	29.36	0.47	36.57	0.79	47.33	1.29
3C	35.56	0.73	29.25	0.47	36.47	0.79	47.34	1.29
3D	34.84	0.73	29.27	0.47	35.72	0.79	46.92	1.29
3E	34.56	0.73	29.07	0.47	35.23	0.79	46.67	1.29
4B	35.54	0.73	30.66	0.47	36.56	0.79	47.64	1.29
4C	35.57	0.73	30.70	0.47	36.17	0.79	47.32	1.29
4D	34.64	0.73	29.16	0.47	35.51	0.79	46.80	1.29
4E	34.30	0.73	28.89	0.47	34.56	0.79	46.55	1.29
5B	35.53	0.73	30.75	0.47	36.50	0.79	47.52	1.29
5C	34.71	0.73	30.79	0.47	36.10	0.79	47.27	1.29
5D	34.24	0.73	28.99	0.47	35.53	0.79	46.76	1.29
6A	34.21	0.73	29.42	0.47	35.25	0.79	46.58	1.29
6B	34.69	0.73	29.51	0.47	36.46	0.79	47.55	1.29
6C	34.39	0.73	29.44	0.47	35.94	0.79	47.13	1.29
6D	34.02	0.73	29.09	0.47	35.15	0.79	46.51	1.29
7B	34.07	0.73	29.02	0.47	36.10	0.79	47.27	1.29
7C	34.22	0.73	29.18	0.47	35.79	0.79	47.06	1.29
7D	34.12	0.73	29.00	0.47	35.21	0.79	47.07	1.29
8A	33.62	0.73	28.23	0.47	35.45	0.79	46.51	1.29
8B	34.56	0.73	28.79	0.47	35.77	0.79	47.70	1.29
8C	34.52	0.73	29.01	0.47	35.52	0.79	47.28	1.29
8D	34.34	0.73	29.02	0.47	35.02	0.79	47.34	1.29
9A	33.95	0.73	28.47	0.47	35.31	0.79	46.80	1.29
9B	34.84	0.73	28.95	0.47	35.34	0.79	47.33	1.29
10B	35.19	0.73	29.12	0.47	35.28	0.79	47.83	1.29
11A	34.24	0.73	29.36	0.47	35.32	0.79	46.84	1.29
11B	34.64	0.73	29.61	0.47	35.19	0.79	47.22	1.29
Min	33.62	0.73	28.23	0.47	34.56	0.79	46.51	1.29
Max	35.57	0.73	30.79	0.47	36.57	0.79	47.83	1.29
Mean	34.62	0.73	29.30	0.47	35.78	0.79	47.04	1.29

Note: ΔT is the differentiated temperature between actual temperature and decreased temperature.

Table C.6 The proportion of green space 0.45 of the area used in the first hotspot location.

	January 21, 2018		February 6, 2018		March 26, 2018		April 11, 2018	
	Decreased temperature	ΔT						
1D	34.36	1.09	28.93	0.70	36.12	1.18	46.24	1.94
1E	34.21	1.09	28.87	0.70	35.79	1.18	46.14	1.94
2B	34.26	1.09	28.97	0.70	36.12	1.18	46.00	1.94
2C	34.32	1.09	28.95	0.70	35.99	1.18	46.14	1.94
2D	34.22	1.09	29.01	0.70	35.82	1.18	46.15	1.94
2E	34.04	1.09	28.82	0.70	35.43	1.18	45.93	1.94
3A	34.34	1.09	29.07	0.70	35.64	1.18	46.01	1.94
3B	35.20	1.09	29.13	0.70	36.18	1.18	46.68	1.94
3C	35.19	1.09	29.01	0.70	36.08	1.18	46.69	1.94
3D	34.48	1.09	29.04	0.70	35.33	1.18	46.27	1.94
3E	34.19	1.09	28.84	0.70	34.83	1.18	46.02	1.94
4B	35.18	1.09	30.43	0.70	36.17	1.18	47.00	1.94
4C	35.20	1.09	30.46	0.70	35.78	1.18	46.67	1.94
4D	34.28	1.09	28.93	0.70	35.11	1.18	46.15	1.94
4E	33.94	1.09	28.66	0.70	34.17	1.18	45.90	1.94
5B	35.17	1.09	30.52	0.70	36.10	1.18	46.88	1.94
5C	34.34	1.09	30.56	0.70	35.70	1.18	46.62	1.94
5D	33.88	1.09	28.76	0.70	35.14	1.18	46.11	1.94
6A	33.84	1.09	29.19	0.70	34.85	1.18	45.93	1.94
6B	34.32	1.09	29.28	0.70	36.06	1.18	46.90	1.94
6C	34.02	1.09	29.21	0.70	35.54	1.18	46.48	1.94
6D	33.65	1.09	28.86	0.70	34.76	1.18	45.86	1.94
7B	33.70	1.09	28.79	0.70	35.70	1.18	46.63	1.94
7C	33.86	1.09	28.94	0.70	35.40	1.18	46.42	1.94
7D	33.75	1.09	28.77	0.70	34.82	1.18	46.42	1.94
8A	33.25	1.09	28.00	0.70	35.05	1.18	45.87	1.94
8B	34.20	1.09	28.55	0.70	35.37	1.18	47.05	1.94
8C	34.16	1.09	28.78	0.70	35.12	1.18	46.64	1.94
8D	33.97	1.09	28.79	0.70	34.63	1.18	46.70	1.94
9A	33.58	1.09	28.24	0.70	34.91	1.18	46.16	1.94
9B	34.48	1.09	28.72	0.70	34.94	1.18	46.68	1.94
10B	34.83	1.09	28.89	0.70	34.89	1.18	47.18	1.94
11A	33.88	1.09	29.13	0.70	34.93	1.18	46.20	1.94
11B	34.27	1.09	29.37	0.70	34.80	1.18	46.57	1.94
Min	33.25	1.09	28.00	0.70	34.17	1.18	45.86	1.94
Max	35.20	1.09	30.56	0.70	36.18	1.18	47.18	1.94
Mean	34.25	1.09	29.07	0.70	35.39	1.18	46.39	1.94

Note: ΔT is the differentiated temperature between actual temperature and decreased temperature.

Table C.7 The proportion of green space 0.60 of the area used in the first hotspot location.

	January 21, 2018		February 6, 2018		March 26, 2018		April 11, 2018	
	Decreased temperature	ΔT						
1D	33.99	1.46	28.69	0.93	35.73	1.57	45.60	2.59
1E	33.84	1.46	28.64	0.93	35.40	1.57	45.49	2.59
2B	33.89	1.46	28.74	0.93	35.73	1.57	45.36	2.59
2C	33.96	1.46	28.72	0.93	35.60	1.57	45.50	2.59
2D	33.86	1.46	28.78	0.93	35.42	1.57	45.51	2.59
2E	33.68	1.46	28.59	0.93	35.04	1.57	45.28	2.59
3A	33.98	1.46	28.84	0.93	35.25	1.57	45.36	2.59
3B	34.84	1.46	28.89	0.93	35.79	1.57	46.03	2.59
3C	34.83	1.46	28.78	0.93	35.68	1.57	46.04	2.59
3D	34.12	1.46	28.80	0.93	34.94	1.57	45.62	2.59
3E	33.83	1.46	28.61	0.93	34.44	1.57	45.38	2.59
4B	34.81	1.46	30.20	0.93	35.77	1.57	46.35	2.59
4C	34.84	1.46	30.23	0.93	35.38	1.57	46.03	2.59
4D	33.91	1.46	28.69	0.93	34.72	1.57	45.51	2.59
4E	33.57	1.46	28.42	0.93	33.78	1.57	45.26	2.59
5B	34.80	1.46	30.29	0.93	35.71	1.57	46.23	2.59
5C	33.98	1.46	30.33	0.93	35.31	1.57	45.98	2.59
5D	33.51	1.46	28.53	0.93	34.75	1.57	45.46	2.59
6A	33.48	1.46	28.95	0.93	34.46	1.57	45.28	2.59
6B	33.96	1.46	29.05	0.93	35.67	1.57	46.25	2.59
6C	33.66	1.46	28.97	0.93	35.15	1.57	45.83	2.59
6D	33.29	1.46	28.63	0.93	34.36	1.57	45.22	2.59
7B	33.34	1.46	28.56	0.93	35.31	1.57	45.98	2.59
7C	33.50	1.46	28.71	0.93	35.01	1.57	45.77	2.59
7D	33.39	1.46	28.53	0.93	34.42	1.57	45.78	2.59
8A	32.89	1.46	27.77	0.93	34.66	1.57	45.22	2.59
8B	33.83	1.46	28.32	0.93	34.98	1.57	46.40	2.59
8C	33.79	1.46	28.54	0.93	34.73	1.57	45.99	2.59
8D	33.61	1.46	28.56	0.93	34.24	1.57	46.05	2.59
9A	33.22	1.46	28.00	0.93	34.52	1.57	45.51	2.59
9B	34.11	1.46	28.49	0.93	34.55	1.57	46.04	2.59
10B	34.46	1.46	28.66	0.93	34.50	1.57	46.54	2.59
11A	33.51	1.46	28.89	0.93	34.54	1.57	45.55	2.59
11B	33.91	1.46	29.14	0.93	34.40	1.57	45.92	2.59
Min	32.89	1.46	27.77	0.93	33.78	1.57	45.22	2.59
Max	34.84	1.46	30.33	0.93	35.79	1.57	46.54	2.59
Mean	33.89	1.46	28.84	0.93	35.00	1.57	45.74	2.59

Note: ΔT is the differentiated temperature between actual temperature and decreased temperature.

Table C.8 The proportion of green space 0.15 of the area used in the second hotspot location.

	January 21, 2018		February 6, 2018		March 26, 2018		April 11, 2018	
	Decreased temperature	ΔT						
1B	35.34	0.36	29.91	0.23	36.46	0.39	47.06	0.65
2A	35.80	0.36	30.31	0.23	36.58	0.39	47.62	0.65
2B	35.90	0.36	30.25	0.23	36.46	0.39	47.53	0.65
3A	36.36	-	30.81	-	36.68	-	48.51	-
3B	-	-	-	-	-	-	-	-
4A	35.97	0.27	30.92	0.17	36.56	0.29	48.00	0.47
4B	35.82	0.36	30.86	0.23	36.89	0.39	48.33	0.65
4C	35.86	0.36	30.50	0.23	36.60	0.39	47.68	0.65
5A	35.30	0.36	30.89	0.23	36.55	0.39	47.77	0.65
5B	35.81	0.36	30.94	0.23	36.79	0.39	48.42	0.65
5C	35.99	0.36	30.87	0.23	36.92	0.39	47.93	0.65
5D	36.88	0.36	31.93	0.23	36.26	0.39	48.18	0.65
6A	35.07	0.36	30.43	0.23	36.57	0.39	46.98	0.65
6B	35.91	0.36	30.88	0.23	36.83	0.39	47.62	0.65
6C	36.30	0.36	31.60	0.23	36.44	0.39	47.70	0.65
7C	35.98	0.36	31.21	0.23	36.35	0.39	46.76	0.65
Min	35.07	0.27	29.91	0.17	36.26	0.29	46.76	0.47
Max	36.88	0.36	31.93	0.23	36.92	0.39	48.51	0.65
Mean	35.89	0.36	30.82	0.23	36.60	0.39	47.74	0.63

Note: ΔT is the differentiated temperature between actual temperature and decreased temperature.

Table C.9 The proportion of green space 0.30 of the area used in the second hotspot location.

	January 21, 2018		February 6, 2018		March 26, 2018		April 11, 2018	
	Decreased temperature	ΔT						
1B	34.98	0.73	29.68	0.47	36.07	0.79	46.41	1.29
2A	35.43	0.73	30.08	0.47	36.18	0.79	46.97	1.29
2B	35.54	0.73	30.02	0.47	36.06	0.79	46.89	1.29
3A	36.00	0.36	30.57	0.23	36.29	0.39	47.86	0.65
3B	36.08	0.15	31.00	0.09	36.72	0.16	48.36	0.26
4A	35.61	0.63	30.69	0.40	36.17	0.68	47.36	1.12
4B	35.45	0.73	30.63	0.47	36.50	0.79	47.68	1.29
4C	35.50	0.73	30.27	0.47	36.21	0.79	47.03	1.29
5A	34.93	0.73	30.66	0.47	36.16	0.79	47.12	1.29
5B	35.44	0.73	30.71	0.47	36.40	0.79	47.77	1.29
5C	35.63	0.73	30.63	0.47	36.52	0.79	47.29	1.29
5D	36.51	0.73	31.70	0.47	35.87	0.79	47.54	1.29
6A	34.71	0.73	30.20	0.47	36.18	0.79	46.34	1.29
6B	35.55	0.73	30.65	0.47	36.43	0.79	46.97	1.29
6C	35.93	0.73	31.37	0.47	36.04	0.79	47.06	1.29
7C	35.62	0.73	30.98	0.47	35.96	0.79	46.12	1.29
Min	34.71	0.15	29.68	0.09	35.87	0.16	46.12	0.26
Max	36.51	0.73	31.70	0.47	36.72	0.79	48.36	1.29
Mean	35.56	0.66	30.61	0.42	36.23	0.72	47.17	1.18

Note: ΔT is the differentiated temperature between actual temperature and decreased temperature.

Table C.10 The proportion of green space 0.45 of the area used in the second hotspot location.

	January 21, 2018		February 6, 2018		March 26, 2018		April 11, 2018	
	Decreased temperature	ΔT						
1B	34.61	1.09	29.45	0.70	35.67	1.18	45.77	1.94
2A	35.07	1.09	29.85	0.70	35.79	1.18	46.33	1.94
2B	35.18	1.09	29.79	0.70	35.67	1.18	46.24	1.94
3A	35.63	0.73	30.34	0.47	35.89	0.79	47.22	1.29
3B	35.72	0.51	30.77	0.33	36.33	0.55	47.71	0.91
4A	35.24	1.00	30.46	0.64	35.78	1.08	46.71	1.77
4B	35.09	1.09	30.39	0.70	36.10	1.18	47.04	1.94
4C	35.13	1.09	30.04	0.70	35.81	1.18	46.38	1.94
5A	34.57	1.09	30.43	0.70	35.77	1.18	46.48	1.94
5B	35.08	1.09	30.47	0.70	36.00	1.18	47.12	1.94
5C	35.26	1.09	30.40	0.70	36.13	1.18	46.64	1.94
5D	36.15	1.09	31.47	0.70	35.47	1.18	46.89	1.94
6A	34.35	1.09	29.97	0.70	35.79	1.18	45.69	1.94
6B	35.18	1.09	30.42	0.70	36.04	1.18	46.32	1.94
6C	35.57	1.09	31.13	0.70	35.65	1.18	46.41	1.94
7C	35.25	1.09	30.74	0.70	35.57	1.18	45.47	1.94
Min	34.35	0.51	29.45	0.33	35.47	0.55	45.47	0.91
Max	36.15	1.09	31.47	0.70	36.33	1.18	47.71	1.94
Mean	35.19	1.03	30.38	0.66	35.84	1.11	46.53	1.82

Note: ΔT is the differentiated temperature between actual temperature and decreased temperature.

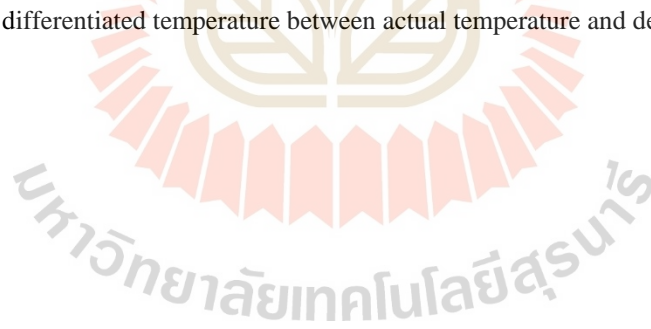


Table C.11 The proportion of green space 0.60 of the area used in the second hotspot location.

	January 21, 2018		February 6, 2018		March 26, 2018		April 11, 2018	
	Decreased temperature	ΔT						
1B	34.25	1.46	29.22	0.93	35.28	1.57	45.12	2.59
2A	34.70	1.46	29.62	0.93	35.40	1.57	45.68	2.59
2B	34.81	1.46	29.55	0.93	35.28	1.57	45.60	2.59
3A	35.27	1.09	30.11	0.70	35.50	1.18	46.57	1.94
3B	35.35	0.87	30.54	0.56	35.93	0.94	47.06	1.55
4A	34.88	1.36	30.22	0.87	35.38	1.47	46.07	2.41
4B	34.72	1.46	30.16	0.93	35.71	1.57	46.39	2.59
4C	34.77	1.46	29.80	0.93	35.42	1.57	45.74	2.59
5A	34.20	1.46	30.19	0.93	35.37	1.57	45.83	2.59
5B	34.71	1.46	30.24	0.93	35.61	1.57	46.48	2.59
5C	34.90	1.46	30.17	0.93	35.74	1.57	45.99	2.59
5D	35.78	1.46	31.23	0.93	35.08	1.57	46.24	2.59
6A	33.98	1.46	29.74	0.93	35.39	1.57	45.04	2.59
6B	34.82	1.46	30.18	0.93	35.65	1.57	45.68	2.59
6C	35.20	1.46	30.90	0.93	35.26	1.57	45.76	2.59
7C	34.89	1.46	30.51	0.93	35.17	1.57	44.82	2.59
Min	33.98	0.87	29.22	0.56	35.08	0.94	44.82	1.55
Max	35.78	1.46	31.23	0.93	35.93	1.57	47.06	2.59
Mean	34.83	1.39	30.15	0.89	35.45	1.50	45.88	2.47

Note: ΔT is the differentiated temperature between actual temperature and decreased temperature.

Table C.12 The proportion of green space 0.15 of the area used in the third hotspot location.

	January 21, 2018		February 6, 2018		March 26, 2018		April 11, 2018	
	Decreased temperature	ΔT						
1A	34.90	0.36	30.15	0.23	36.95	0.39	47.12	0.65
2A	35.05	0.36	30.33	0.23	37.07	0.39	47.18	0.65
3A	35.85	0.36	31.67	0.23	37.02	0.39	47.54	0.65
3B	35.02	0.27	30.47	0.17	36.65	0.29	47.16	0.47
4A	35.92	0.36	31.76	0.23	36.87	0.39	47.77	0.65
4B	35.34	0.29	30.38	0.19	36.95	0.31	47.23	0.52
5A	35.34	0.36	30.32	0.23	36.98	0.39	47.54	0.65
5B	34.99	0.36	29.92	0.23	36.50	0.39	47.11	0.65
6A	35.55	0.19	30.32	0.12	36.60	0.21	47.81	0.34
6B	35.21	0.32	29.88	0.20	36.05	0.34	47.20	0.56
6C	34.89	0.36	29.44	0.23	35.52	0.39	47.04	0.65
Min	34.89	0.19	29.44	0.12	35.52	0.21	47.04	0.34
Max	35.92	0.36	31.76	0.23	37.07	0.39	47.81	0.65
Mean	35.28	0.33	30.42	0.21	36.65	0.36	47.34	0.58

Note: ΔT is the differentiated temperature between actual temperature and decreased temperature.

Table C.13 The proportion of green space as 0.30 of the area used in the third hotspot location.

	January 21, 2018		February 6, 2018		March 26, 2018		April 11, 2018	
	Decreased temperature	ΔT						
1A	34.53	0.73	29.92	0.47	36.55	0.79	46.47	1.29
2A	34.69	0.73	30.10	0.47	36.67	0.79	46.54	1.29
3A	35.49	0.73	31.44	0.47	36.62	0.79	46.90	1.29
3B	34.66	0.63	30.23	0.40	36.26	0.68	46.52	1.12
4A	35.56	0.73	31.53	0.47	36.48	0.79	47.12	1.29
4B	34.98	0.66	30.15	0.42	36.56	0.71	46.59	1.16
5A	34.97	0.73	30.09	0.47	36.59	0.79	46.90	1.29
5B	34.62	0.73	29.69	0.47	36.11	0.79	46.46	1.29
6A	35.19	0.56	30.08	0.36	36.20	0.60	47.16	0.99
6B	34.85	0.68	29.64	0.43	35.66	0.73	46.55	1.21
6C	34.52	0.73	29.21	0.47	35.13	0.79	46.40	1.29
Min	34.52	0.56	29.21	0.36	35.13	0.60	46.40	0.99
Max	35.56	0.73	31.53	0.47	36.67	0.79	47.16	1.29
Mean	34.91	0.69	30.19	0.44	36.26	0.75	46.69	1.23

Note: ΔT is the differentiated temperature between actual temperature and decreased temperature.

Table C.14 The proportion of green space 0.45 of the area used in the third hotspot location.

	January 21, 2018		February 6, 2018		March 26, 2018		April 11, 2018	
	Decreased temperature	ΔT						
1A	34.17	1.09	29.68	0.70	36.16	1.18	45.83	1.94
2A	34.32	1.09	29.87	0.70	36.28	1.18	45.89	1.94
3A	35.12	1.09	31.20	0.70	36.23	1.18	46.25	1.94
3B	34.29	1.00	30.00	0.64	35.87	1.08	45.87	1.77
4A	35.20	1.09	31.30	0.70	36.08	1.18	46.48	1.94
4B	34.61	1.02	29.92	0.65	36.17	1.10	45.94	1.81
5A	34.61	1.09	29.86	0.70	36.19	1.18	46.25	1.94
5B	34.26	1.09	29.46	0.70	35.71	1.18	45.81	1.94
6A	34.82	0.92	29.85	0.59	35.81	1.00	46.52	1.64
6B	34.48	1.04	29.41	0.67	35.27	1.13	45.91	1.85
6C	34.16	1.09	28.98	0.70	34.73	1.18	45.75	1.94
Min	34.16	0.92	28.98	0.59	34.73	1.00	45.75	1.64
Max	35.20	1.09	31.30	0.70	36.28	1.18	46.52	1.94
Mean	34.55	1.06	29.96	0.68	35.86	1.14	46.04	1.88

Note: ΔT is the differentiated temperature between actual temperature and decreased temperature.

Table C.15 The proportion of green space 0.60 of the area used in the third hotspot location.

	January 21, 2018		February 6, 2018		March 26, 2018		April 11, 2018	
	Decreased temperature	ΔT						
1A	33.80	1.46	29.45	0.93	35.77	1.57	45.18	2.59
2A	33.96	1.46	29.64	0.93	35.89	1.57	45.24	2.59
3A	34.76	1.46	30.97	0.93	35.84	1.57	45.60	2.59
3B	33.93	1.36	29.77	0.87	35.47	1.47	45.22	2.41
4A	34.83	1.46	31.07	0.93	35.69	1.57	45.83	2.59
4B	34.25	1.38	29.69	0.88	35.77	1.50	45.30	2.46
5A	34.24	1.46	29.62	0.93	35.80	1.57	45.60	2.59
5B	33.89	1.46	29.22	0.93	35.32	1.57	45.17	2.59
6A	34.46	1.29	29.62	0.82	35.41	1.39	45.87	2.28
6B	34.12	1.41	29.18	0.90	34.87	1.52	45.26	2.50
6C	33.79	1.46	28.74	0.93	34.34	1.57	45.10	2.59
Min	33.79	1.29	28.74	0.82	34.34	1.39	45.10	2.28
Max	34.83	1.46	31.07	0.93	35.89	1.57	45.87	2.59
Mean	34.19	1.42	29.72	0.91	35.47	1.54	45.40	2.52

Note: ΔT is the differentiated temperature between actual temperature and decreased temperature.

Table C.16 The actual LULC and simulated LULC in the first hotspot location.

	Actual LULC			Simulated LULC		
	TR	BU	RD	TR	BU	RD
1D	0.00	0.49	0.51	0.45	0.49	0.06
1E	0.00	0.66	0.34	0.45	0.55	0.00
2B	0.00	0.65	0.35	0.45	0.55	0.00
2C	0.00	0.42	0.58	0.45	0.42	0.13
2D	0.00	0.84	0.16	0.45	0.55	0.00
2E	0.00	0.90	0.10	0.45	0.55	0.00
3A	0.00	0.95	0.05	0.45	0.55	0.00
3B	0.00	1.00	0.00	0.45	0.55	0.00
3C	0.00	0.55	0.45	0.45	0.55	0.00
3D	0.00	0.63	0.37	0.45	0.55	0.00
3E	0.00	0.61	0.39	0.45	0.55	0.00
4B	0.00	0.78	0.22	0.45	0.55	0.00
4C	0.00	0.58	0.42	0.45	0.55	0.00
4D	0.00	1.00	0.00	0.45	0.55	0.00
4E	0.00	1.00	0.00	0.45	0.55	0.00
5B	0.00	0.70	0.30	0.45	0.55	0.00
5C	0.00	0.81	0.19	0.45	0.55	0.00
5D	0.00	1.00	0.00	0.45	0.55	0.00
6A	0.00	0.83	0.17	0.45	0.55	0.00
6B	0.00	0.64	0.36	0.45	0.55	0.00
6C	0.00	1.00	0.00	0.45	0.55	0.00
6D	0.00	1.00	0.00	0.45	0.55	0.00
7B	0.00	0.53	0.47	0.45	0.53	0.02
7C	0.00	0.89	0.11	0.45	0.55	0.00
7D	0.00	0.96	0.04	0.45	0.55	0.00
8A	0.00	0.50	0.50	0.45	0.50	0.05
8B	0.00	0.73	0.27	0.45	0.55	0.00
8C	0.00	1.00	0.00	0.45	0.55	0.00
8D	0.00	0.90	0.10	0.45	0.55	0.00
9A	0.00	0.45	0.55	0.45	0.45	0.10
9B	0.00	0.77	0.23	0.45	0.55	0.00
10B	0.00	0.83	0.17	0.45	0.55	0.00
11A	0.00	0.42	0.58	0.45	0.42	0.13
11B	0.00	0.68	0.32	0.45	0.55	0.00

Note: TR, BU, and RD represented tree, construction, and road.

Table C.17 The actual LULC and simulated LULC in the second hotspot location.

	Actual LULC			Simulated LULC		
	TR	BU	RD	TR	BU	RD
1B	0.00	0.94	0.06	0.60	0.40	0.00
2A	0.00	0.73	0.27	0.60	0.40	0.00
2B	0.00	0.79	0.21	0.60	0.40	0.00
3A	0.15	0.85	0.00	0.60	0.40	0.00
3B	0.24	0.62	0.14	0.60	0.40	0.00
4A	0.04	0.67	0.30	0.60	0.40	0.00
4B	0.00	0.71	0.29	0.60	0.40	0.00
4C	0.00	0.66	0.34	0.60	0.40	0.00
5A	0.00	0.57	0.43	0.60	0.40	0.00
5B	0.00	1.00	0.00	0.60	0.40	0.00
5C	0.00	0.60	0.40	0.60	0.40	0.00
5D	0.00	0.72	0.28	0.60	0.40	0.00
6A	0.00	0.52	0.48	0.60	0.40	0.00
6B	0.00	0.92	0.08	0.60	0.40	0.00
6C	0.00	0.45	0.55	0.60	0.40	0.00
7C	0.00	0.56	0.44	0.60	0.40	0.00

Note: TR, BU, and RD represented tree, construction, and road.

Table C.18 The actual LULC and simulated LULC in the third hotspot location.

	Actual LULC			Simulated LULC		
	TR	BU	RD	TR	BU	RD
1A	0.00	0.79	0.21	0.30	0.70	0.00
2A	0.00	1.00	0.00	0.30	0.70	0.00
3A	0.00	0.76	0.24	0.30	0.70	0.00
3B	0.04	0.42	0.54	0.30	0.42	0.28
4A	0.00	0.66	0.34	0.30	0.66	0.04
4B	0.03	0.64	0.33	0.30	0.64	0.06
5A	0.00	0.52	0.48	0.30	0.52	0.18
5B	0.00	0.76	0.24	0.30	0.70	0.00
6A	0.07	0.56	0.37	0.30	0.56	0.14
6B	0.02	0.98	0.00	0.30	0.70	0.00
6C	0.00	0.59	0.41	0.30	0.59	0.11

Note: TR, BU, and RD represented tree, construction, and road.

Table C.19 The feasibility test results in the first hotspot location (°C).

	January 21, 2018			February 6, 2018			March 26, 2018			April 11, 2018		
	Sample	Simulate	ΔT	Sample	Simulate	ΔT	Sample	Simulate	ΔT	Sample	Simulate	ΔT
1D	33.69	34.36	-0.67	28.85	28.93	-0.08	35.76	36.12	-0.36	46.16	46.24	-0.08
1E	34.49	34.21	0.28	29.18	28.87	0.31	35.47	35.79	-0.32	46.16	46.14	0.02
2B	34.49	34.26	0.23	29.18	28.97	0.21	35.47	36.12	-0.65	46.16	46.00	0.16
2C	34.49	34.32	0.17	29.62	28.95	0.67	35.16	35.99	-0.83	46.16	46.14	0.02
2D	34.49	34.22	0.27	29.18	29.01	0.17	35.47	35.82	-0.35	46.16	46.15	0.01
2E	34.49	34.04	0.45	29.18	28.82	0.36	35.47	35.43	0.04	46.16	45.93	0.23
3A	34.49	34.34	0.15	29.18	29.07	0.11	35.47	35.64	-0.17	46.16	46.01	0.15
3B	35.60	35.20	0.40	29.18	29.13	0.05	35.47	36.18	-0.71	46.16	46.68	-0.52
3C	35.60	35.19	0.41	29.18	29.01	0.17	35.47	36.08	-0.61	46.16	46.69	-0.53
3D	34.49	34.48	0.01	29.18	29.04	0.14	35.35	35.33	0.02	46.16	46.27	-0.11
3E	34.49	34.19	0.30	29.18	28.84	0.34	34.90	34.83	0.07	46.16	46.02	0.14
4B	35.60	35.18	0.42	29.78	30.43	-0.65	35.47	36.17	-0.70	46.16	47.00	-0.84
4C	35.60	35.20	0.40	29.78	30.46	-0.68	35.47	35.78	-0.31	46.16	46.67	-0.51
4D	34.49	34.28	0.21	29.18	28.93	0.25	35.04	35.11	-0.07	46.16	46.15	0.01
4E	33.57	33.94	-0.37	29.18	28.66	0.52	34.90	34.17	0.73	46.16	45.90	0.26
5B	35.08	35.17	-0.09	29.78	30.52	-0.74	35.47	36.10	-0.63	46.16	46.88	-0.72
5C	34.49	34.34	0.15	29.78	30.56	-0.78	35.47	35.70	-0.23	46.16	46.62	-0.46
5D	33.57	33.88	-0.31	29.18	28.76	0.42	35.04	35.14	-0.10	46.16	46.11	0.05
6A	33.69	33.84	-0.15	29.18	29.19	-0.01	35.04	34.85	0.19	46.16	45.93	0.23
6B	34.49	34.32	0.17	29.18	29.28	-0.10	35.47	36.06	-0.59	46.16	46.90	-0.74
6C	33.69	34.02	-0.33	29.25	29.21	0.04	35.47	35.54	-0.07	46.16	46.48	-0.32
6D	33.69	33.65	0.04	29.18	28.86	0.32	34.90	34.76	0.14	45.60	45.86	-0.26
7B	33.69	33.70	-0.01	28.85	28.79	0.06	35.76	35.70	0.06	46.16	46.63	-0.47
7C	33.57	33.86	-0.29	29.18	28.94	0.24	35.47	35.40	0.07	46.16	46.42	-0.26
7D	33.57	33.75	-0.18	29.18	28.77	0.41	34.90	34.82	0.08	46.16	46.42	-0.26
8A	33.69	33.25	0.44	27.56	28.00	-0.44	35.35	35.05	0.30	46.16	45.87	0.29
8B	34.49	34.20	0.29	29.18	28.55	0.63	35.35	35.37	-0.02	46.16	47.05	-0.89
8C	34.49	34.16	0.33	29.18	28.78	0.40	35.04	35.12	-0.08	46.16	46.64	-0.48
8D	33.57	33.97	-0.40	29.18	28.79	0.39	34.90	34.63	0.27	46.16	46.70	-0.54
9A	33.69	33.58	0.11	29.22	28.24	0.98	34.90	34.91	-0.01	46.16	46.16	0.00
9B	34.49	34.48	0.01	29.18	28.72	0.46	34.90	34.94	-0.04	46.16	46.68	-0.52
10B	34.70	34.83	-0.13	29.18	28.89	0.29	34.90	34.89	0.01	46.16	47.18	-1.02
11A	34.49	33.88	0.61	30.03	29.13	0.90	35.16	34.93	0.23	46.16	46.20	-0.04
11B	34.49	34.27	0.22	30.06	29.37	0.69	35.16	34.80	0.36	46.16	46.57	-0.41
Min	33.57	33.25	0.32	27.56	28.00	-0.44	34.90	34.17	0.73	45.60	45.86	-0.26
Max	35.60	35.20	0.40	30.06	30.56	-0.50	35.76	36.18	-0.42	46.16	47.18	-1.02
RMSE		0.31			0.46			0.37			0.44	

Note: 1. The proportion of green space is 0.45 in the area.

2. ΔT referred to the differentiated temperature between sample and simulated results.

Table C.20 The feasibility test results in the second hotspot location (°C).

	January 21, 2018			February 6, 2018			March 26, 2018			April 11, 2018		
	Sample	Simulate	ΔT	Sample	Simulate	ΔT	Sample	Simulate	ΔT	Sample	Simulate	ΔT
1B	34.13	34.25	-0.12	29.40	29.22	0.18	35.52	35.28	0.24	45.54	45.12	0.42
2A	35.11	34.70	0.41	29.46	29.62	-0.16	35.52	35.40	0.12	46.38	45.68	0.70
2B	35.11	34.81	0.30	29.40	29.55	-0.15	35.52	35.28	0.24	45.54	45.60	-0.06
3A	35.19	35.27	-0.08	30.12	30.11	0.01	35.52	35.50	0.02	46.38	46.57	-0.19
3B	35.19	35.35	-0.16	30.12	30.54	-0.42	35.52	35.93	-0.41	46.38	47.06	-0.68
4A	35.11	34.88	0.23	30.12	30.22	-0.10	35.52	35.38	0.14	46.38	46.07	0.31
4B	35.11	34.72	0.39	30.12	30.16	-0.04	35.52	35.71	-0.19	46.38	46.39	-0.01
4C	35.11	34.77	0.34	29.46	29.80	-0.34	35.52	35.42	0.10	45.54	45.74	-0.20
5A	34.13	34.20	-0.07	30.12	30.19	-0.07	35.52	35.37	0.15	45.54	45.83	-0.29
5B	35.11	34.71	0.40	30.12	30.24	-0.12	35.52	35.61	-0.09	46.38	46.48	-0.10
5C	35.19	34.90	0.29	30.12	30.17	-0.05	35.52	35.74	-0.22	46.38	45.99	0.39
5D	35.19	35.78	-0.59	30.12	31.23	-1.11	35.52	35.08	0.44	46.38	46.24	0.14
6A	34.13	33.98	0.15	29.46	29.74	-0.28	35.52	35.39	0.13	45.54	45.04	0.50
6B	35.11	34.82	0.29	30.12	30.18	-0.06	35.52	35.65	-0.13	45.54	45.68	-0.14
6C	35.19	35.20	-0.01	30.12	30.90	-0.78	35.52	35.26	0.26	45.54	45.76	-0.22
7C	35.19	34.89	0.30	30.12	30.51	-0.39	35.52	35.17	0.35	45.54	44.82	0.72
Min	34.13	33.98	0.15	29.40	29.22	0.18	35.52	35.08	0.44	45.54	44.82	0.72
Max	35.19	35.78	-0.59	30.12	31.23	-1.11	35.52	35.93	-0.41	46.38	47.06	-0.68
RMSE	0.30			0.39			0.23			0.39		

Note: 1. The proportion of green space is 0.60 in the area.

2. ΔT referred to the differentiated temperature between sample and simulated results.

Table C.21 The feasibility test results in the third hotspot location (°C).

	January 21, 2018			February 6, 2018			March 26, 2018			April 11, 2018		
	Sample	Simulate	ΔT	Sample	Simulate	ΔT	Sample	Simulate	ΔT	Sample	Simulate	ΔT
1A	34.52	34.53	-0.01	29.72	29.92	-0.20	36.14	36.55	-0.41	46.37	46.47	-0.10
2A	34.70	34.69	0.01	29.72	30.10	-0.38	37.18	36.67	0.51	46.65	46.54	0.11
3A	35.00	35.49	-0.49	31.13	31.44	-0.31	37.18	36.62	0.56	46.37	46.90	-0.53
3B	34.30	34.66	-0.36	29.78	30.23	-0.45	36.14	36.26	-0.12	46.71	46.52	0.19
4A	35.66	35.56	0.10	31.13	31.53	-0.40	36.95	36.48	0.47	47.47	47.12	0.35
4B	34.95	34.98	-0.03	29.74	30.15	-0.41	36.95	36.56	0.39	46.37	46.59	-0.22
5A	35.25	34.97	0.28	29.74	30.09	-0.35	37.18	36.59	0.59	46.63	46.90	-0.27
5B	34.70	34.62	0.08	29.72	29.69	0.03	36.14	36.11	0.03	46.37	46.46	-0.09
6A	35.25	35.19	0.06	29.79	30.08	-0.29	36.14	36.20	-0.06	47.85	47.16	0.69
6B	34.95	34.85	0.10	29.72	29.64	0.08	35.36	35.66	-0.30	46.37	46.55	-0.18
6C	34.52	34.52	0.00	29.42	29.21	0.21	35.25	35.13	0.12	46.37	46.40	-0.03
Min	34.30	34.52	-0.22	29.42	29.21	0.21	35.25	35.13	0.12	46.37	46.40	-0.03
Max	35.66	35.56	0.10	31.13	31.53	-0.40	37.18	36.67	0.51	47.85	47.16	0.69
RMSE	0.21			0.31			0.38			0.31		

Note: 1. The proportion of green space is 0.30 in the area.

2. ΔT referred to the differentiated temperature between sample and simulated results.

Table C.22 The feasibility results in the first hotspot location based on the selected proportion of green space ($^{\circ}\text{C}$).

	March 31, 2014		April 16, 2014		March 20, 2016		April 5, 2016	
	Decreased temperature	ΔT						
1D	43.73	1.66	39.25	2.08	42.96	0.55	44.84	1.35
1E	43.38	1.66	40.60	2.08	41.31	0.55	44.61	1.35
2B	44.12	1.66	39.06	2.08	42.28	0.55	43.76	1.35
2C	44.20	1.66	39.12	2.08	42.32	0.55	44.73	1.35
2D	43.83	1.66	39.26	2.08	43.02	0.55	44.79	1.35
2E	43.63	1.66	39.18	2.08	41.56	0.55	44.03	1.35
3A	43.59	1.66	39.27	2.08	41.82	0.55	43.45	1.35
3B	43.97	1.66	39.29	2.08	42.10	0.55	44.00	1.35
3C	44.24	1.66	39.23	2.08	42.41	0.55	44.73	1.35
3D	44.26	1.66	40.31	2.08	41.38	0.55	43.78	1.35
3E	44.18	1.66	39.25	2.08	41.49	0.55	43.69	1.35
4B	44.44	1.66	39.10	2.08	43.00	0.55	43.95	1.35
4C	44.31	1.66	39.25	2.08	41.79	0.55	43.90	1.35
4D	44.20	1.66	40.31	2.08	40.89	0.55	43.93	1.35
4E	44.40	1.66	39.42	2.08	41.04	0.55	43.22	1.35
5B	44.46	1.66	39.14	2.08	43.02	0.55	43.93	1.35
5C	44.11	1.66	40.17	2.08	41.37	0.55	43.53	1.35
5D	43.77	1.66	40.36	2.08	40.55	0.55	43.70	1.35
6A	44.05	1.66	39.06	2.08	41.66	0.55	43.13	1.35
6B	44.25	1.66	39.17	2.08	41.85	0.55	43.84	1.35
6C	43.91	1.66	39.40	2.08	40.78	0.55	43.65	1.35
6D	43.66	1.66	39.21	2.08	40.77	0.55	43.71	1.35
7B	44.15	1.66	39.11	2.08	41.17	0.55	43.35	1.35
7C	43.89	1.66	39.18	2.08	40.67	0.55	43.48	1.35
7D	43.48	1.66	39.31	2.08	40.86	0.55	43.91	1.35
8A	43.25	1.66	38.97	2.08	41.06	0.55	42.86	1.35
8B	43.50	1.66	39.17	2.08	41.42	0.55	43.49	1.35
8C	43.41	1.66	39.10	2.08	41.00	0.55	43.50	1.35
8D	43.74	1.66	39.14	2.08	41.03	0.55	44.08	1.35
9A	42.86	1.66	38.94	2.08	41.09	0.55	43.10	1.35
9B	43.09	1.66	39.08	2.08	41.03	0.55	44.02	1.35
10B	42.62	1.66	39.34	2.08	41.71	0.55	43.92	1.35
11A	43.10	1.66	39.16	2.08	41.59	0.55	44.06	1.35
11B	43.45	1.66	39.13	2.08	42.17	0.55	44.80	1.35
Min	42.62	1.66	38.94	2.08	40.55	0.55	42.86	1.35
Max	44.46	1.66	40.60	2.08	43.02	0.55	44.84	1.35
Mean	43.80	1.66	39.35	2.08	41.59	0.55	43.87	1.35

Note: 1. The proportion of green space is 0.45 in the area.

2. ΔT is the differentiated temperature between actual temperature and decreased temperature.

Table C.23 The feasibility results in the second hotspot location based on the selected proportion of green space ($^{\circ}\text{C}$).

	March 31, 2014		April 16, 2014		March 20, 2016		April 5, 2016	
	Decreased temperature	ΔT						
1B	43.06	2.21	39.45	2.78	41.95	0.73	44.09	1.80
2A	42.98	2.21	38.54	2.78	42.06	0.73	44.48	1.80
2B	43.12	2.21	39.46	2.78	41.86	0.73	44.49	1.80
3A	44.18	1.66	38.96	2.08	42.41	0.55	44.74	1.35
3B	44.33	1.33	39.60	1.67	42.43	0.44	45.22	1.08
4A	43.91	2.06	38.63	2.59	42.93	0.68	44.01	1.68
4B	43.88	2.21	39.73	2.78	42.99	0.73	44.33	1.80
4C	43.64	2.21	38.61	2.78	43.09	0.73	43.64	1.80
5A	43.65	2.21	38.54	2.78	42.99	0.73	43.69	1.80
5B	43.82	2.21	39.25	2.78	41.52	0.73	43.93	1.80
5C	43.65	2.21	38.52	2.78	43.21	0.73	43.59	1.80
5D	43.07	2.21	38.31	2.78	42.62	0.73	43.04	1.80
6A	42.86	2.21	38.20	2.78	41.90	0.73	43.35	1.80
6B	42.91	2.21	38.50	2.78	42.07	0.73	43.83	1.80
6C	42.73	2.21	38.33	2.78	42.57	0.73	43.50	1.80
7C	41.94	2.21	38.33	2.78	42.51	0.73	43.26	1.80
Min	41.94	1.33	38.20	1.67	41.52	0.44	43.04	1.08
Max	44.33	2.21	39.73	2.78	43.21	0.73	45.22	1.80
Mean	43.36	2.11	38.81	2.65	42.44	0.69	43.95	1.72

Note: 1. The proportion of green space is 0.60 in the area.

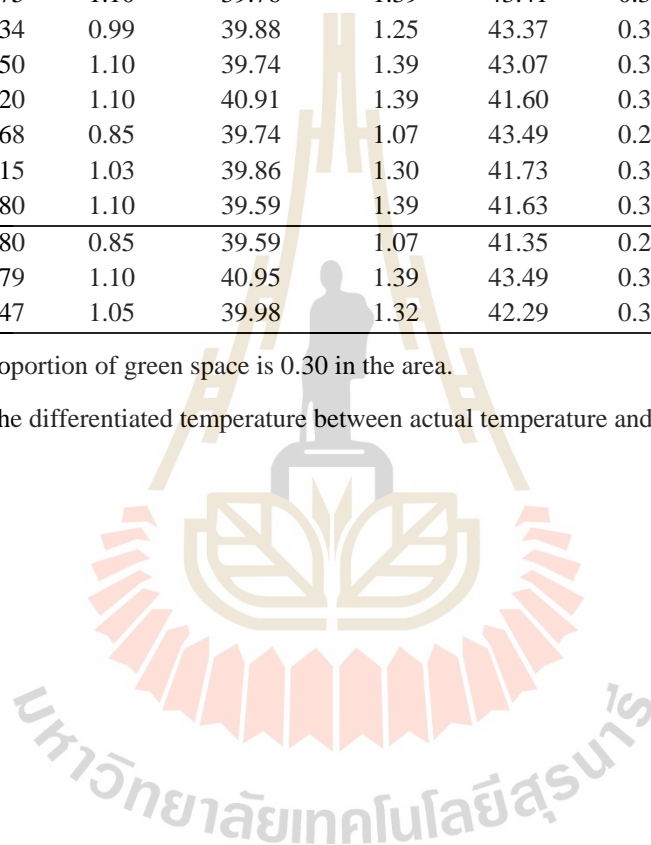
2. ΔT is the differentiated temperature between actual temperature and decreased temperature.

Table C.24 The feasibility results in the third hotspot location based on the selected proportion of green space ($^{\circ}\text{C}$).

	March 31, 2014		April 16, 2014		March 20, 2016		April 5, 2016	
	Decreased temperature	ΔT						
1A	44.79	1.10	39.76	1.39	41.52	0.36	44.22	0.90
2A	44.75	1.10	40.95	1.39	41.35	0.36	44.02	0.90
3A	44.79	1.10	39.80	1.39	41.76	0.36	44.38	0.90
3B	44.46	0.96	39.77	1.20	42.21	0.32	44.53	0.78
4A	44.75	1.10	39.76	1.39	43.41	0.36	45.23	0.90
4B	44.34	0.99	39.88	1.25	43.37	0.33	44.33	0.81
5A	44.50	1.10	39.74	1.39	43.07	0.36	45.19	0.90
5B	44.20	1.10	40.91	1.39	41.60	0.36	44.31	0.90
6A	44.68	0.85	39.74	1.07	43.49	0.28	45.43	0.69
6B	44.15	1.03	39.86	1.30	41.73	0.34	44.33	0.84
6C	43.80	1.10	39.59	1.39	41.63	0.36	44.27	0.90
Min	43.80	0.85	39.59	1.07	41.35	0.28	44.02	0.69
Max	44.79	1.10	40.95	1.39	43.49	0.36	45.43	0.90
Mean	44.47	1.05	39.98	1.32	42.29	0.35	44.57	0.86

Note: 1. The proportion of green space is 0.30 in the area.

2. ΔT is the differentiated temperature between actual temperature and decreased temperature.



CURRICULUM VITAE

Name Ekkaluk Salakkham

Date of Birth April 11, 1984

Place of Birth Sisaket Province, Thailand

Education

2002-2006 Bachelor of Science in Environmental Science, Faculty of Science, Khon Kaen University.

2006-2010 Master of Science in Remote Sensing and Geographic Information System, Faculty of Science, Khon Kaen University.

Work Experience

2011-present Lecturer at the Department of Geography and Geoinformation, Buriram Rajabhat University.

2007-2010 Research assistant at Geo-informatics Centre for Development of Northeast Thailand, Khon Kaen University.